SYNTHESIS AND STRUCTURAL CHARACTERIZATION OF MODIFIED $LiMnPO_4$ CATHODE MATERIALS FOR LITHIUM ION BATTERIES

RAJAMMAL KARUPPIAH

FACULTY OF SCIENCE
UNIVERSITY OF MALAYA
KUALA LUMPUR

2016

SYNTHESIS AND STRUCTURAL CHARACTERIZATION OF MODIFIED $LiMnPO_4$ CATHODE MATERIALS FOR LITHIUM ION BATTERIES

RAJAMMAL KARUPPIAH

THESIS SUBMITTED IN FULFILMENT OF THE REQUIREMENTS FOR THE DEGREE OF DOCTOR OF PHILOSHOPY

DEPARTMENT OF PHYSICS
FACULTY OF SCIENCE
UNIVERSITY OF MALAYA
KUALA LUMPUR

2016

UNIVERSITY OF MALAYA

ORIGINAL LITERARY WORK DECLARATION

Name of Candidate: Rajammal A/P Karuppiah

Registration/Matric No: SHC 120072

Name of Degree:Doctor of Philoshopy

Title of Thesis: Synthesis and structural characterization of modified $LiMnPO_4$ cathode materials for lithium ion batteries

Field of Study: Advanced Materials

I do solemnly and sincerely declare that:

(1) I am the sole author/writer of this Work;
(2) This Work is original;
(3) Any use of any work in which copyright exists was done by way of fair dealing and for permitted purposes and any excerpt or extract from, or reference to or reproduction of any copyright work has been disclosed expressly and sufficiently and the title of the Work and its authorship have been acknowledged in this Work;
(4) I do not have any actual knowledge nor do I ought reasonably to know that the making of this work constitutes an infringement of any copyright work;
(5) I hereby assign all and every rights in the copyright to this Work to the University of Malaya ("UM"), who henceforth shall be owner of the copyright in this Work and that any reproduction or use in any form or by any means whatsoever is prohibited without the written consent of UM having been first had and obtained;
(6) I am fully aware that if in the course of making this Work I have infringed any copyright whether intentionally or otherwise, I may be subject to legal action or any other action as may be determined by UM.

Candidate's Signature Date:

Subscribed and solemnly declared before,

Witness's Signature Date:

Name:

Designation:

ABSTRACT

Rechargeable lithium ion batteries are favorable option for portable electronic devices, electric vehicles and hybrid electric vehicles. Attractive factors such as high energy density, long cycle life and environment friendliness are the main inspirations to make lithium ion batteries as the best choice for energy storage systems. Cathode materials play important role in determining performance of lithium ion batteries. Lithium manganese phosphate, $LiMnPO_4$ is one of the promising cathode materials due to its high energy capacity, non-hazardous, cheap and better chemical and thermal stability. However, poor electronic and ionic conductivities, Jahn-Teller distortion involving Mn^{3+} ions and larger interface strain due to the volume change between $LiMnPO_4$ and $MnPO_4$ during lithiation and delithiation found to be major drawbacks of its applications. In order to overcome such downsides, various strategies have been carried out as following: (a) particle size reduction and morphology control to improve Li^+ diffusion, (b) metal oxide coating to enhance electronic conductivity (c) cation substitution to raise Li^+ ions diffusion. In this work, different modifications were approached to study improved electrochemical activity of $LiMnPO_4$. $LiMnPO_4$ cathode materials were prepared by sol gel method with the aid of oxalic acid and effects of different sintering temperatures on structural and electrochemical characterizations were studied. The calcination temperatures have high impact on structural and electrochemical properties. The obtained $LiMnPO_4$ at 700 °C (calcination temperatures) has smaller crystallite size and low strain value than that of other samples. It exhibited superior electrochemical performance among the samples. It delivered initial discharge capacity of 103.4 $mAhg^{-1}$ at 0.05 C. Apart from that, sodium was substituted partially to lithium site of $LiMnPO_4$. $Li_{0.97}Na_{0.03}MnPO_4$ sintered at 600°C and 700°C delivered discharge capacities of 87.74 mAh g^{-1} and 99.83 mAh g^{-1}at the 60th cycle which shows capacity retention of 81.23 % and 84.15 % correspondingly. While ZnO coating with

different weight percentages were applied on $LiMnPO_4$ to observe the improvement. Galvanostatic charge-discharge tests showed that the ZnO coated $LiMnPO_4$ sample has an enhanced electrochemical performance compared to pristine $LiMnPO_4$. The 2 wt.% of ZnO based $LiMnPO_4$ exhibited maximum discharge capacity of 102.2 mAh g^{-1} than that of pristine $LiMnPO_4$ (86.2 mAh g^{-1}) and 1wt.% of ZnO based $LiMnPO_4$ (96.3 mAh g^{-1}) respectively. The maximum cyclic stability of 96.3 % was observed in 2 wt.% of ZnO based $LiMnPO_4$ up to 100 cycles. Another modification with aluminium and copper co-doping was made into $LiMnPO_4$ structure. The doping of Al and Cu for Mn in $LiMnPO_4$ exhibited lattice shrinkage and improvement of electronic conductivity. $LiMn_{0.8}Al_{0.1}Cu_{0.1}PO_4$ delivered highest discharge capacity of 166 $mAhg^{-1}$ and $LiMn_{0.9}Al_{0.05}Cu_{0.05}PO_4$ exhibited initial discharge capacity of 152 $mAhg^{-1}$ at 0.05C. Al, Cu co-doped samples seem favourable candidate for cathode materials at low current rates while ZnO coated samples would be outstanding choice for high current rates. Doping and metal oxide coating can be used together in future work for better electrochemical properties.

ABSTRAK

Bateri ion litium boleh dicas semula adalah pilihan yang baik untuk peranti elektronik mudah alih, kenderaan elektrik dan kenderaan elektrik hibrid. Faktor-faktor yang menarik seperti kepadatan tenaga yang tinggi, kitaran hidup panjang dan kemesraan alam adalah inspirasi utama untuk membuat bateri ion litium sebagai pilihan terbaik bagi sistem penyimpanan tenaga. Bahagian katod memainkan peranan penting dalam menentukan prestasi bateri ion litium. Litium mangan fosfat, $LiMnPO_4$ adalah salah satu bahan katod yang mempunyai masa depan yang cerah kerana kapasiti tenaga yang tinggi, tidak berbahaya, bahan kimia murah dan kestabilan terma. Walau bagaimanapun konduksi elektronik dan ionik yang lemah, gangguan Jahn -Teller yang melibatkan ion Mn^{3+} dan ketegangan antara permukaan yang lebih besar disebabkan oleh perubahan isipadu antara $LiMnPO_4$ dan $MnPO_4$ semasa lithiation dan delithiation didapati kelemahan utama aplikasinya. Dalam usaha untuk mengatasi kelemahan itu, pelbagai strategi telah dijalankan seperti berikut: (a) pengurangan saiz zarah dan kawalan morfologi untuk meningkatkan penyebaran Li^+, (b) lapisan oksida logam untuk meningkatkan kekonduksian elektronik (c) penggantian separa dalam kation untuk meningkatkan penyebaran Li^+ ion. Dalam kerja ini, pengubahsuaian yang berbeza telah didekati untuk mengkaji aktiviti elektrokimia baik daripada $LiMnPO_4$. Bahan katod $LiMnPO_4$ telah disediakan dengan kaedah sol gel dengan bantuan asid dan kesan suhu pemanasan yang berbeza pada pencirian struktur dan elektrokimia telah dikaji. Suhu pemanasan mempunyai impak yang tinggi ke atas sifat-sifat struktur dan elektrokimia. The $LiMnPO_4$ diperolehi pada suhu 700 °C (suhu pemanasan) mempunyai zarah yang lebih kecil dan nilai tegangan rendah berbanding dengan sampel lain. Ia mempamerkan prestasi elektrokimia unggul di kalangan sampel. Ia menyampaikan kapasiti permulaan sebanyak 103.4 $mAhg^{-1}$ pada 0.05 C. Selain itu, sodium diganti sebahagiannya ke bahagian litium $LiMnPO_4$. $Li_{0.97}Na_{0.03}MnPO_4$ dipanaskan pada 600 °C dan 700 °C

menyampaikan kapasiti 87.74 $mAhg^{-1}$ dan 99.83 $mAhg^{-1}$ pada kitaran ke-60 yang menunjukkan pengekalan kapasiti 81.23 % dan 84.15 % masing-masing. Sementara itu, salutan ZnO yang berlainan peratus telah digunakan pada $LiMnPO_4$ untuk mengkaji peningkatan. Ujian Galvanostatik menunjukkan sampel $LiMnPO_4$ bersalut ZnO mempunyai prestasi elektrokimia yang dipertingkatkan berbanding $LiMnPO_4$. 2 wt. % ZnO berdasarkan $LiMnPO_4$ dipamerkan kapasiti pelepasan maksimum 102.2 $mAhg^{-1}$ berbanding dengan LiMnPO4 (86.2 $mAhg^{-1}$) manakala 1 wt. % ZnO mempunyai kapasiti 96.3 $mAhg^{-1}$. Kestabilan kitaran maksimum 96.3 % diperhatikan dalam 2 wt. % ZnO sehingga 100 kitaran. Satu lagi pengubahsuaian dengan aluminium dan kuprum telah dibuat ke dalam struktur $LiMnPO_4$. Penggantian Al dan Cu untuk sebahagian Mn dalam $LiMnPO_4$ mempamerkan pengecutan kekisi dan peningkatan kekonduksian elektronik. $LiMn_{0.8}Al_{0.1}Cu_{0.1}PO_4$ mempunyai kapasiti pelepasan tertinggi 166 $mAhg^{-1}$ dan $LiMn_{0.9}Al_{0.05}Cu_{0.05}PO_4$ menunjukkan kapasiti permulaan sebanyak 152 $mAhg^{-1}$ pada 0.05C. Sampel yang didopkan Al, Cu bersama merupakan calon yang baik untuk bahan katod pada kadar arus yang rendah manakala sampel bersalut ZnO akan menjadi pilihan cemerlang untuk kadar arus yang tinggi. Dop dan lapisan oksida logam boleh digunakan bersama dalam kerja-kerja masa depan untuk bahan elektrokimia yang lebih baik.

ACKNOWLEDGEMENTS

Humble pranams to divine lotus feet……

mayi sarvāṇi karmāṇi
sannyasyādhyātma-cetasā
nirāśīr nirmamo bhūtvā
yudhyasva vigata-jvaraḥ *(Bhagavad Gita 3.30)*

'Therefore, surrendering all your works unto Me, with full knowledge of Me, without desires for profit, with no claims to proprietorship, and free from lethargy, do your duty'

With the blessings of almighty GOD, I have gone through PhD cycle with full of hard work, success, failure, pain, gain, happiness, frustration, encouragement, self-motivation and some other new unique experiences.

My great thanks to supervisors Prof. Dr. Ramesh T. Subramaniam and Dr. Ramesh Kasi for their kind guidance and support. They have always advised me for betterment and made hidden abilities within me visible.

I would like to express my thanks to Dr. Navaneethan for his valuable guidance. Special thanks to all my friends, labmates, administrative and technical staff members of University of Malaya. I also appreciate all the teachers who have taught me since my Tamil primary school SJK(T) Emerald to higher institution. Their teachings have molded strong foundation for my knowledge and skills.

I am very grateful for my mother Madam Dhanaletchumy Nadesapillai. She is superwoman in my life. Her sacrifices and love bring me to continuous achievement. My meaning of life blooms from her since at early age. I would like to convey my thanks to all family members for their understanding and support.

I extend my sincere gratitude to my dear loving husband. Tight knot with him in the middle of PhD journey showed me new experiences. His motivation and love throughout my study is very meaningful and wonderful.

TABLE OF CONTENTS

LIST OF FIGURES

LIST OF TABLES

LIST OF SYMBOLS AND ABBREVIATIONS

For example:

XRD	:	X-Ray Diffraction
FESEM	:	Field emission scanning electron microscope
TEM	:	Transmission electron microscope
EIS	:	Electrochemical impedance specroscopy
TAB	:	Teflonized acetylene black
C	:	Current rate
Li	:	Lithium
$LiPF_6$	:	Lithium hexafluoro phosphate
ZnO	:	Zinc oxide
Na	:	Sodium
Al	:	Aluminum

LIST OF APPENDICES

CHAPTER 1: INTRODUCTION

1.1 Introduction of research

The rapid emergence of portable electronic devices and electric vehicles remarkably increases the exploration for new energy sources (Kim et al., 2011). The important key factors for energy sources are cheap, environmental friendly, good cycle life, safety and high specific energy (Kucinskis, Bajars, & Kleperis, 2013). With unique features, lithium ion batteries are considered as the energy source of choice compared to others. Specifically, lithium ion batteries possess two main intrinsic characteristics. It has longer cycle life and cheaper cost than lead acid batteries (Diouf & Pode, 2015). Nevertheless, current lithium ion battery technology still lacks its efficiency for hybrid and electric vehicles. Cost reduction, safety enrichment and particularly energy density enhancement are the major improvements (Scrosati, Hassoun, & Sun, 2011). High energy density of energy sources can be enhanced by increasing discharge capacity or increasing the working voltage of cathode materials (Lee, Huq, & Manthiram, 2013). In this background, continuous research effortss are being focused on developing successful cathodes that fulfills the requirements for lithium ion batteries (Wei, He, Zhang, Shen, & Ma, 2016).

Lithium manganese phosphate, $LiMnPO_4$ is becoming an attractive high energy cathode material. It has a redox potential of 4.1 V vs Li/Li^+ which is greater than $LiFePO_4$ (Lin Chen et al., 2016; Huang et al., 2016). The voltage is also beneficial because it is within current electrolytes stability limits (Deyu Wang et al., 2009). However, poor electronic and ionic conductivity of $LiMnPO_4$ cathode materials are its main hindrances for applications (Voepel et al., 2016; Zhang, Luo, Chang, Bao, & Liu, 2016).

It is noteworthy that the surface morphologies are essential factor for electrochemical properties. Recently hemoglobin-like $LiMnPO_4$ microspheres are prepared for better electrochemical activity due to presence of three dimensional (3D) hierarchical structures (Gu et al., 2015). $LiMnPO_4$ nanorods (< 30 nm) are produced by controlling boiling temperature, solvent, concentration of surfactants, reaction temperature and time (Kwon & Fromm, 2012). Cui et al (Cui, Xu, Kou, Wu, & Chen, 2014) reported that synthesized irregular flaky shaped $LiMnPO_4$ is achieved by-hollow-sphere Li_3PO_4 precursor, which is used to control the particle growth of $LiMnPO_4$. Also, Doi et al (Doi, Yatomi, Kida, Okada, & Yamaki, 2009) stated by controlling particle size, the diffusion and conduction path are shortened, which lead to improve the conductivity. On the other hand, Doan et al (Nam, Doan, Bakenov, & Taniguchi, 2010) reported that the carbon coated nanostructured $LiMnPO_4$ via combination of spray pyrolysis and dry ball milling revealed good electrochemical properties at high temperature and high charge/discharge rate of 2C. Herein, carbon layer also found to be effectively suppress the crystal growth during heat treatment, resulting in a significant improvement of cycling performance (Su, Liu, & Chen, 2013b).

Doping with metal elements plays an important role to enhance the ionic conductivity of $LiMnPO_4$ such as Fe (Xue Zhou, Ye Xie, Yuanfu Deng, 2015; Yang, Mi, Zhang, Wu, & Zhou, 2015), Cr (Gan et al., 2015), Zn (Fang et al., 2012), Ni (Ottmann, Jähne, Meyer, & Klingeler, 2015), V (Gutierrez et al., 2014) etc. Moreover, some researchers focused on dual substitution (Akimoto & Taniguchi, 2013; Kisu, Iwama, Onishi, & Nakashima, 2014; Vishwanathan Ramar and Palani Balaya, 2013). Recent work indicated that Cesium (Ce) doped $LiMnPO_4$ lead to attain easy diffusion of lithium ion in bulk materials (Kou, Chen, Tao, Dong, & Chen, 2015). In another work, electrochemically inactive cations were replaced partially for Mn, hence

$LiMn_{0.88}Mg_{0.1}Zr_{0.02}PO_4$ exhibited high discharge capacity (134.0 $mAhg^{-1}$) and lower irreversible capacity loss (Lee et al., 2010). This enhancement is accredited to great kinetic properties which are due to the reduced distortion of local structure. The co-substitution of iron (Fe) and magnesium (Mg) are evenly spread over $LiMnPO_4$ lead to shrinkage crystal lattice (Hu et al., 2010).

Besides that, $LiMn_2O_4$ was incorporated with $LiMnPO_4$ by one step polyol assisted pyro-synthesis (Kang et al., 2013). Herein, thermal stability of this composite was improved due to the incorporation of electrically active $LiMn_2O_4$ with non-electrically active $LiMnPO_4$ and the discharge capacity was found to be ~142 $mAhg^{-1}$.

Surface modification is another effective method to overcome cycling instability at higher voltages (Cho et al., 2015; Lu, Wu, Chen, Liu, & Zhang, 2015). Coating reduces the side reactions of cathode and electrolyte which causes negative effects to the electrochemical performance (Liu, Huang, Lin, Chen, & Liao, 2014; Shi et al., 2012). So far carbon coating has lead to enhance the electronic conductivity of $LiMnPO_4$ (Li-e Li, Jing Liu, Liang Chen, Huayun Xu, 2013; Moon, Muralidharan, & Kim, 2012; Su, Liu, & Chen, 2013a). Zhu et al stated that the insitu carbon (4.54 wt.%) coated $LiMnPO_4$ exhibits improved capacity (Hua-jun Zhu, Zhai, Yang, Liu, & Chen, 2014b). Also, Su et al proved that carbon coating promotes excellent rate capability in energy storage (Su et al., 2013a). Insitu carbon coated $LiMnPO_4$ prepared by solvothermal method in ethylene glycol has resulted the specific capacity of ~130 $mAhg^{-1}$ at 0.1 C (Liu, Liu, Huang, & Yu, 2013).

Until now, there are limited works published on metal oxide coated $LiMnPO_4$. Recently CeO_2/C hybrid coated $LiMnPO_4$ have been successfully synthesized by Chen

et al (Chen, Tao, Wang, Zhang, & Chen, 2015a). They found that nanometer sized CeO coating played role as an innerconnector in the carbon network which positively enhanced cycling stability (Chen et al., 2015a). Meanwhile Dong et al (Dong, Zhao, Duan, & Liang, 2014) reported that the Li_3VO_4 coated $LiMnPO_4$ electrode created three dimensional path of Li^+ ion transport path and also lowered Mn dissolution, thus hindered phase formation on the $LiMnPO_4$ surface which deteriorates rate capability.

By considering all these, present research has been carried out focusing different modifications that have not been so far explored on $LiMnPO_4$. Effects of sintering temperature on $LiMnPO_4$ cathode materials synthesized via sol gel method are explained. Modifications such as ZnO coating, ion doping at Li and Mn sites are studied.

1.2 Objectives of the research

Improvements of $LiMnPO_4$ to be used as a cathode materials in lithium ion batteries are the strong motivation of this work. The objectives of current research are stated as follows:

1. To optimize sintering temperature with ecofriendly, fast and easy modified sol gel route to prepare $LiMnPO_4$ cathode materials.
2. To ameliorate $LiMnPO_4$ cathode materials by non-hazardous metal oxide coating, ion doping at Li and Mn sites.
3. To characterize obtained $LiMnPO_4$ cathode materials in order to study the structural and electrochemical properties.

1.3 Scope of the thesis

This thesis is aimed to enhance $LiMnPO_4$ cathode materials using non-hazardous modifications. Chapter 1 summarizes the significant points of whole research work that presented in thesis.

Chapter 2 delivers insight of research topic and related literature review covering lithium ion batteries, types of cathode materials, outline about $LiMnPO_4$, synthesis methods that involved in recent reported works, various techniques that have been occupied to improve $LiMnPO_4$ cathode materials. This chapter will clearly explain the element of cathode materials in lithium ion batteries.

Chapter 3 provides $LiMnPO_4$ cathode materials preparation including steps and raw materials that have been used throughout the study. The characterization techniques of x-ray diffraction, field emission scanning electron microscope, transmission electron microscope, Raman microscope, electrochemical impedance spectroscopy are presented with relevant theoretical background. Cell preparation and capacity calculation are also explained in this chapter.

Chapter 4 describes the initial step with varying sintering temperatures on $LiMnPO_4$ precursor that attained from oxalic acid assisted sol gel method. The optimized temperature that gives good structural and electrochemical properties is evaluated. By employing optimized temperature accompanied by synthesis technique, further modifications have been intensified.

Chapter 5 demonstrates partial sodium replacement at lithium sites of $LiMnPO_4$ without changing its structure. Crystallite size and strain of the grains are analyzed and

presented. Effects of sodium on LiMnPO4 are explained based on electrochemical activity.

Chapter 6 elaborates next modification involving metal oxide coating. Different weight percentages of zinc oxide coating were applied on $LiMnPO_4$ and the best coating amount that yield enhanced electrochemical properties are evaluated.

Chapter 7 proceeds with modification about metal ion substitution. Aluminum and copper dual substitution in $LiMnPO_4$ are tested. The optimized component containing both dopants is determined.

Chapter 8 discusses results that achieved during all the modifications on $LiMnPO_4$. Results are compared for better understanding.

Chapter 9 summarizes conclusions drawn from the modified $LiMnPO_4$ cathode materials and subsequently indicates suggestions for future works.

CHAPTER 2: LITERATURE REVIEW

2.1 Evolution of lithium ion batteries

Batteries are capable of delivering stored chemical energy efficiently which is making it favourable option for hybrid vehicles (HEVs), plug-in hybrid vehicles (PHEVs) and electric vehicles (EVs) (Scrosati et al., 2011). A battery consists of positive and negative electrodes separated by an electrolyte. The potential difference between two electrodes is denoted as battery voltage (Gasteiger, Krischer, & Scrosati, 2013). The batteries can be categorized into primary (no rechargeable) or secondary (rechargeable). Rechargeable batteries can be recharged after discharging for number of times (cycle life). There are four main commercial rechargeable battery types such as lead acid introduced in 1850, presence of nickel-cadmium in 1899, nickel-metal hydride entered in 1989 and lithium ion commercialized starting 1991. Energy density of these batteries is depicted in Figure 2.1.

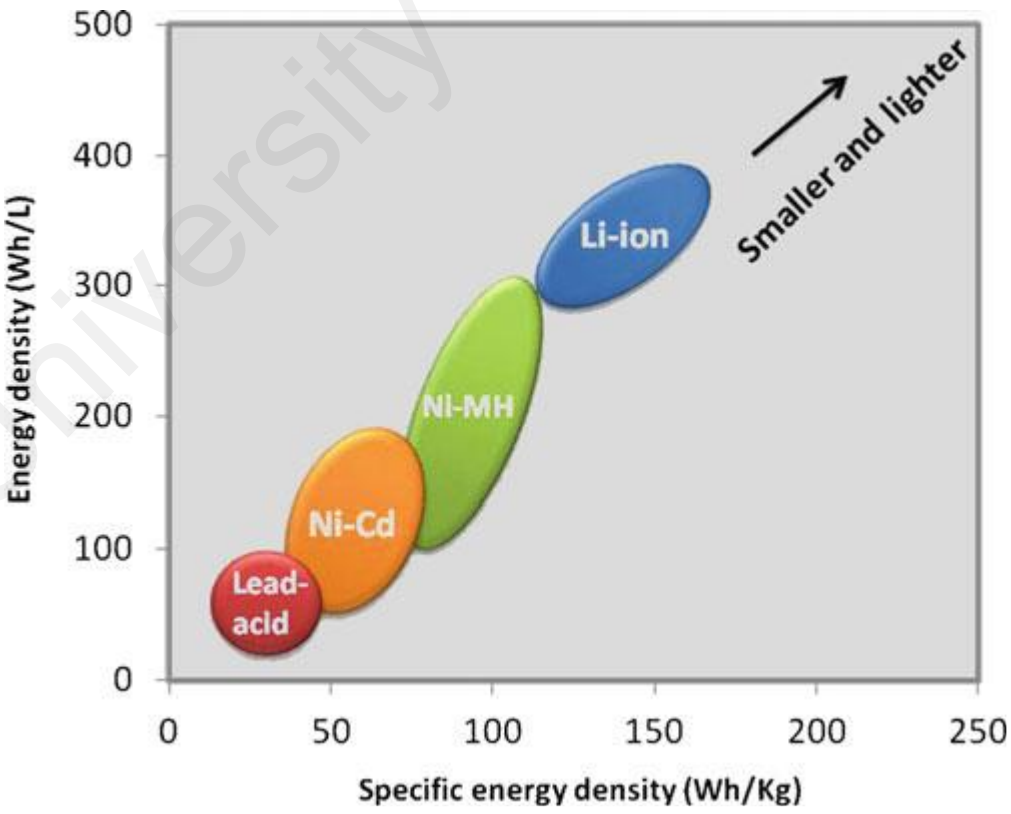

Figure 2.1: Energy density of commercial batteries
(Siegel, Richard W; Hu, Evelyn; Cox, 1999)

Table 2.1: Properties of commercial battery technologies (Diouf & Pode, 2015; Siegel, Richard W; Hu, Evelyn; Cox, 1999)

Properties	Lead acid	NiCd	NiMH	Li-ion
Anode	Pb	Cd	Intermetallic	Graphite
Cathode	PbO	NiOOH	NiOOH	$LiCoO_2$
Electrolyte	H_2SO_4(aq)	KOH(aq)	KOH(aq)	$LiPF_6$
Voltage	2.1	1.2	1.2	3.7
Energy density (Wh/kg)	30 – 50	45 – 80	60 – 120	150 – 190
Internal resistance	<100	100 – 300	200 – 300	150 – 300
Cycle life (80% discharge)	200 – 300	1000	300 – 500	500 – 1000
Fast charge time	8 – 16 h	1 h	2 – 4 h	2 – 4 h
Self discharge /month (room temperature)	5%	20%	30%	<10%
Toxicity	Very high	Very high	Low	Low

As summarized in Table 2.1, lithium ion batteries own unique features to become option for portable electronic devices and vehicle technology (Liu, Neale, & Cao, 2016; Scrosati et al., 2011). Table 2.2 gives clear explanation of highly dependent electric vehicles on lithium ion batteries.

Table 2.2: Types of electric vehicles(EV) and its battery requirements
(Etacheri et al., 2011)

a Modes of operation	battery capacity needed, kWh	Energy density, Wh/kg	Weight of battery, Kg	Speed, kilometres per hour	Distance on one charge, kilometres
 Hybrid	<3	40-50 (Ni-MH)	60 (Ni-MH)	100+	15
 Plug in Hybrid	5.6-18	90-100 (Li-ion)	60-200 (Li-ion)	100+	10-60
 Full EV	35-54	90-100 (Li-ion)	450 (Li-ion)	>100	150-200

Nowadays, hybrid electric cars exist with internal combustion engines. Only short driving distance can be managed by electrical propulsion via small batteries. Ni-MH batteries can be used for these category electric vehicles. Concerning future view, significant gasoline usage needs to be reduced and propulsion mainly on electrical power have to be focused. In order to achieve that, car batteries with high energy is needed. Unfortunately, Ni-MH batteries will not meet the criteria to occupy full electric vehicles due to its low energy density (Etacheri, Marom, Elazari, Salitra, & Aurbach, 2011). Lithium ion batteries are excellent candidate to fulfill the electric vehicle requirements.

The performances of lithium ion batteries are greatly influenced by the structure and properties of the electrode materials and electrolytes, exclusively the characteristics of cathode materials (Gong & Yang, 2011; Hu, Pang, & Zhou, 2013).

Figure 2.2 represents working principles of lithium ion batteries. In commercial, Li-ion batteries are equipped graphite as an anode and lithium transition metal oxides as cathodes. Charging process denotes moving of Li-ions from the cathode passing through the electrolyte and intercalating in graphite. Li-ions migrate from graphite to cathode during cell discharging process. At the same time, equivalent number of electrons accompanied during intercalation and deintercalation through external circuit for charge compensation (Scrosati & Garche, 2010).

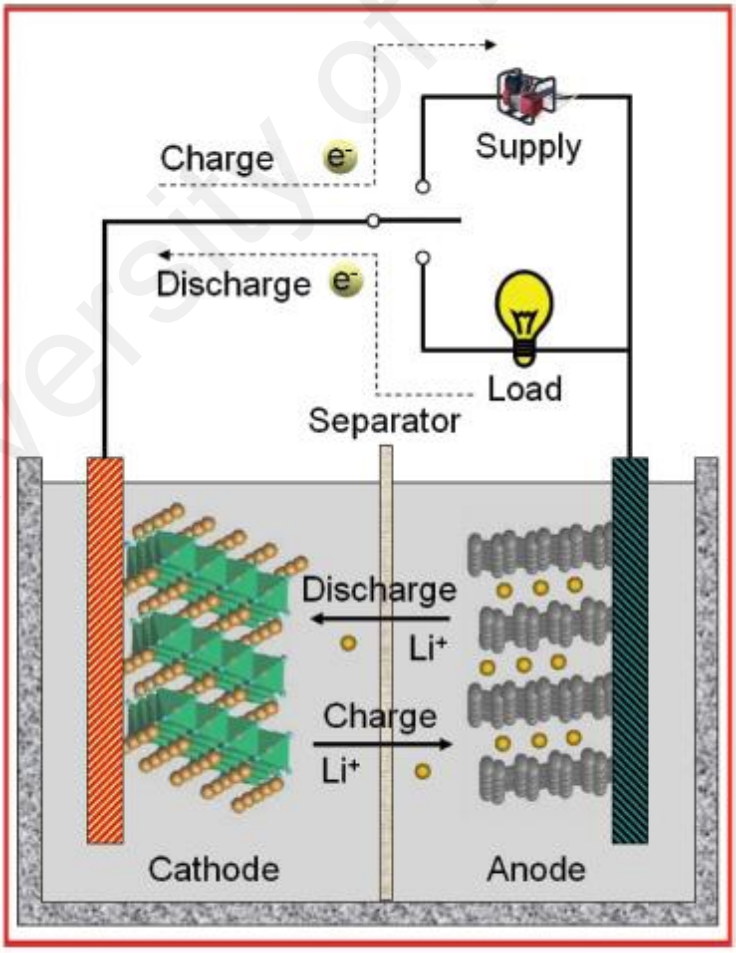

Figure 2.2: Schematic diagram of lithium ion batteries (Deng, Kim, Lee, & Cho, 2009)

Since Li^+ shuttles between the anode and cathode throughout charge-discharge, this Li-ion cell also expressed as rocking chair, swing or shuttle-cock cell (Pitchai, Thavasi, Mhaisalkar, & Ramakrishna, 2011).

The half-cell reaction at respective electrodes can be summarized as following (Pitchai et al., 2011):

At the cathode:

$$Li_{1-x}CoO_2 + xLi^+ + xe^- \longleftrightarrow LiCoO_2$$

At the anode:

$$LiC_6 \longleftrightarrow Li_{1-x}C_6 + xLi^+ + xe^-$$

Overall reaction:

$$LiC_6 + Li_{1-x}CoO_2 \longleftrightarrow Li_{1-x}C_6 + LiCoO_2$$

$\longrightarrow$ Discharge	$\longleftarrow$ Charge

Energy of a battery relies on voltage and its capacity, thus battery with higher energy density is attained when the voltage and capacity higher. When same anode material is occupied in the battery, cathode with higher potential increases capacity of the cathode which leads to high energy battery (Yoshio, Brodd, & Kozawa, 2015). Hence, cathode material is the key component that plays vital role in determining the performance of Li-ion (Hu et al., 2013; Zaghib et al., 2013). Key elements for a material to be chosen as cathode in lithium ion batteries include (Dou, 2013, 2015; Wei et al., 2016; Whittingham, 2004):

- **High energy density**

High energy density materials provide high voltage and capacity which able to perform within electrochemical stability windows of electrolytes.

- **High power density**

Power density is measured by characteristics such as rate capability, fast charging and reduced resistance of the cell.

- **Long term stability**

Enable for long cycling performances and capacity retention. Both cathode materials and interface with electrolyte should be stable.

- **Safety**

Safety of the Li-ion batteries is one of the important aspects that need to be considered at the materials selection level. Heat generation due to exothermic reactions with electrolyte should be lessened.

- **Cost**

The cost of batteries is determined by the cost of the materials used during synthesis and fabrication. Cathode materials should be cheap that encourages and aids manufacturer for commercialization.

Among these parameters, high energy density is the most significant for Li-ion batteries applications in mobile devices, whereas cost efficiency and fast charging are essential requirements for Li-ion batteries utilization in electric vehicles (Xu, Lee, Jeong, Kim, & Cho, 2013).

2.2 Types of cathode materials

Considering above mentioned factors, different types of cathode materials are being employed as cathode materials in lithium ion batteries. Each type of cathode materials own its unique structural characteristics that aiding in electrochemical applications (Bhaskar et al., 2014a). Significant morphologies with various dimensions comprising such as nanoparticles, nanotubes, core-shell structures are schematically given in Figure 2.3.

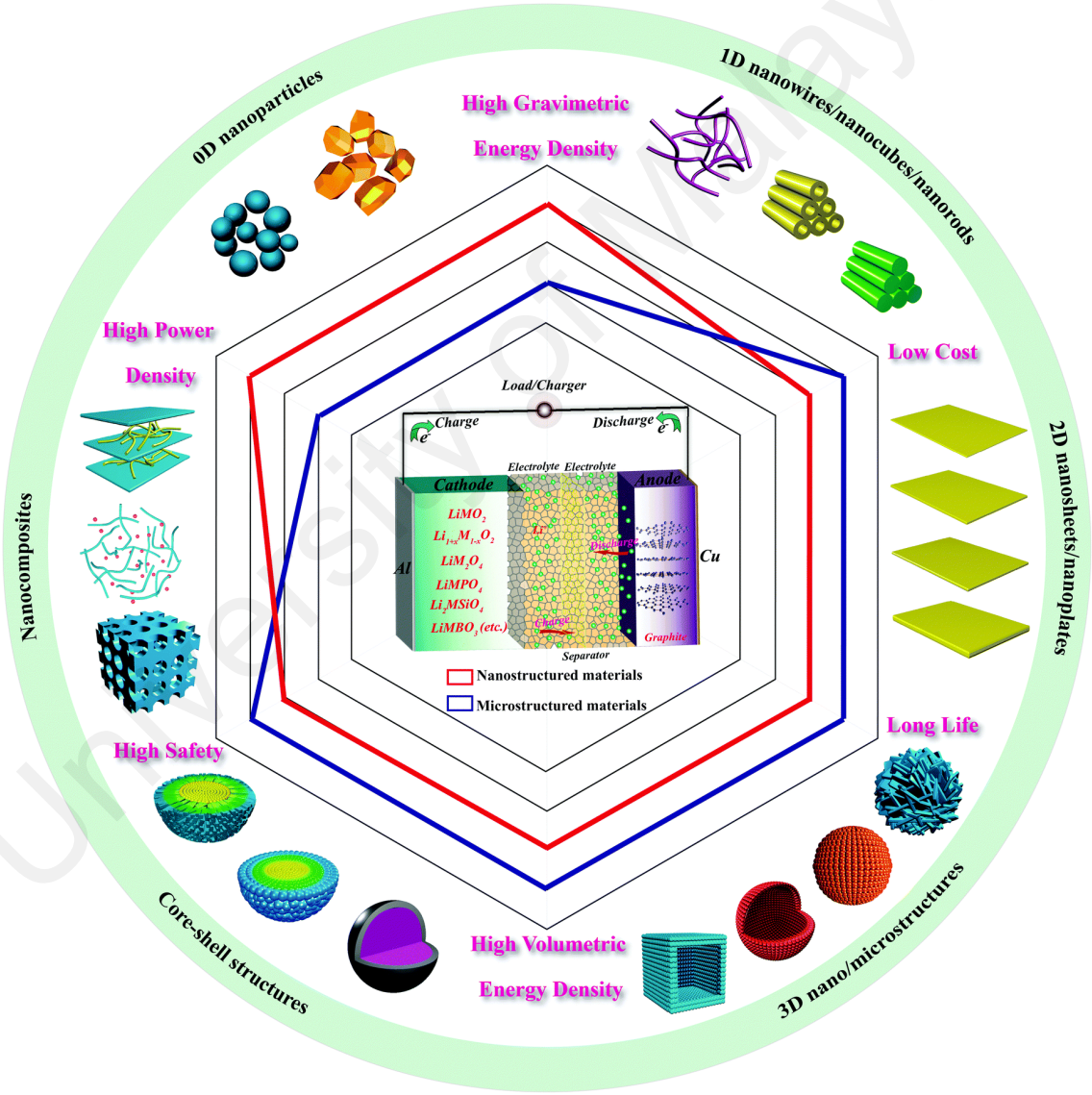

Figure 2.3: Cathode materials with unique and varied crystal structures
(Chen, Zhao, Zhang, & Wu, 2016)

2.2.1 Spinel type cathode materials, LiA_2O_4

Spinel type cathode materials with their general formula LiA_2O_4, grouped into Fd3m space group. Li ions occupy 8a tetrahedral sites while A metal ions occupy 16d octahedral sites. Empty 16c octahedral sites and 8a tetrahedral sites creates three dimensional diffusion path for lithium (Bhaskar et al., 2014b; Xia, Luo, & Xie, 2012). Figure 2.4 shows example of spinel structure. Among the spinels, manganese based structures getting wider attention (Potapenko & Kirillov, 2014).

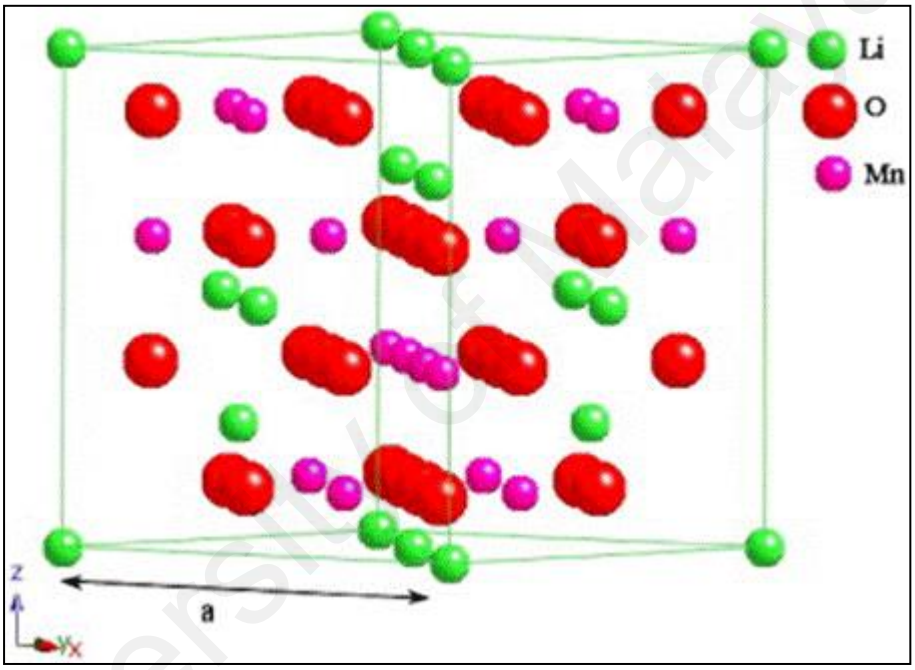

Figure 2.4: Spinel structure of $LiMn_2O_4$ (Xia et al., 2012)

Lithium manganese oxide spinel, $LiMn_2O_4$ is inexpensive, non-toxic and environmentally friendly compared to $LiCoO_2$. It can achieve high potential against lithium electrode (3.0 V– 4.5 V) with theoretical capacity of 148 $mAhg^{-1}$ (Potapenko & Kirillov, 2014; Xiao et al., 2013). However, its applications are limited by capacity fading upon repeated cycling process. This capacity fading happens due to Jahn-Teller distortion, electrolyte decomposition at higher working voltage, structural instability and unstable reaction by two phases (Chen, Wu, Huang, & Zhang, 2016; Tang et al.,

2013; Thirunakaran, Ravikumar, Gopukumar, & Sivashanmugam, 2016; Wang, Lai, Li, Zhang, & Huang, 2015; Yazhou Wang et al., 2013).

Lithium manganese nickel oxide, $LiNi_{0.5}Mn_{1.5}O_4$ is another attractive spinel with high working voltage of 4.7 V and capacity about 147 $mAhg^{-1}$ (Jin, Lu, Wang, Yang, & Duh, 2014; Mn et al., 2016; Song, Kim, Kim, Hong, & Choi, 2016; Zeng et al., 2014). High rate capability contributed by three dimensional (3D) lithium ion diffusion in the spinel lattice (Zhi-gang Gao et al., 2016; Jiang et al., 2016; Luo, 2015).

Even though high voltage corresponds to high energy density but it becomes challenging factor for practical applications in lithium ion batteries. It is well known that conventional electrolytes are undergoing oxidative decomposition at voltage above 4.5 V versus Li/Li^+ which causes solid electrolyte interface (SEI) film formed on the cathode surface. Besides that, commercial electrolytes containing of $LiPF_6$ salt may cause side reactions with presence of water. It also increases HF attack thus deteriorate $LiNi_{0.5}Mn_{1.5}O_4$ materials (Chen et al., 2016; Hanafusa, Kotani, Ishidzu, Oka, & Nakamura, 2016; Song et al., 2016). Storage performance of $LiNi_{0.5}Mn_{1.5}O_4$ at higher temperature also another main drawback for its applications (Haiyan Li, Luo, Xie, Zhang, & Yan, 2015).

2.2.2 Silicate type cathode materials, Li_2ASiO_4

Lithium metal orthosilicates, Li_2MSiO_4 (M = Mn, Fe and Co) are another promising cathode materials because of their high capacity about 330 $mAhg^{-1}$ and alternative to toxic and expensive cathode materials (Qu, Liu, Fang, Yang, & Hirano, 2015; Yan-chao Wang, Zhao, Zhai, Li, & Nan, 2014). Figure 2.5 depicts structures of Li_2MSiO_4.

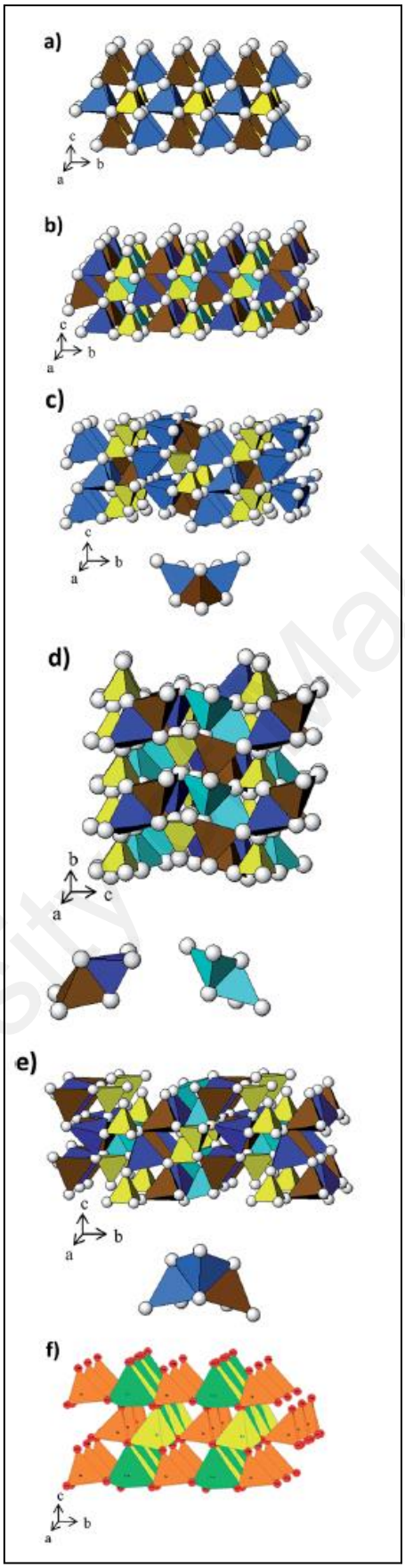

Figure 2.5: Structures of Li_2MSiO_4 (a) orthorhombic $\beta_{\parallel}$ ($Pmn2_1$) (b) orthorhombic β_1 ($Pbn2_1$, $Pna2_1$) (c) orthorhombic $\gamma_{\parallel}$ (Pmna, Pmnb, Cmma) (d) monoclinic γ_s ($P2_1/n$, $P2_1$) (e) monoclinic γ_o ($P2_1/n$) (f) monoclinic (P_n)
(Girish & Shao, 2015)

Stable Si-O bond enables thermal and chemical stability for energy applications (Zhang et al., 2015). Remarkably, two lithium ions can be extracted per Li_2MSiO_4 formula which would increase the capacity (Deng, Zhang, Fu, Yang, & Ma, 2010; Qu, Fang, Zhang, Yang, & Hirano, 2013; Zhai, Zhao, Cheng, Zhao, & Nan, 2015). However with these exceptional advantages, low electronic conductivity and small lithium diffusion coefficient found to be major drawbacks to its practical applications (Gummow, Han, Sharma, & He, 2014; Xu et al., 2015; Yi et al., 2014; Zhang et al., 2015; Hai Zhu et al., 2015). More efforts are continuously being taken to improve the materials such as novel hierarchical shuttle like architecture (Yang, Kang, He, et al., 2013), incorporation of nanospheres (Yang, Kang, Hu, et al., 2013), different synthesis techniques (Oghbaei, Baniasadi, & Asgari, 2016; Qu, Fang, Yang, & Hirano, 2012, 2014; Rong, Jing, & Leilei, 2015), carbon coating (Moriya, Miyahara, Hokazono, & Sasaki, 2014; Ni & Li, 2015; Rong et al., 2015), metal ion doping (Longo, Xiong, Kc, & Cho, 2014; Yang, Wang, Deng, Lv, & Xu, 2016) etc.

2.2.3 Tavorite type cathode materials, $LiAPO_4F$

Tavorite structured fluorophosphates, $LiMPO_4F$ and Li_2MPO_4F (M = Fe, Mn, Co, Ti etc) and fluorosulphates $LiMPO_4F$ (M = Fe, Mn, Ni, Co etc) have been studied extensively as favorable cathode materials for lithium ion batteries. The structure contains 1D chains of corner sharing metal octahedral (MF_2O_4) which controls 1D electron transport, connected by corner sharing phosphate tetrahedral (PO_4) (Chen et al., 2014). Figure 2.6 displays structure of tavorite $LiVPO_4F$.

Among tavorites, $LiVPO_4F$ found to be interesting cathode materials as many research works focusing to improve the materials. It exhibits excellent structural

stability, thermal stability and cycling properties (Ma et al., 2014; Yongli Wang, Zhao, Ji, Wang, & Wei, 2014; Xiao, Lai, & Lu, 2013). Nevertheless, it's low conductivity of 10^{-11} S cm^{-1} inhibits its usage in high energy applications (Prabu, Reddy, Selvasekarapandian, Rao, & Chowdari, 2012; Yang & Yang, 2015).

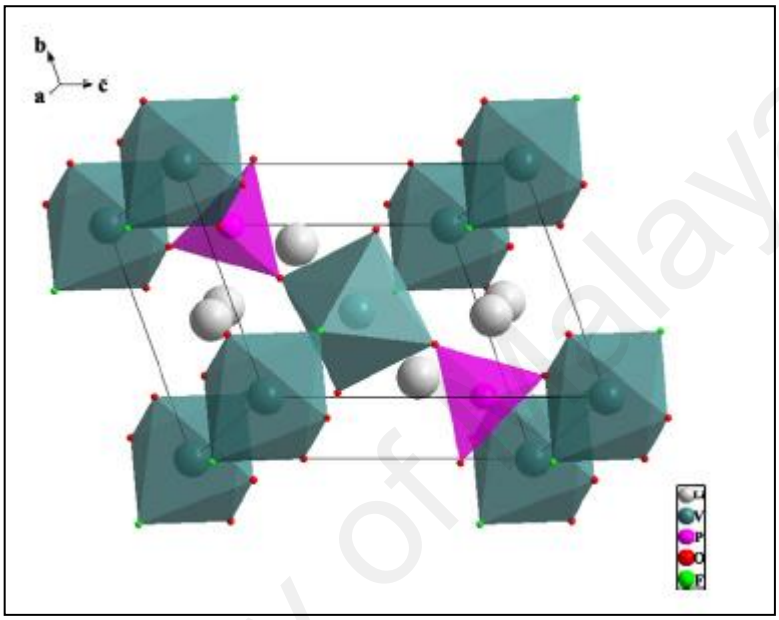

Figure 2.6: Structure of tavorite $LiVPO_4F$
(Sun et al., 2014)

Enhancements can be made from different synthesis approaches (Jie-qun, Sheng-kui, Ling, Kang, & Fan, 2012), carbon nanotubes modification (Jiping Li, Bao, & Mo, 2014), doping with metal ions (Lv, Xu, Li, Chen, & Liu, 2016; Sun, Xu, Chen, Ding, & Zheng, 2014; Yu & Jiang, 2016), silver coating (Yang & Yang, 2015) etc. Other tavorites such as $LiFePO_4F$ (Prabu, Reddy, et al., 2012), $LiFeSO_4F$ (Dong et al., 2013), Li_2CoPO_4F and Li_2NiPO_4F (Lee & Soo, 2013) are continuously being intensely studied.

2.2.4 Borate type cathode materials, $LiABO_3$

Remarkably, $(BO_3)^{3-}$ polyoxanions exhibit low mass compared to $(SO_4)^{2-}$, $(AsO_4)^{2-}$, $(MoO_4)^{2-}$, $(WO_4)^{2-}$, $(PO_4)^{3-}$, $(SiO_4)^{3-}$, $(AsO_4)^{3-}$, $(VO_4)^{3-}$ and $(WO_4)^{3-}$ groups

(Ma et al., 2013). Figure 2.7 depicts structure of borate $LiZnBO_3$. It contributes to theoretical capacity of 220 $mAhg^{-1}$ (Li, Xu, Li, Wang, & Zhai, 2013; Tao et al., 2014). Poor ionic and electronic conductivities lead to capacity decay which deteriorates cycling properties (Afyon, Kundu, Darbandi, & Hahn, 2014; Afyon, Mensing, Krumeich, & Nesper, 2014).

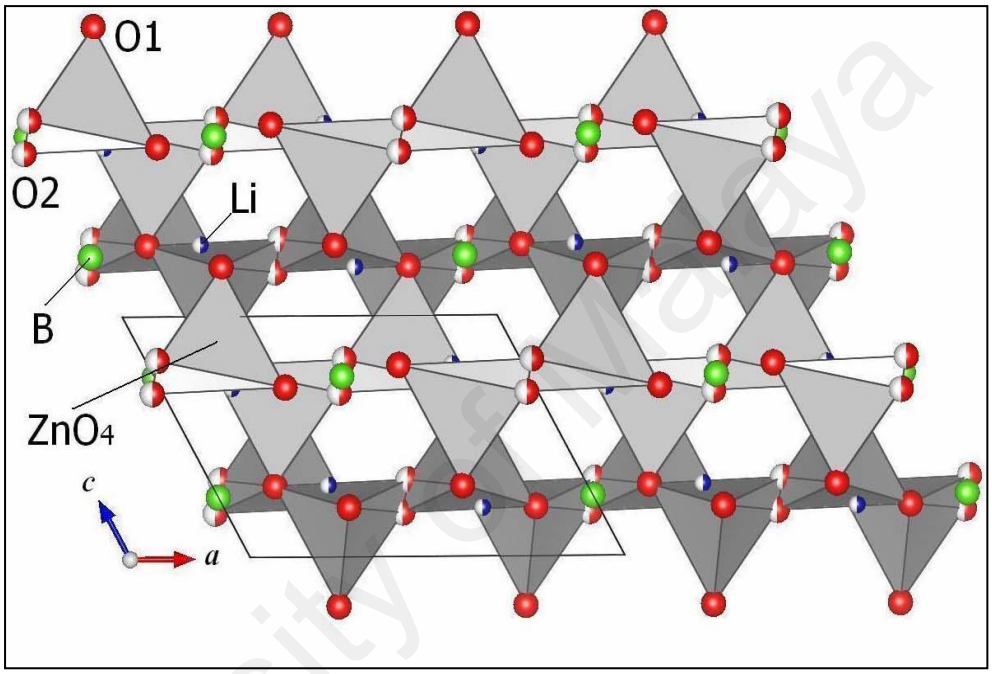

Figure 2.7: Structure of borate $LiZnBO_3$ (Tsuyumoto & Kihara, 2013)

To overcome such drawbacks, employment of nanoparticles and carbon coatings found to be very helpful (Afyon, Kundu, et al., 2014; Kim, Seo, & Ceder, 2015). It includes few interesting works that have been carried out such as mesoporous $LiFeBO_3$/C hollow spheres. Figure 2.8 illustrates the formation of mesoporous $LiFeBO_3$/C hollow spheres.

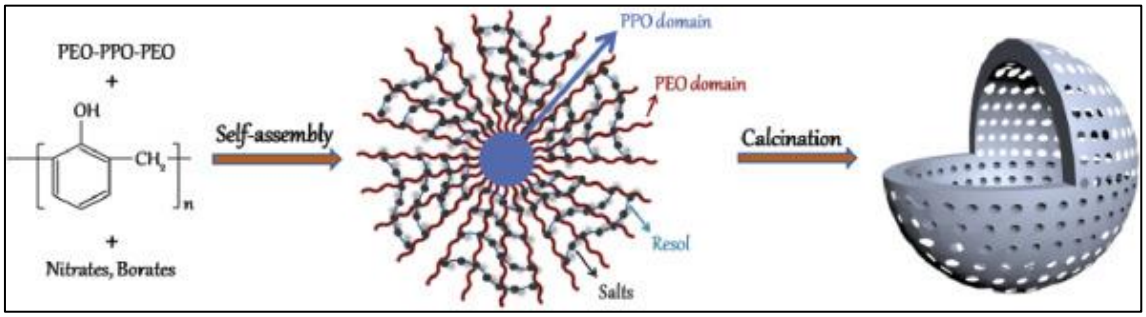

Figure 2.8: Illustration of the formation of mesoporous $LiFeBO_3$/C hollow spheres (Zhongxue Chen et al., 2015)

Porous shell effectively reduced Li ion channels thus increases capacity and fast rate capability. Carbon coating on the surface provides shield to $LiFeBO_3$ from moisture (Zhongxue Chen et al., 2015).

Meanwhile in another work, multi-layer core shell $LiFeBO_3$/C was synthesized via spray drying and carbothermal process as in Figure 2.9. Multi-layer core shell hinders moisture in the air to degrade the electrochemical properties (Zhang et al., 2014).

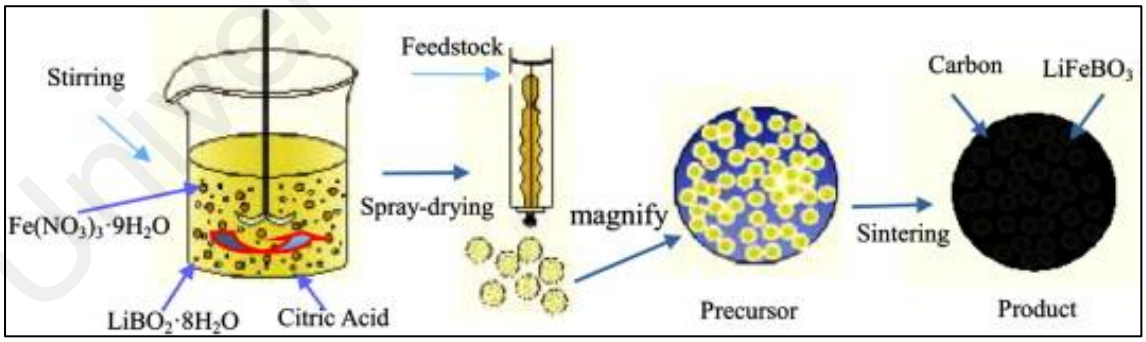

Figure 2.9: Synthesis process of multi-layer core shell $LiFeBO_3$/C (Zhang et al., 2014)

Various synthesis methods have been explored namely carbothermal method (Ma et al., 2013), ceramic route (Tao et al., 2014), solid state reaction followed by high energy milling (Lee & Lee, 2014), impregnation-precipitation technique (Tang, He, He, Xu, &

Song, 2015), solid state reaction without presence of carbon black in the starting materials (Ling Chen et al., 2010), microwave solid state reaction (Ma, Muslim, & Su, 2015), thermal spray drying process (Lee et al., 2013) etc.

Apart from that, doping with metal ions (Cheol et al., 2015; Kim et al., 2015; Roux, Bourbon, Colin, & Pralong, 2015; Yamane, Kawano, Fukuda, Suehiro, & Sato, 2012), carbon coating (Afyon, Kundu, et al., 2014; Li et al., 2013) and particle size reduction to nanometers (Afyon, Kundu, Krumeich, & Nesper, 2013; Afyon, Mensing, et al., 2014) are found to be alternative ways that can enhance borate type electrodes properties.

2.2.5 Olivine type cathode materials, $LiAPO_4$

Olivine group materials are another attractive type cathode materials as introduced by Padhi et al. (Padhi, Nanjundaswamy, & Goodenough, 1997). Among the phospates, $LiFePO_4$ exhibits potential of 3.5 V, $LiCoPO_4$ is at 4.9 V, $LiNiPO_4$ is about 5.1 V and $LiMnPO_4$ is around 4.1 V (Hu et al., 2014). However, its low electronic conductivity of olivines found to be challenging factor to be applied in electrochemical devices (Alyoshin, Pleshakov, Ehrenberg, & Mikhailova, 2014). Different approaches are continuously being approached to enhance the properties of olivine group cathode materials.

Carbon coating has been measured as one of the improvement technique towards olivine type cathode materials. TWEEN 80 (Hu et al., 2016), polydopamine as shown in Figure 2.10 (Han, Meng, Ma, & Nan, 2016), carbon nanotubes (Toprakci et al., 2012), graphene as in Figure 2.11 (Kim et al., 2014) have been applied as coating materials for $LiFePO_4$ Graphitic carbon foams was applied to $LiNiPO_4$ (Dimesso & Becker, 2012) while $LiCoPO_4$ cross linked with graphene (Chen, Chen, Du, Cui, & Zuo, 2016).

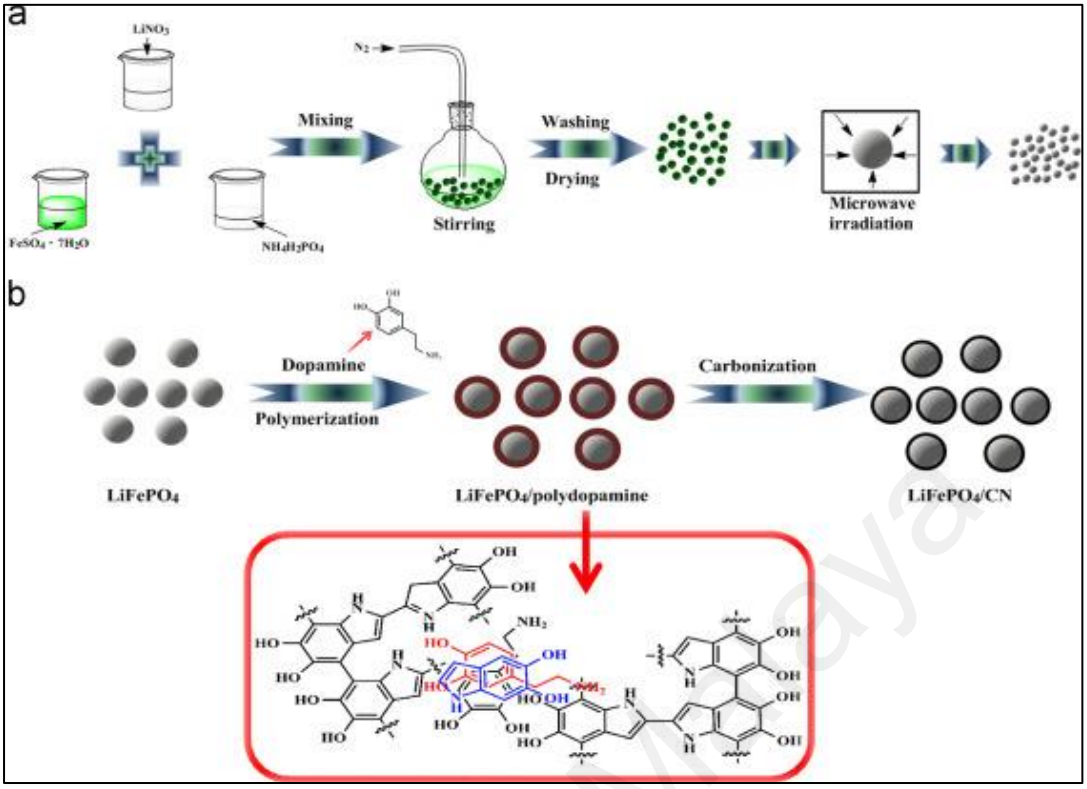

Figure 2.10: Preparation of nitrogen doped carbon decorated $LiFePO_4$ via microwave heating route (Han et al., 2016)

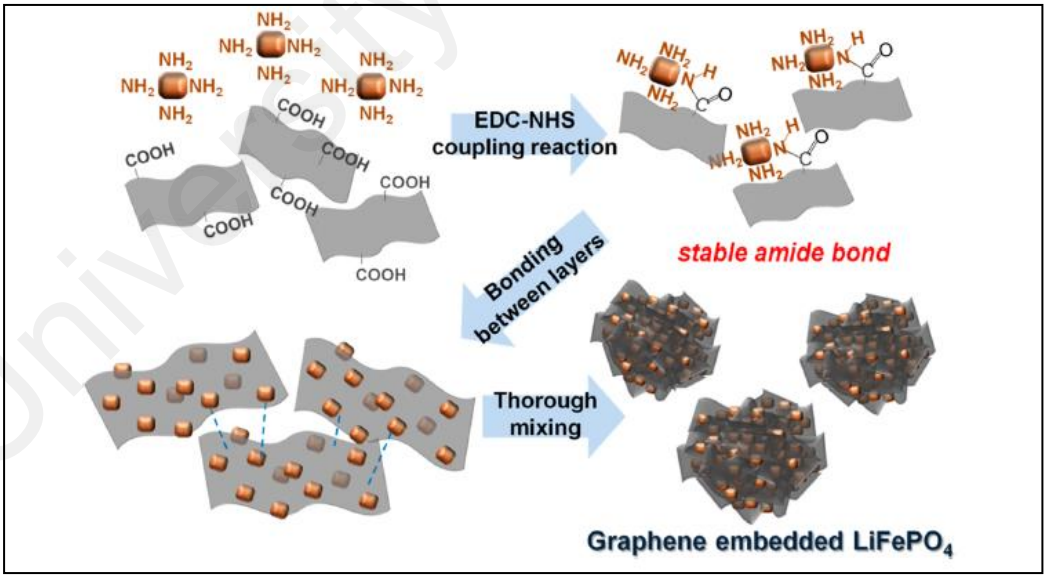

Figure 2.11: Fabrication method for graphene embedded $LiFePO_4$ (Kim et al., 2014)

Meanwhile doping such as Ce^{3+} doped $LiFePO_4$ (Nannan, Yongsheng, Xiaoke, & Li, 2016), Ni and Mn doped $LiFePO_4$ (Yuan, Wang, Wu, Shu, & Yang, 2016), yttrium substituted $LiCoPO_4$ (Huanhuan Li et al., 2014), Fe doped $LiCoPO_4$ (Allen, Jow, & Wolfenstine, 2011; Jan L Allen et al., 2014; L. Fang, Zhang, Zhang, Liu, & Wang, 2016), zinc substituted $LiCoPO_4$ (Karthickprabhu, Hirankumar, Maheswaran, Bella, & Sanjeeviraja, 2014), europium doped $LiNiPO_4$ (Prabu, Selvasekarapandian, Kulkarni, Karthikeyan, & Sanjeeviraja, 2012), Fe doped $LiNiPO_4$ (Feng, Zhang, Fang, Ouyang, & Wang, 2015; Qing, Yang, Shirley, & Sigmund, 2013), co doped $LiNiPO_4$ (Rommel, Rothballer, Schall, Brünig, & Weihrich, 2014), Mg substituted $LiNiPO_4$ (Dimesso, Spanheimer, & Jaegermann, 2013) also have been tested.

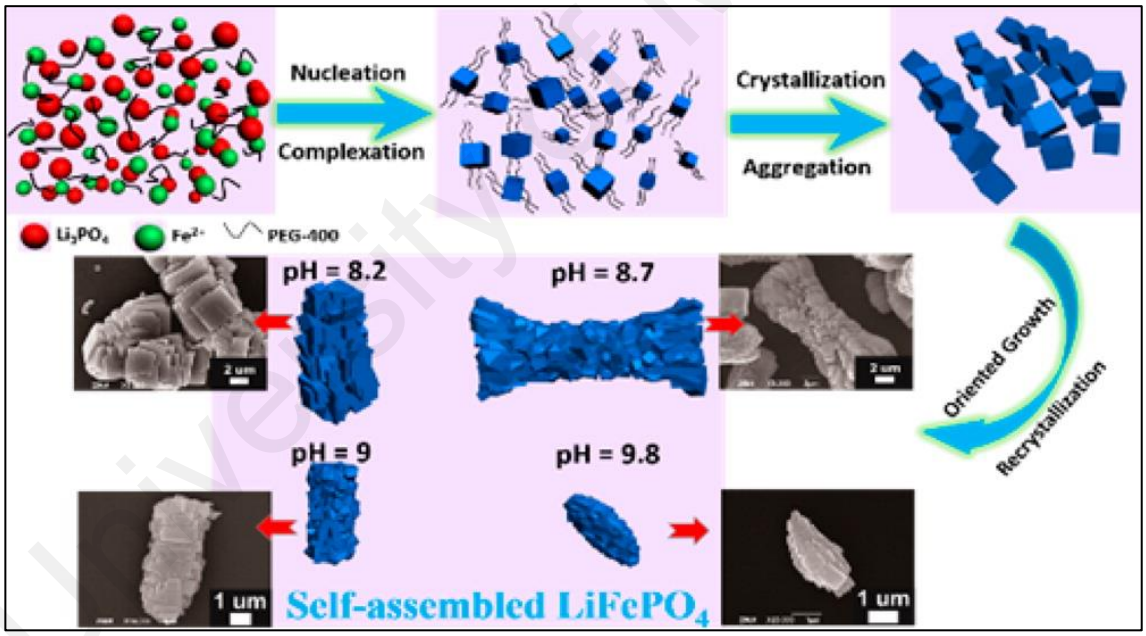

Figure 2.12: Self-assembled $LiFePO_4$ nanostructures via hydrothermal synthesis (Lin et al., 2014)

Besides that, different synthesis processes were reported namely hydrothermal (Lin et al., 2014), citric acid and ammonium mediated hydrothermal (Lu et al., 2011), solvothermal (Brutti et al., 2015; Assat, & Manthiram, 2015; Li, Zhang, Mu, Liu, & Wang, 2015; Ma, Shao, et al., 2014; Örnek & Kazancioglu, 2016; Li Wang et al., 2012;

Jianxin Zhu et al., 2013), electrospinning method (Lee et al., 2014), spray pyrolysis (The Nam Long Doan & Taniguchi, 2011), sol gel assisted carbothermal reduction method (Örnek, Can, & Ye, 2016), etc.

Figure 2.12 and Figure 2.13 compares $LiFePO_4$ structure formation via hydrothermal reaction. As in Figure 2.12, different pH conditions during hydrothermal process leads to various types structures. In this work, higher solubility of precursors at low pH value of 8.2 and 8.7 results in high crystals growth. In an alkaline conditions of pH value 9 and 9.8, OH^- ions at the interface produced shielding effect that can lower growth rate. Thus, it results in cube clusters like, dumbbell like, rod like and rugby like morphologies with increasing pH environments (Lin et al., 2014).

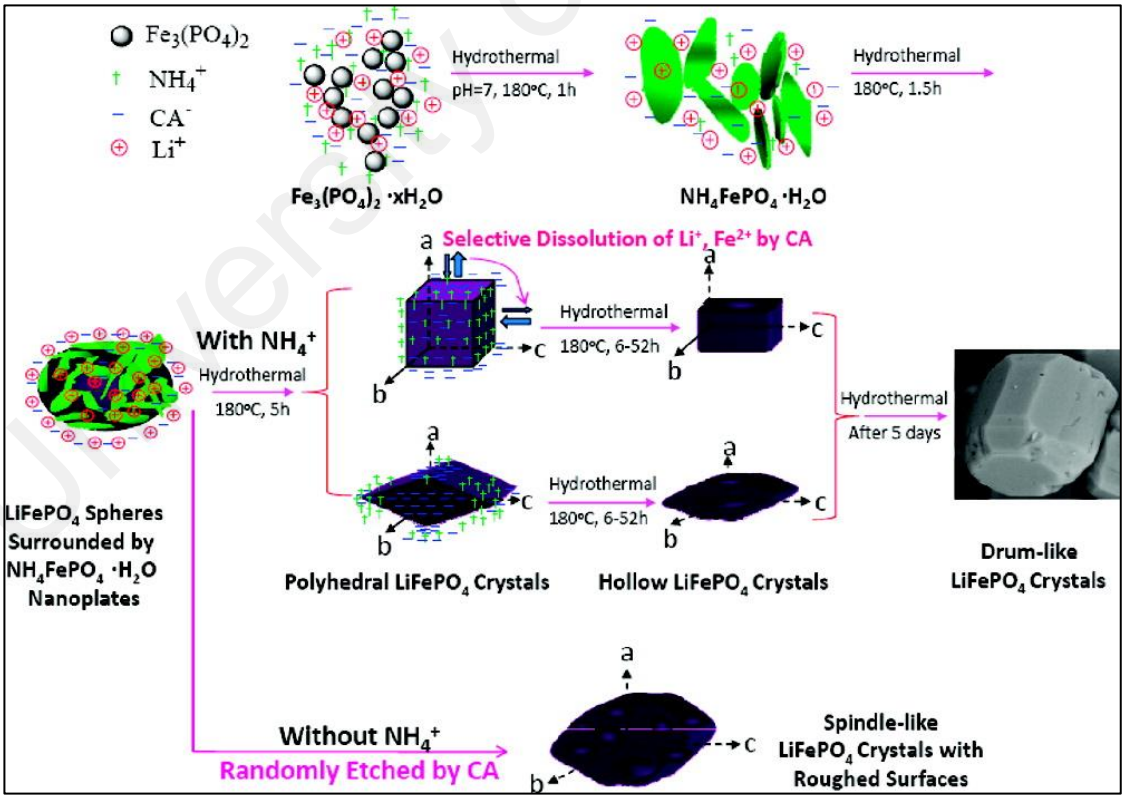

Figure 2.13: $LiFePO_4$ formation of citric acid and ammonium mediated hydrothermal treatment (Lu et al., 2011)

In Figure 2.13, hydrothermal technique approaches with citric acid (CA) and ammonium (NH_4). Citric acid produced cubic and rhombic $LiFePO_4$ structures, hollow structures formed after 15 hours. Since the hollow structures also metastable, finally it transformed to barrel like morphology. It is noteworthy that without NH_4, spindle like rough structure produced merely etching by citric acid. Hence, NH_4 similarly plays significant role by controlling the morphologies (Lu et al., 2011).

Figure 2.14: Nanoscale LiFePO4 crystals as seed crystals for second crystallization process (Han et al., 2013)

Apart from the above mentioned synthesis methods, some other unique preparations have also been reported recently. Nanoscale $LiFePO_4$ crystals were employed as seed crystals for second crystallization process as displayed in Figure 2.14 (Han et al., 2013). Heterogeneous nucleation sites takes place in the second crystallization process and produced uniform, porous and round $LiFePO_4$ particles.

2.3 Structure and characteristics of $LiMnPO_4$

Lithium manganese phosphate ($LiMnPO_4$) is mainly focused as a suitable candidates in the olivine group among $LiFePO_4$, $LiCoPO_4$ and $LiNiPO_4$ for cathode applications (Koleva, Zhecheva, & Stoyanova, 2011; Zhang et al., 2015). $LiMnPO_4$ crystallizes in orthorhombic olivine structure as in Figure 2.15. In $LiMnPO_4$, P-O covalent bond enables good thermal and cycling stability (Qin, Zhou, Xia, Tang, & Liu, 2012; Yoshida et al., 2013). The theoretical energy density of $LiMnPO_4$ is 701 Wh kg^{-1} with poor lithium diffusion and low electronic/ ionic conductivity, lead to affects the electrochemical property (Aono, Urita, Yamada, & Moriguchi, 2012; Dong et al., 2012).

Superior energy density of $LiMnPO_4$ which originates from its Mn^{2+}/Mn^{3+} redox potential at 4.1 V (vs. Li/Li+) records about 0.65 V greater than $LiFePO_4$ (Longfei Zhang, Qu, Zhang, Li, & Zheng, 2014). The potential also within the safe working range which one of the important aspect for scheming advanced future batteries (Barpanda, Djellab, Recham, & Tarascon, 2011).

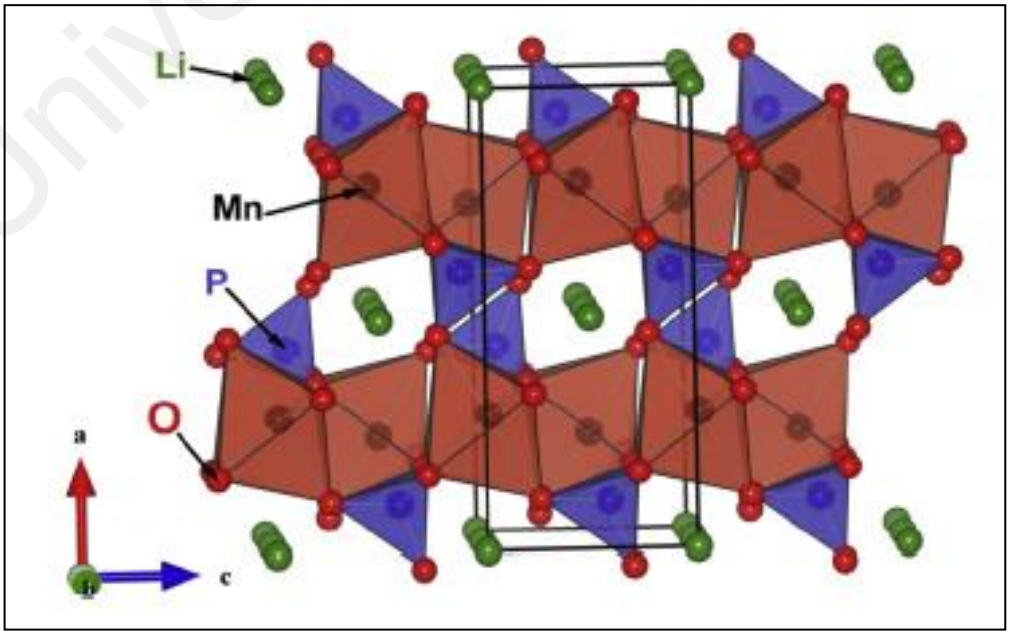

Figure 2.15: Olivine structure of $LiMnPO_4$
(Pieczonka, Liu, & Kim, 2013)

Besides that, high working voltage also creates the theoretical specific energy of $LiMnPO_4$ about 684 Wh/kg, which is 20% greater than that of $LiFePO_4$ (578 Wh/kg) (Xiao, Chernova, Upreti, Chen, & Li, 2011). Furthermore, $LiMnPO_4$ has good compatibility with recent organic electrolytes namely ethylene carbonate (EC), propylene carbonate (PC) and dimethoxyethane (DME) (Pan, Xu, & Zhen, 2012). Following subtopics will give outline on synthesis methods and approaches that have been utilized to improve the electrochemical properties of $LiMnPO_4$.

2.3.1 Synthesis methods

2.3.1.1 Sol gel method

Remarkable benefits of sol gel method can be listed as homogeneous mixing at the atomic or molecular level, lower processing temperature, shorter heating time, enhanced crystallinity, even particle distribution and nanosized particles (Fu et al., 2005). Sol gel method facilitates structural control of the materials within nanometer (Jugovic & Uskokovi, 2009). Availability of wide range of carbon sources would be another important factor that stimulates usage of sol gel technique in the processing of cathode materials (Zhao et al., 2012). Bhuwaneswari et al (Bhuwaneswari, Dimesso, & Jaegermann, 2010) have explained clearly about sol gel mechanism in their reported work. Liquid medium is used for a mixing of reactants at maximum level uniformly. Presence of chelating agent and complexing agent (carboxylic, hydrocarboxylic, polyhydroxy acid) enables metal ions in the solution confined into a solid phase compound by chemical reaction. It can be observed that solution evaporates to become gel, which generally denoted as precursors. Precursors will be further sintered at optimal temperatures for a desired crystallinity.

$LiMnPO_4/C$ was prepared by sol gel method using citric acid (Sheng-kui, You, Jie-qun, & Jian, 2012). It suggested that the role of citric acid as chelating agent and carbon source could limit the particle size. Carbon monoxide released by citric acid during calcination able to sustain Mn^{2+} stability. Thus, the results confirmed that good electrochemical reversibility achieved by sol gel technique. $LiMnPO_4/C$ formed at temperature of 500 °C for 10 hours delivered first discharge capacity of 122.6 $mAhg^{-1}$ and 112.4 $mAhg^{-1}$ after 30 cycles at 0.05 C.

In another work, sol gel method was accompanied by ball milling and liquid nitrogen quenching to produce $LiMnPO_4$ (Wu, Zhong, Lv, & Liu, 2013). The samples that prepared under liquid nitrogen quenching deliver discharge capacities of 131.6 $mAhg^{-1}$ at 0.05 C compared to sample that synthesized under natural cooling. Additionally, $LiMnPO_4$ obtained under liquid nitrogen quenching produced discharge capacities of 125.8 $mAhg^{-1}$, 103.3 $mAhg^{-1}$ and 56.4 $mAhg^{-1}$ at current rates of 0.1 C, 0.5 C and 1 C rates respectively.

2.3.1.2 **Solid state method**

Solid state synthesis is occupied for mass production which is suitable for industrial applications. High temperature and pressure setting are required to carry out this synthesis method. However, longer time procedures for repeated grinding and calcination cause formation of larger particles which lowers the electrochemical performance (Satyavani, Kumar, & Subba Rao, 2015). Few works have been reported on $LiMnPO_4$ obtained by solid state technique.

Recent work has prepared $LiMnPO_4$ via solid state method using different manganese oxides and sintering temperatures. $LiMnPO_4$/C samples obtained from MnO_2, Mn_2O_3 and mixed manganese oxide (the molar ratio of MnO_2 and Mn_2O_3 is 4 : 1) exhibit initial discharge capacity of 87 $mAhg^{-1}$, 121 $mAhg^{-1}$ and 153 $mAhg^{-1}$ respectively whereas sample prepared at 600 °C maintains 94% of its initial discharge capacity at the end of 200 cycles (Zheng et al., 2015).

Two level hierarchical shaped $LiMnPO_4$/C were prepared by facile surfactant assisted solid state method as displayed in Figure 2.16 (Longfei Zhang, Qu, Zhang, Li, & Zheng, 2014).

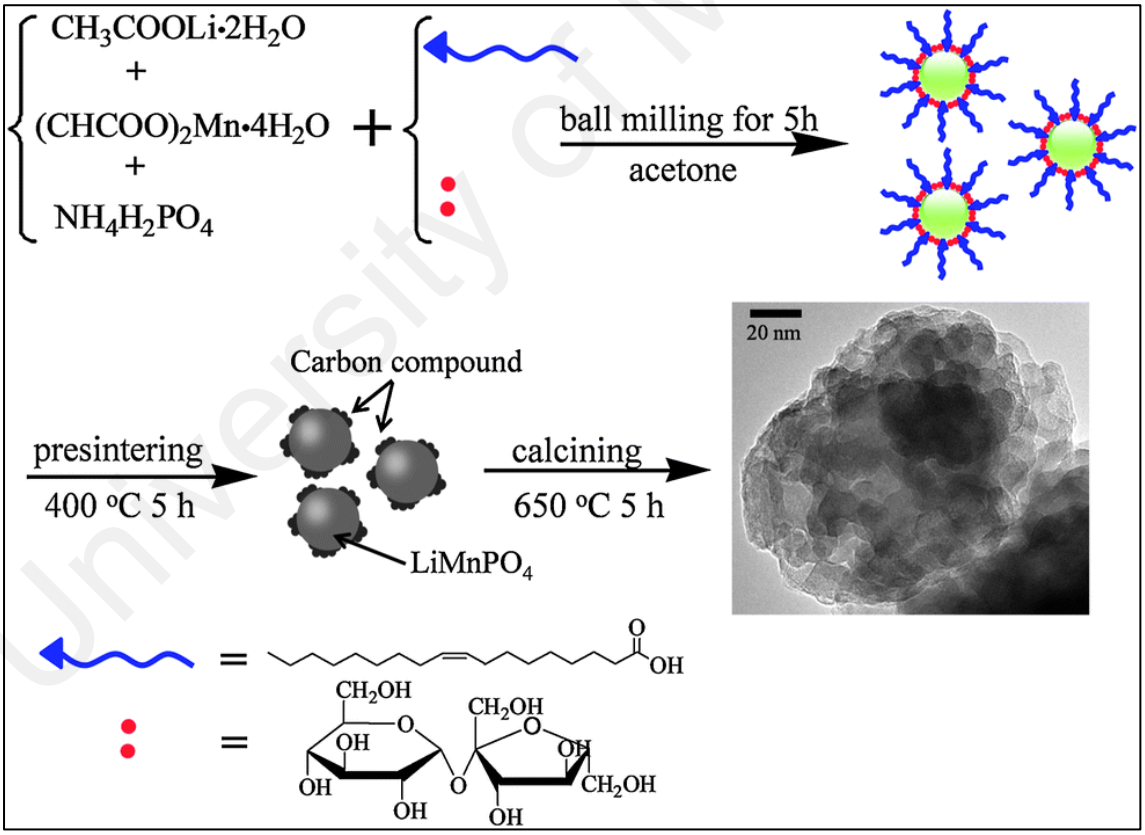

Figure 2.16: Diagram of facile surfactant assisted solid state method
(Longfei Zhang et al., 2014)

Nanosized (5-10 nm) $LiMnPO_4$ particles which connected by 3 dimensional conductive carbon skeleton significantly reduces Li diffusion path and supplies

continuous electrical conductivity at two scales such as inside the grains and between the grains. Obtained $LiMnPO_4$ particles exhibited capacity of 130.1 $mAhg^{-1}$ at 0.05 C, 116.3 $mAhg^{-1}$ at 1 C and 60.1 $mAhg^{-1}$ at 20 C. This sample displayed enhanced electrochemical performance. This synthesis technique also provides solution for other materials with low electrical conductivity.

2.3.1.3 **Hydrothermal method**

Hydrothermal method is a great technique loaded with benefits such as simple, homogeneous, controlled morphology, low cost etc. Water is functioning as reaction medium, appropriate starting materials are placed in Teflonlined autoclave which then heated at temperature higher than the boiling water (100 °C) to produce vapor pressure in a closed system (Rui, Yan, Skyllas-kazacos, & Mariana, 2014). Hydrothermal/solvothermal methods have developed as noteworthy technique to produce $LiMnPO_4$ powders.

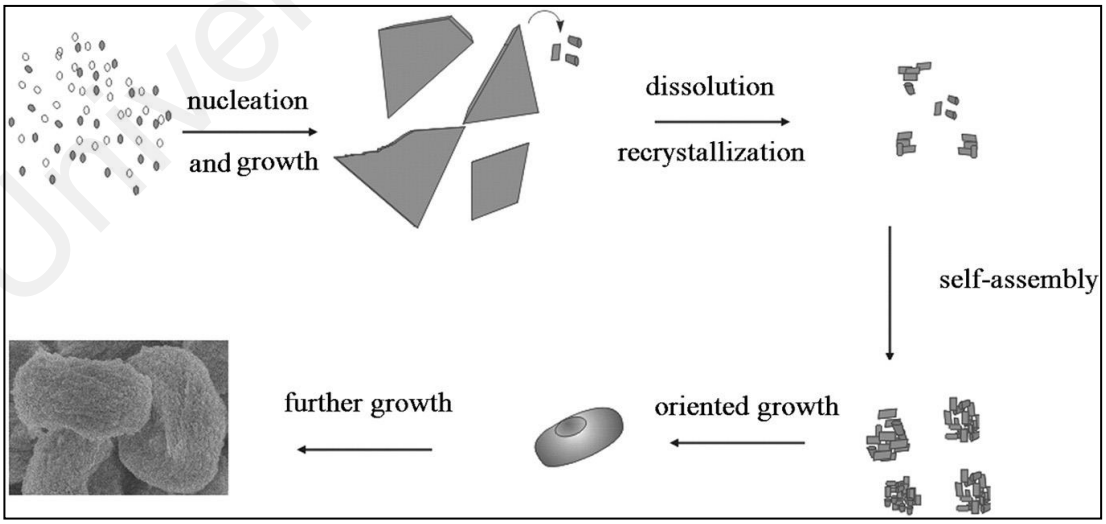

Figure 2.17: Evolution process of hemoglobin like $LiMnPO_4$ microspheres
(Gu et al., 2015)

Another unique work presented by hemoglobin like $LiMnPO_4$ microspheres which were prepared by hydrothermal method (Gu et al., 2015). The hemoglobin like $LiMnPO_4$ particles comprised nanorods with diameter of 100 nm. The growth of hemoglobin like $LiMnPO_4$ particles are clearly depicted in Figure 2.17. Carbon coated $LiMnPO_4$ microspheres achieved capacity about 110 $mAhg^{-1}$ at 0.1 C and 99 $mAhg^{-1}$ at 1 C.

Flower like $LiMnPO_4$ nanostructures self-assembled with nanosheets were prepared by hydrothermal method as in Figure 2.18 (Bao et al., 2015). The primary nanosheets are about 30 nm thickness. Hydrothermal process causes Ostwald ripening which makes primary nanosheets of flower like $LiMnPO_4$ nanostructures become thicker and smoother. It showed charge discharge capacities of 81.7 $mAhg^{-1}$ and 79.0 $mAhg^{-1}$ respectively. Even though it exhibited low specific capacity, but it retains 95 % of its initial capacity after 80 cycles.

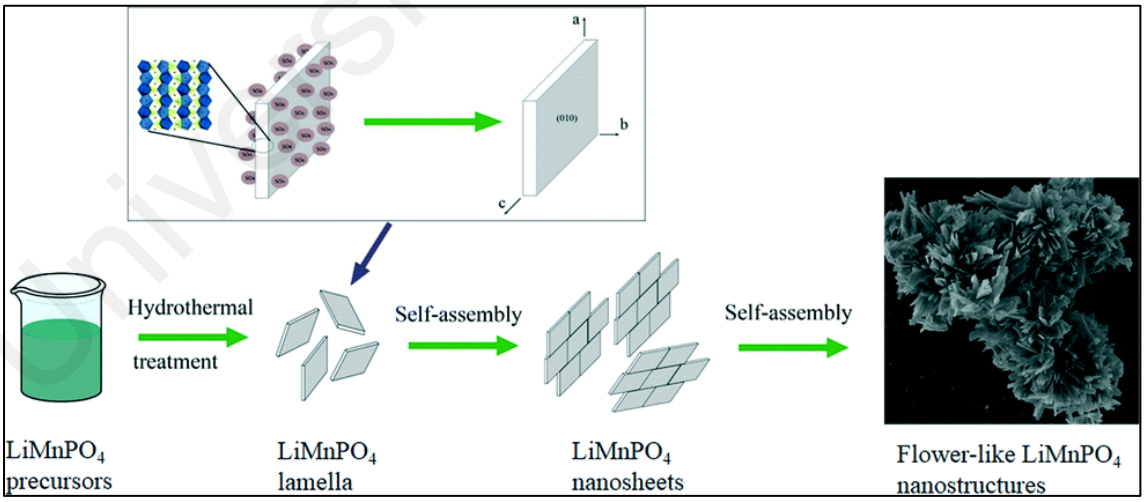

Figure 2.18: Formation of flower like $LiMnPO_4$ nanostructures
(Bao et al., 2015)

Dispersed $LiMnPO_4$ wedges were prepared by hydrothermal method at 200 °C for 10 h (Zhi Gao et al., 2013). This study suggested that morphology of the dispersed

wedges could be adjusted by amount of reagents used. As prepared $LiMnPO_4$ wedges displayed discharge capacity of 124 $mAhg^{-1}$, 107 $mAhg^{-1}$, 97 $mAhg^{-1}$, 87 $mAhg^{-1}$ and 82 $mAhg^{-1}$ at 0.05 C, 0.1 C, 0.2 C, 0.5 C and 1 C respectively. Better dispersion and smaller crystallites enhanced the electrochemical properties of dispersed $LiMnPO_4$ wedges.

$LiMnPO_4$ plates with thickness of around 100 nm were obtained by hydrothermal method (Pan, Xu, Hong, Fang, & Zhen, 2013). Well dispersed morphology produces high percentage of exposed (010) facets and thinner along [010] direction which improved electrochemical properties. The synthesized $LiMnPO_4$ plates showed discharge capacity of 139.2 $mAhg^{-1}$ and 158.7 $mAhg^{-1}$ at 25 °C and 55 °C respectively in the current rate of 0.05 C. At 50 °C, the samples indicated 147.6 $mAhg^{-1}$, 141.1 $mAhg^{-1}$, 133.6 $mAhg^{-1}$, 121.4 $mAhg^{-1}$ and 110.7 $mAhg^{-1}$ corresponded to current rate at 0.1 C, 0.2 C, 0.5 C, 1 C and 2 C.

2.3.1.4 **Solvothermal method**

Solvothermal method is similar as hydrothermal but organic solvent is utilized as reaction medium replacing water. It is also easy synthesis which requires oven or autoclave (Xia et al., 2014).

$LiOH{\cdot}H_2O$, $MnSO_4{\cdot}H_2O$ and H_3PO_4 were used as starting materials in solvothermal method in a mixed solvent of ethylene glycol and water (11:1 volume ratio) (Zilong Tang, 2015). Ethylene glycol in the mixed solvent has aided in the formation of $LiMnPO_4$ nanorods by controlling morphology and size of the particles. $LiMnPO_4$/C

nanorods delivered high capacity of 168 $mAhg^{-1}$ at 0.05 C and 110 $mAhg^{-1}$ at 10 C. It also revealed capacity retention of 94.5 % after 100 cycles at 0.5 C.

In another similar work, $LiMnPO_4$ nanosheets of various sizes and orientations with two different facets were synthesized via solvothermal method (Dinh, Mho, Yeo, Kang, & Kim, 2015). Dodecylbenzenesulfonic acid (DBSA) and poly(ethylene glycol)-block-poly(propylene glycol)-block-poly-(ethylene glycol) (P123) were occupied as surfactants while ascorbic acid as antioxidant. Two different facets {100} and {010} were attained by changing the source mixing sequence. DBSA and P123 surfactants controlled lateral size of each nanosheet. Significantly, $LiMnPO_4$/C nanosheets of size (50-100) × 200 nm with the {010} facet exhibited high rate capability at 55 °C. It delivered discharge capacities 147 $mAhg^{-1}$, 135 $mAhg^{-1}$, 123 $mAhg^{-1}$ and 112 $mAhg^{-1}$ at 1 C, 2 C, 5 C and 10 C accordingly.

Solvothermal technique was applied using manganese sulfate ($MnSO_4 \cdot H_2O$), manganese chloride ($MnCl_2 \cdot 4H_2O$), manganese acetate ($Mn(Ac)_2 \cdot 4H_2O$) and manganese nitrate ($Mn(NO_3)_2$, 50 wt.%) as different manganese salts to prepare $LiMnPO_4$ (Zhou et al., 2014). This work explained the effect of anion species in the solvothermal process on phase impurity, structural and morphology of the samples. It concluded that NO_3^- ions have strong oxidation ability in acidic medium. SO_4^{2-} ions with higher charge number ease the growth of the high-index planes, Ac^- anion with larger volume has atomic-scale template effect which restricts crystal growth to the equilibrium state. On the other hand, $MnCl_2$ formed structure with high purity and crystal growth along ac planes. $LiMnPO_4$ contains $MnSO_4$, $MnCl_2$, $Mn(Ac)_2$ in its precursor showed first discharge capacity of 145 $mAhg^{-1}$, 129 $mAhg^{-1}$ and 81 $mAhg^{-1}$ respectively.

Zhang et al (Zhang et al., 2015) developed cetyltrimethyl ammonium bromide (CTAB) mediated solvothermal method in mixed water-diethylene glycol (DEG) solvents. CTAB and DEG promote $LiMnPO_4$ nanoplates formation. $LiMnPO_4$/C from this work delivered discharge capacity of 148.6 $mAhg^{-1}$ at 0.1 C, 127.6 $mAhg^{-1}$ at 1 C and 93.8 $mAhg^{-1}$ at 5 C.

In a microwave assisted solvothermal method, $LiMnPO_4$ materials were prepared in water-diethylene glycol solution (Su, Liu, Long, Yao, & Lv, 2015). Microwave assisted solvothermal process offers more nuclei and reduces crystal growth rate which results in irregular and flaky morphology. This synthesis method significantly reduced reaction time. The samples achieve discharge capacity of 131.4 $mAhg^{-1}$ at 0.1 C and 85.2 $mAhg^{-1}$ at 5 C.

Another work reported on simple solvothermal process using $LiOH{\cdot}H_2O$, H_3PO_4 and $MnSO_4{\cdot}H_2O$ as the precursors and ethylene glycol as medium (Guo et al., 2014). This work studied the influence of different ratios of the starting materials and summarized the role of H^+ during solvothermal process. When precursor containing $LiOH/H_3PO_4/MnSO_4$ in the ratio of 3 : 1 : 1, spindlelike $LiMnPO_4$ were obtained. By reducing LiOH proportion, increasing the amount of H_3PO_4 or addition of small quantity of H_2SO_4 reduced the size of the particles with plate-like shapes. $LiOH/H_3PO_4/MnSO_4$ in the ratio of 3 : 1.1 : 1 exhibited superior electrochemical properties. The sample showed capacity of 157.4 $mAhg^{-1}$, 143.8 $mAhg^{-1}$, 136.5 $mAhg^{-1}$, 122.5 $mAhg^{-1}$ and 108.2 $mAhg^{-1}$ at current rate of 0.1 C, 1 C, 2 C and 5 C correspondingly.

Graphene oxide was used as an additive in solvothermal method to synthesize $LiMnPO_4$ (Wang, Wang, Wang, & Xia, 2014). Graphene oxide content was varied (5 mg, 10 mg, 20 mg, 40 mg and 80 mg) to evaluate the particle size variation accordingly. Particle size of smaller than 50 nm was attained when the graphene oxide amount is at 20 mg. It exhibited specific capacity of 140 $mAhg^{-1}$ at C/10 and 85 $mAhg^{-1}$ at 1 C.

Solvothermal synthesis shown in Figure 2.19 was equipped to obtain nano $LiMnPO_4$ materials using Li_3PO_4 nanorods and $MnSO_4 \cdot H_2O$ as precursors (Yang et al., 2012). The morphology of the Li_3PO_4 precursor found to be depend on the volume ratio of polyethylene glycol 600 (PEG600) to water. Apart from that, reactant feeding order, reaction time and pH also intensively studied in this research. Based on results, $LiMnPO_4$ produced at 180 °C for 4 hours at a pH value of 6.46 which then sintered with glucose at 600 °C for 3 hours in argon atmosphere displayed good discharge capacity. It achieved capacity of 147 $mAhg^{-1}$ at 0.05 C and showed capacity retention of 93 % after 200 cycles at 1 C.

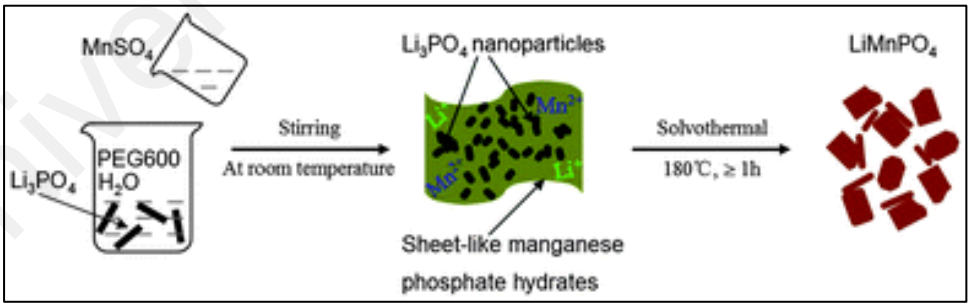

Figure 2.19: Reaction process and morphology formation
(Yang et al., 2012)

Attractively, flower like $LiMnPO_4$ microspheres were prepared via template free solvothermal method (Nie et al., 2012). $LiMnPO_4$ microspheres contain nanoplates with an open 3D microstructure as in Figure 2.20. From thermodynamics view, $LiMnPO_4$

nanosheets will combine to form dumblike microstructures to suppress the overall surface energy which is referred as Ostwald ripening process. Presence of hydroxyl enriched glucose aids in crystal growth and carbon layer on the $LiMnPO_4$ nanoplates. As prepared samples showed charge and discharge capacities of 53.3 $mAhg^{-1}$ and 56.2 $mAhg^{-1}$ respectively. Poor capacity due to the larger micrometer sized particles which could be improved with further optimization.

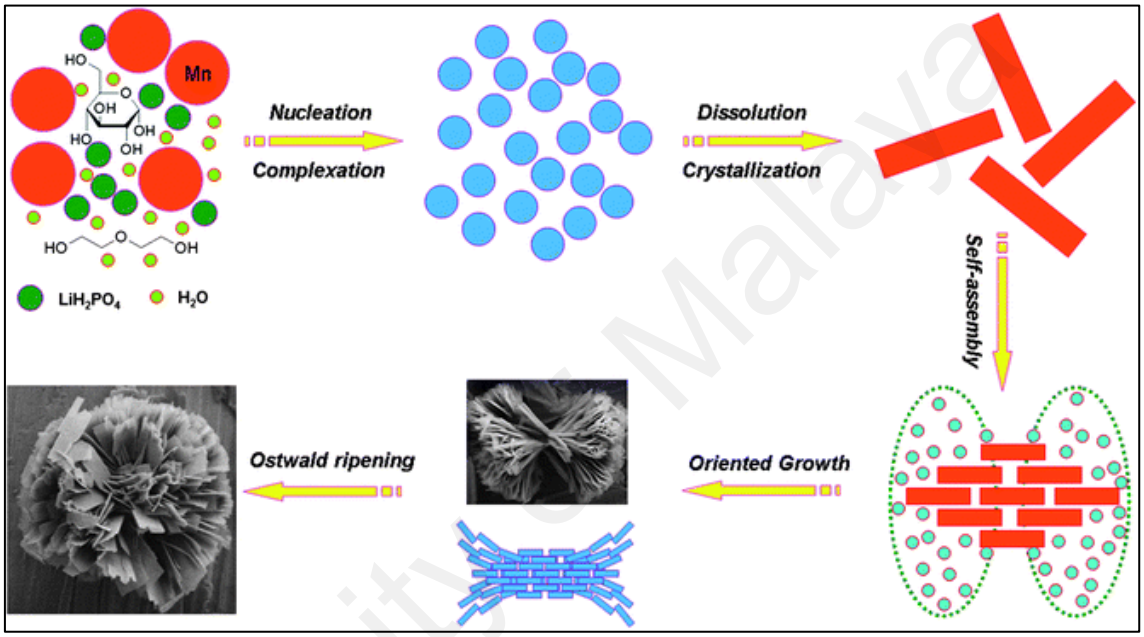

Figure 2.20: Growth mechanism of flower like $LiMnPO_4$ microspheres
(Nie et al., 2012)

Uniquely, novel 3D foldaway lantern-like $LiMnPO_4$ structures have been processed by solvothermal method as presented in Figure 2.21 (Dezhi Chen et al., 2012). Ethylene glycol used in this method played dual role as solvent and crystal growth modifier. The sample exhibited initial discharge capacity of 133 $mAhg^{-1}$ at 0.1 C and showed 125 $mAhg^{-1}$ after 30 cycles.

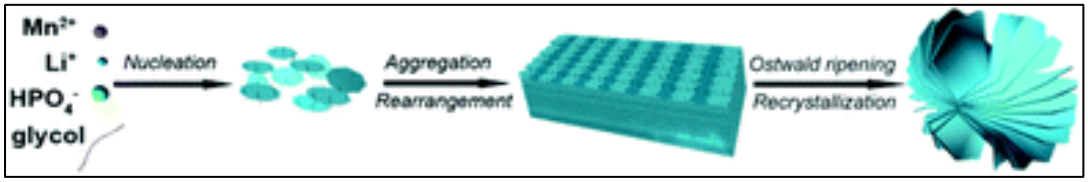

Figure 2.21: 3D foldaway lantern like $LiMnPO_4$ structures formation
(Dezhi Chen et al., 2012)

2.3.1.5 **Spray pyrolysis method**

Spray pyrolysis is an excellent method to produce fine particles from nano to micro sizes (Soo, Na, Chan, & Bin, 2014). In this process, precursor solution is atomized in a

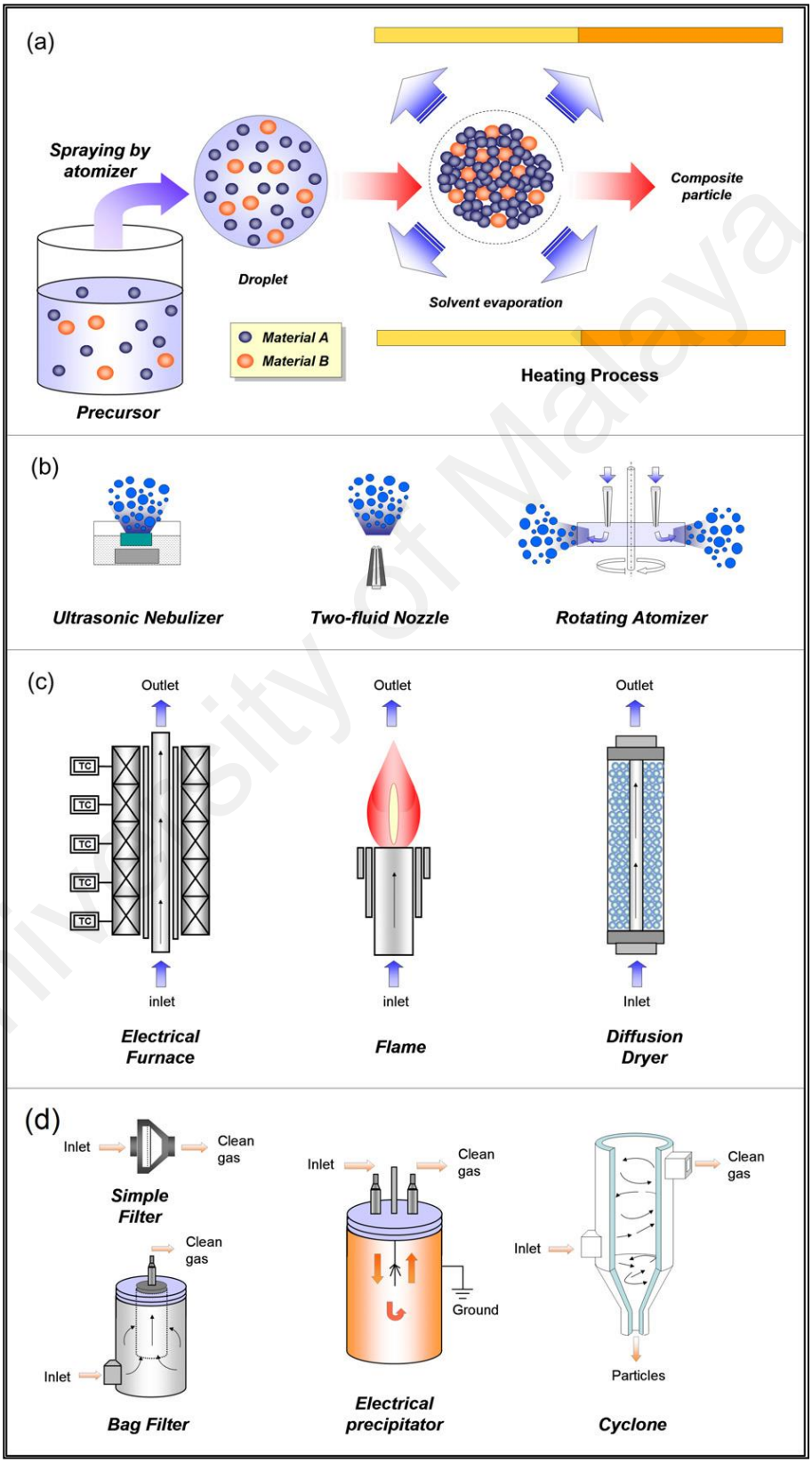

Figure 2.22: Illustration of nanoparticles formation via spray drying method (Asep Bayu Dani Nandiyanto & Okuyama, 2011)

droplet producing apparatus followed by evaporation in a heated reactor. Then it will decompose to particles and films as depicted in Figure 2.22 (Asep Bayu Dani Nandiyanto & Okuyama, 2011). $LiMnPO_4$ cathode materials were synthesized via combination of spray pyrolysis and spray drying followed by heat treatment (Bakenov & Taniguchi, 2011). $LiNO_3$, H_3PO_4 and $Mn(NO_3)_2 \cdot 6H_2O$ were used as starting materials. The electrochemical tests at 0.05 C revealed initial discharge capacities of 112 $mAhg^{-1}$ at room temperature and 130 $mAhg^{-1}$ at 55 °C.

Doan and coworkers have prepared $LiMnPO_4$ cathode materials by a combination of spray pyrolysis and wet ball milling continued with heat treatment (Nam, Doan, & Taniguchi, 2011). They used $LiNO_3$, H_3PO_4 and $Mn(NO_3)_2 \cdot 6H_2O$ as starting materials. The sample obtained at spray pyrolysis temperature of 300 °C exhibited biggest specific area with well distribution of carbon. It showed 123 $mAhg^{-1}$ and 165 $mAhg^{-1}$ at cutoff voltages of 4.4 V and 5.0 V respectively.

2.3.1.6 **Polyol method**

Polyol route has been found to be another effective method using low cost solvents to produce nanosized particles in shorter reaction time (Muruganantham, Sivakumar, & Subadevi, 2016, 2015a). Four main steps are compressed during polyol process. At first step, polyol occupy multi roles as solvent, fuel, carbon source, reducing agent and capping agent throughout the process. Followed by second step where high flammable and cheap fuel sustains the combustion process. High energy that released from polyol combustion consumed for thermal decomposition of precursors, nucleation and continuous particle growth during third step. At final stage, polyol carbonization at high

temperatures produced carbon coated nanoparticles (Mathew et al., 2014). Above mentioned steps during polyol process are clearly depicted in Figure 2.23.

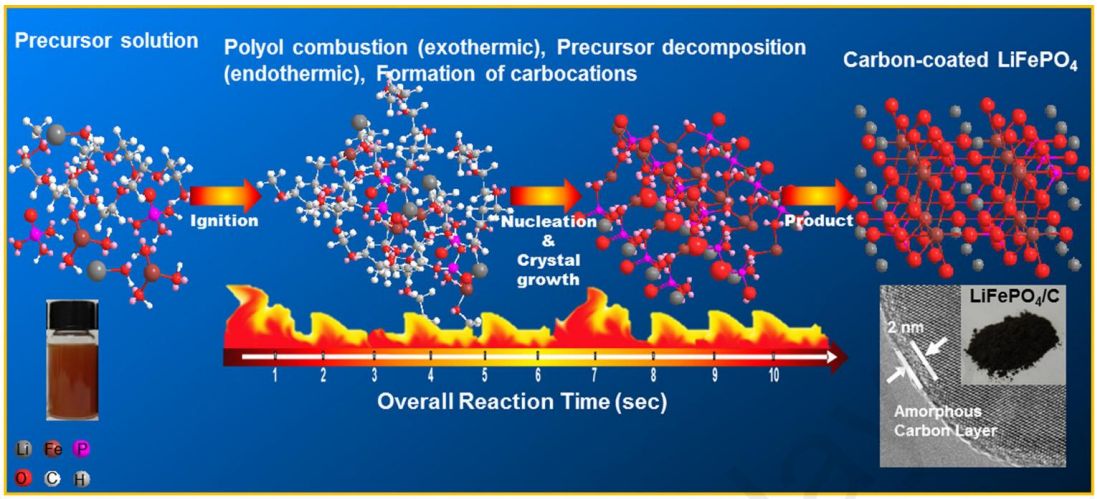

Figure 2.23: Polyol process to produce $LiFePO_4$ nanoparticles (Mathew et al., 2014)

$LiMnPO_4$ nanoplates were prepared by polyol method varying stirring rates from 300 rpm to 700 rpm (Zhu, Liu, Yang, & Shen, 2014). The results obtained from this work suggest that stirring rate has noteworthy effect on particle size and electrochemical properties. Particles size decreases with increasing stirring rate. Adequate stirring enhances the mixing, thus makes more uniform environment for nucleation and particle growth. Nevertheless, bulky particles shattered during the high rate stirring. Although the sample obtained from 700 rpm delivered initial discharge capacity of 129 $mAhg^{-1}$ at 0.05 C, the discharge capacity reached to 150 $mAhg^{-1}$ after 20 cycles.

Three dimensional $LiMnPO_4$ microflowers were prepared via polyvinyl pyrrolidone (PVP) assisted polyol process (Kumar, Venkateswarlu, & Satyanarayana, 2012). The microflowers were porous with nanopetals creates high surface area, detect free and enhanced ionic transportation in the nanopetals. It exhibited initial discharge capacity of 164 $mAhg^{-1}$ at 0.1 C. Table 2.3 summarizes the methods that have been explored to synthesize $LiMnPO_4$ cathode materials and the initial discharge capacity achieved.

Table 2.3: Methods used to prepare $LiMnPO_4$ cathode materials and its discharge capacity

Synthesis method	Starting materials	Initial discharge capacity	Current rate	Ref.
Sol gel method	$Mn(CH_3COO)_2 \cdot 4H_2O$ $CH_3COOLi \cdot 2H_2O$ H_3PO_4	122.6 $mAhg^{-1}$	0.05 C	(Sheng-kui et al., 2012)
Sol gel method	Li_3PO_4 $Mn(CH_3COO)_2 \cdot 4H_2O$	131.6 $mAhg^{-1}$ 125.8 $mAhg^{-1}$ 103.3 $mAhg^{-1}$ 56.4 $mAhg^{-1}$	0.05 C 0.1 C 0.5 C 1 C	(Wu et al., 2013)
Solid state method	$CH_3COOLi \cdot 2H_2O$ $(CH_3COO)_2Mn \cdot 4H_2O$ $NH_4H_2PO_4$	130.1 $mAhg^{-1}$ 116.3 $mAhg^{-1}$ 60.1 $mAhg^{-1}$	0.05 C 1 C 20 C	(Longfei Zhang et al., 2014)

Synthesis method	Starting materials	Initial discharge capacity	Current rate	Ref.
Hydrothermal method	$Li_2SO4 \cdot H_2O$ $MnSO_4 \cdot H_2O$ $NH_4H_2PO_4$	(25 °C) 139.2 $mAhg^{-1}$ 121.0 $mAhg^{-1}$ 114.0 $mAhg^{-1}$ 106.1 $mAhg^{-1}$ 94.1 $mAhg^{-1}$ 79.5 $mAhg^{-1}$ (50 °C) 158.7 $mAhg^{-1}$ 147.6 $mAhg^{-1}$ 141.4 $mAhg^{-1}$ 133.6 $mAhg^{-1}$ 121.4 $mAhg^{-1}$ 110.7 $mAhg^{-1}$	0.05 C 0.1 C 0.2 C 0.5 C 1 C 2 C 0.05 C 0.1 C 0.2 C 0.5 C 1 C 2 C	(Pan et al., 2013)

Synthesis method	Starting materials	Initial discharge capacity	Current rate	Ref.
Hydrothermal method	$Li_2SO4 \cdot H_2O$ $MnSO_4 \cdot H_2O$ $NH_4H_2PO_4$	79 $mAhg^{-1}$	0.1 C	(Bao et al., 2015)
Hydrothermal method	$Li_2SO4 \cdot H_2O$ $MnSO_4 \cdot H_2O$ $NH_4H_2PO_4$	124 $mAhg^{-1}$ 107 $mAhg^{-1}$ 97 $mAhg^{-1}$ 87 $mAhg^{-1}$ 82 $mAhg^{-1}$	0.05 C 0.1 C 0.2 C 0.5 C 1 C	(Zhi Gao et al., 2013)
Solvothermal method	$MnSO_4 \cdot H_2O$ Li_3PO_4	131.4 $mAhg^{-1}$ 85.2 $mAhg^{-1}$	0.1 C 5 C	(Su et al., 2015)
Solvothermal method	$LiOH \cdot H_2O$ $MnSO_4 \cdot H_2O$ H_3PO_4	168 $mAhg^{-1}$ 110 $mAhg^{-1}$	0.05 C 10 C	(Zilong Tang, 2015)

Synthesis method	Starting materials	Initial discharge capacity	Current rate	Ref.
Solvothermal method	LiOH $MnSO_4 \cdot 4H_2O$ H_3PO_4	147 $mAhg^{-1}$ 135 $mAhg^{-1}$ 123 $mAhg^{-1}$ 112 $mAhg^{-1}$	1 C 2 C 5 C 10 C	(Dinh et al., 2015)
Solvothermal method	H_3PO_4 LiOH $(MnCl_2 \cdot 4H_2O)$ $(Mn(Ac)_2 \cdot 4H_2O)$ $(Mn(NO_3)_2$	145 $mAhg^{-1}$ Mn(Ac) 129 $mAhg^{-1}$ MnCl2 81 $mAhg^{-1}$ $MnSO_4$	0.01 C	(Zhou et al., 2014)
Solvothermal method	$MnSO_4 \cdot H_2O$ Li_3PO_4	148.6 $mAhg^{-1}$ 127.6 $mAhg^{-1}$ 93.8 $mAhg^{-1}$	0.1 C 1 C 5 C	(Zhang et al., 2015)

Synthesis method	Starting materials	Initial discharge capacity	Current rate	Ref.
Solvothermal method	$LiOH \cdot H_2O$ H_3PO_4 $MnSO_4 \cdot H_2O$	157.4 $mAhg^{-1}$ 143.8 $mAhg^{-1}$ 136.5 $mAhg^{-1}$ 122.5 $mAhg^{-1}$ 108.2 $mAhg^{-1}$	0.1 C 1 C 2 C 3 C 5 C	(Guo et al., 2014)
Solvothermal method	$MnSO_4 \cdot H_2O$ Li_3PO_4	140 $mAhg^{-1}$ 85 $mAhg^{-1}$	0.1 C 1 C	(Wang et al., 2014)
Solvothermal method	$MnSO_4 \cdot H_2O$ Li_3PO_4	147 $mAhg^{-1}$	0.05 C	(Yang et al., 2012)
Solvothermal method	$LiOH \cdot H_2O$ H_3PO_4 $(CH_3COO)_2Mn \cdot 4H_2O$	133 $mAhg^{-1}$	0.1 C	(Dezhi Chen et al., 2012)

Synthesis method	Starting materials	Initial discharge capacity	Current rate	Ref.
Spray drying	$LiNO_3$ H_3PO_4 $Mn(NO_3)_2 \cdot 6H_2O$	112 $mAhg^{-1}$ (room temperature) 130 $mAhg^{-1}$ 55 °C	0.05 C	(Bakenov & Taniguchi, 2011)
Spray drying	$LiNO_3$ H_3PO_4 $Mn(NO_3)_2 \cdot 6H_2O$	147 $mAhg^{-1}$ 145 $mAhg^{-1}$ 123 $mAhg^{-1}$ 65 $mAhg^{-1}$	0.05 C 0.1 C 1 C 10 C	(Nam et al., 2011)
Polyol method	LiH_2PO_4 $(CH_3COO)_2Mn \cdot 4H_2O$	129 $mAhg^{-1}$	0.05 C	(Zhu et al., 2014)
Polyol method	$CH_3COOLi \cdot 2H_2O$ $(CH_3COO)_2Mn \cdot 4H_2O$ $NH_4H_2PO_4$	164 $mAhg^{-1}$	0.1 C	(Kumar, Venkateswarlu, & Satyanarayana, 2012)

2.3.2 **Chosen method for current work**

Various synthesis techniques have been analyzed for current work. Sol gel route is selected to synthesize samples for this work. Sol gel technique is one of the effective methods in wet chemistry route which attracts most of the recent electrode material preparations (Hildebrandt et al., 2012; Liu, Qiu, Mai, Wu, & Zhang, 2015; Singhal, Namgyal, Jauhar, Lakshmi, & Bansal, 2013; Zhang et al., 2013). Sol gel method consuming aqueous or alcoholic medium made of complexing agent to dissolve the starting materials such as acetates, nitrates, hyroxides etc. During evaporation of the solvent, the sol becomes gel. Hydroxy and carboxylic chains that contained in the complexing agent form chemical bond with the metal ions to produce dry solid which referred as precursor. Subsequently, required calcination process at sufficient time will produce complete end product (Bhuwaneswari et al., 2010). The benefits of sol gel method can be listed as homogeneous mixing at molecular level, control of particle size, short heating time and synthesis temperature (Fu et al., 2005; Hildebrandt et al., 2012; Kandhasamy, Pandey, & Minakshi, 2012).

Chelating agents are greatly accountable for homogeneous distribution of metal ions and phase purity in the sol gel method which has main effect on the structural properties (Lingjun et al., 2015; Dunqiang Wang, Cao, Huang, & Wu, 2013a). Few examples of chelating agents that accommodated during sol gel method to produce cathode materials are listed in Table 2.4.

Table 2.4: Chelating agents used in sol gel method to produce cathode materials

Cathode materials	Chelating agents	Reference
$Li_3V_2(PO_4)_3/C$	Composite of glycine and beta-cyclodextrin	(Lijuan Wang, Liu, Tang, Ma, & Zhang, 2012)
$LiFePO_4$	ethylenediaminetetraacetic acid	(Li, Hua, & Wang, 2011)
$LiMn_2O_4$ $LiMn_{1.4}Cr_{0.2}Ni_{0.4}O_4$	Citric acid	(Yi, Shu, Zhu, & Zhu, 2009)
LiV_3O_8	Oxalic acid Citric acid Tartaric acid Malic acid	(Dunqiang Wang, Cao, Huang, & Wu, 2013b)
$LiFePO_4/C$	Acetic acid	(Yang, Kang, Jiang, & Ahn, 2012)
$LiFePO_4/C$	Lauric acid	(Cheng et al., 2011)
$Li[Li_{0.2}Co_{0.13}Ni_{0.13}Mn_{0.54}]O_2$	Oxalic acid Tartaric acid Succinic acid	(Zhao et al., 2013)
$LiNi_{0.5}Mn_{1.5}O_4$ $LiNi_{0.4}Cr_{0.15}Mn_{1.45}O_4$	Tartaric acid	(Wang et al., 2015)

Cathode materials	Chelating agents	Reference
$LiFePO_4/C$	Oxalic acid	(Dou et al., 2012)
$LiFePO_4/C$	Citric acid	(Wi et al., 2012)
Li_2MnSiO_4	Adipic acid	(Aravindan et al., 2010)
LiV_3O_8	Oxalic acid	(Pan et al., 2011)
$Li_3V_2(PO_4)_3/C$	Citric acid Salicylic acid Polyacrylic acid	(Xiang et al., 2013)
Li_2FeSiO_4/C	Tartaric acid	(Gao, Wang, Zhang, Zhang, & Song, 2014)
$LiCo_{1/3}Mn_{1/3}Ni_{1/3}PO_4$	Aitric acid Triethanolamine Polyvinylpyrrolidone	(Kandhasamy, Singh, et al., 2012)
$LiFePO_4/C$	Tannic acid Tartaric acid Stearic acid	(Gao et al., 2014)

Interestingly, Zhang et al have found that addition of oxalic acid during synthesis and further calcination process leads to gas evolution and formed macroporous morphologhy (Zhang, Liu, & Huang, 2012). To exemplify the benefits of macroporous structure, model in Figure 2.24 referred.

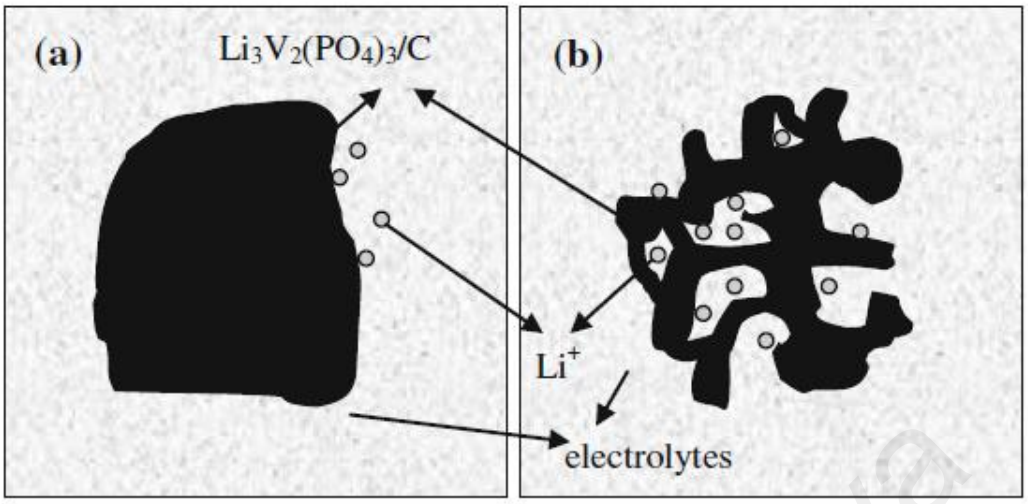

Figure 2.24: (a) Bulk morphologhy (b) Macroporous morphologhy
(Zhang et al., 2012)

Bulk morphology limits the diffusion of electrolyte into the material whereas macroporous morphology gives sufficient space for electrolyte to penetrate easily. This would be advantageous factor for lithium diffusion hence upgrades electrochemical activity.

Another remarkable fact is that oxalic acid acts as carbon source. Oxalic acid is a low molecular weight acid which forms minimal carbon as in the following equation (Kim, Cho, Kam, Kim, & Lee, 2010).

$$4(C_2H_2O_4) \rightarrow 2C + 4H_2O + 6CO_2 \uparrow$$

For example, ascorbic acid is good reductive agent but it has many carbon atoms. Hence, it will be hard to control carbon production or coating which turns to be hurdle in electrochemical performance.

Adding to that, decomposition of oxalic acid will be able to create continuous carbon network embedded within particles thus reduces agglomeration (Lijuan Wang, Zhou, & Guo, 2010a). From the viewpoint of crystal field theory, the lower the stability constant, easier for decomposition takes place (Yang et al., 2012). Oxalic acid categorized as complexing agent with lower stability constant about 5.2 (Muruganantham, Sivakumar, Subadevi, & Wu, 2015).

Other than that, addition of small amount of concentrated nitric acid during synthesis process to produced greatly dispersed nanoparticles (Liu, Gao, & Ji, 2011; Muhammad et al., 2015; Raja, Mahanty, & Basu, 2009).

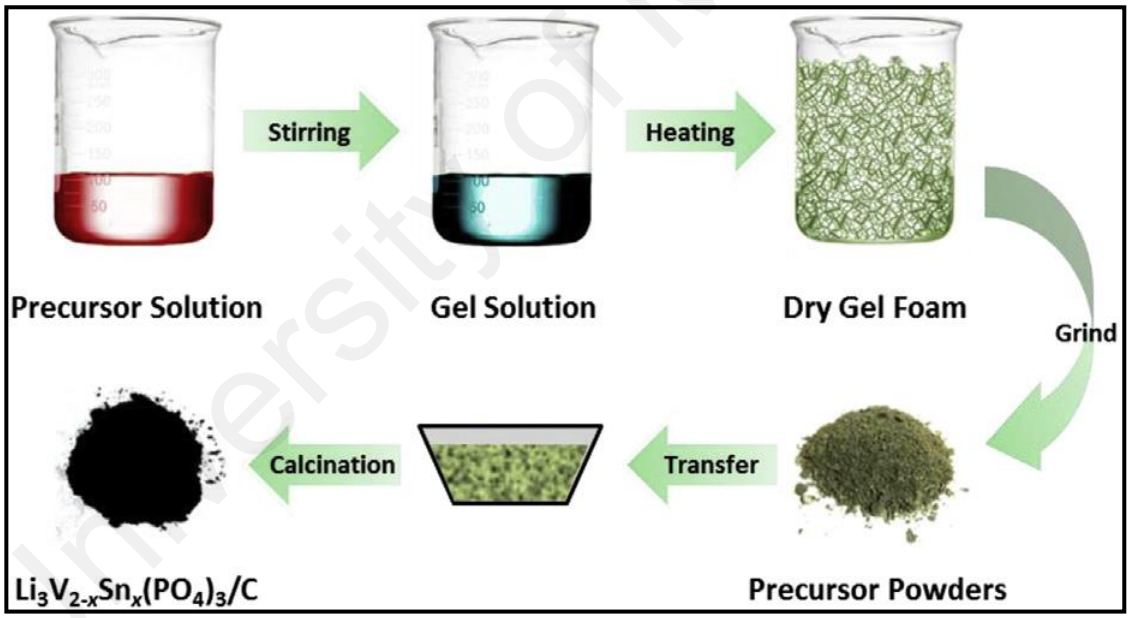

Figure 2.25: Schematic of $Li_3V_{2-x}Sn_x(PO_4)_3/C$ synthesis process (Xia et al., 2015)

Similar synthesis technique has been used by recent researchers to produce $Li_3V_{2-x}Sn_x(PO_4)_3/C$ (Y. Xia et al., 2015), $LiMn_2O_4$ and $LiMg_xSn_yAl_zMn_{2-x-y-z}O_4$ (x, y, z = Mg, Sn, Al) (x = 0.00-0.09; y = 0.04-0.1; z = 0.35-0.20) (Thirunakaran, Ravikumar, Vanitha, Gopukumar, & Sivashanmugam, 2011), $LiMn_2O_4$, $LiCr_xMn_{2-x}O_4$ and

$LiAl_xMn_{2-x}O_4$ (x=0.0-0.4) (Thirunakaran, Sivashanmugam, Gopukumar, Dunnill, & Gregory, 2008), $LiMn_{1.94}MO_4$ (M = $Mn_{0.06}$, $Mg_{0.06}$, $Si_{0.06}$, ($Mg_{0.03}Si_{0.03}$) (Zhao et al., 2015) etc. Figure 2.25 illustrates schematic of synthesis procedures to obtain final product via sol gel route.

2.3.3 Approaches to improve the electrochemical properties of $LiMnPO_4$

2.3.3.1 Carbon coating

Nanosized $LiMnPO_4$/C cathode materials were prepared using oleylamine mediated solvothermal method as in Figure 2.26 (Fan et al., 2016). Oleylamine acting as a capping agent, immersed on the surface of $LiMnPO_4$ and preventing the growth of the particles during the synthesis process. After heating in atmosphere of N_2, the oleylamine layer decomposed and formed a thin carbon coating layer on the $LiMnPO_4$ surface.

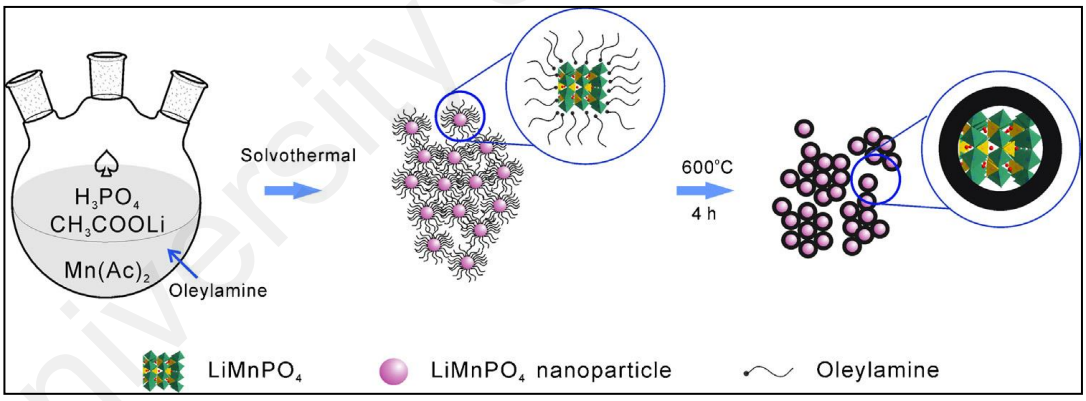

Figure 2.26: Schematic diagram of oleylamine-assisted solvothermal in-situ carbon coating (Fan et al., 2016)

Small size of 20–40 nm $LiMnPO_4$ delivered capacity of 168 $mAhg^{-1}$ at 0.1 C. Carbon layers reduce the side reactions between active materials and electrolyte. Besides that, it also shields the $LiMnPO_4$ pulverization during lithiumation/delithiumation.

$LiMnPO_4$ nanocrystals have been produced by colloidal synthesis followed by surface etching with $LiPF_6$ and carbon coating by glucose (Lin Chen et al., 2016). Etching procedure as displayed in Figure 2.27 shows beneficial towards improved electrochemical performances.

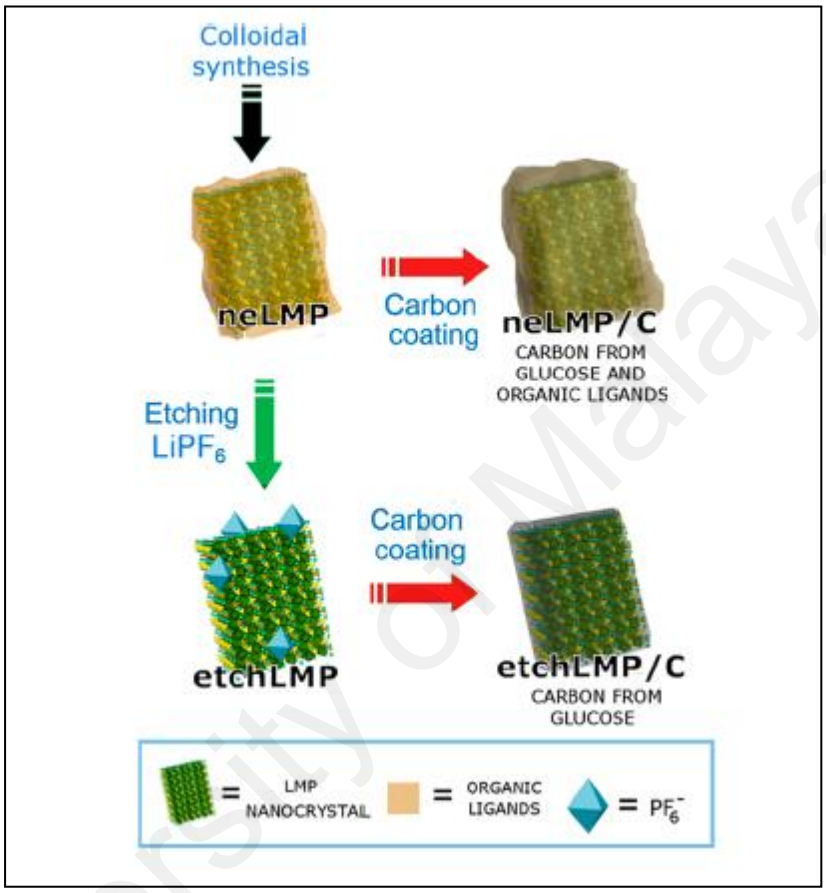

Figure 2.27: Etching process with $LiPF_6$ and carbon coating by glucose (Lin Chen et al., 2016)

Etching process is advantageous from following points of view:

(i) Hydrophobic surfactants are removed and replaced with hydrophilic PF_6. This promotes nanoparticles solubility in glucose solution and enables good conductive carbon layer.

(ii) To synthesize composite electrodes with less carbon additive and polymeric binder.

Carbon coated etched $LiMnPO_4$ nanocrystals displayed capacity of 118 $mAhg^{-1}$ at 1C with 92% capacity retention after 120 cycles. The recorded capacity is higher compared to non-etched carbon coated $LiMnPO_4$.

Hollow spindle $LiMnPO_4$ materials were developed with the aid of glucose in dimethyl sulfoxide (DMSO)/H_2O (Fu et al., 2015). The particles contain hollow spindles of average width 200 nm, length of 500 nm – 700 nm and wall thickness of 30 nm – 60 nm. $LiMnPO_4$/C exhibited splendid initial discharge capacity of 161.8 $mAhg^{-1}$, 137.7 $mAhg^{-1}$ and 110.8 $mAhg^{-1}$ at 0.05 C, 0.1 C and 0.2 C respectively. After 100 cycles, 92 % of its initial discharge capacity maintains at 0.2 C. Impressive electrochemical performance highly ascribed to the hollow spindle structure which eases electrolyte penetration, thus increased solid liquid interface. Besides that, carbon layer wrapping the hollow spindle enhances electronic conductivity and wall thickness in nanometers reduced lithium ion diffusion path.

Insitu polymerization technique was used to prepare polydopamine derived carbon coating on $LiMnPO_4$/C (Hong, Tang, & Zhang, 2015). $LiMnPO_4$/C material with 6.84 wt.% carbon delivered 126 $mAhg^{-1}$ at 0.5 C, 118 $mAhg^{-1}$ at 5 C and 106 $mAhg^{-1}$ at 10 C. It also exhibited 91.5 % of its initial capacity after 100 cycles at 0.5 C. Electrochemical results suggest that thin carbon layer that sufficient to cover $LiMnPO_4$ fully gives space for electron conduction in all directions without lithium ion pathways unhindered.

Facile oleic acid assisted solid state technique has been approached to prepare $LiMnPO_4$/C nanocomposites with two level hierarchical structures (Longfei Zhang et al., 2014). $LiMnPO_4$ with 7.5 wt.% carbon exhibited specific capacity of 130.1 $mAhg^{-1}$

at 0.05 C, 116.3 $mAhg^{-1}$ at 1 C and 60.1 $mAhg^{-1}$ at 20 C. At the same time, it also retains 97.5 % of its capacity after 50 cycles at 0.1 C. Residual surfactant and carbon precursor create three-dimensional (3D) network particularly surrounding and between the particles. This is favorable for smooth electrons movements and reduced lithium ion pathways.

$LiMnPO_4$ samples were coated by conductive carbon by pyrolyzing sucrose (Dinh, Mho, Kang, & Yeo, 2013). This work also explained that the amount of conductive carbon applied on the samples is one of the essential factors. The amount of carbon varied up to 20 wt. %, which 10 wt. % carbon displayed high capacity. At 25 °C, the sample delivered 153 $mAhg^{-1}$ at first cycle and 146 $mAhg^{-1}$ at 110th cycle. At 55 °C, the sample exhibited 171 $mAhg^{-1}$ and 166 $mAhg^{-1}$ at first cycle and 110th cycle respectively.

Li and coworkers have prepared $LiMnPO_4$ nanorods and applied carbon layer on them from citric acid, ascorbic acid, glucose, sucrose, and betacyclodextrin (Li et al., 2013). $LiMnPO_4$ coated with beta-cyclodextrin as the carbon source presented improved capacity among other carbon sources. It demonstrated capacity of 153.4 $mAhg^{-1}$ at a rate of 0.1 C and retained about 120 $mAhg^{-1}$ after 50 cycles. The enhanced electrochemical performance accredited to molecule structure rich with oxygenous groups advantageous to their uniform adsorption on the electrodes which will effectively produce electron-conductive carbon layer after calcinations.

$LiMnPO_4$/C was prepared by an acetate assisted antisolvent precipitation method followed by ball milling and heat treatment (Su et al., 2013b). Precursors of $Mn_3(PO_4)_2$ and Li_3PO_4 nanoparticles which obtained from precipitation technique were ball milled

with glucose. Carbon coated $LiMnPO_4$ with the particle size about 60 nm was formed after heat treatment. The sample displayed discharge capacity of 154 $mAhg^{-1}$, 134 $mAhg^{-1}$, 120 $mAhg^{-1}$, 90 $mAhg^{-1}$ and 61 $mAhg^{-1}$ at the rates of 0.05 C, 0.2 C, 1 C, 5 C and 10 C respectively.

Nanosized $LiMnPO_4$ was produced by solvothermal method in ethylene glycol solvent (Liu, Liu, Huang, & Yu, 2013). C_6H_5COOLi (lithium benzoate), CH_3COOLi (lithium acetate) and $C_5H_7LiO_2$ (2,4-pentanedionato lithium) were used as lithium salts together $MnSO_4 \cdot 2H_2O$, $NH_4H_2PO_4$ and citric acid. This work suggested that insitu carbon coating can be achieved effectively by decomposition of the organic group in lithium salt during solvothermal synthesis process. Decomposition of benzoyloxy forms insitu carbon coating during synthesis. Figure 2.28 explains that good polarity of benzoyloxy in ethylene glycol solvent helps it in adhere to $LiMnPO_4$. Further high temperature and pressure decompose benzoyloxy to amorphous carbon.

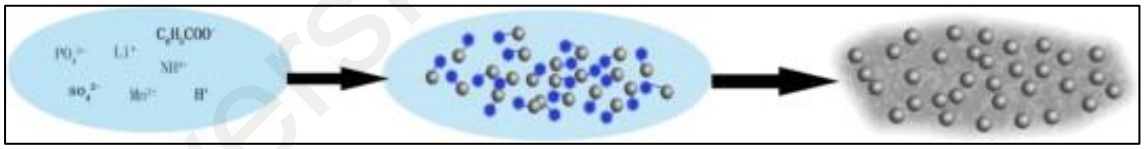

Figure 2.28: Carbon formation mechanism by lithium benzoate(C_6H_5COOLi) (Liu et al., 2013)

Interestingly, mesoporous $LiMnPO_4$ particles containing of interconnected nano-grains and pores of comparable size with a thin layer of carbon coating was synthesized by Ramar et al (Ramar, Saravanan, Gajjela, Hariharan, & Balaya, 2013). They used high energy ball mill with soft template method followed by a post heat treatment. Figure 2.29 illustrates the procedures that have been approached. This type of structure provides benefits such as nanoparticles reduce lithium ion path, uniform carbon coating surrounds active materials enhance electronic conductivity, electronic network

improved by interconnectivity of primary and secondary particles, mesopores existence within or between secondary particles allow smoother liquid electrolyte penetration, lattice strain that made during milling removed by post heat treatment.

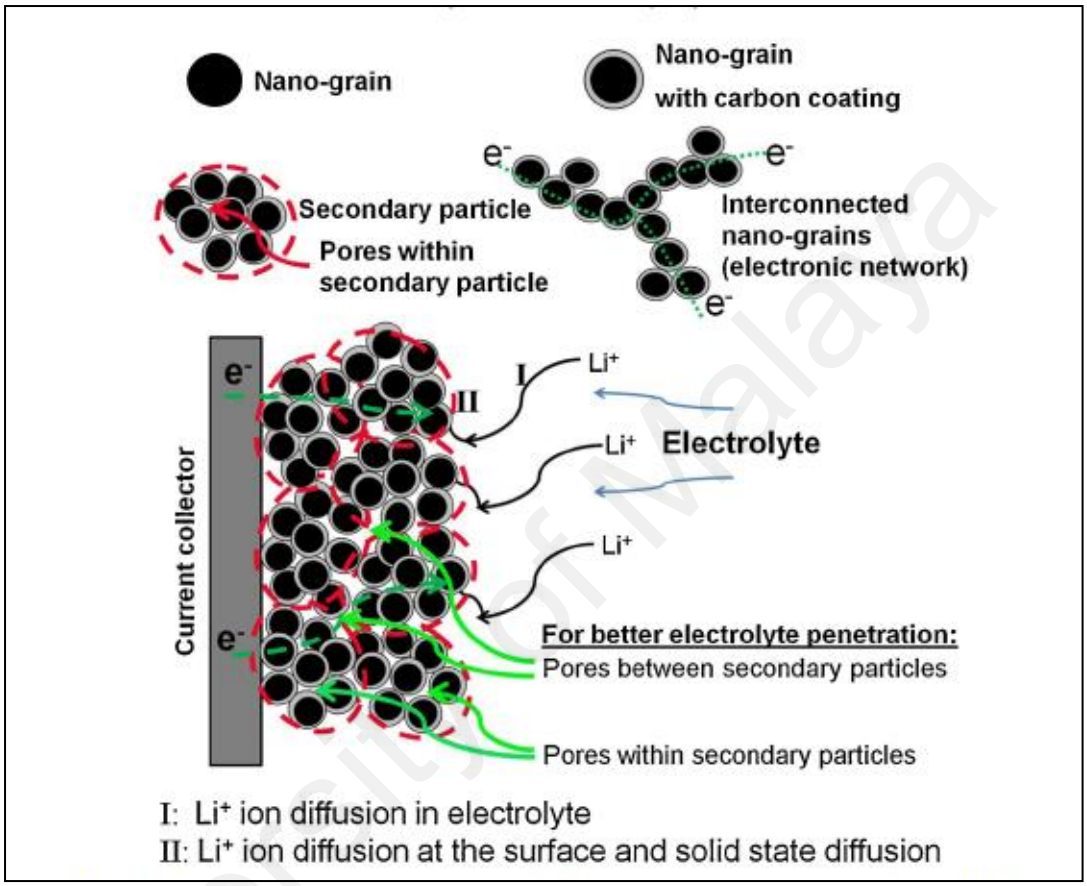

Figure 2.29: Schematic diagram of mesoporous $LiMnPO_4$ particles containing of interconnected nano-grains and pores with a thin layer of carbon coating (Ramar et al., 2013)

Carbon coated $LiMnPO_4$ was synthesized by polyvinyl pyrrolidone (PVP) assisted solid-state technique (Ran et al., 2013). PVP was added during ball milling which helps in smaller particle size and uniform carbon coating. This work promotes simple and cheap synthesis methods compared with wet chemical methods. The samples that with PVP showed excellent capacity of 134 $mAhg^{-1}$ at 0.1 C, 120 $mAhg^{-1}$ at 0.5 C, 108 $mAhg^{-1}$ at 1 C. While the discharge capacities of samples without PVP exhibited 105 $mAhg^{-1}$ at 0.1 C, 92 $mAhg^{-1}$ at 0.5 C and 88 $mAhg^{-1}$ at 1 C.

2.3.3.2 **Metal oxide coating**

Surface modification is one of the effective methods to overcome cycling instability at higher voltages (Xue Zhou, Ye Xie, Yuanfu Deng, 2015; Yang et al., 2015). Coating reduces the side reactions of cathode and electrolyte which causes negative effects to the electrochemical performance (Fang et al., 2012; Gan et al., 2015).

Until now, there are limited works published on metal oxide coated $LiMnPO_4$. Recently CeO_2/C hybrid coated $LiMnPO_4$ has been successfully synthesized by Chen et al (Chen, Tao, Wang, Zhang, & Chen, 2015b). They found that nanometer sized CeO_2 coating played role as an innerconnector in the carbon network which positively enhanced cycling stability (Chen et al., 2015b). Meanwhile Dong et al (Dong et al., 2014) reported that the Li_3VO_4 coated $LiMnPO_4$ electrode created three dimensional path of Li^+ ion transport path and also lowered Mn dissolution, thus hindered phase formation on the $LiMnPO_4$ surface which deteriorates rate capability.

2.3.3.3 **Ion doping**

Apart from that, substitution or cation doping is another excellent way to enrich the electrochemical performance. Different metal ions have been approached to substitute manganese site of $LiMnPO_4$ and few recent works have been summarized in Table 2.5. $LiMn_{1-1.5x}Ce_xPO4$/C (x = 0, 0.01, 0.03, 0.05) were prepared and $LiMn_{0.955}Ce_{0.03}PO_4$/C exhibited the best cycling stability and rate capability (Kou et al., 2015). It delivered highest discharge capacity of 132.3 $mAhg^{-1}$ at 0.1 C and retains 95.4 % of its capacity after 50 cycles. Ce^{3+} effectively doped into the crystal lattice of $LiMnPO_4$, which can improve the electronic conductivity, enhance the lithium ion diffusion kinetics and increase the structural stability of $LiMnPO_4$.

Table 2.5: Summary of doped $LiMnPO_4$ cathode materials

Synthesis method	$LiMnPO_4$ derivatives	Ref.
Solid state reaction	$LiM(II)PO_4$, [M(II)=Mn,$Mn_{0.9}Co_{0.1}$,$Mn_{0.8}Co_{0.1}Mg_{0.1}$]	(Sronsri, Noisong, & Danvirutai, 2016)
Solvothermal method	$LiMn_{1-x}Fe_xPO_4$ (x = 0, 0.2, 0.5, 1)	(Zou et al., 2016)
Polyol method	$LiMn_xFe_{1-x}PO_4$ (x = 0.2, 0.5, 0.8)	(Xu et al., 2016)
Sol gel method	$LiMn_{1-x}Fe_xPO_4$ (x = 0, 0.2, 0.4, 0.6, 0.8)	(Seo et al., 2016)
Solid state reaction	$LiMnPO_4$/C, $LiMn_{0.85}Fe_{0.15}PO_4$/C, $LiMn_{0.92}Ti_{0.08}PO_4$/C, $Li(Mn_{0.85}Fe_{0.15})_{0.92}Ti_{0.08}PO_4$/C	(Huang et al., 2016)
Freeze drying method	$LiMn_{0.8}Fe_{0.1}M_{0.1}PO_4$ (M = Fe, Co, Ni, Cu)	(Iturrondobeitia et al., 2015)
Hydrothermal process	$LiMn_{1-x}Ni_xPO_4$ $0 \leq x \leq 0.45$	(Ottmann, Jähne, Meyer, & Klingeler, 2015)
Co-precipitation method	$LiMn_{0.8}Fe_{0.2}PO_4$	(Yang, Bi, Qin, Liu, & Zhang, 2015)
Solid-state method	$LiFe_{0.5}Mn_{0.5}PO_4$	(Xue Zhou, Ye Xie, Yuanfu Deng, 2015)

Synthesis method	$LiMnPO_4$ derivatives	Ref.
Sol gel process	$LiMn_{0.6}Fe_{0.4}PO_4$	(Kim, Vijaya, Zhu, & Kim, 2015)
Solvothermal synthesis	$LiMn_{1-1.5x}Ce_xPO_4$, (x = 0, 0.01, 0.03, 0.05)	(Kou et al., 2015)
Solid-state method	$LiMn_{1-x}V_xPO_4$, ($0 \leq x \leq 0.075$)	(Dai, Fang, Yang, Ma, & Dai, 2015)
Two step technique	$LiMn_{1-x}Cr_xPO_4$, (x = 0, 0.03, 0.06, and 0.1)	(Gan et al., 2015)
Two-step solid-state method	$LiMn_{0.9}Fe_{0.1-x}Co_xPO_4$, (x = 0, 0.05 and 0.1)	(Xiang et al., 2015)
Solvothermal method	$LiMn_{1-x}Fe_xPO_4$, (x = 0, 0.1, 0.2, 0.3, 0.4, 0.5)	(Hu et al., 2014)
Sol–gel method	$LiMn_{0.6}Fe_{0.4}PO_4$	(Liu, Liao, & Yu, 2014)
Ionothermal synthesis	$LiMn_{0.95}Fe_{0.05}PO_4$	(Li, Liu, Jin, Meng, & Liu, 2014)
Solid-state method	$LiMn_{1-x}Fe_xPO_4$ (x = 0.1, 0.2, 0.3)	(Tao Liu, Wu, & Wu, 2014)
Solvothermal process	$LiMn_{1-x}Fe_xPO_4$ (x = 0, 0.1, 0.2)	(Hong, Tang, Hong, & Zhang, 2014)

Synthesis method	$LiMnPO_4$ derivatives	Ref.
Solvothermal process	$LiMn_{0.9}Fe_{0.1}PO_4$	(Dai et al., 2013)
Solid-state method	Zn (0.02, 0.1)	(Fang et al., 2012)
Solid-state reactions	$LiFe_{1-x}Mn_xPO_4$ (x = 0.85, 0.75, 0.65)	(Li Chen, Yuan, Feng, & Li, 2012)
Polyol method	$LiMn_{0.71}Fe_{0.29}PO_4$	(Jo, Yoo, Jung, & Cho, 2012)
Combustion method	$LiMn_{0.5}Co_{0.5}PO_4$, $LiMn_{0.33}Co_{0.33}Ni_{0.33}PO_4$	(Minakshi & Kandhasamy, 2012)
Hydrothermal method	Cu (2 %, 5 %)	(Ni & Gao, 2011)
Solid-state reaction	$LiMn_{1-x}M_xPO_4$, (M=Mg^{2+},Ca^{2+},Zr^{4+})	(Lee et al., 2010)
Solid-state reaction	$LiMn_{0.9}Fe_{0.1}PO_4$, $LiMn_{0.9}Fe_{0.05}Mg_{0.05}PO_4$	(Hu et al., 2010)

In another work, $LiMn_{0.9}Fe_{0.1-x}Co_xPO_4/C$ (x = 0, 0.05 and 0.1) showed lattice shrinkage after substitution since radii of Fe^{2+} and Co^{2+} smaller compared to Mn^{2+} (Xiang et al., 2015). Structural analysis suggested that substitution reduce the Mn-O and P-O bond length but increase the Li-O bond length. This strengthens physical stability

and widens Li diffusion channels. $LiMn_{0.9}Fe_{0.05}Co_{0.05}PO_4/C$ displayed discharge capacity of 145 $mAhg^{-1}$ at a current rate 0.05 C.

Yi Gan et al synthesized $LiMn_{1-x}Cr_xPO_4$ (x = 0, 0.03, 0.06 and 0.1) via two step technique (Gan et al., 2015). Results demonstrated that $LiMn_{0.94}Cr_{0.06}PO_4$ has enhanced cycling properties compared to $LiMn_{0.97}Cr_{0.03}PO_4$. At the same time, aging tests also exhibited that its high stability over high electrolyte concentration (1.5M $LiPF_6$). Cr^{3+} doping successfully stabilize the electrolyte/carbon interface due to reduced reactivity of oxygen atoms in substituted $LiMnPO_4$.

Solid state method has been used to prepare $LiMn_{1-x}V_xPO_4/C$ (x = 0.025, 0.05 and 0.075) (Dai et al., 2015). SEM reveals that smaller particles observed for vanadium doped $LiMnPO_4$. However, $Li_3V_2(PO_4)_3$ impurity produced when amount of vanadium exceeded to 0.075. The result also demonstrated that appropriate V^{3+} doping in Mn site of $LiMnPO_4$ reduces charge transfer resistance, thus enhanced electrochemical performance. In this work, $LiMn_{0.975}V_{0.025}PO_4/C$ found to be reveals best electrochemical results.

Among substitution research approaches on $LiMnPO_4$, doping Mn site with Fe has been receiving wide attention to enhance electrochemical performance. $LiMnPO_4$ shrinks about 8.9 % while $LiFePO_4$ shrinks about 6.8 % during cycling. Fe substitution at optimum level is favorable for $LiMnPO_4$ (Li Chen et al., 2012).

Recent works have been used solvothermal method to prepare $LiMn_{1-x}Fe_xPO_4$ (x = 0, 0.2, 0.5, 1) as illustrated in Figure 2.30 (Zou et al., 2016). Deionized water and ethylene glycol was utilized as mixed solvent while ascorbic acid acts as an antioxidant,

surfactant and carbon source. $LiFe_{0.15}Mn_{0.85}PO_4$ exhibited high energy density of 546 $Whkg^{-1}$. It also showed good cycling properties about 97.1 % at the 100th cycle and 120.2 $mAhg^{-1}$ at 20 C.

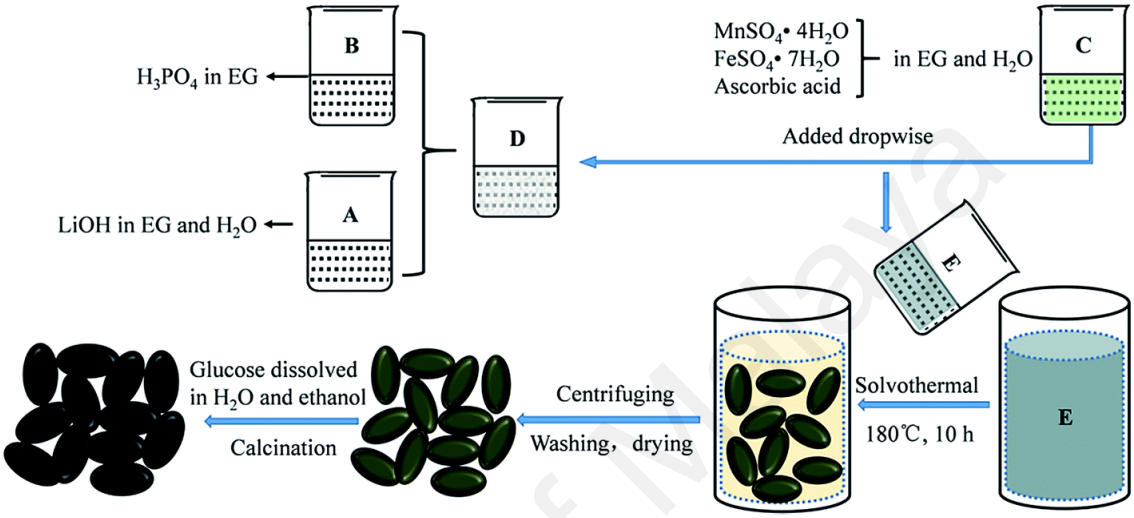

Figure 2.30: Novel solvothermal method to prepare $LiMn_{1-x}Fe_xPO_4$ (x = 0, 0.2, 0.5, 1) (Zou et al., 2016)

$LiFe_xMn_{1-x}PO_4$ ($x \leq 0.15$) nanoplates have been synthesized via two pot precursors mixing technique (Liao et al., 2015). $LiFe_{0.15}Mn_{0.85}PO_4$ recorded discharge capacities of 138.0 $mAhg^{-1}$, 130.0 $mAhg^{-1}$ and 120.9 $mAhg^{-1}$ at 5 C, 10 C and 20 C respectively. The sample also exhibited good cycling stability which maintained 70% of its initial capacity after 1000 cycles. Long cycle life ascribed to Fe doping in Mn sites that suppressed Mn^{2+}dissolution. This work delivers simple method to achieve superior electrochemical properties with low Fe doping amount.

Co-precipitation method assisted by dimethyl sulfoxide (DMSO) was employed to produce nano-$LiMn_{0.8}Fe_{0.2}PO_4$ (Yang et al., 2015). Polyvinylpyrrolidone (PVP) was used as anti-agglomeration agent. Nano-$LiMn_{0.8}Fe_{0.2}PO_4$ with 5.7 wt% carbon exhibited

discharge capacity of 160.6 $mAhg^{-1}$ at 0.05 C. Discharge capacities of 113 $mAhg^{-1}$, 102 $mAhg^{-1}$ and 83 $mAhg^{-1}$ are recorded at 10 C, 20 C and 50 C respectively. The discharge capacity at -15°C is 97 $mAhg^{-1}$ at 0.1 C. High rate and low temperature performances of nano-$LiMn_{0.8}Fe_{0.2}PO_4$/C found to be efficient to be used in lithium ion batteries.

Hong et al have synthesized $LiMn_{1-x}Fe_xPO_4$ (x = 0, 0.1, 0.2) with solvothermal method using water and polyethylene glycol (PEG200) mixed solvent (Hong et al., 2014). The mixed solvent found to be advantageous for dispersion and dissolution of the starting materials. $LiMn_{0.8}Fe_{0.2}PO_4$ nanorods delivered specific capacity of 165.3 $mAhg^{-1}$ at 0.05C and 131.6 $mAhg^{-1}$ at 0.5C. Electrochemical performances prove that small Fe amount substitution in Mn site significantly enhances its electrochemical properties.

Shuttle shaped $LiMn_{0.95}Fe_{0.05}PO_4$/C was produced by ionothermal method utilizing two imidazolium based ionic liquids as reaction medium namely 1-ethyl-3-methylimidazolium trifluoromethanesulonate, [EMIM]OTf and 1-buty-3-methylimidazolium trifluoromethanesulonate, [BMIM]OTf (Li et al., 2014). $LiMn_{0.95}Fe_{0.05}PO_4$/C samples synthesized in [BMIM]OTf displays uniform and smaller particle distribution. It exhibited high discharge capacities of 159.2 $mAhg^{-1}$, 146.0 $mAhg^{-1}$, 135.1 $mAhg^{-1}$, 125.3 $mAhg^{-1}$, 115.5 $mAhg^{-1}$ and 84.4 $mAhg^{-1}$ at current rate of 0.1 C, 0.2 C, 0.5 C, 1 C, 2 C and 5 C accordingly.

$LiMn_{0.9}Fe_{0.1}PO_4$ nanorods, nanoparticles and nanoplates were prepared via solvothermal technique at pH = 9, 11 and 12.5 respectively (Hu et al., 2014). $LiMn_{0.9}Fe_{0.1}PO_4$ nanoplates reveal highest rate performance signifying pH = 12.5 as optimal condition. To explore the effects of Fe doping, $LiMn_{1-x}Fe_xPO_4$ (x = 0, 0.1, 0.2,

0.3, 0.4, 0.5) nanoplates were prepared in same condition of pH = 12.5. The initial discharge capacities of Fe doped samples exhibited above 150 $mAhg^{-1}$ at 0.05 C. $LiMn_{0.5}Fe_{0.5}PO_4$ showed approximately 100 % capacity retention at the 100th cycle, higher than $LiMnPO_4$.

Apart from cation doping on Mn sites, boron was doped in P-site of $LiMnPO_4$ via solid state method (Hu et al., 2014). $LiMnP_{0.9}B_{0.1}O_{4-\delta}$ exhibited discharge capacity of 130 $mAhg^{-1}$ at 0.1 C and remains 71 % of the capacity at 2 C. The discharge capacity of boron doped $LiMnPO_4$ improved 30 % at 0.1 C and 131 % at 2 C compared to pristine. No capacity fading observed after 50 cycles at 0.2 C. Boron doping in P site found to be enhanced electrode stability and high rate capability.

Pre-synthesized $FePO_4{\cdot}2H_2O$ nanocrystallites were used to prepare $LiFe_xMn_{1-x}PO_4$ (x = 0.85, 0.75, 0.65) by solid state method (Li Chen et al., 2012). The obtained samples showed well-ordered structures and two plateaus at 3.5 V and 4.1 V in their charge/discharge curves. $LiFe_{0.25}Mn_{0.75}PO_4/C$ performed excellent electrochemical activity by delivering discharge capacity of 130 $mAhg^{-1}$ at 0.05 C which can be accredited to optimum Fe substitution and $FePO_4{\cdot}2H_2O$ nanoparticles starting materials.

2.3.3.4 **Particle size reduction**

Microsized porous $LiMnPO_4$ nanoflakes embedded with interrelated $LiMnPO_4$ nanocrystals (30 nm – 50 nm) were prepared (Xia, Liu, Xu, Cheng, & Wu, 2015). The nanocrystals reduced the path of diffusion for both lithium and electrons. At the same time, porous $LiMnPO_4$ nanoflakes enable homogeneous carbon coating that can improve electronic conductivity. It also improves easy electrolyte penetration. Porous

$LiMnPO_4$ nanoflakes achieved discharge capacities of 151 $mAhg^{-1}$, 142 $mAhg^{-1}$, 135 $mAhg^{-1}$, 130 $mAhg^{-1}$ and 128 $mAhg^{-1}$ at 0.01 C, 0.1 C, 0.5 C, 1 C and 2 C accordingly.

Zhao et al (Zhao et al., 2014) have performed crystallite size control method to produce $LiMnPO_4$. Li_3PO_4 crystallites were embedded in carbon matrix which obtained from the pyrolysis of sucrose. Smaller $LiMnPO_4$ crystallites (8 - 12 nm) were formed by carbon coated Li_3PO_4 and $MnSO_4$ via solvothermal technique. This sample exhibited higher discharge potential plateau, superior electrochemical performance and high cycling stability. This work also concluded that carbon matrix shortens lithium ion diffusion path and improves electrical conductivity.

In a different study, nanosized $Mn_3(PO_4)_2{\cdot}3H_2O$ particles were formed by a T-type micro-channel reactor and followed by calcination under argon atmosphere after adding lithium and carbon sources (Hua-jun Zhu, Zhai, Yang, Liu, & Chen, 2014a). Nanosized $LiMnPO_4/C$ from this process showed 137 $mAhg^{-1}$ at 0.05 C. This strategy diminished the impurities, thus blocked [010] channels for Li^+ migration were reduced and enriched Li^+ diffusion coefficient. This technique provides cheap and simple way to $LiMnPO_4/C$ mass product which can be utilized in hybrid electric vehicles.

$LiMnPO_4$ nanocrystals were prepared by solvothermal method in a solution of water and polyethylene glycol (PEG) (Qin et al., 2012). Morphology transition was detected from a nanorod to a thick nanoplate (~50 nm in thickness) and to a smaller thin nanoplate (20–30 nm in thickness) by changing the pH value of the reaction suspension. Different 3D sizes as thin nanoplates, thick nanoplates and nanorods were noticeably affect the electrochemical performance. Thin nanoplates structure which has smaller b direction compared to thick nanoplates and nanorods demonstrated improved cycling

performance due to its reduced lithium diffusion channels. $LiMnPO_4$ thin nanoplates/graphene exhibited capacity of 149 $mAhg^{-1}$ at 0.1 C, 90 $mAhg^{-1}$ at 1 C and 64 $mAhg^{-1}$ at 5 C.

2.4 Summary of the chapter

Literature review in this chapter introduces types of cathode materials for lithium ion battery applications. Structural properties and synthesis techniques that have been used to produce $LiMnPO_4$ are discussed. Approaches to enhance electrochemical properties of $LiMnPO_4$ have also been explored. Further modifications on $LiMnPO_4$ cathode materials can be analyzed through this chapter.

CHAPTER 3: EXPERIMENTAL PROCEDURES

3.1 Introduction

In this chapter, synthesis of $LiMnPO_4$ based cathode materials; structural characterization techniques and electrochemical analyses are expounded. The synthesis method that involves in each system such as partial sodium substitution, zinc oxide coating, aluminum and copper co-doping are thoroughly described in related chapter accordingly. This chapter provides details on equipments that have been used throughout the experimental and calculations that related to crystallite size, strain and electrochemical properties.

3.2 Synthesis method

Current work has adopted oxalic acid aided sol gel technique to produce $LiMnPO_4$ and its derivatives. Synthesis procedures can be summarized as in Figure 3.1 whereas specific synthesis route are elaborated at particular chapters subsequently.

In this work, oxalic acid has been adopted as chelating agent due to its additional excellent properties which can act as carbon source and reducing agent simultaneously (Lijuan Wang et al., 2012; Wei et al., 2015). Recent researches on cathode materials which produced via oxalic acid assisted sol gel synthesis yielded beneficial outcomes that good for enhanced electrochemical properties.

Small amount of concentrated nitric acid was added during synthesis process targeted towards greatly dispersed nanoparticles formation (Liu et al., 2011; Muhammad et al., 2015; Raja et al., 2009). It also aids to maintain the pH value at 3 (Kandhasamy, Pandey, et al., 2012; Lingjun et al., 2015; Minakshi, Kandhasamy, & Meyrick, 2012; Minakshi & Meyrick, 2013; Teng et al., 2013; Thayumanasundaram & Rangasamy, 2014)

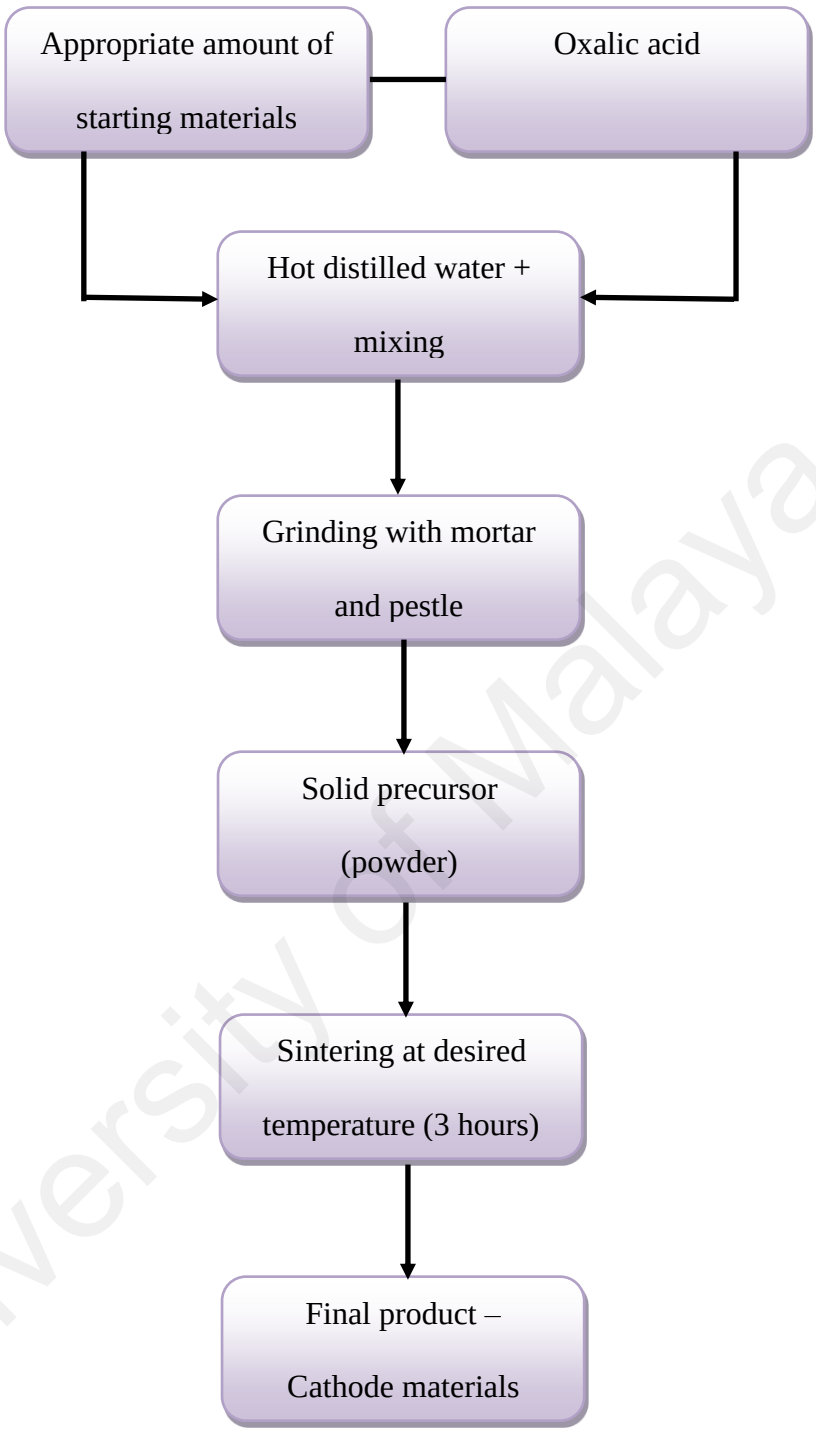

Figure 3.1: Flow chart of sol gel method used for current work

3.3 Characterization techniques

3.3.1 Thermogravimetric Analysis (TGA)

Thermogravimetric analysis (TGA) is a thermal analysis method that givs information about change of sample weight as a function of temperature or time. The change of sample weight is due to the physical or chemical changes that occur within the sample. In this study, TGA (Q500 V20.13 Build 39) was used to determine sintering temperature.

3.3.2 X-Ray Diffraction (XRD)

X-Ray diffraction (XRD) is a potential tool for structural characterization of the materials. XRD profiles providing main data such as peak position (2θ), peak intensity (I), interplanar spacing (*d*) and full width half maximum (FWHM) (Jiajie Li & Hitch, 2016). Peak at 2θ denotes presence or absence of the certain component in the material including specific strong peaks that verify the structure of the materials. At the same time, minor peaks at 2θ also give hint on impurities. Bragg's law implies that shifting in 2θ indicates expansion or shrinking in lattice dimensions.

Lattice parameters of orthorhombic structured samples were calculated by following formula:

$$\frac{1}{d^2} = \frac{h^2}{a^2} + \frac{k^2}{b^2} + \frac{l^2}{c^2} \tag{3.1}$$

Where *d* is interplanar spacing, *a*, *b*, *c* are lattice parameters and *h*, *k*, *l* are miller indices.

X-ray line broadening can be used to obtain microstrain and crystallite size of the sample. This method concludes that both particle size and strain contributes to the line broadening (Fell, Chi, Meng, & Jones, 2012).

$$\beta_{Total} = \beta_{Particle\ size} + \beta_{Strain} \tag{3.2}$$

Broadening owing to particle size is represented by the Scherrer equation while broadening due to strain got by differentiating the Bragg's law (Kwon, Song, & Mumm, 2011; Lemine, 2009; Muruganantham, Sivakumar, & Subadevi, 2015b)

$$\beta_{Total} = \frac{0.9\lambda}{t\cos\theta} + 4\tan\theta\left(\frac{\Delta d}{d}\right) \tag{3.3}$$

Rearranging equation (by multiplying with cos θ):

$$\beta_{Total} = \frac{0.9\lambda}{t\cos\theta} + 4\tan\theta\left(\frac{\Delta d}{d}\right)$$

$$\beta_{Total}\cos\theta = \frac{0.9\lambda}{t} + 4\varepsilon\sin\theta \qquad \text{Where} \quad \left(\varepsilon = \frac{\Delta d}{d}\right) \tag{3.4}$$

where β is the full width half maximum (FWHM) in Radians, θ is the Bragg angle, λ is the wavelength of the radiation (1.54056 Å), t is mean crystallite size and ε is average strain. In the plot of β cos θ versus 4 sin θ, slope of the line representing strain while intercept of the line depicting inverse crystallite size. Microstrain from this plot shows minor defects within the crystalline structure, imperfections including site disorders and vacancies (Fell et al., 2012; Muruganantham, Sivakumar, & Subadevi, 2015b).

3.3.3 Field Emission Scanning Electron Microscopy (FESEM)

Field Emission Scanning Electron Microscopy (FESEM) analysis uses a focused beam of high energy electrons to obtain signal at the surface of the samples. FESEM images provide details on surface morphology, grains orientation in the sample, particles shapes and structures (Ma, Shieh, & Qiao, 2006).

It working principle relates to back scattered electrons (BSE) which resulted from elastic interactions between the incident electrons and the sample (Richards, Owen, & Gwynn, 1999). Few amount of inelastic scattering also occur with less energy than incident beam, hence generates secondary electrons (SE) as in Figure 3.2. This work used FESEM model Quanta FEG 450 and images were captured at different magnifications for clearer visualization of the sample morphologies.

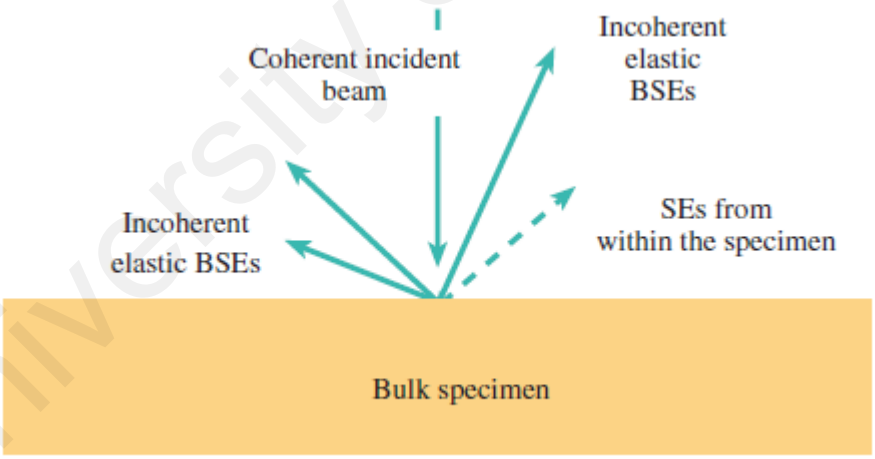

Figure 3.2: Electron scattering during specimen testing in FESEM (Williams & Carter, 2009)

3.3.4 Energy dispersive X-ray spectroscopy (EDAX)

Energy dispersive X-ray spectroscopy (EDAX) is a method to find compositions of the sample. EDAX was performed for selected samples in this research when necessary.

EDAX analysis (EDX-OXFORD) was coupled with FESEM equipment as stated earlier.

3.3.5 Transmission Electron microscopy (TEM)

Transmission Electron microscopy (TEM) sends high energy electrons to pass through the selected area of samples causing magnified version to form on a screen. It provides information on crystallites distribution inside the particles (Brent Fultz & Howe, 2015; Ma et al., 2006). TEM involves forward scattering through the specimen, thus enables diffraction pattern or an image on the viewing screen. Forward scattering comprises elastic scattering, diffraction especially Bragg diffraction, refraction and inelastic scattering as clearly depicted in Figure 3.3 (Williams & Carter, 2009).

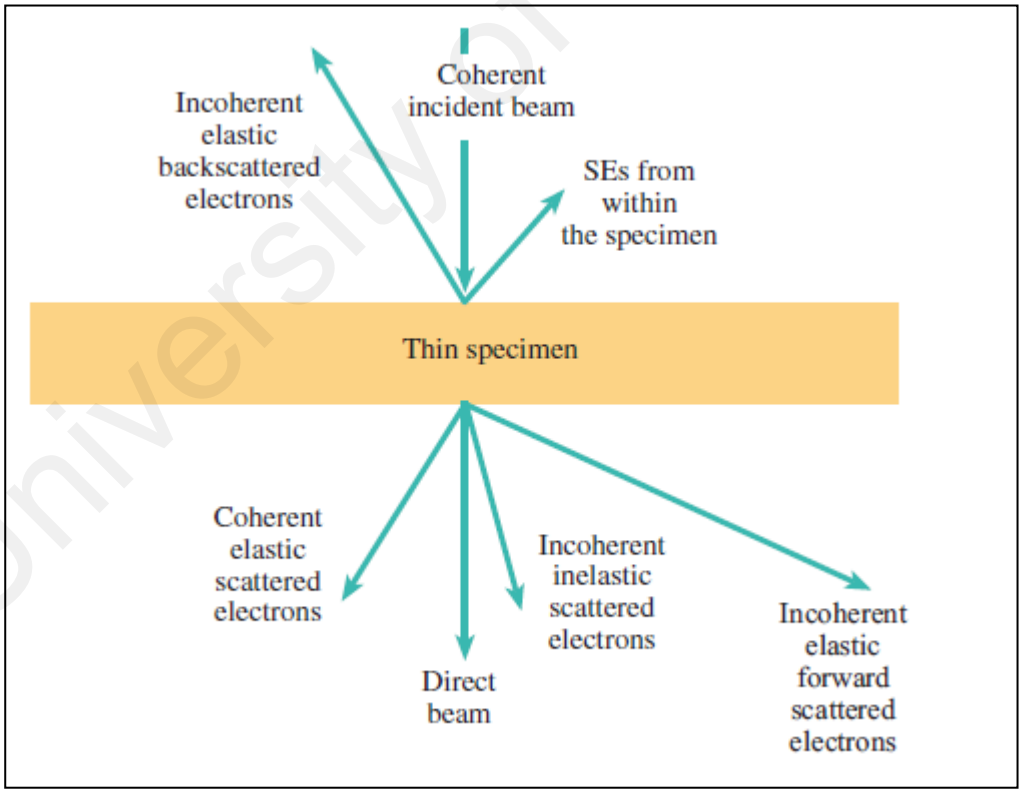

Figure 3.3: Electron scattering during specimen testing in TEM
(Williams & Carter, 2009)

TEM samples were prepared by sonication of small amount of cathode material with ethanol. The obtained solution was smeared onto a carbon coated copper grid as thin

layer and left for drying. TEM in this study was performed using Leo Libra 120 electron microscope with a LaB_6 filament as electron source at 12.5 kV.

3.3.6 Raman Spectroscopy

Raman spectroscopy is another technique of choice to identify the compounds of various materials (Fallis, 2013). It provides Raman spectrum plot of intensity versus frequency shifts in wavenumbers (cm^{-1}). Frequency difference (shift) between incident radiation and Raman scattered radiation relates to vibrational energy level of the molecules or the crystals (Baddour-hadjean & Pereira-Ramos, 2010). There are two main types of molecular vibrations (Reichenbächer & Popp, 2012):

(a) Stretching modes - A stretching vibration is characterized by movement along the bond axis with change of the interatomic distance either increasing or decreasing distance.

(b) Bending modes - A bending vibration denotes variation of the bond angle between bonds or the movement of a group of atoms with respect to the remainder of the molecule with an accompanying change of bond angle.

Phosphor-olivines are included in the list of Raman active compounds (Ziółkowska, Korona, Kamińska, Grzanka, & Andrzejczuk, 2011). Example of $LiMnPO_4$ Raman spectra are shown in Figure 3.4. Olivine vibrations are grouped into internal and external modes. Internal modes related to the PO_4 tetrahedron oscillations denoted as V_1, V_2, V_3 and V_4. Meanwhile external modes correspond to the translations and rotations of Li^+ and Mn^{2+}. Sharp peak at 950 cm^{-1} corresponds to intramolecular symmetric vibrations of the PO_4^{3-} anion. Two weaker peaks at 1002 cm^{-1} and 1070 cm^{-1}

are attributed to asymmetric stretching modes of the PO_4^{3-} anion. The bands between 400 cm^{-1} and 800 cm^{-1} endorsed for bending modes of PO_4^{3-} anion (Korona et al., 2011; Markevich et al., 2011; Michalska et al., 2015).

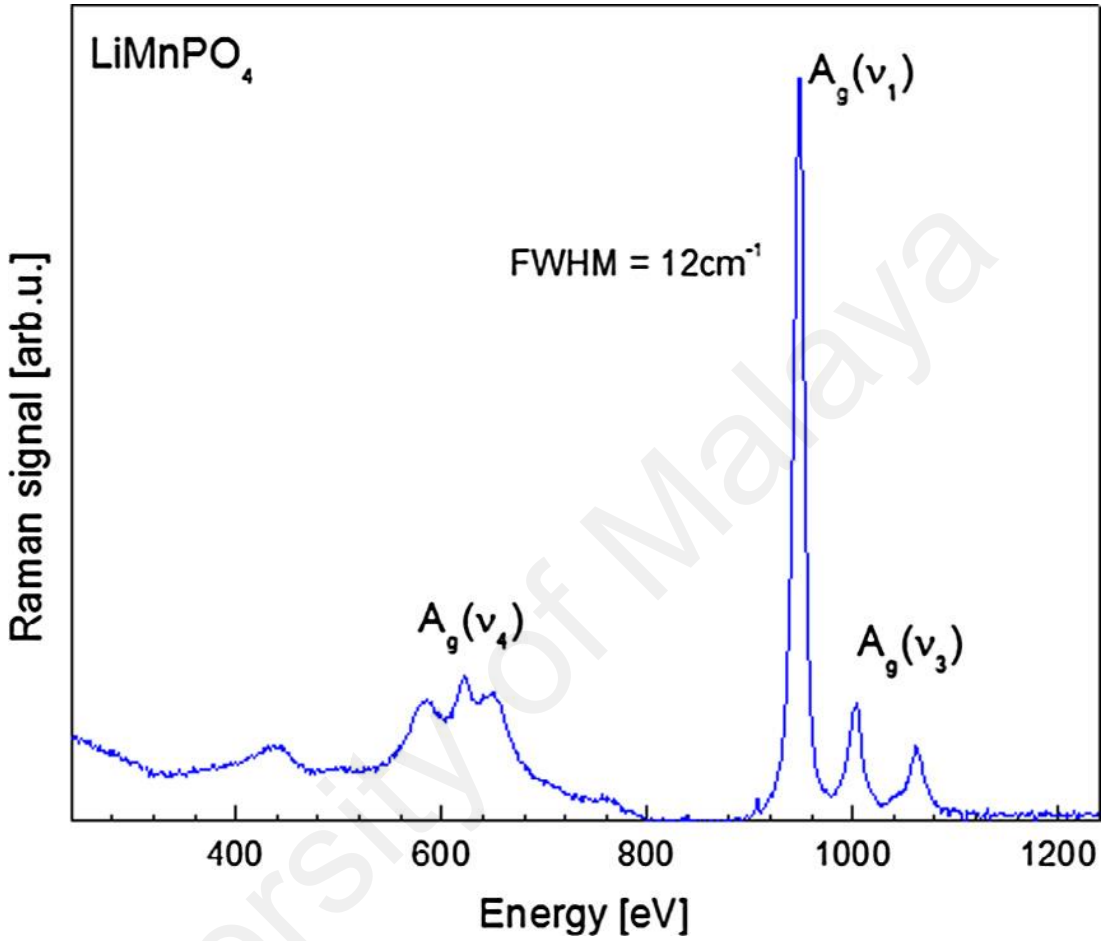

Figure 3.4: Raman spectra of $LiMnPO_4$ (Michalska et al., 2015)

3.4 Electrochemical testing

3.4.1 Cell preparation

Electrochemical tests were performed using two electrode coin cells which fabricated in Argon filled glove box. Cathode materials obtained from present study were used as working electrode while lithium metal as counter and reference electrode since it is a half cell configuration. 1M $LiPF_6$ in a mixture of ethylene carbonate and dimethyl

carbonate at 1:1 (v/v) was used as an electrolyte and polypropylene as separator. Configuration of half-cell battery is shown in Figure 3.5.

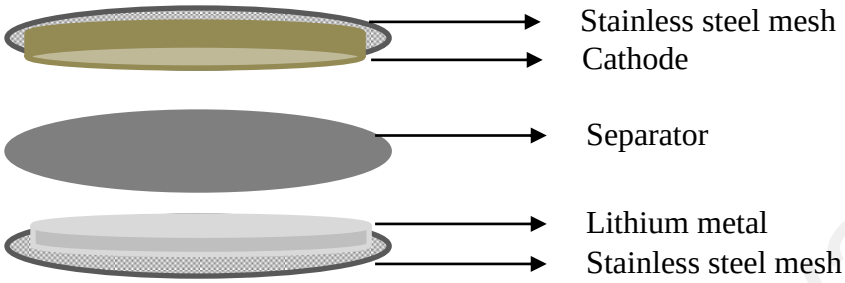

Figure 3.5: Configuration of half cell batteries

3.4.2 Galvanostatic charging and discharging

Galvanostatic charging and discharging processes analyze the electrochemical performances of fabricated coin cells in terms of capacity. Theoretical capacity of the electrode can be calculated using following equation:

$$Theoretical\ capacity = \left(\frac{Faraday constant \times nLi}{M \times 3600} \right) \times 1000 \qquad (3.5)$$

Here the value of the Faraday constant is 96485 C mol^{-1}, *n* relates number of Li ions and *M* is the molecular weight of the electrode. Theoretical capacity of $LiMnPO_4$ can be obtained using above equation:

$$Theoretical\ capacity of\ LiMnPO_4 = \left(\frac{96485C\ mol^{-1} \times 1}{156.85\ gmol^{-1} \times 3600} \right) \times 1000$$
$$= 171 mAhg^{-1}$$

Current that applied on cells during charging and discharging process depends on C rate. C rate is defined as the rate at which a battery is charged or discharges relative to its theoretical capacity. It is generally denoted in terms of 0.5 C, 1 C, 2 C etc. Current, *i* can be chosen according to the C rate as stated below:

$$i = Theoretical\ capacity(mAhg^{-1}) \times C\ rate \times W_{act} \tag{3.6}$$

Where W_{act} is the weight of active material in the working electrode. It can be calculated as given:

$$W_{act} = \left(W_{electrode} - W_{bare\ electrode}\right) \times Percentage\ of\ the\ active\ material \tag{3.7}$$

As indicated in equation (3.7), $W_{electrode}$ is a sum of layered cathode materials on stainless steel mesh and $W_{bare\ electrode}$ is the weight of the stainless steel mesh before electrode coating (Kayyar, Huang, Samiee, & Luo, 2012). Hence, capacity that during experiment can be determined by following equation:

$$Experimental\ capacity = \frac{time(h) \times current\ applied(mA)}{W_{act}\ (g)} \tag{3.8}$$

3.4.3 Electrochemical impedance spectroscopy

Electrochemical impedance spectroscopy is used to determine the electrode kinetics, charge transfer between electrode electrolyte interface and lithium diffusion which are influential factors for electrochemical activity of lithium ion batteries (Gaberscek,

Dominko, & Jamnik, 2007; Hudaya, Hun, Kee, & Choi, 2014; Prabu et al., 2011; Schmidt et al., 2011). The typical Nyquist plot is given in the Figure 3.6.

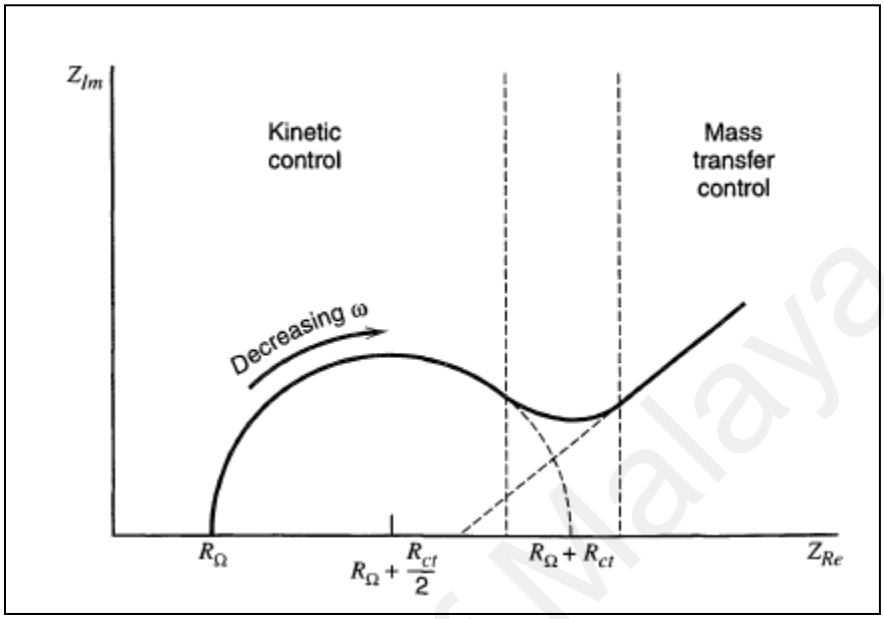

Figure 3.6: Typical Nyquist plot
(Bard et al., 1944)

It can be noticed that Nyquist plot comprises of semicircle and a straight line. Semicircle at high to medium frequency region is R_Ω representing the ohmic resistance between the electrolyte and electrode. Besides that, the radius of the semicircle in a medium frequency range specifies charge transfer resistance (R_{ct}). The inclined line in the low frequency region attributes to the Warburg impedance associated to lithium ion diffusion within electrode (Amaresh et al., 2013; Gaberscek et al., 2007; Kong et al., 2016; Lu-lu Zhang et al., 2013).

3.5 Summary of the chapter

Synthesis method is described generally and theories behind XRD, FESEM and TEM and EIS explained. Calculations related to Williamson hall method to evaluate crystallite size and strain is described. Results obtained by this techniques and instruments will be presented in chapter 4 to chapter 7.

CHAPTER 4: SYNTHESIS AND STRUCTURAL CHARACTERIZATION OF $LiMnPO_4$ BY SOL GEL METHOD

4.1 Introduction

In this chapter, $LiMnPO_4$ by sol gel method is presented. Effects of different sintering temperatures are analyzed. Particularly strain and crystallite size of the materials are evaluated and discussed using Williamson-hall method. Further, the electrochemical performance of synthesized nanostructured $LiMnPO_4$ is investigated via charge-discharge analysis.

4.2 Experimental details

4.2.1 Materials

Lithium acetate ($LiC_2H_3O_2$), oxalic acid ($C_2H_2O_4$) and nitric acid (HNO_3) were obtained from Aldrich. Manganese acetate ($Mn(CH_3COO)_2 \cdot 4H_2O$) and ammonium dihydrogen phosphate ($(NH_4)H_2PO_4$) were acquired from Friendmann Schmidt.

4.2.2 Synthesis of $LiMnPO_4$ materials

Sol gel method was adopted to prepare nanostructured $LiMnPO_4$ utilizing oxalic acid as a chelating agent and carbon source. The stoichiometric ratio of lithium acetate, manganese acetate, ammonium dihydrogen phosphate and oxalic acid is of 1:1:1:1. All the materials were dissolved in distilled water (at 120 °C) under vigorous stirring. 5 mL of concentrated nitric acid was added into the above solution. Then, the mixture was heated continuously until attain the solid product.

As in Figure 4.1, the TGA curve becomes flat starting 500 °C and no peaks observed in DTG curve. This clearly validates that no any phase transformation takes place after 500 °C. Sintering temperatures were chosen based on TGA results.

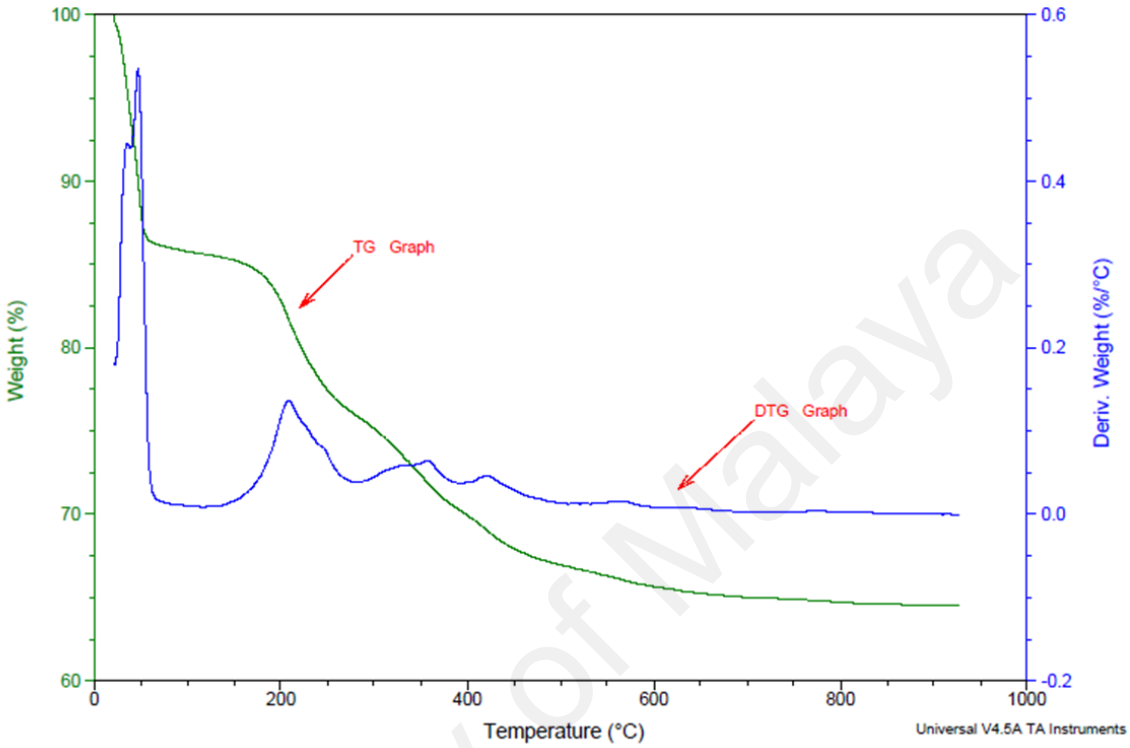

Figure 4.1: TGA/DTG curves of $LiMnPO_4$ precursor

The obtained sample was ground using mortar and followed by calcination at 500 °C, 600 °C, 700 °C and 800 °C for 3 hours respectively. Finally, the obtained samples were labelled as LMP5 (500 °C), LMP6 (600 °C), LMP7 (700 °C) and LMP8 (800 °C) respectively.

4.2.3 Structural and electrochemical characterizations

Structural and surface morphologies of the samples were analysed by X-ray diffraction (XRD, Siemens D 5000 diffractometer), scanning electron microscopy (SEM, Quanta FEG 450) and transmission electron microscopy (TEM, Leo Libra 120). The surface purity of synthesized samples was examined via Raman spectrometer (In-

via Raman Microscope) using wavelength of 532 nm (blue laser). The thermal properties of the samples were examined by TGA (TGA Q500 V20.13 Build 39).

In order to fabricate the coin cells 72 wt.% of $LiMnPO_4$/C and 28 wt.% of Teflonised Acetylene Black (TAB) were mixed well in ethanol medium and pasted on stainless steel mesh, which act as a cathode. Lithium metal was used as an anode, a porous polypropylene film as separator and 1 M $LiPF_6$ in ethylene carbonate (EC)/ dimethyl carbonate (DMC) (1:1 in volume) served as an electrolyte. Neware battery system was equipped to study charge and discharge performance in the potential range of 2.5 V– 4.5 V at room temperature with a current rate of 0.05 C. Electrochemical impedance spectroscopy (EIS) measurements were carried out.

4.3 Results and discussion

4.3.1 X-Ray Diffraction (XRD)

XRD patterns of the synthesized samples at different calcination temperatures (500 °C, 600 °C, 700 °C, 800 °C) for 3 hours are shown in Figure 4.2. All the diffraction peaks are identified as olivine orthorhombic $LiMnPO_4$ structure (JCPDS No. 74-0375) with Pnma space group (Zhang et al., 2015; Zheng et al., 2015). No impurity peaks detected for all samples indicate that samples are exhibiting pure $LiMnPO_4$ crystals. 2θ and FWHM values for corresponding *hkl* are listed in Table 4.1.

While increasing the calcination temperatures, the structural crystallinity increases due to increase in their diffraction peaks intensity (Liu, Wang, Tao, Dai, & Yu, 2015). There are no other peaks corresponding to carbon, which may due to the small amount of carbon traces from oxalic acid (Dou et al., 2012; Muruganantham, Sivakumar, Subadevi, et al., 2015).

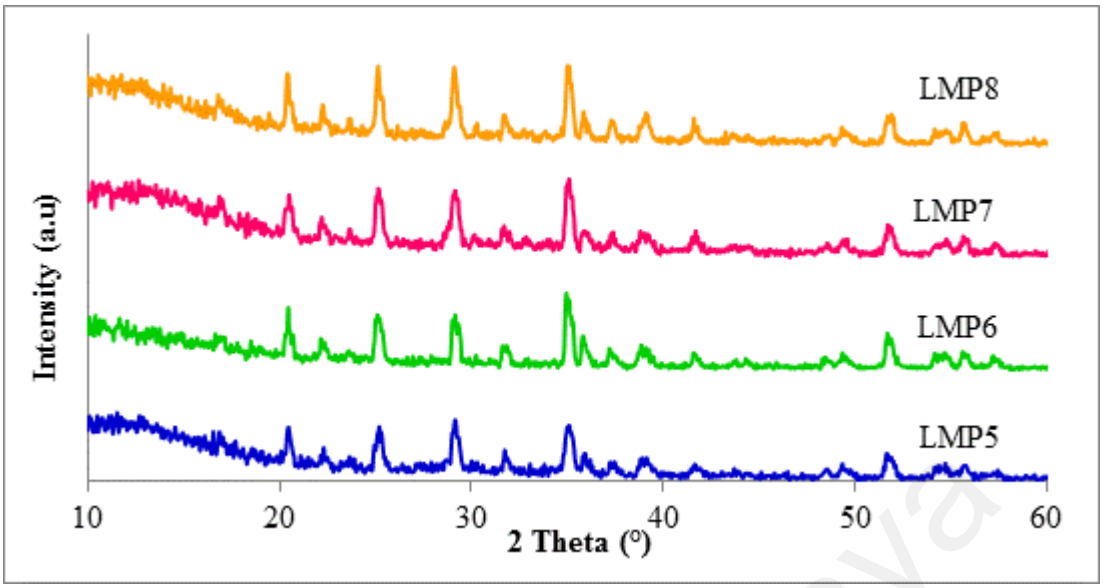

Figure 4.2: XRD patterns of LiMnPO$_4$ obtained from different sintering temperatures LMP5 at 500 °C, LMP6 at 600 °C, LMP7 at 700 °C and LMP8 at 800 °C

Table 4.1: 2θ, FWHM and d spacing LiMnPO$_4$ obtained from different sintering temperatures

LMP 5

hkl	2θ (°)	FWHM (°)	d spacing (Å)
(011)	20.4667	0.301	4.33662
(111/021)	25.1762	0.331	3.53665
(200/121)	29.1869	0.416	3.06159
(131)	35.0915	0.477	2.54595
(221)	39.0611	0.575	2.31332
(112/022)	41.6939	0.476	1.76775
(222)	51.7681	0.686	1.51535

LMP 6

hkl	2θ (°)	FWHM (°)	d spacing (Å)
(011)	20.5074	0.256	4.32967
(111/021)	25.1693	0.417	3.53954
(200/121)	29.1807	0.415	3.06052
(131)	35.0971	0.475	2.54588
(221)	38.8341	0.645	2.3172
(112/022)	41.7124	0.476	1.76641
(222)	51.7412	0.722	1.52589

LMP 7

hkl	2θ (°)	FWHM (°)	d spacing (Å)
(011)	20.4697	0.188	4.3391
(111/021)	25.1496	0.349	3.54008
(200/121)	29.1802	0.307	3.06538
(131)	34.9773	0.359	2.55109
(221)	38.9856	0.356	2.31583
(112/022)	41.360	0.503	1.7673
(222)	51.680	0.671	1.51494

LMP 8

hkl	2θ (°)	FWHM (°)	d spacing (Å)
(011)	20.4073	0.178	4.34525
(111/021)	25.1191	0.431	3.54089
(200/121)	29.1106	0.468	3.06382
(131)	35.0189	0.474	2.55658
(221)	39.1395	0.489	2.29966
(112/022)	41.6524	0.505	1.76002
(222)	51.8138	0.779	1.51502

At the same time, crystalline structures experience stress and distortion internally throughout the heating process (Yao, Shen, Zhang, Gregory, & Wang, 2012). Hence, strain and crystallite size of the prepared samples were examined via Williamson – Hall (W-H) method as in equation 3.4 explained in methodology (Kwon et al., 2011; Yao et al., 2012). W-H plots for all the samples are displayed in Figure 4.3.

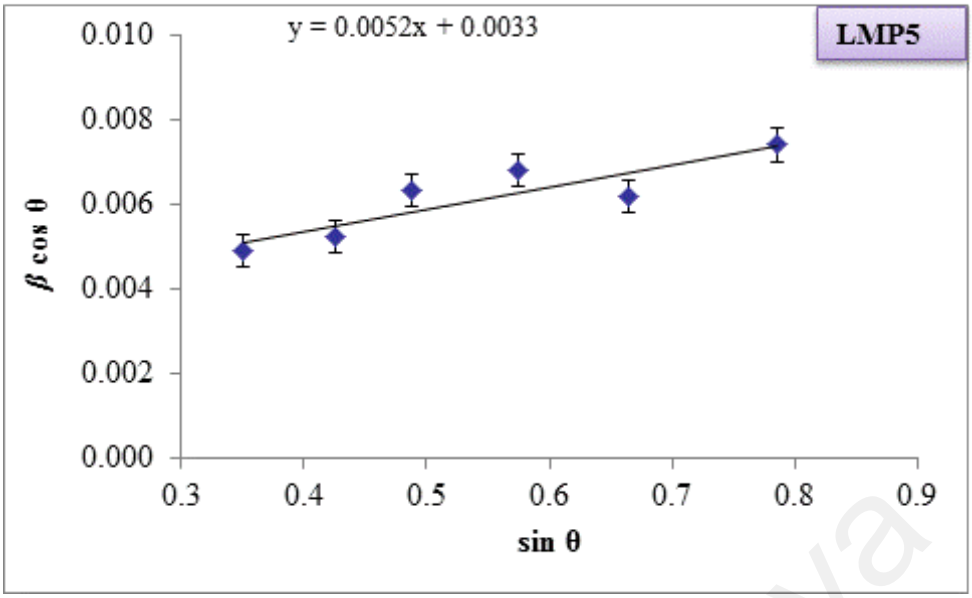

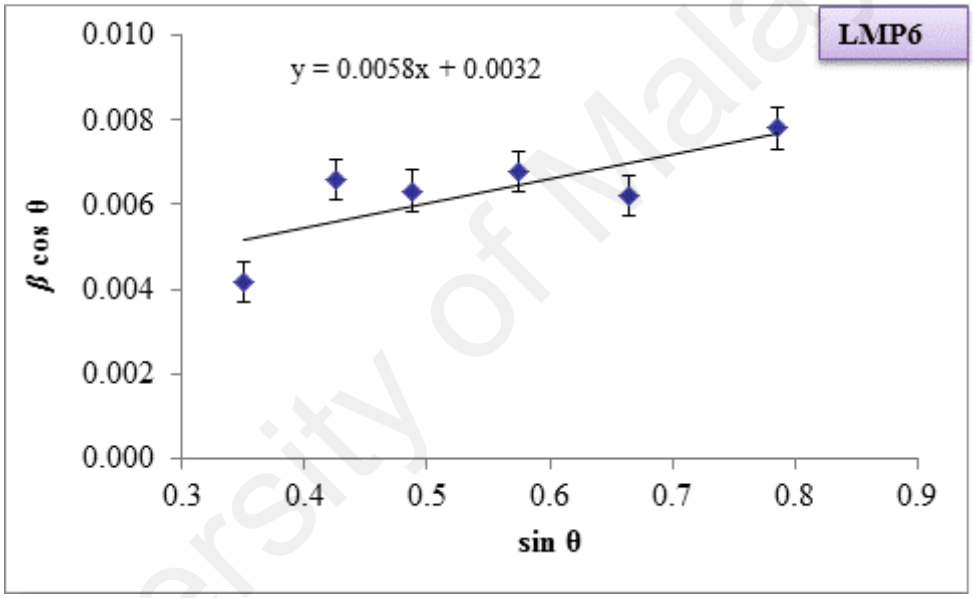

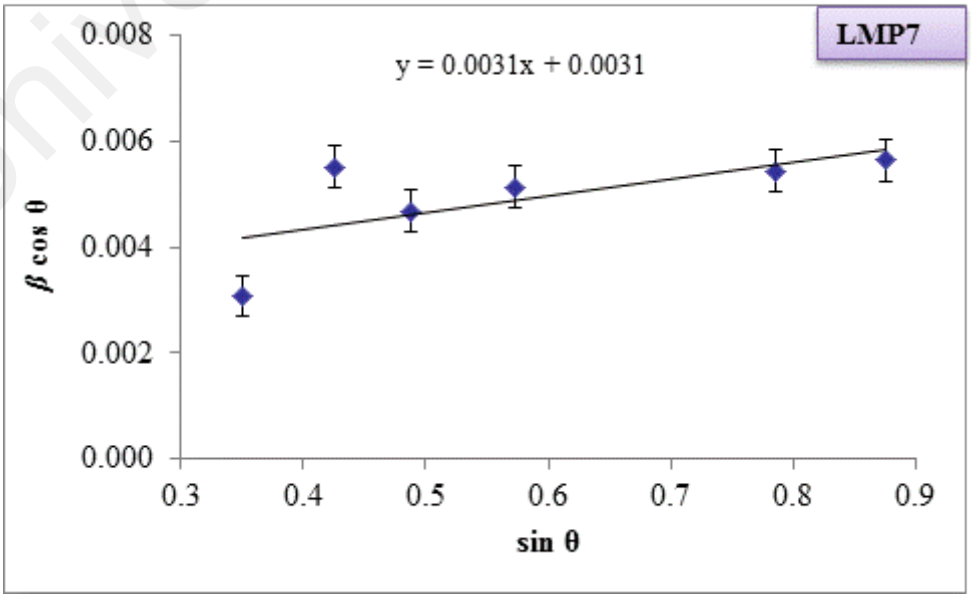

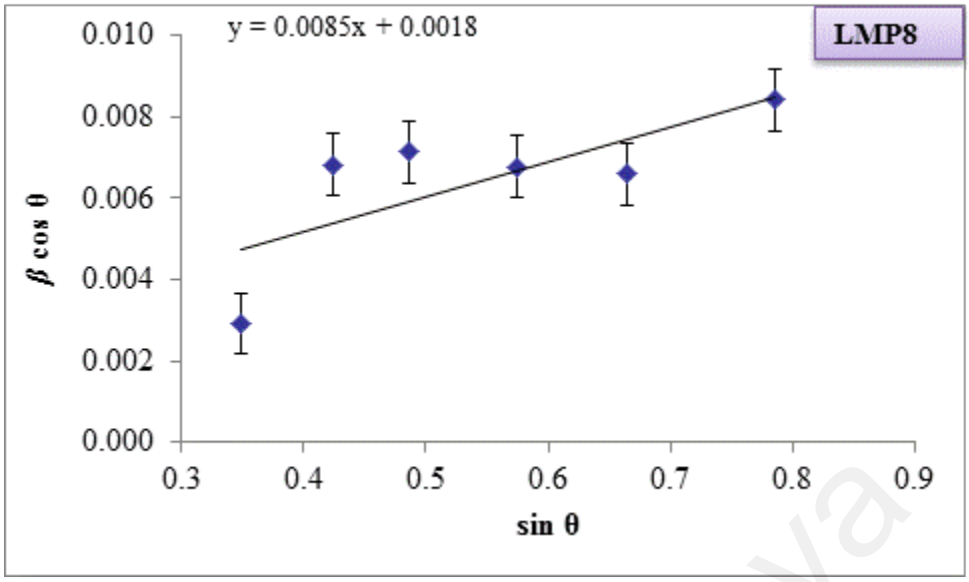

Figure 4.3: Williamson-hall plots of $LiMnPO_4$ obtained from different sintering temperatures

Table 4.2: Mean crystallite size and strain values of $LiMnPO_4$ at different sintering temperatures

Sample & Sintering Temperature	Intercept	Slope	Crystallite size (nm)	Strain
LMP5 (500 °C)	0.0052	0.0033	42.0	1.30×10^{-3}
LMP6 (600 °C)	0.0058	0.0032	43.0	1.45×10^{-3}
LMP7 (700 °C)	0.0031	0.0031	45.0	7.75×10^{-4}
LMP8 (800 °C)	0.0085	0.0018	77.0	2.13×10^{-4}

Besides that, the average crystalline sizes of $LiMnPO_4$ are from 42 nm to 77 nm with increasing calcination temperatures, proving that the particles are made up of closely packed crystallites (Zhao et al., 2014). Apart from the particle sizes and crystallites of cathode materials, strain is another important factor that needs to be considered because strain denotes the crystal lattice defects such as displacement, stacking errors etc (Muruganantham, Sivakumar, & Subadevi, 2015b). The lowest strain value of 7.75×10^{-4} is observed in LMP7, while the highest strain value of 2.13×10^{-3} observed at

LMP8 respectively. From these results, it can be noticed that crystal lattice defects is reduced at optimal temperature at 700 °C as shown by low strain value.

4.3.2 Field Emission Scanning Electron Microscopy (FESEM)

Further, the samples were analyzed by FESEM as surface morphology and particle size are essential factors that influencing electrochemical properties of lithium ion batteries (Xiao et al., 2013). Figure 4.4 to Figure 4.7 exhibits FESEM micrographs of samples obtained from different calcination temperatures. FESEM images at different magnifications clearly present particle distributions throughout the sample.

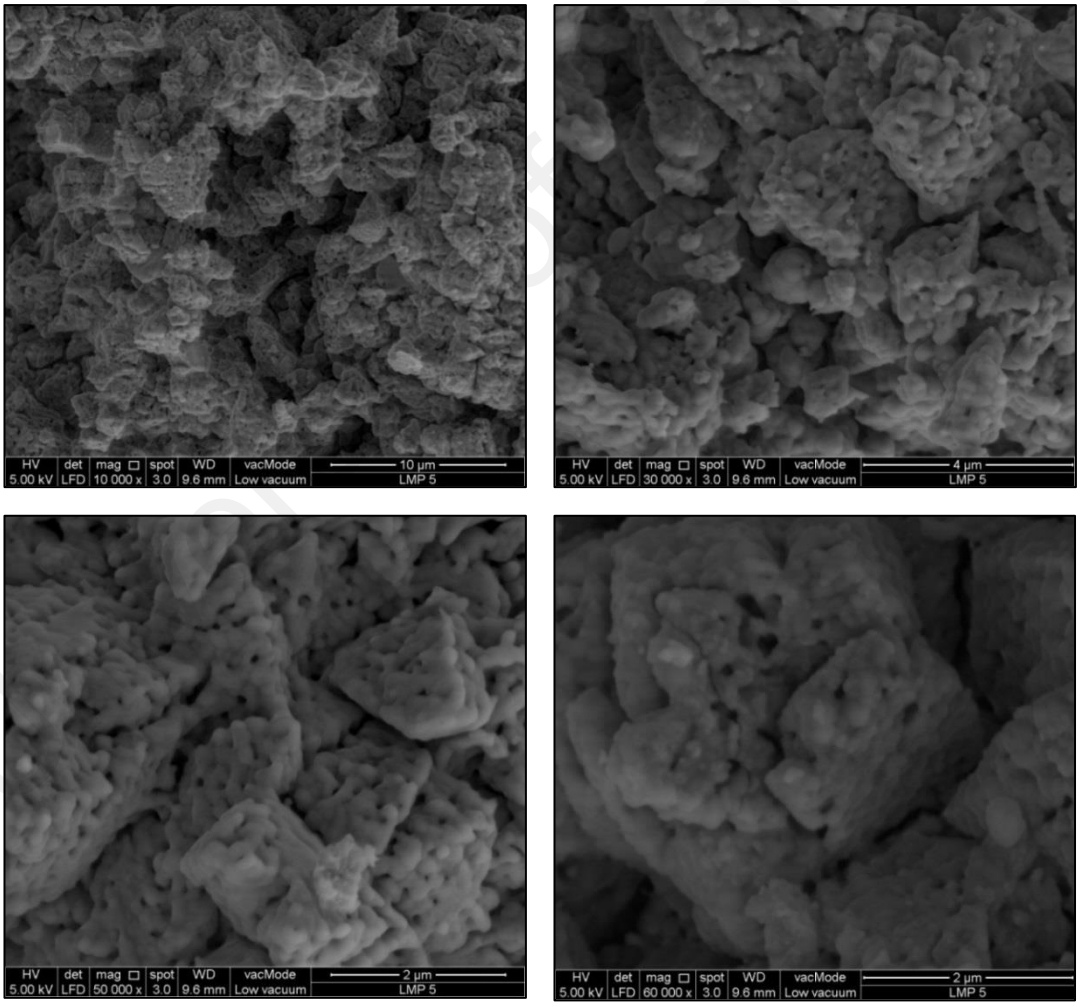

Figure 4.4: FESEM images of $LiMnPO_4$ sintered at 500°C

At sintering temperatures of 500 °C and 600 °C, the particles are smaller with uniform distribution (Figure 4.4 and Figure 4.5). When temperature increases to 700 °C and 800 °C (Figure 4.6 and Figure 4.7), particles became larger and well crystallized. The particles are about 170 nm at sintering temperature of 500 °C and 360 nm – 430 nm at 600 °C. At sintering temperatures of 700 °C and 800 °C, the particles that formed are in the size range of 860 nm – 1100 nm and 1650 nm – 1910 respectively. Another essential point, oxalic acid which acts as an organic fuel during calcination reduces particles agglomeration (Dunqiang Wang et al., 2013b; Lijuan Wang, Zhou, & Guo, 2010b). As grain growth is temperature dependent process, average particle size found to be increasing with increase of heating temperature (Naceur, Megriche, & El Maaoui, 2014).

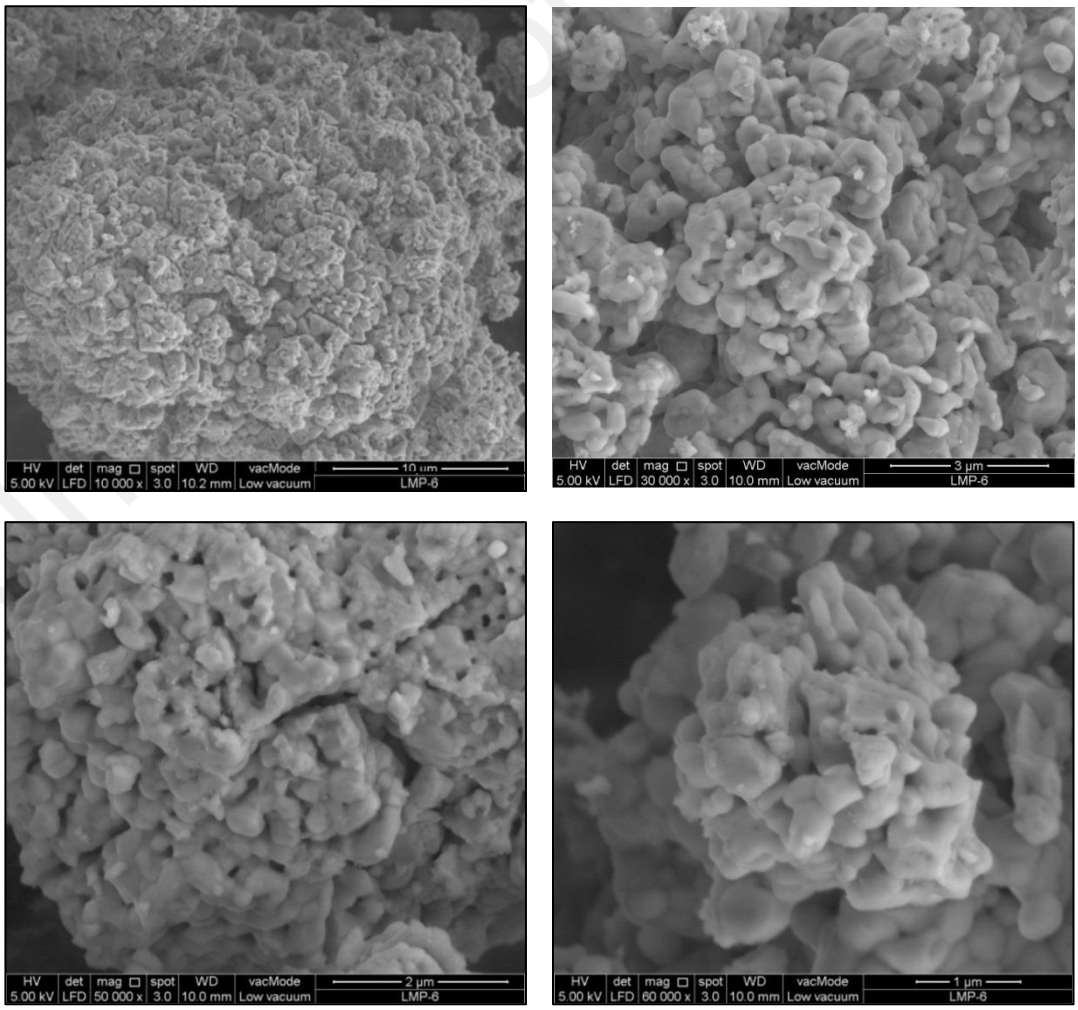

Figure 4.5: FESEM images of $LiMnPO_4$ sintered at 600°C

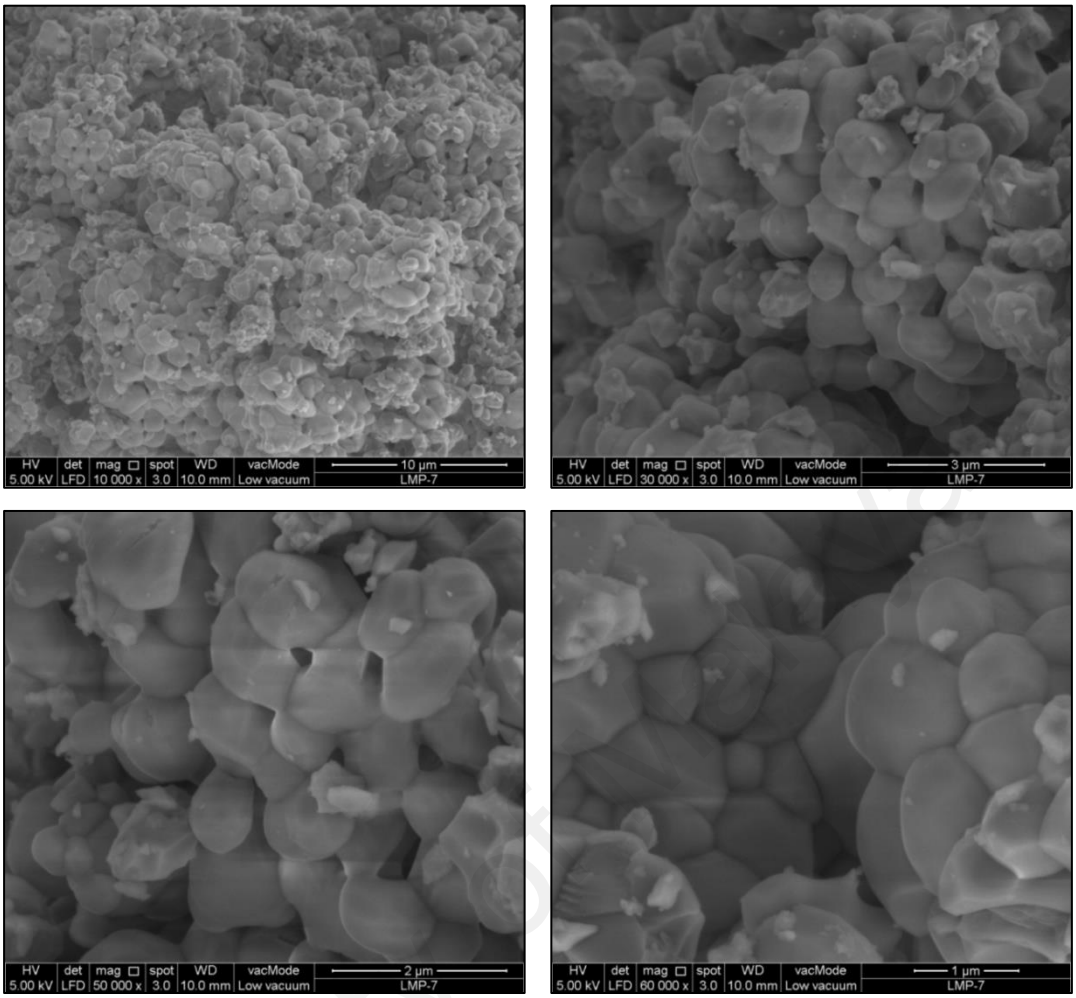

Figure 4.6: FESEM images of $LiMnPO_4$ sintered at 700°C

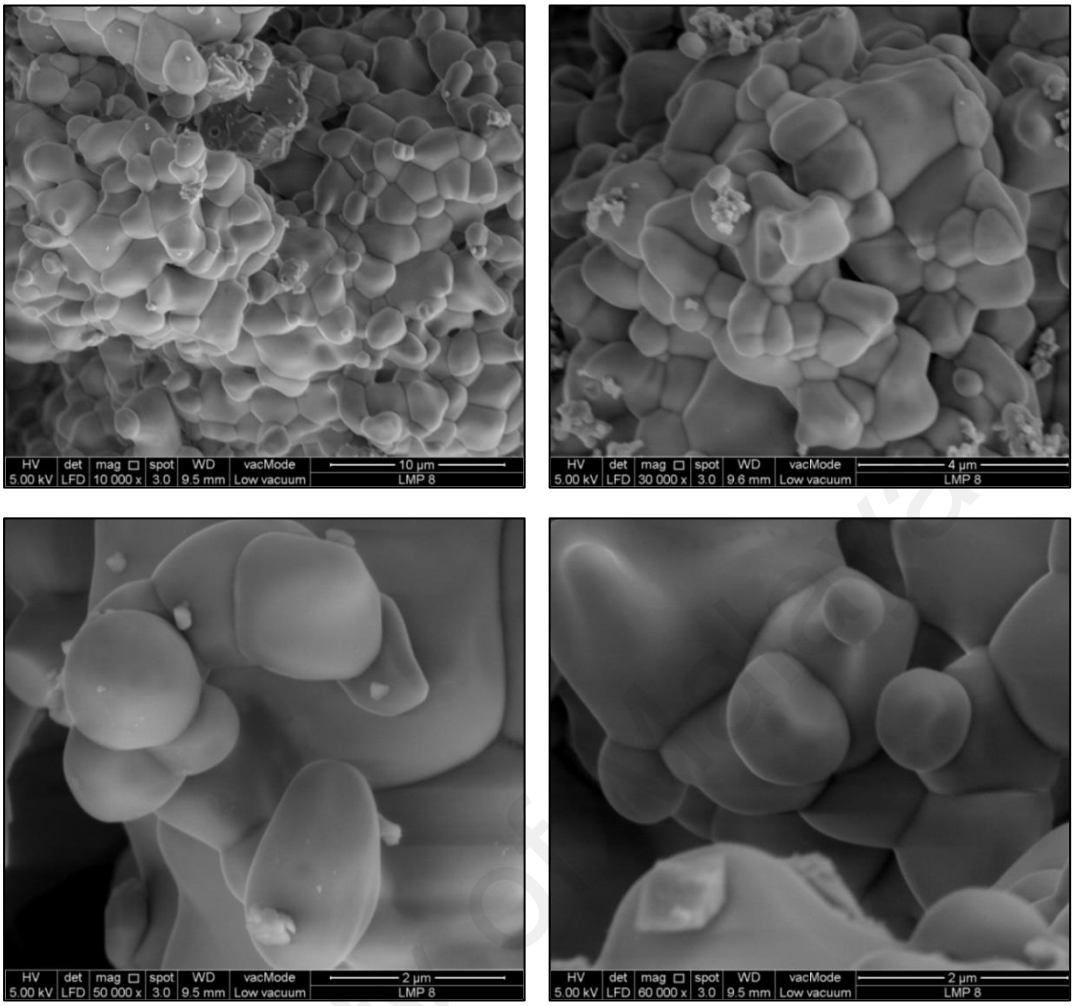

Figure 4.7: FESEM images of $LiMnPO_4$ sintered at 800°C

Hence, calcination at high temperature encourages particles growth subsequently augmented the particle size (Syamimi, Amin Matori, Lim, Abdul Aziz, & Mohd Zaid, 2014). Sintering temperature plays active role in shaping the particles which indirectly accountable for particle size distribution (Ju & Kim, 2013). At the same time, it should be noted that particle sizes that determined from FESEM images are different compared to crystallite sizes of the samples. This provides significant information about the obtained samples contain agglomerated crystals and it is not made up of single crystal (Guo et al., 2013). Sintering temperature merges crystallites while reducing lattice defects (Shirsath, Kadam, Gaikwad, Ghasemi, & Morisako, 2011).

4.3.3 Transmission Electron microscopy (TEM)

TEM images as in Figure 4.8 demonstrate crystallites that contained in the particles. Crystallites size increases with sintering temperature in the range of 40 nm to 50 nm up to sintering temperature of 700°C and 70 nm – 80 nm at 800°C. These results agree with Williamson Hall results as tabulated in Table 4.2.

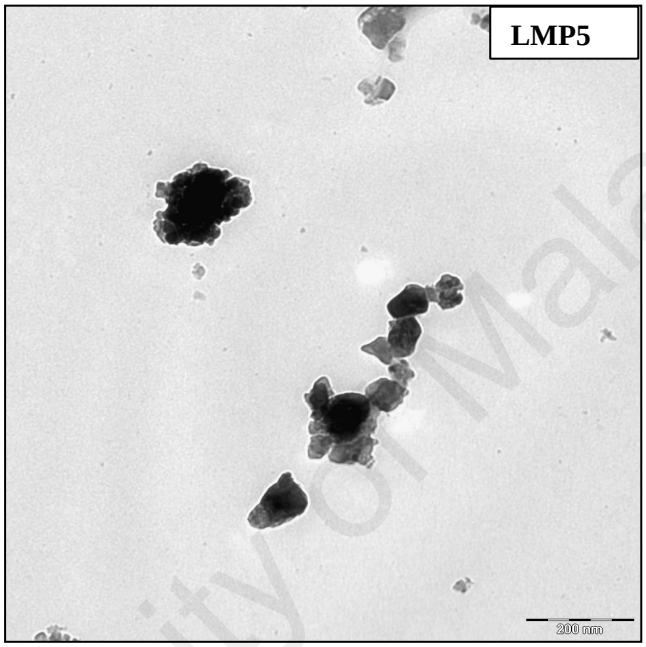

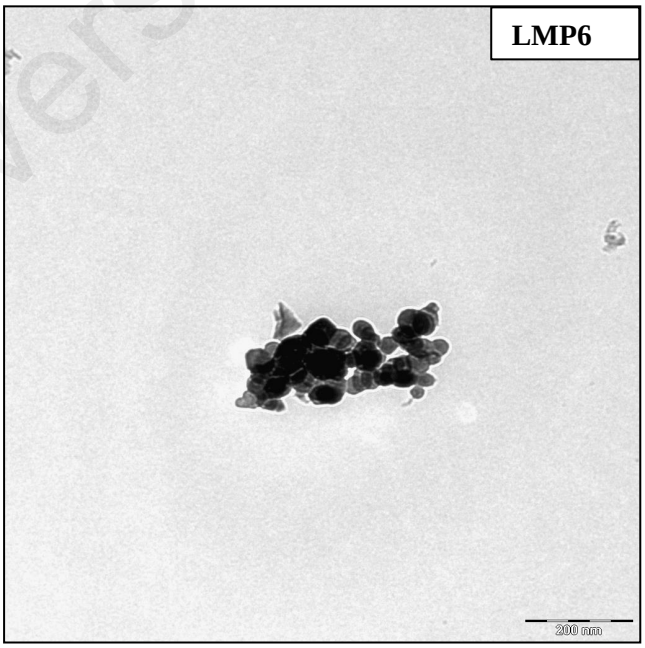

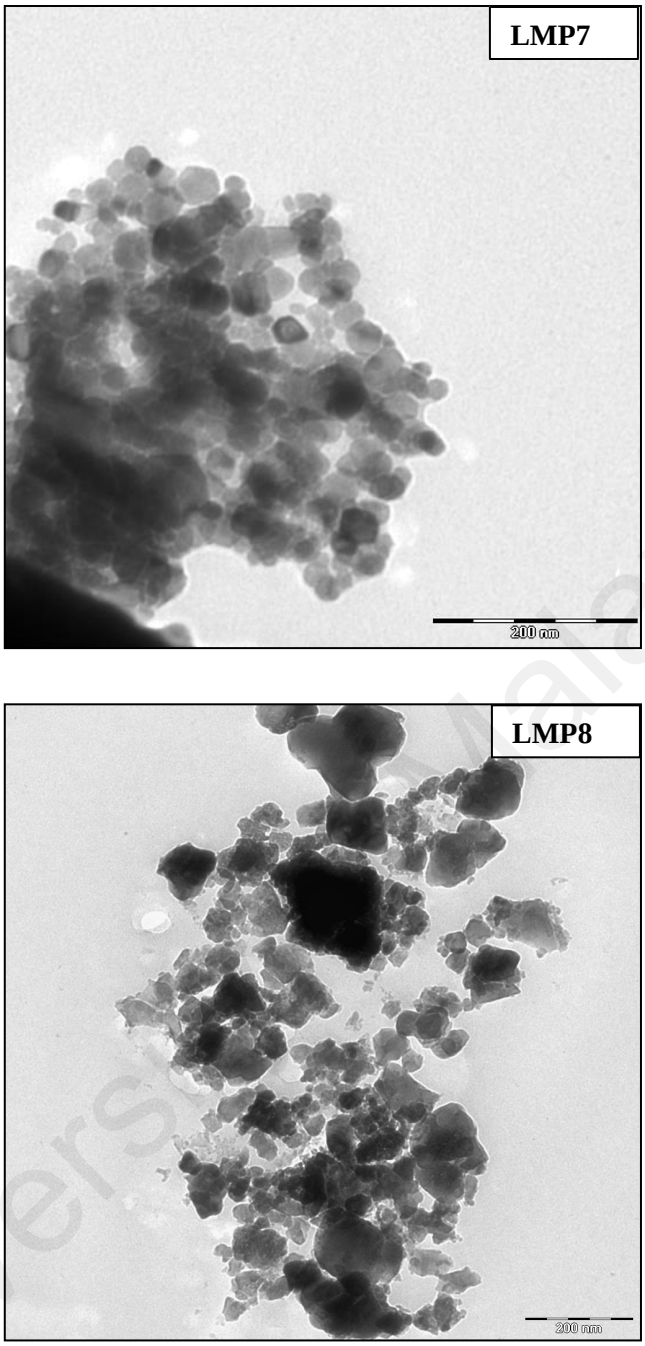

Figure 4.8: TEM images of $LiMnPO_4$ sintered at different sintering temperatures

4.3.4 Raman Spectroscopy

Raman spectroscopy is a tool to investigate the phosphate materials (Rosaiah & Hussain, 2014). Herein, olivine vibrations can be expressed in terms of internal and external modes. The observed internal modes resemble PO_4 tetrahedron oscillations

whereas external modes correspond to $Li^{+,}$ Mn^{2+} and PO_4^{3-} ions respectively (Michalska et al., 2015).

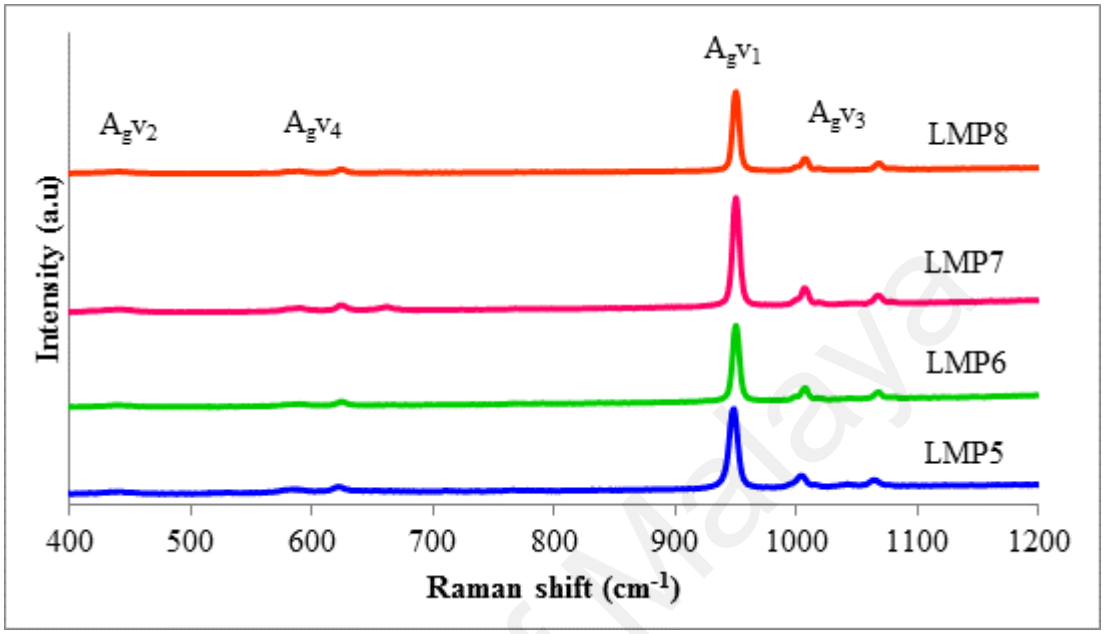

Figure 4.9: Raman spectra of $LiMnPO_4$ obtained from different calcination temperatures

Characteristic Raman peak for olivine observed at 950 cm^{-1} for all the samples as displayed by Figure 4.9 and the most intense peak is at LMP7 among them (Kim, Park, Lee, Lee, & Song, 2012; Korona et al., 2011; Markevich et al., 2011). This peak indicates A_g symmetric P-O stretching vibration band of v_1.The doublet peaks at 1005 cm^{-1} and 1070 cm^{-1} represent asymmetric stretching vibration of PO_4 tetrahedron. Additionally, the broad peak at 438 cm^{-1} belongs to symmetric A_gv_2 mode. The other peaks at 590 cm^{-1}, 627 cm^{-1} and 661 cm^{-1} denote symmetric A_gv_4 modes respectively (Michalska et al., 2015). Raman spectra are another evidence for $LiMnPO_4$ structure formation as stated in XRD.

4.3.5 Electrochemical analysis

The electrochemical properties of $LiMnPO_4$ cathodes produced at different heating temperatures were examined via coin cells by equipping lithium metal as both the counter and reference electrodes. Figure 4.10 displays charge discharge profiles of the 1st and 50th cycles for the as prepared samples in the voltage range of 2.5 V – 4.5 V at current rate of 0.05 C (1C = 171 $mAhg^{-1}$). LMP5, LMP6, LMP7 and LMP8 exhibit initial charge capacities of 50.7 $mAhg^{-1}$, 76.1 $mAhg^{-1}$, 151.5 $mAhg^{-1}$ and 100.7 $mAhg^{-1}$ and discharge capacities of 38.1 $mAhg^{-1}$, 57.1$mAhg^{-1}$, 103.4 $mAhg^{-1}$ and 68.9 $mAhg^{-1}$ respectively. Table 4.3 summarizes initial performance of the samples.

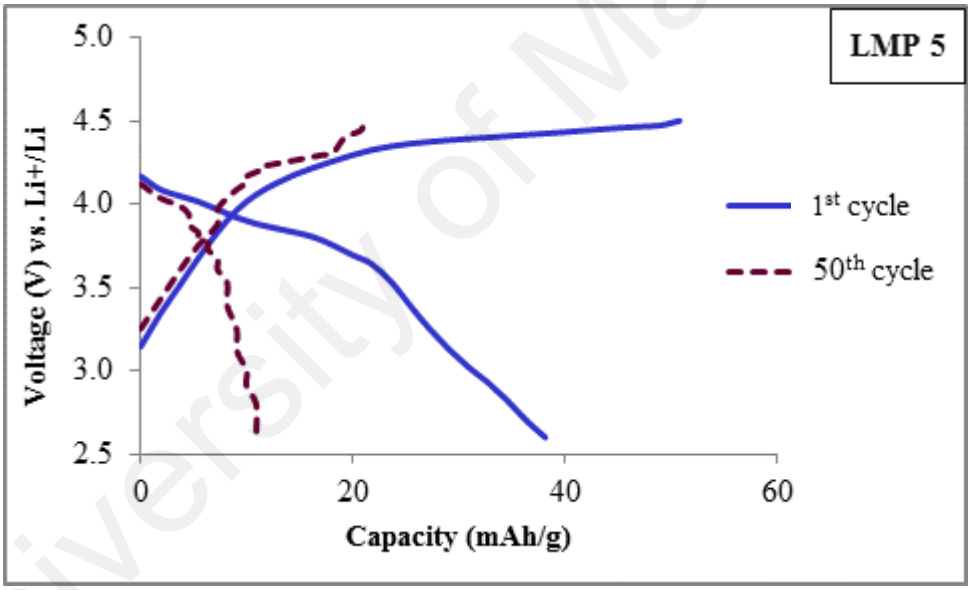

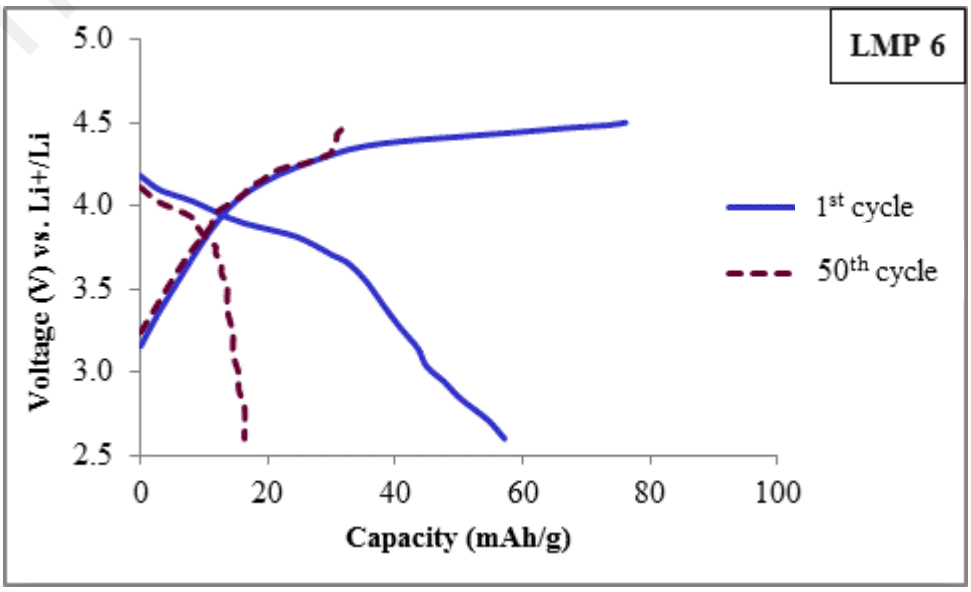

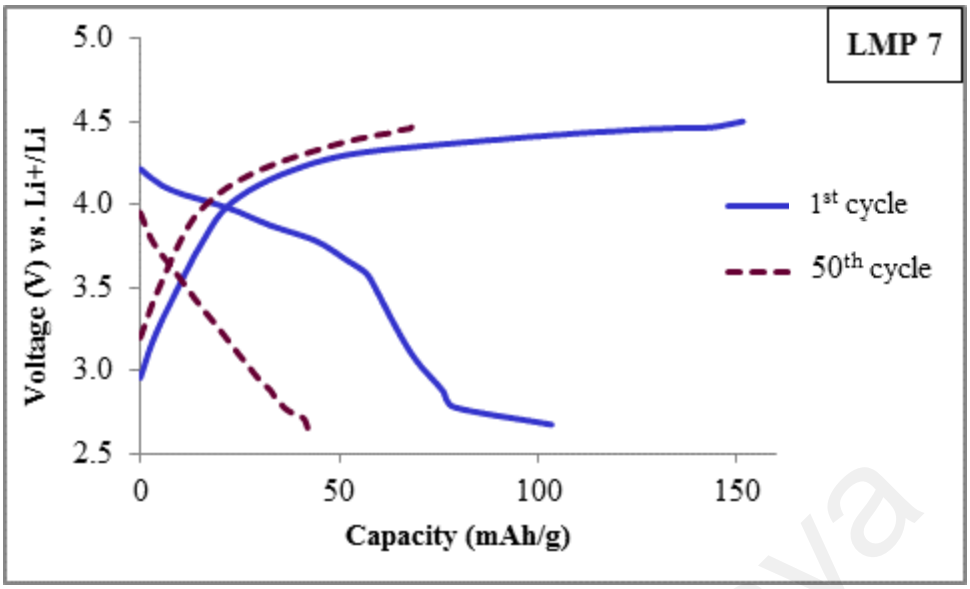

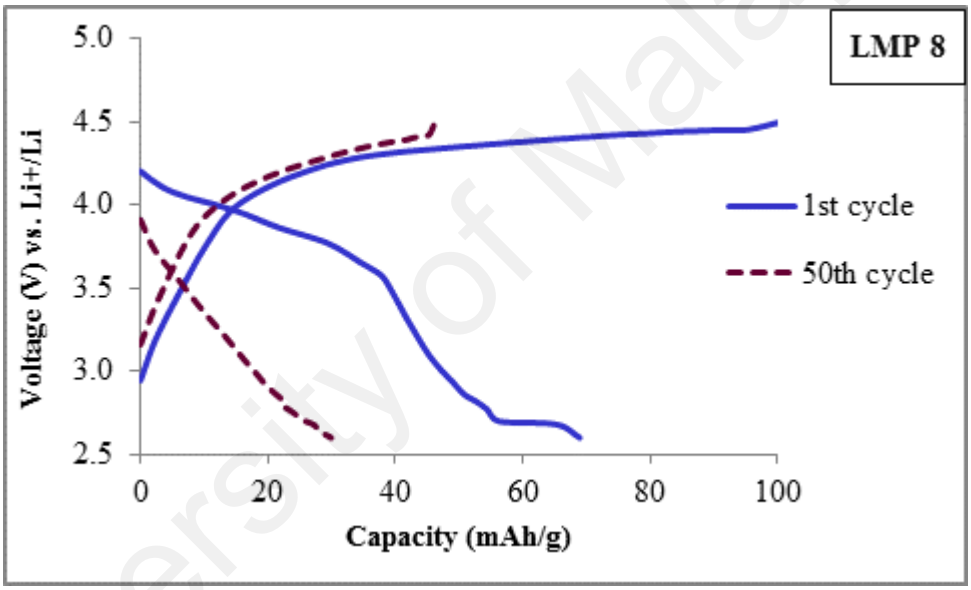

Figure 4.10: Charge discharge curves of $LiMnPO_4$ obtained from different calcination temperatures

Table 4.3: Initial electrochemical performance of $LiMnPO_4$ obtained from different calcination temperatures

Sample & Sintering Temperature	Initial charge capacity ($mAhg^{-1}$)	Initial discharge capacity ($mAhg^{-1}$)
LMP5 (500 °C)	50.7	38.1
LMP6 (600 °C)	76.1	57.1
LMP7 (700 °C)	151.5	103.4
LMP8 (800 °C)	100.7	68.9

These results suggest that maximum discharge capacity is achieved by LMP7 with coulombic efficiency of 68.3 %. This can be mainly ascribed to the nanostructured crystallites accompanied with reduced strain which promotes good lithium ions intercalation. Even though LMP5 and LMP6 have smaller particles but feeble structure with high strain at low calcination temperature lead to deteriorate its electrochemical performance (Zhao, Hu, Zhou, Fang, & Cai, 2015). Also, LMP8 attained poor electrochemical performance than that of LMP7 due to large particles sizes with high strain, resulting in poor lithium ions intercalation (Zheng, Wu, & Yang, 2011).

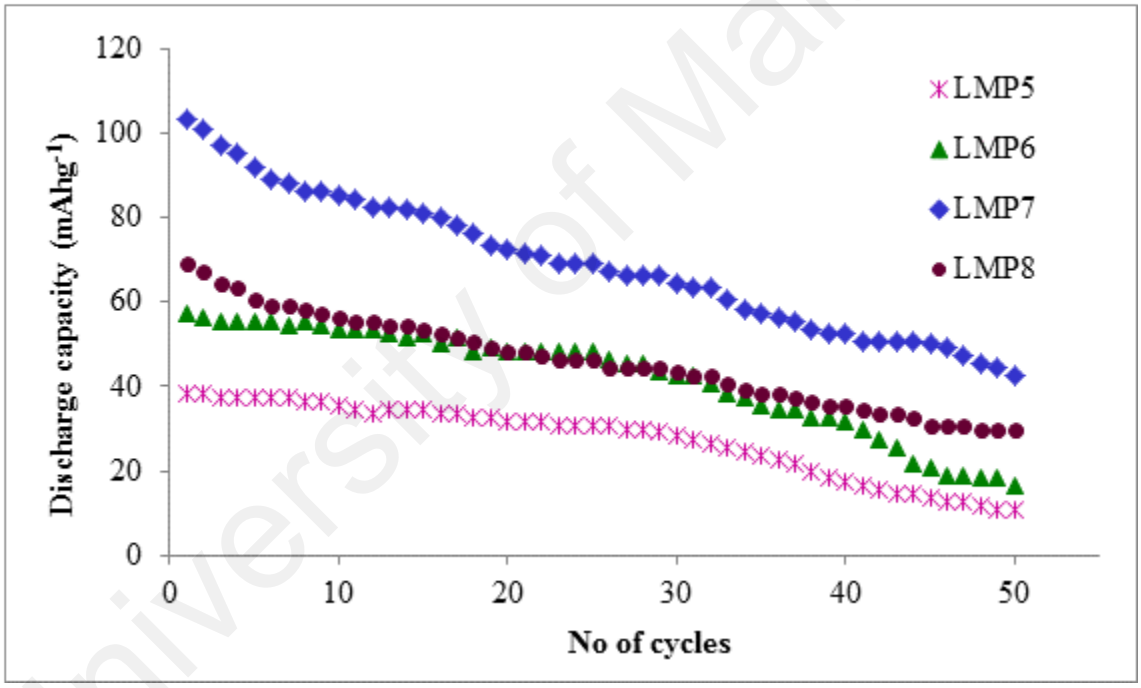

Figure 4.11: Discharge capacities versus cycle numbers at a current of 0.05 C for $LiMnPO_4$ sintered at 500 °C, 600 °C, 700 °C and 800 °C

Cycling stability of LMP5, LMP6, LMP7 and LMP8 cathode materials at room temperature for 50 cycles are presented in Figure 4.11. Remarkably, LMP7 demonstrates good cycling stability than that of other samples. At 30th cycle, the discharge capacities of LMP5, LMP6, LMP7 and LMP8 are 28.1 mAhg^{-1}, 42.6 mAhg^{-1}, 64.4 mAhg^{-1} and 43.5 mAhg^{-1} respectively. The discharge capacity of LMP7 reached

42.6 $mAhg^{-1}$ at the end of 50th cycles, leading to capacity retention of 41.2 %. The discharge capacities of other samples such as LMP5, LMP6 and LMP8 corresponds to 10.8 $mAhg^{-1}$, 16.3 $mAhg^{-1}$and 29.9 $mAhg^{-1}$ at the end of 50th cycles respectively as tabulated in Table 4.4.

Table 4.4: Discharge capacities at 30th and 50th cycles

Sample & Sintering Temperature	30th cycle ($mAhg^{-1}$)	50th cycle ($mAhg^{-1}$)
LMP5 (500 °C)	28.1	10.8
LMP6 (600 °C)	42.6	16.3
LMP7 (700 °C)	64.4	42.6
LMP8 (800 °C)	43.5	29.9

These results are confirmed that the LMP7 is having superior electrochemical properties due to smaller crystallite size, suggesting effective ion transfer mechanism between electrolyte and active materials (Cai et al., 2015; Zhongxue Chen et al., 2015) . Short diffusion paths enable lithium ion travel easily during charging and discharging process even at higher current rate (Yingchao Chen, Xie, Pan, & Zheng, 2011; Das, Pohl, Chakravadhanula, Kübel, & Fichtner, 2014).

Electrochemical impedance spectra were further analyzed in the frequency range of 0.01 Hz to 100 kHz. Nyquist plot shown in Figure 4.12 comprised of a depressed semicircle in the high to medium frequency region and an inclined line in the low region.

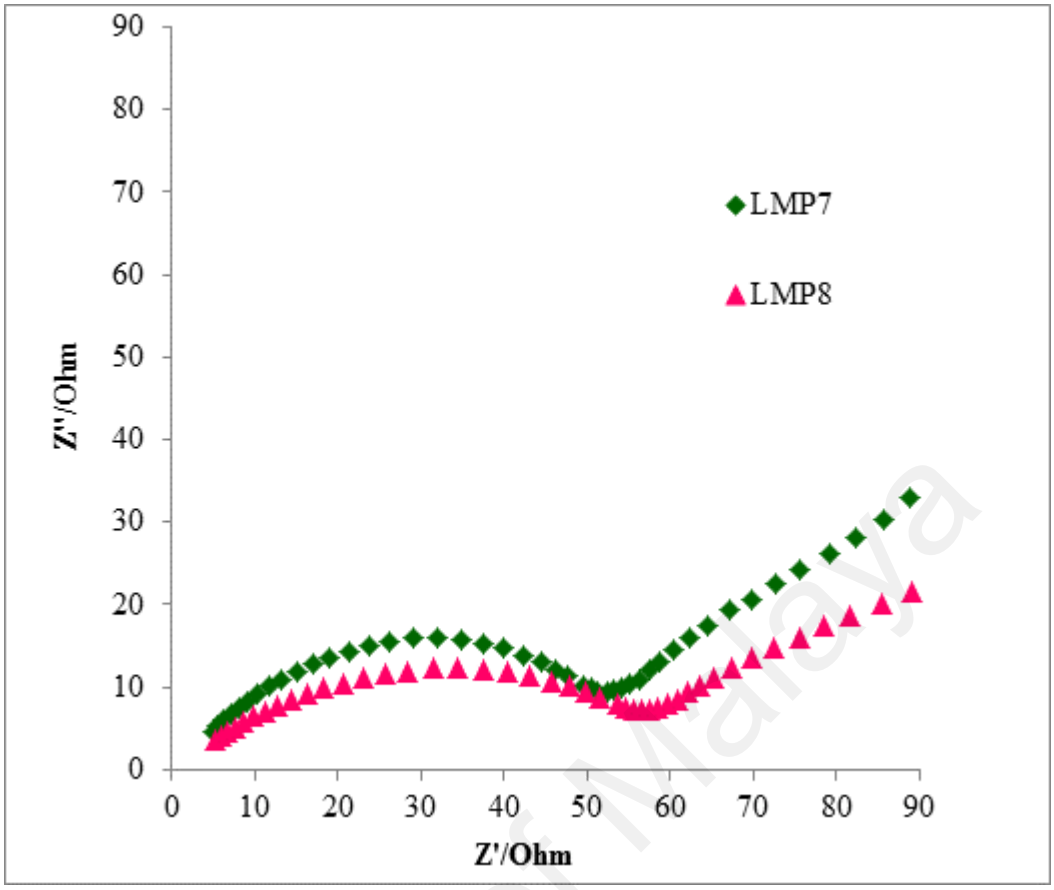

Figure 4.12: EIS spectra of $LiMnPO_4$

EIS spectra can be well expounded by relating semicircle to charge transfer resistance at cathode – electrolyte interface whereas slope line linking to lithium ion solid state diffusion within crystals (Yajing Wang, Zhu, Wang, & Wang, 2016; Wang et al., 2016; Xu, Wang, & Shen, 2016). R_{ct} values for LMP7 and LMP8 are 59 Ω and 57 Ω respectively. Further investigations will be carried out for enhancing electrochemical performance as a future work.

4.4 Conclusion

Olivine structured $LiMnPO_4$ was effectively synthesized by modified sol gel method with aid of oxalic acid and nitric acid and followed by calcination at different temperatures. The calcination temperatures have high impact on structural and electrochemical properties. The obtained $LiMnPO_4$ at 700 °C (calcination temperatures),

LMP7 sample has smaller crystallite size and low strain value than that of other samples. The initial discharge capacity of 103.4 $mAhg^{-1}$ (0.05 C) is observed in LMP7 sample. Therefore, these results conclude that sintering temperature can be optimized in the preparation of $LiMnPO_4$ via sol gel method for improved electrochemical properties which is crucial for future energy storage applications.

CHAPTER 5: Na DOPED $LiMnPO_4$ AS IMPROVED CATHODE MATERIALS FOR LITHIUM ION BATTERIES

5.1 Introduction

This chapter reports the preparation and electrochemical characterizations of $Li_{1-x}Na_xMnPO_4$ with different mole ratios, x = 0.00, 0.01, 0.02, 0.03, 0.04, 0.05 calcined at 600 °C and 700 °C. To the best of our knowledge, partial Na^+ substitution for Li^+ site has not been focused for $LiMnPO_4$ based energy storage applications.

5.2 Experimental details

5.2.1 Materials

Lithium acetate ($LiC_2H_3O_2$) and sodium acetate ($C_2H_3NaO_2$) were purchased from Aldrich. Manganese acetate $Mn(CH_3COO)_2 \cdot 4H_2O$ and ammonium dihydrogen phosphate $(NH_4)H_2PO_4$ were obtained from Friendmann Schmidt.

5.2.2 Synthesis of $Li_{1-x}Na_xMnPO_4$ ($0.00 \leq x \leq 0.05$) materials

$Li_{1-x}Na_xMnPO_4$ ($0.00 \leq x \leq 0.05$) were synthesized by sol gel method. Lithium acetate, sodium acetate and manganese acetate were dissolved together with ammonium dihydrogen phosphate in the molar ratios of 1:x= 0.00, 0.01, 0.02, 0.03, 0.04, 0.05:1:1 respectively. Dissolution of this mixture was done in distilled water under magnetic stirring at 120 °C and maintain until a solid product was formed. Finally, the obtained solid material was sintered at 600 °C and 700 °C for 3 hours. The following designations (Table 5.1) are used throughout this study.

Table 5.1: Designation of $Li_{1-x}Na_xMnPO_4$ ($0.00 \leq x \leq 0.05$)

Sample	Sintering temperature	Designation
$LiMnPO_4$	600 °C	LMP6
$Li_{0.99}Na_{0.01}MnPO_4$	600 °C	LMP1-6
$Li_{0.98}Na_{0.02}MnPO_4$	600 °C	LMP2-6
$Li_{0.97}Na_{0.03}MnPO_4$	600 °C	LMP3-6
$Li_{0.96}Na_{0.04}MnPO_4$	600 °C	LMP4-6
$Li_{0.95}Na_{0.05}MnPO_4$	600 °C	LMP5-6
$LiMnPO_4$	700 °C	LMP7
$Li_{0.99}Na_{0.01}MnPO_4$	700 °C	LMP1-7
$Li_{0.98}Na_{0.02}MnPO_4$	700 °C	LMP2-7
$Li_{0.97}Na_{0.03}MnPO_4$	700 °C	LMP3-7
$Li_{0.96}Na_{0.04}MnPO_4$	700 °C	LMP4-7
$Li_{0.95}Na_{0.05}MnPO_4$	700 °C	LMP5-7

5.2.3 Structural and electrochemical characterizations

XRD measurements were obtained using Siemens D 5000 diffractometer equipped with Cu-*Kα* radiation (λ=1.54060 Å). The diffraction intensity was recorded in the range from 10º to 80º with step size 0.02° to identify structural parameters of the samples. The surface morphologies of synthesized samples were examined by field emission scanning electron microscopy (Microscope model JSM 7600-F) and transmission electron microscopy (TEM, Leo Libra 120). Raman spectra of samples were collected via Raman spectrometer (In-via Raman Microscope) using wavelength of 532 nm (blue laser).

Prior to battery fabrication, 80 wt% of active materials ($Li_{1-x}Na_xMnPO_4$) was mixed with 20wt. % of carbon to form $Li_{1-x}Na_xMnPO_4$/C. Then 20 mg of $Li_{1-x}Na_xMnPO_4$/C and 8 mg of teflonized acetylene (TAB) were mixed in ethanol and followed by

pressing on stainless steel mesh and dried at 120°C for 12 hours. Then, the cell were assembled in an argon atm using $Li_{1-x}Na_xMnPO_4$ based electrode as a cathode, lithium metal as an anode and 1 M $LiPF_6$ dissolved in a mixture of ethylene carbonate (EC)/ dimethyl carbonate (DMC) (1:1 in volume) as an electrolyte, respectively. Cyclic voltammetric tests were carried out using autolab with the potential range of 2.5 V- 4.5 V. All the samples were charged at 0.6 mA and discharged at 0.3 mA between 2.5 and 4.5 V on a Neware battery system. Electrochemical impedance spectroscopy (EIS) tests were carried out on Gamry in a frequency range of 0.05 Hz – 10kHz.

5.3 Results and discussion

5.3.1 X-Ray Diffraction (XRD)

The phase purity and structural properties were examined using XRD. Figure 5.1 and Figure 5.2 represent the pristine $LiMnPO_4$ and $Li_{1-x}Na_xMnPO_4$ ($0.00 \leq x \leq 0.05$) at sintering temperatures of 600 °C and 700 °C. At both sintering temperatures, the observed diffraction peaks of (011), (111/021), (200/121), (131), (221), (112/022) and (222) planes are consistent with $LiMnPO_4$. Thus, no impurity phases detected for $Li_{1-x}Na_xMnPO_4$ ($0.00 \leq x \leq 0.05$) samples indicating that Na ions effectively incorporated into crystal structure (Wei He et al., 2013). This verifies that it can be well indexed into orthorhombic structure of $LiMnPO_4$ (JCPDS No. 74-0375) with space group of Pnmb (Zhang et al., 2015; Zheng et al., 2015). Sharp and well defined peaks are signifying that it has been completely crystallized. Figure 5.3 shows 2θ shift to lower angles which indicating doping of sodium ions into lithium sites (Wei He et al., 2013).

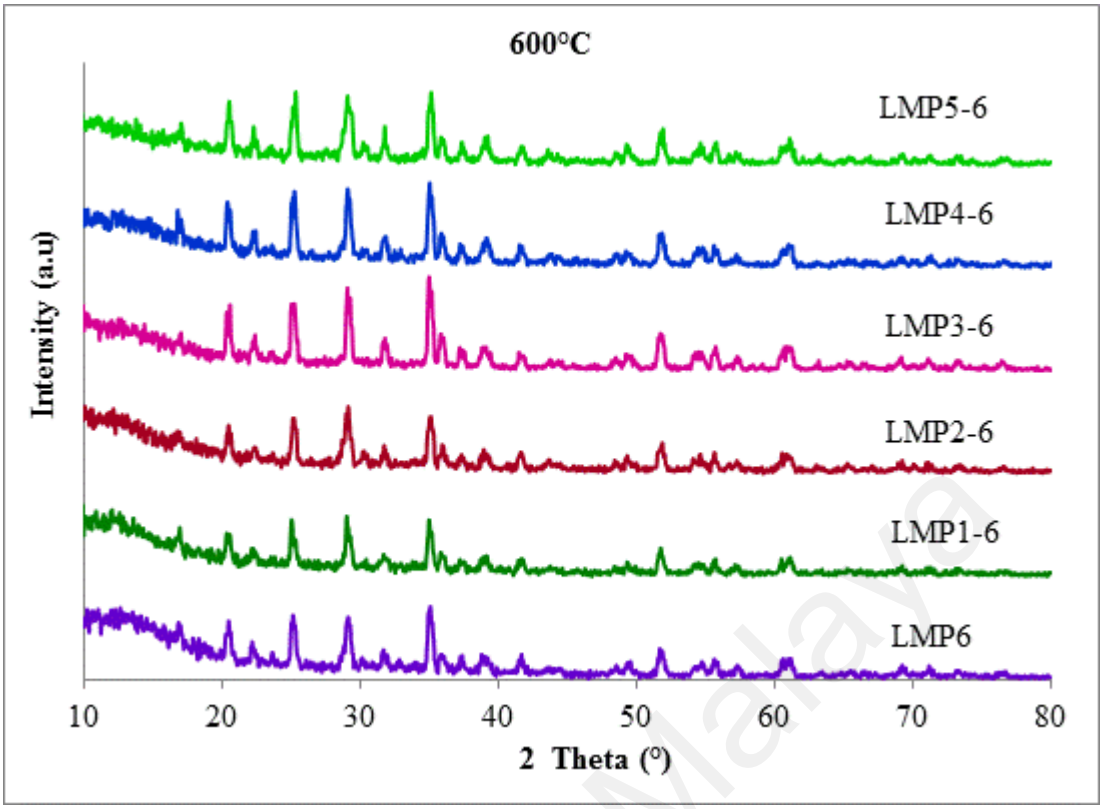

Figure 5.1: XRD of $Li_{1-x}Na_xMnPO_4$ sintered at 600°C

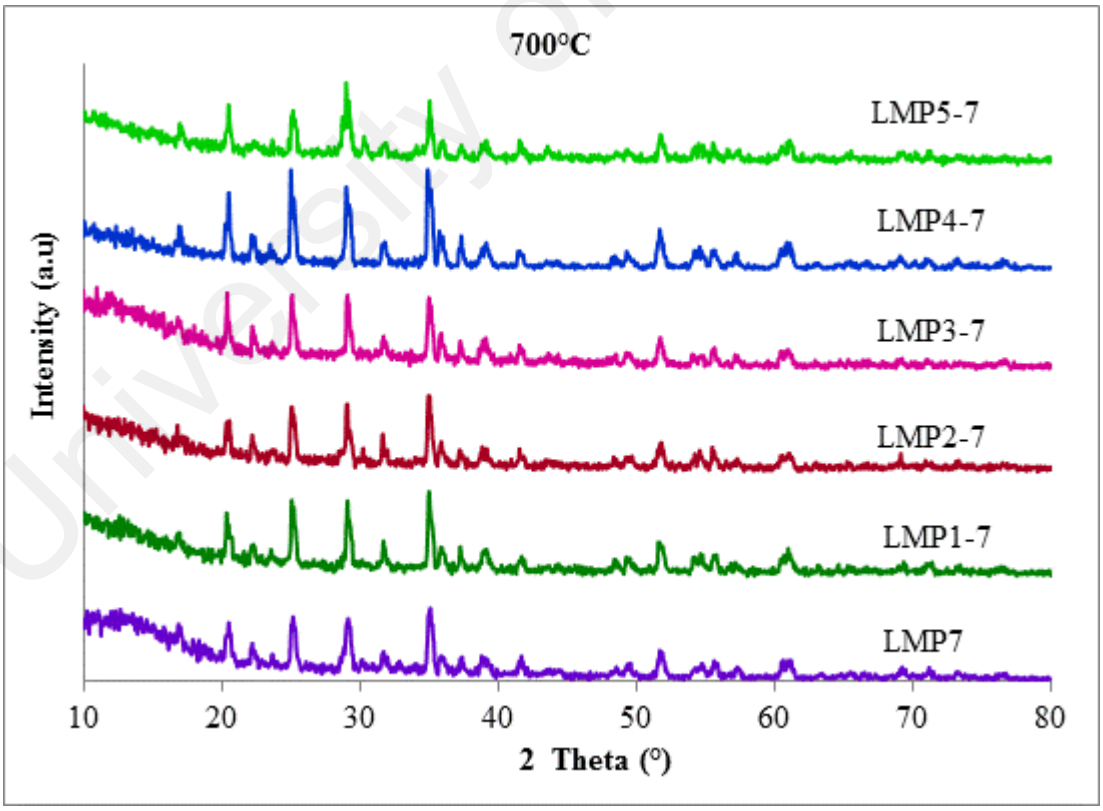

Figure 5.2: XRD of $Li_{1-x}Na_xMnPO_4$ sintered at 700°C

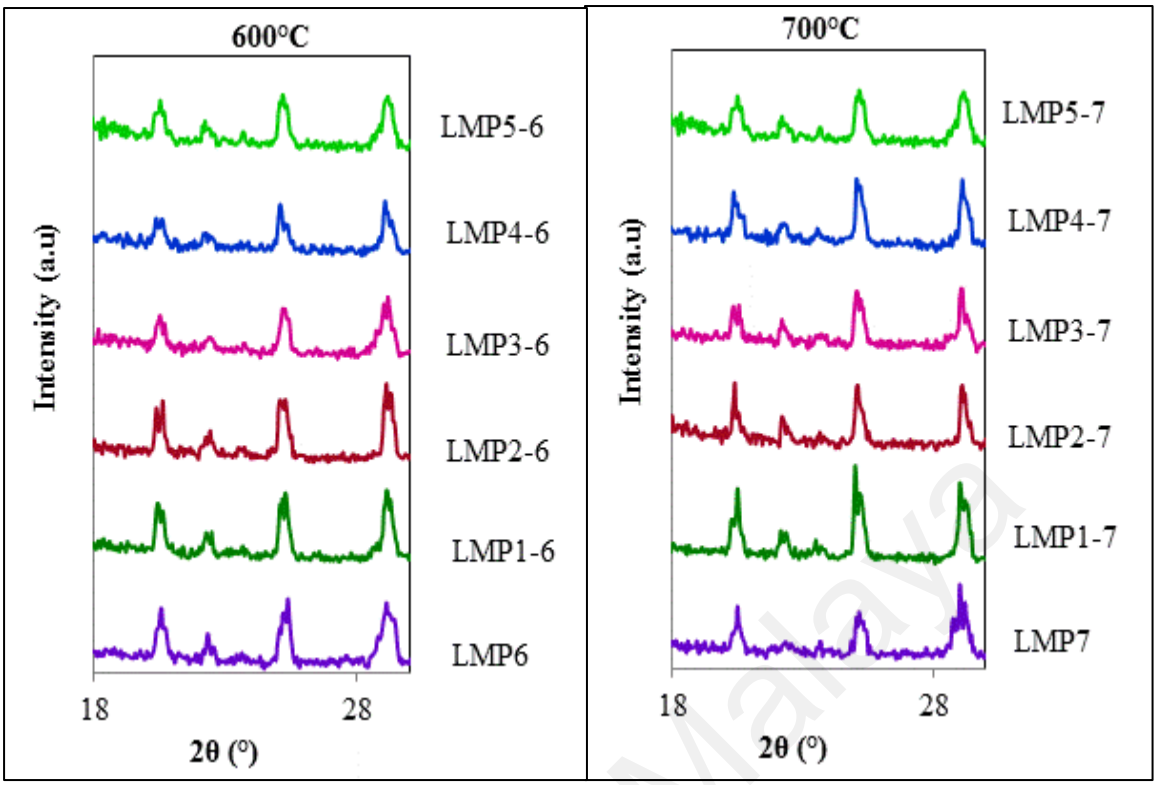

Figure 5.3: Peak shift in 2θ values for $Li_{1-x}Na_xMnPO_4$ samples

Table 5.2 and 5.3 tabulated 2θ, full width half maximum (FWHM) and d spacing corresponds to hkl for the samples treated at 600 °C and 700 °C respectively.

Table 5.2: 2θ, FWHM and d spacing of $Li_{1-x}Na_xMnPO_4$ sintered at 600°C

LMP1-6

hkl	2θ (°)	FWHM (°)	d-spacing (Å)
(011)	20.568	0.247	4.37180
(111/021)	25.168	0.426	3.51818
(200/121)	29.077	0.430	3.06100
(131)	35.006	0.370	2.55448
(221)	39.080	0.718	2.30843
(112/022)	41.534	0.460	2.16706
(222)	51.784	0.546	1.76201

LMP2-6

hkl	2θ (°)	FWHM (°)	d-spacing (Å)
(011	20.350	0.307	4.37342
(111/021)	25.065	0.292	3.51908
(200/121)	29.082	0.398	3.06300
(131)	35.008	0.451	2.55264
(221)	39.176	0.510	2.30531
(112/022)	41.700	0.479	2.16560
(222)	51.772	0.472	1.75901

LMP3-6

hkl	2θ (°)	FWHM (°)	d-spacing (Å)
(011)	20.407	0.261	4.37680
(111/021)	25.277	0.391	3.52155
(200/121)	29.107	0.372	3.06547
(131)	35.054	0.418	2.55779
(221)	39.193	0.461	2.29672
(112/022)	41.550	0.438	2.17170
(222)	51.868	0.480	1.76136

LMP4-6

hkl	2θ (°)	FWHM (°)	d-spacing (Å)
(011)	20.526	0.280	4.37757
(111/021)	25.355	0.375	3.52250
(200/121)	29.131	0.474	3.06808
(131)	35.127	0.411	2.56105
(221)	39.041	0.384	2.29765
(112/022)	41.673	0.440	2.16423
(222)	51.942	0.537	1.76440

LMP5-6

hkl	2θ (°)	FWHM (°)	d-spacing (Å)
(011)	20.460	0.311	4.38003
(111/021)	25.222	0.416	3.52398
(200/121)	29.175	0.386	3.06853
(131)	35.101	0.487	2.56122
(221)	38.986	0.474	2.30306
(112/022)	41.643	0.449	2.17249
(222	51.847	0.497	1.76400

Table 5.3: 2θ, FWHM and d spacing of $Li_{1-x}Na_xMnPO_4$ sintered at 700°C

LMP1-7

hkl	2θ (°)	FWHM (°)	d-spacing (Å)
(011)	20.392	0.242	4.38627
(111/021)	25.097	0.234	3.53953
(200/121)	29.086	0.366	3.06614
(131)	35.016	0.401	2.56055
(221)	39.132	0.523	2.30440
(112/022)	41.553	0.388	2.16368
(222)	51.753	0.439	1.76986

LMP2-7

hkl	2θ (°)	FWHM (°)	d-spacing (Å)
(011)	20.511	0.261	4.38989
(111/021)	25.019	0.228	3.54539
(200/121)	29.033	0.405	3.06950
(131)	34.932	0.425	2.56050
(221)	39.100	0.506	2.30017
(112/022)	41.529	0.477	2.17155
(222)	51.740	0.418	1.76499

LMP3-7

hkl	2θ (°)	FWHM (°)	d-spacing (Å)
(011)	20.553	0.248	4.39342
(111/021)	25.059	0.392	3.55072
(200/121)	29.063	0.255	3.07001
(131)	34.997	0.334	2.56188
(221)	38.843	0.548	2.31656
(112/022)	41.554	0.345	2.17151
(222)	51.780	0.446	1.76414

LMP4-7

hkl	2θ (°)	FWHM (°)	d-spacing (Å)
(011)	20.503	0.166	4.39664
(111/021)	25.155	0.431	3.55627
(200/121)	29.025	0.334	3.07306
(131)	35.051	0.257	2.56650
(221)	39.146	0.380	2.30197
(112/022)	41.614	0.383	2.17275
(222)	51.774	0.407	1.76539

LMP5-7

hkl	2θ (°)	FWHM (°)	d-spacing (Å)
(011)	20.379	0.285	4.39824
(111/021)	25.139	0.382	3.55744
(200/121)	29.100	0.351	3.07397
(131)	35.015	0.260	2.55800
(221)	39.057	0.414	2.29937
(112/022)	41.711	0.362	2.16851
(222)	51.600	0.528	1.76431

However, the lattice parameters were varied with respect to amount of Na doping in $LiMnPO_4$, as given in Table 5.4. From chapter 4, LMP6 reveals lattice parameters a = 6.121 Å, b = 10.253 Å and c = 4.827 Å while LMP7 with a = 6.131 Å, b = 10.289 Å and c = 4.824 Å. Calculated lattice parameters a for LMP 1-6, LMP 2-6, LMP 3-6, LMP 4-6 and LMP 5-6 are 6.122 Å, 6.126 Å, 6.131 Å, 6.136 Å and 6.137 Å

respectively which corresponds to volume of 303.66 $Å^3$, 304.00 $Å^3$, 304.67 $Å^3$, 305.10 $Å^3$ and 305.39 $Å^3$ accordingly. Lattice constants b and c also increases with Na doping.

Similar pattern observed for samples sintered at temperature of 700 °C where lattice constant *a* for LMP 1-7, LMP 2-7, LMP 3-7, LMP 4-7 and LMP 5-7 are 6.138 Å, 6.139 Å, 6.140 Å, 6.146 Å and 6.148 Å individually. Volumes were recorded as 308.33 $Å^3$, 309.48 $Å^3$, 310.52 $Å^3$, 311.87 $Å^3$ and 312.17 $Å^3$ for LMP 1-7, LMP 2-7, LMP 3-7, LMP 4-7 and LMP 5-7. It is noteworthy that lattice constants a, b, c and volume of the samples tend to increase with Na doping amount. Analogous results reported by recent researchers on Na doped LiV_3O_8 (Lu, Shang, Zhang, & Deng, 2015), $LiNi_{1/3}Co_{1/3}Mn_{1/3}O_2$ (Gong et al., 2014), Li_2MnSiO_4 (Wang, Yang, Ma, & Shen, 2015) etc. This could be another evidence to strongly support that Na ions inserted into Li sites, since radius of Na ion (1.02 Å) larger than radius of Li ion (0.76 Å) (Gong et al., 2014; Zhu, Zhang, Deng, Yi, & Ye, 2015).

Both *a*, *b* and *c* lattices increased with increasing Na metal doping. While *c* axis enlargement indicates the expansion of Li pathway within the structure (Hee et al., 2013), the enlargement in *a* site provides smoother Li diffusion during intercalation process. This is due to Li^+ ion movement favorably occurs through (010) channel in orthorhombic structure because of its low diffusion energy accompanied by continuous chain LiO_6 octahedra (Zhu et al., 2015).

Table 5.4: Calculated lattice parameters of $Li_{1-x}Na_xMnPO_4$ ($0.00 \leq x \leq 0.05$) obtained at sintering temperature of 600°C and 700°C

Sample	a(Å)	b(Å)	c(Å)	Volume(Å^3)
LMP1-6	6.122	10.265	4.832	303.66
LMP 2-6	6.126	10.266	4.834	304.00
LMP 3-6	6.131	10.272	4.838	304.67
LMP 4-6	6.136	10.276	4.839	305.10
LMP 5-6	6.137	10.278	4.842	305.39
LMP 1-7	6.138	10.380	4.840	308.33
LMP 2-7	6.139	10.414	4.841	309.48
LMP 3-7	6.140	10.443	4.843	310.52
LMP 4-7	6.146	10.476	4.844	311.87
LMP 5-7	6.148	10.478	4.846	312.17

Moreover it has been proved by the simulation method that Li ion moves through the *a* axis due its lower activation energy, which was supported by Oh et al. (Oh, Hong, Jung, & Ryu, 2015). Therefore, this Na doping expands interplanar distance for smooth Li diffusion during intercalation process, suggesting enhanced electrochemical performance (Wei He et al., 2013; Zhu et al., 2015).

On comparing sintering temperature, lattice parameters and volume of the $Li_{1-x}Na_xMnPO_4$ ($0.00 \leq x \leq 0.05$) samples at 700 °C are greater than 600 °C. This

denotes that heating temperature plays one of the essential roles in the expansion of unit cell (Xiang et al., 2014). Structural properties for $Li_{1-x}Na_xMnPO_4$ ($0.00 \leq x \leq 0.05$) samples were further analyzed by Williamson – Hall (W-H) method as illustrated in following graphs (Figure 5.4 and Figure 5.5). This method provides information about strain and crystallite size of the samples (Reddy et al., 2011).

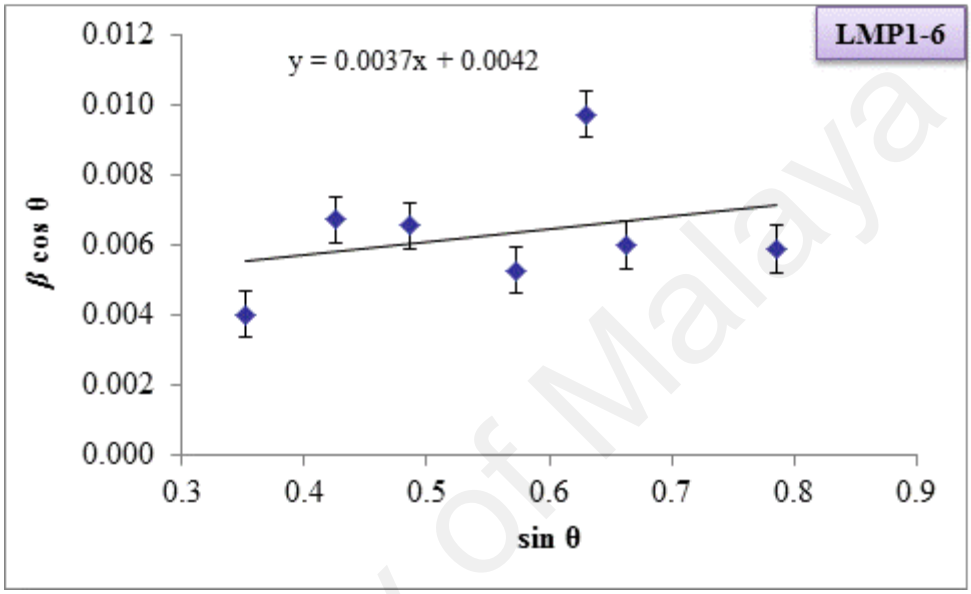

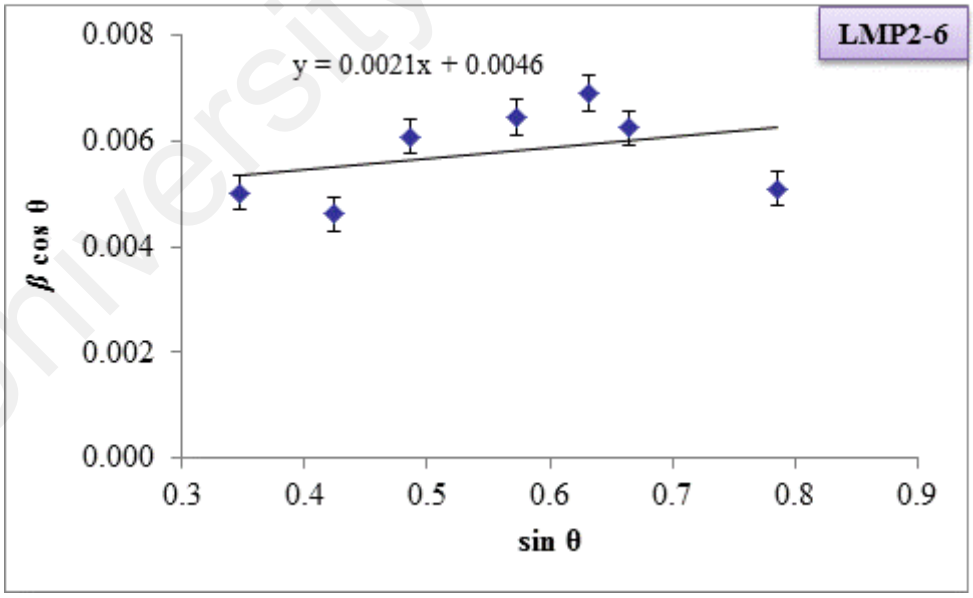

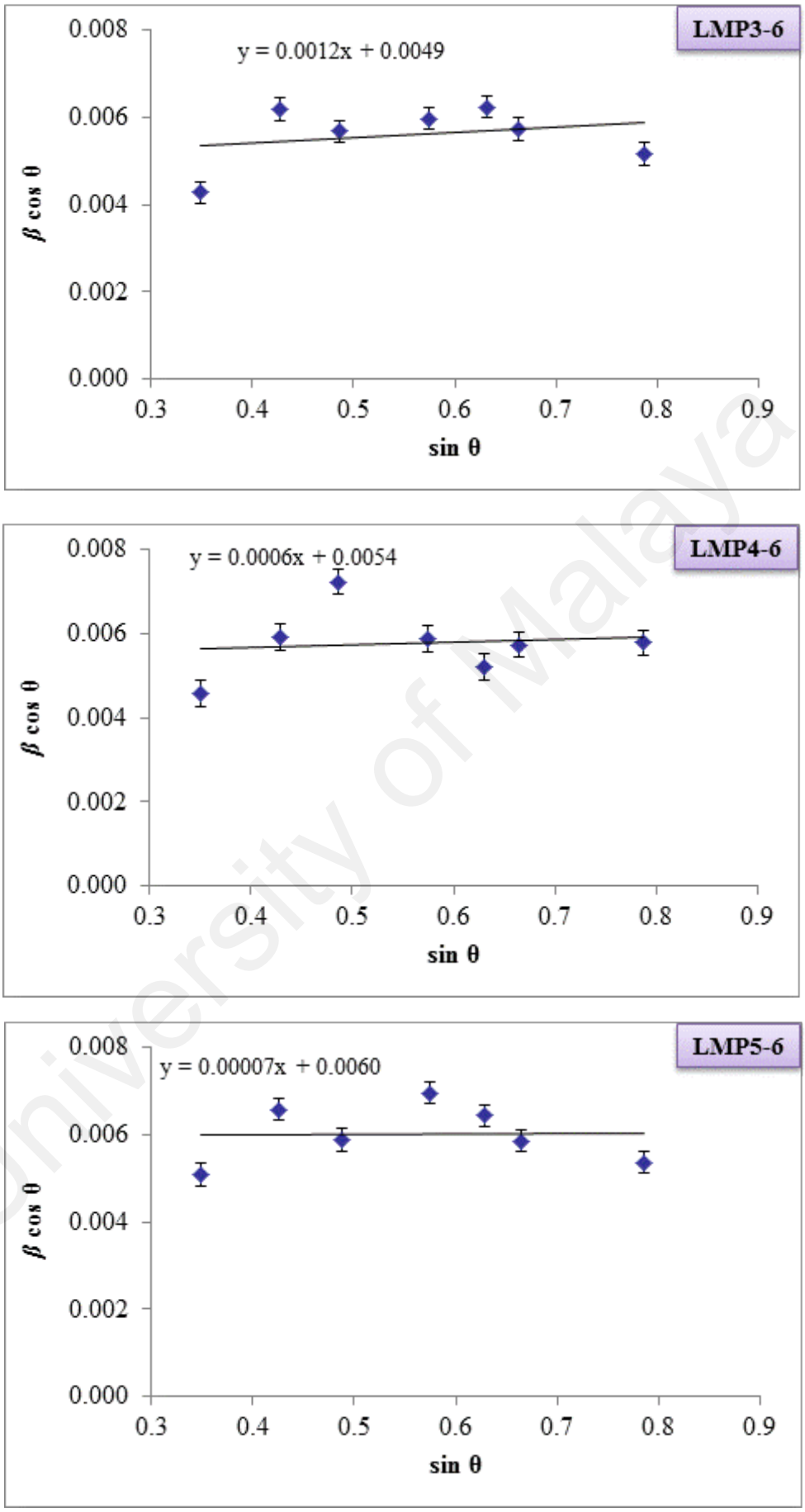

Figure 5.4: Williamson-hall plots of $Li_{1-x}Na_xMnPO_4$ sintered at 600°C

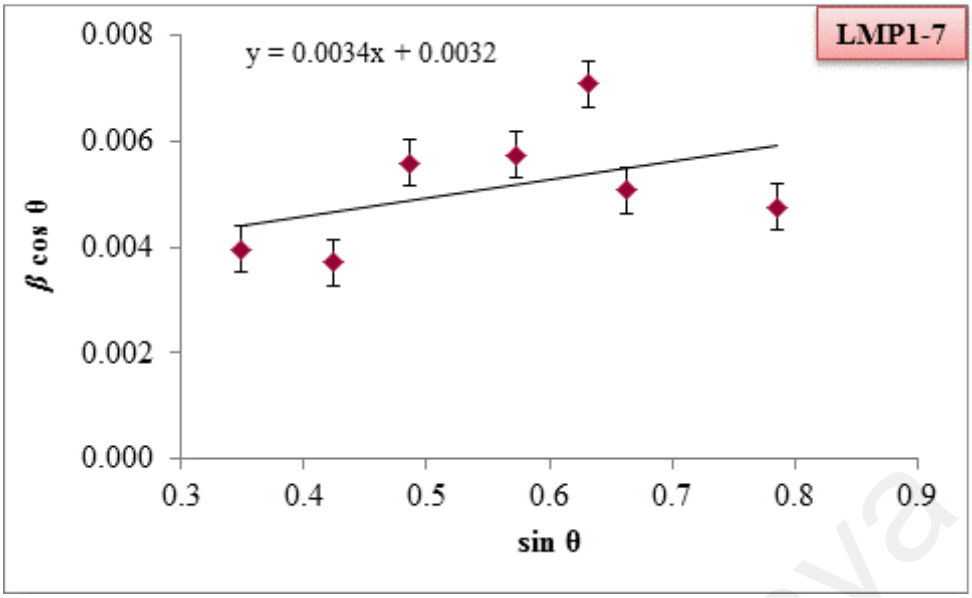

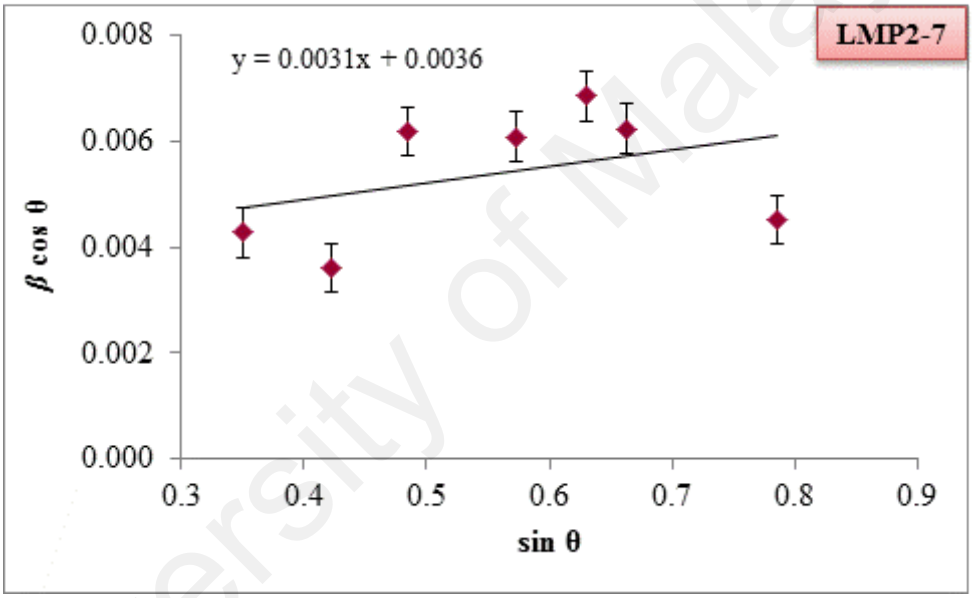

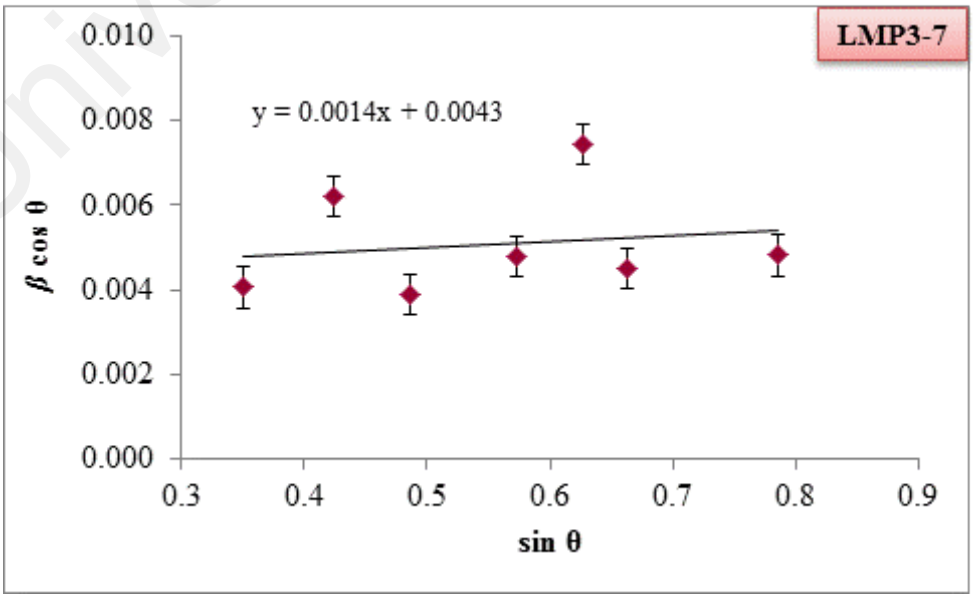

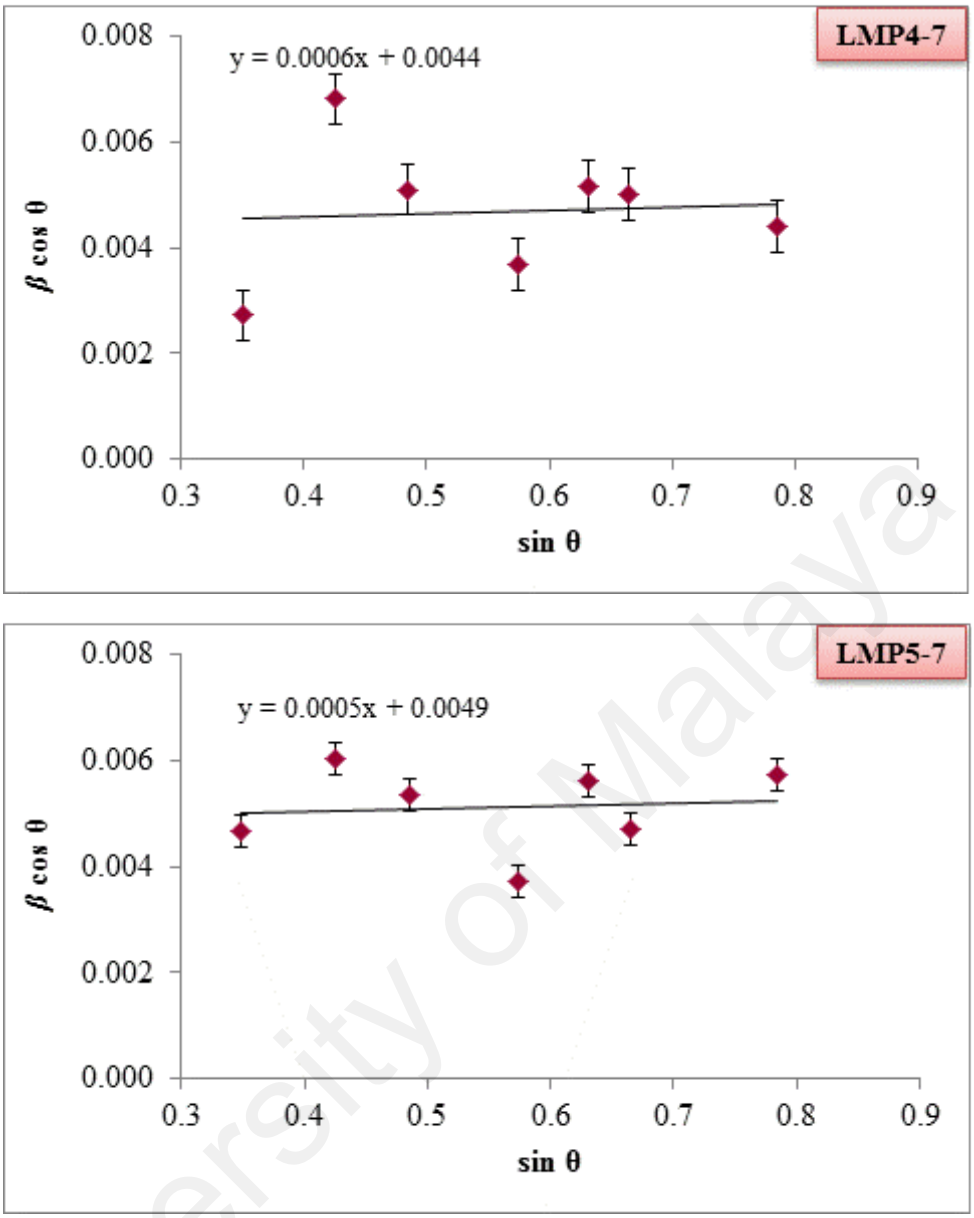

Figure 5.5: Williamson-hall plots of $Li_{1-x}Na_xMnPO_4$ sintered at 700°C

From the plots of β cos θ vs sin θ, it can be noticed that each graph has its slope and y intercept. Crystallite size of the particles can be deduced from the y intercept while strain estimated from slope of the graph. Table 5.5 and Table 5.6 summarize crystallite size and strain of the samples via Williamson – Hall (W-H) method.

Table 5.5: Mean crystallite size and strain values of $Li_{1-x}Na_xMnPO_4$ ($0.00 \leq x \leq 0.05$) sintered at 600°C

Sample	Intercept	Slope	Crystallite size (nm)	Strain
LMP1-6	0.0042	0.0037	33.0	9.25×10^{-4}
LMP2-6	0.0046	0.0021	30.1	5.25×10^{-4}
LMP3-6	0.0049	0.0012	28.3	3.00×10^{-4}
LMP4-6	0.0054	0.0006	25.7	1.50×10^{-4}
LMP5-6	0.0060	0.00007	23.1	1.75×10^{-5}

Table 5.6: Mean crystallite size and strain values of $Li_{1-x}Na_xMnPO_4$ ($0.00 \leq x \leq 0.05$) sintered at 700°C

Sample	Intercept	Slope	Crystallite size (nm)	Strain
LMP1-7	0.0034	0.0032	40.8	8.00×10^{-4}
LMP2-7	0.0036	0.0031	38.5	7.75×10^{-4}
LMP3-7	0.0043	0.0014	32.2	3.50×10^{-4}
LMP4-7	0.0044	0.0006	31.5	1.50×10^{-4}
LMP5-7	0.0049	0.0005	28.3	1.25×10^{-4}

Crystallite size of LMP1-6 is about 33.0 nm decreased to 30.1 nm, 28.3 nm, 25.7 nm and 23.1 nm for LMP2-6, LMP3-6, LMP4-6 and LMP5-6 respectively. While strain of LMP1-6 is around 9.25×10^{-4} and it dropped to 1.75×10^{-4} for LMP5-6. LMP1-7 recorded crystallite size of 40.8 nm accompanied with strain of 8.00×10^{-4}. The value of crystallite size and strain decreased to 38.5 nm; 7.75×10^{-4}, 32.2 nm; 3.50×10^{-4}, 31.5 nm; 1.50×10^{-4} and 28.3 nm; 1.25×10^{-4} relatively for LMP2-7, LMP3-7, LMP4-7 and LMP5-7. Both heating temperatures of 600 °C and 700 °C indicate that crystallite size and strain are decreased with Na doping amount. It could be due to the melting point of NaOH which is 318.4 °C lower compared to the melting point of LiOH at 471 °C. Melting point achieved easily with increase of Na doping which results in crystallite size reduction (Wang, Lin, Wu, & Zhao, 2014).

5.3.2 Field Emission Scanning Electron microscopy (FESEM)

FESEM analysis was used to study the surface morphology of synthesized samples. Figure 5.6-5.10 displays surface morphology of $Li_{1-x}Na_xMnPO_4$ ($0.00 \leq x \leq 0.05$) particles formed at calcination temperature of 600°C while Figure 5.11- 5.15 illustrates samples obtained at calcination temperature of 700°C. At both sintering temperatures, more agglomeration occurred for $Li_{0.99}Na_{0.01}MnPO_4$ and $Li_{0.98}Na_{0.02}MnPO_4$ $Li_{0.97}Na_{0.03}MnPO_4$ compared to $Li_{0.96}Na_{0.04}MnPO_4$ and $Li_{0.99}Na_{0.05}MnPO_4$. It can be noticed that agglomerated particles and individual particles are present together in the samples and agglomerated particles are formed by smaller individual particles. Sintering temperature at 700 °C promotes larger agglomeration than 600 °C.

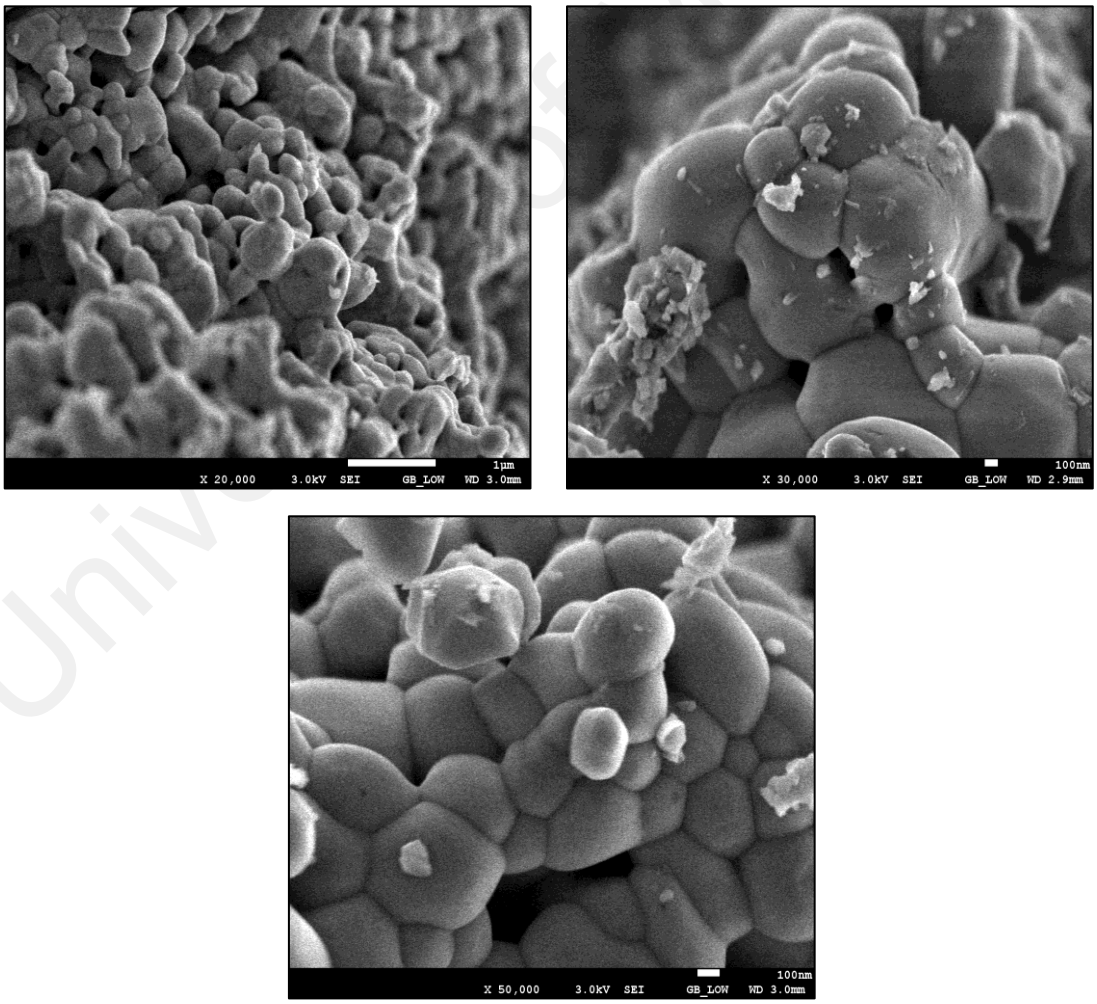

Figure 5.6: FESEM images of $Li_{0.99}Na_{0.01}MnPO_4$ sintered at 600°C (LMP1-6)

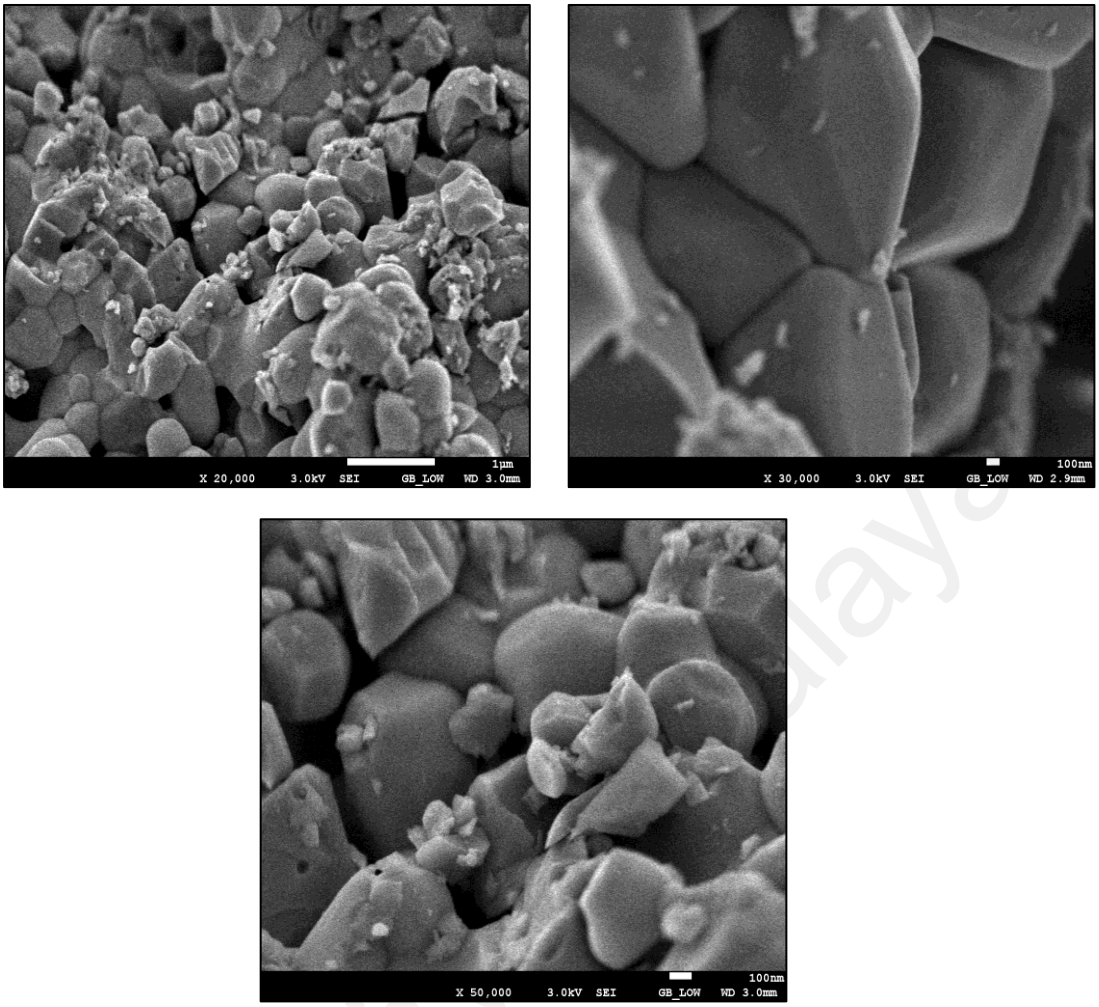

Figure 5.7: FESEM images of $Li_{0.98}Na_{0.02}MnPO_4$ sintered at 600°C (LMP2-6)

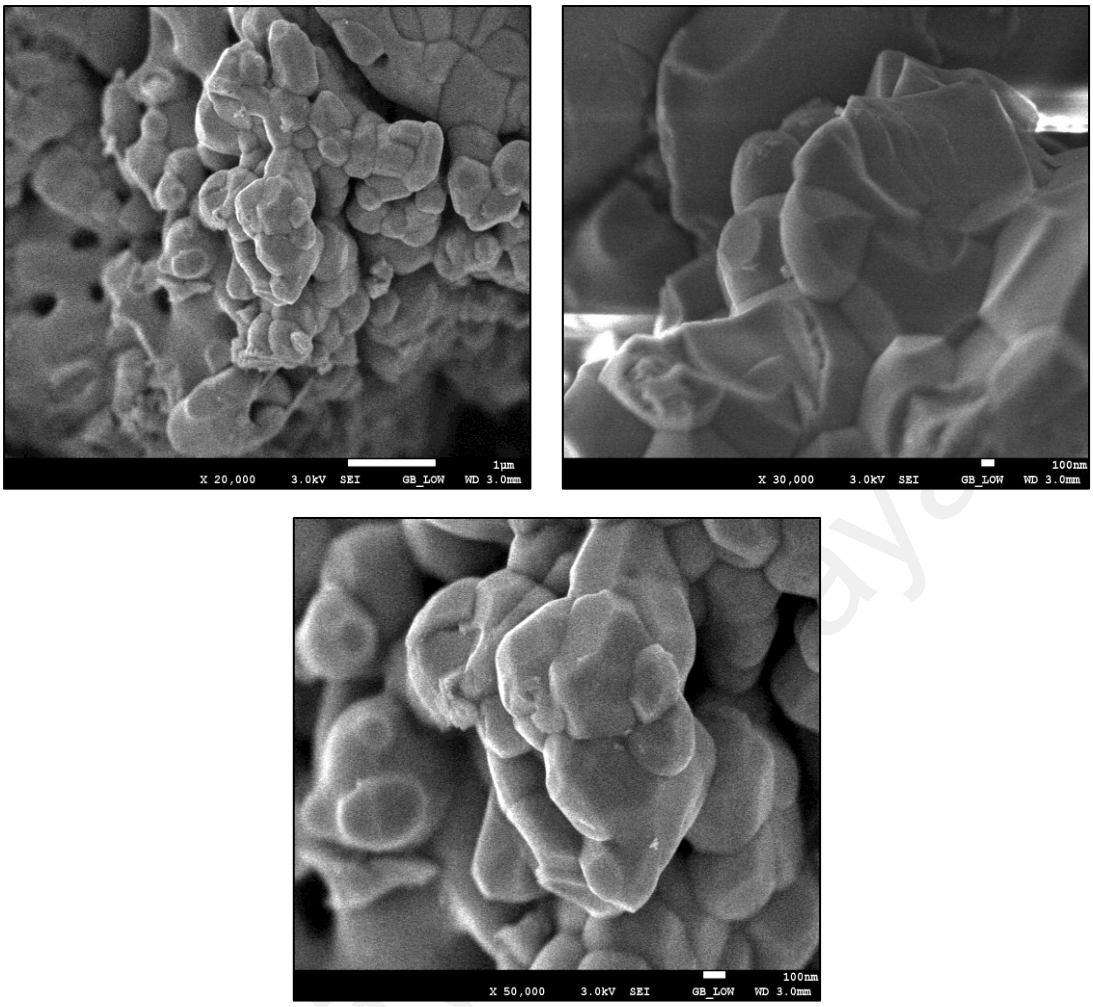

Figure 5.8: FESEM images of $Li_{0.97}Na_{0.03}MnPO_4$ sintered at 600°C (LMP3-6)

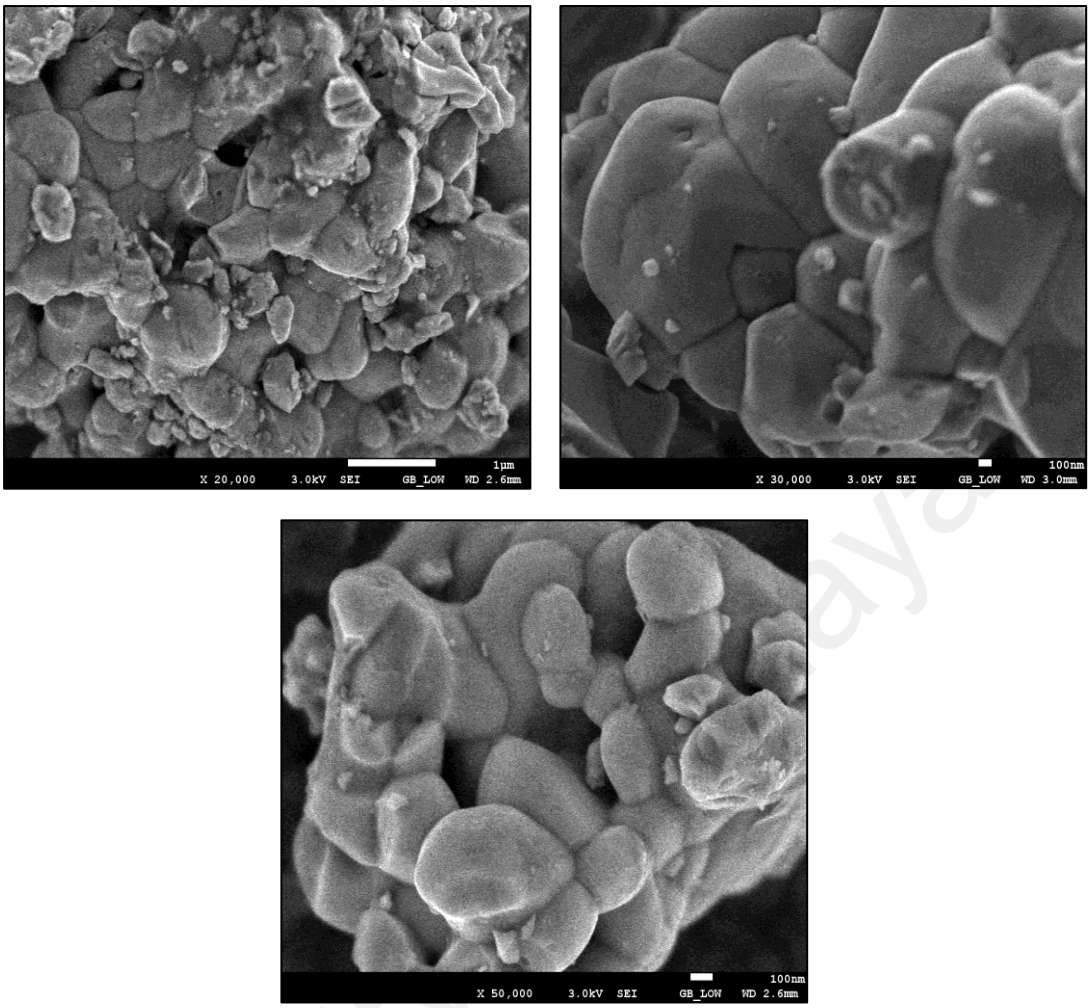

Figure 5.9: FESEM images of $Li_{0.96}Na_{0.04}MnPO_4$ sintered at 600°C (LMP4-6)

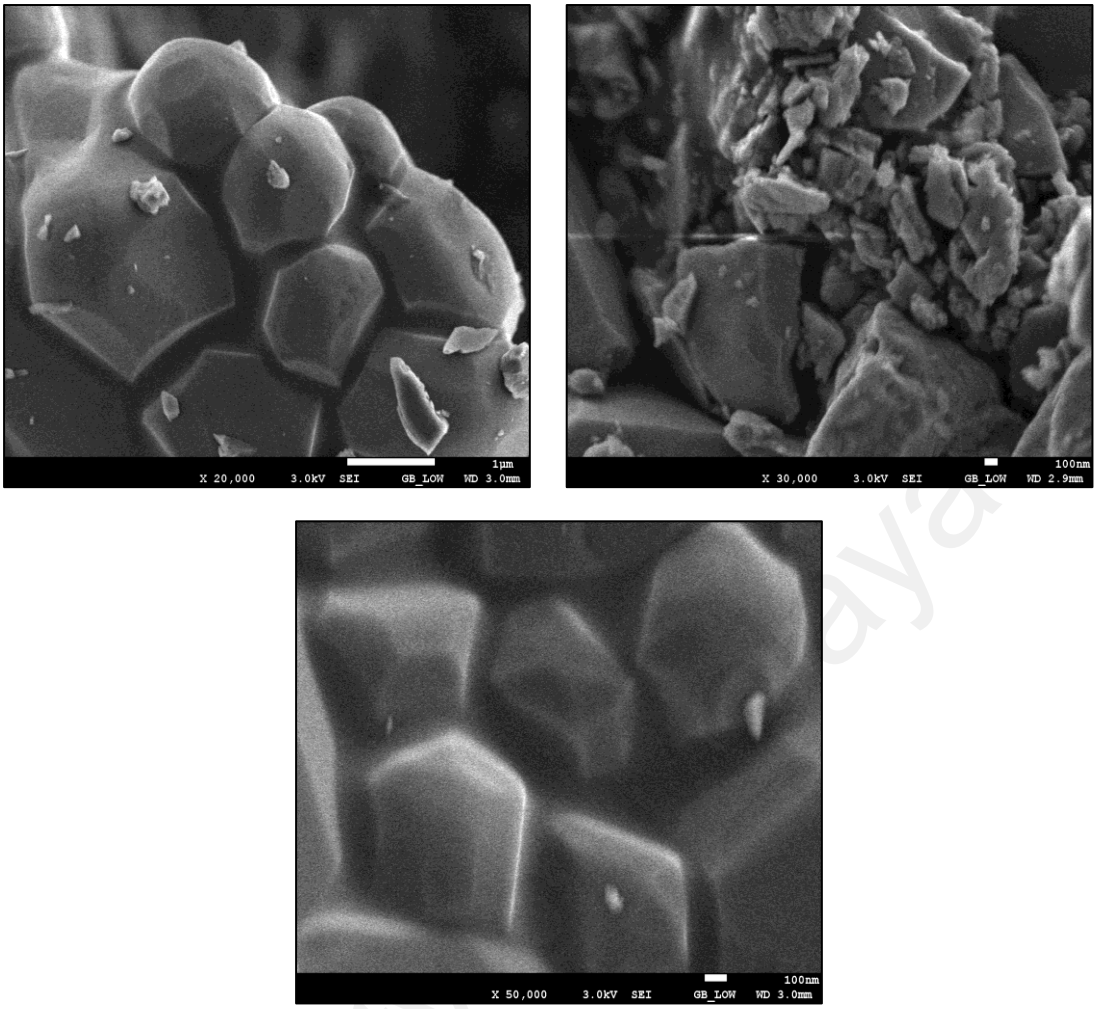

Figure 5.10: FESEM images of $Li_{0.95}Na_{0.05}MnPO_4$ sintered at 600°C (LMP5-6)

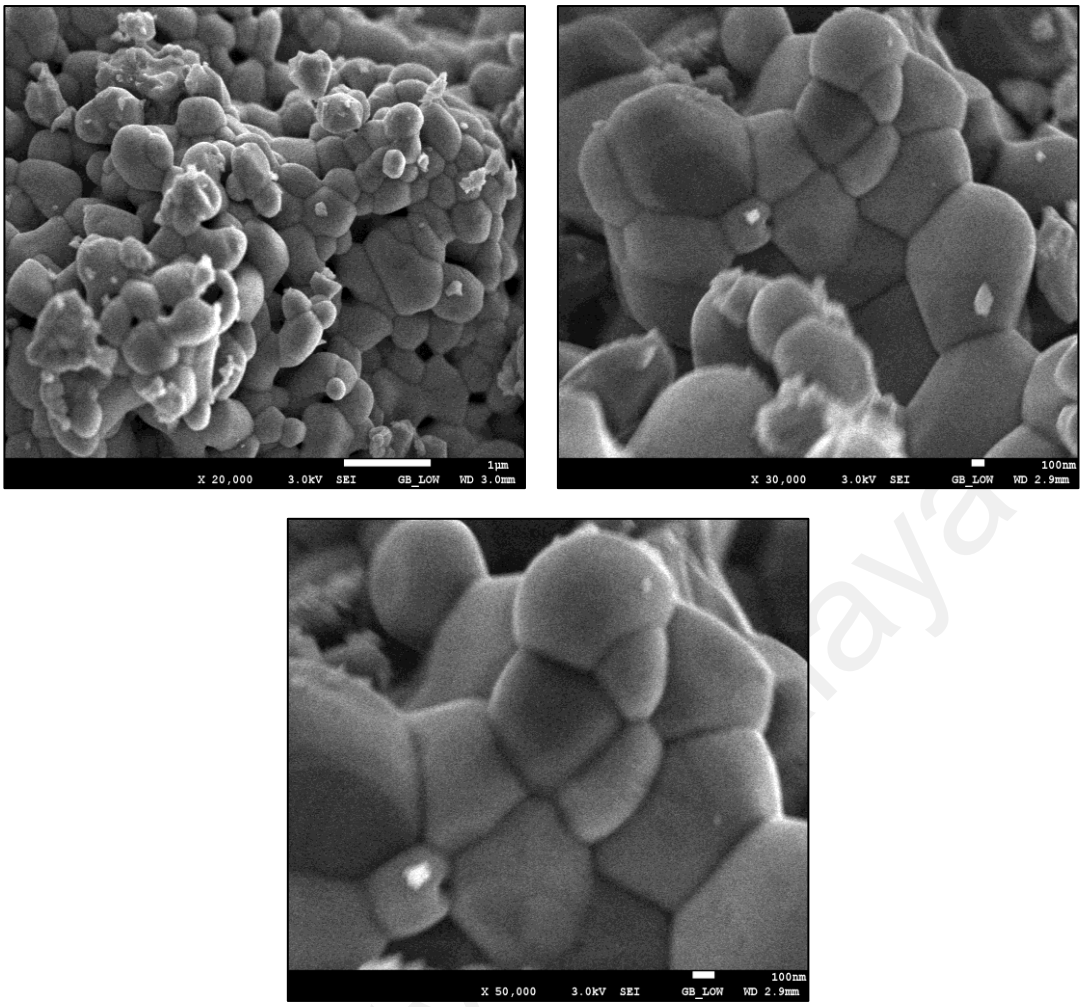

Figure 5.11: FESEM images of $Li_{0.99}Na_{0.01}MnPO_4$ sintered at 700°C (LMP1-7)

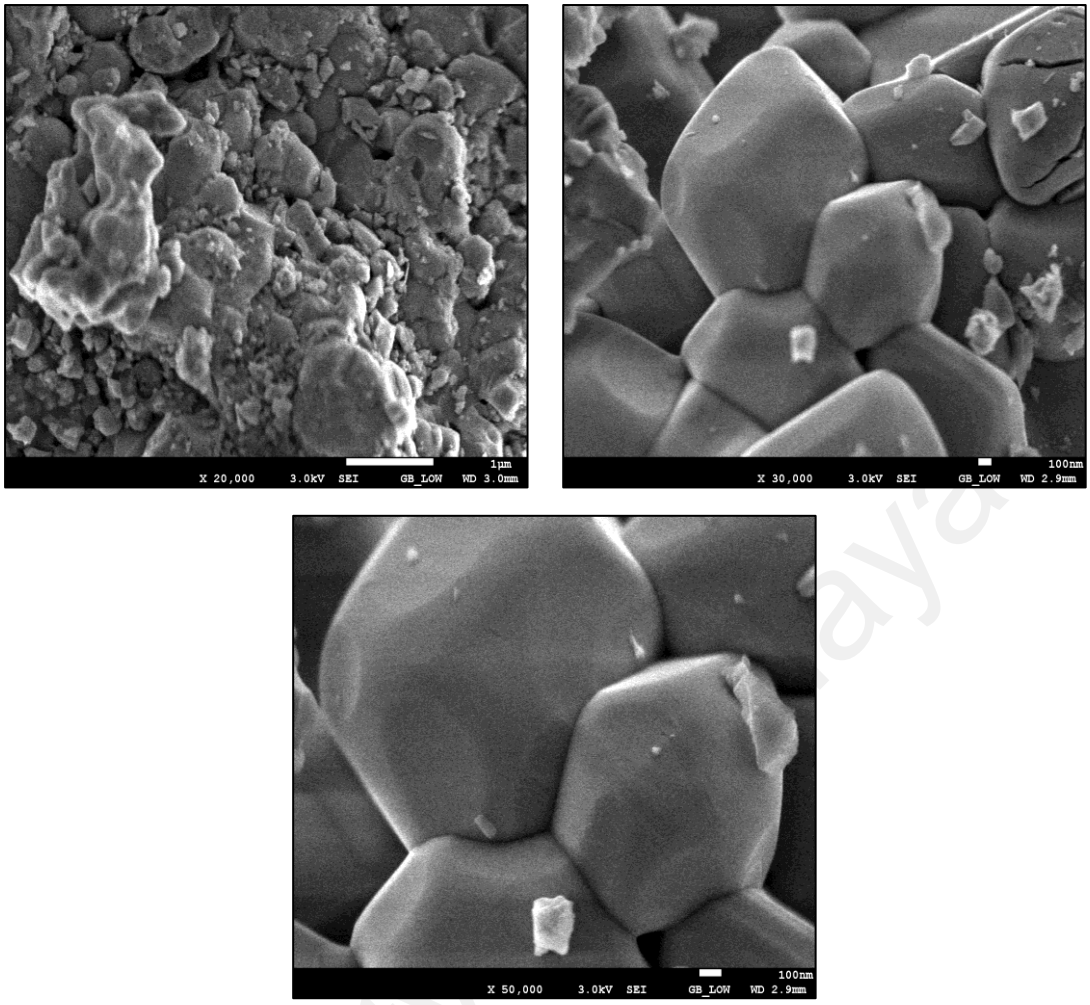

Figure 5.12: FESEM images of $Li_{0.98}Na_{0.02}MnPO_4$ sintered at 700°C (LMP2-7)

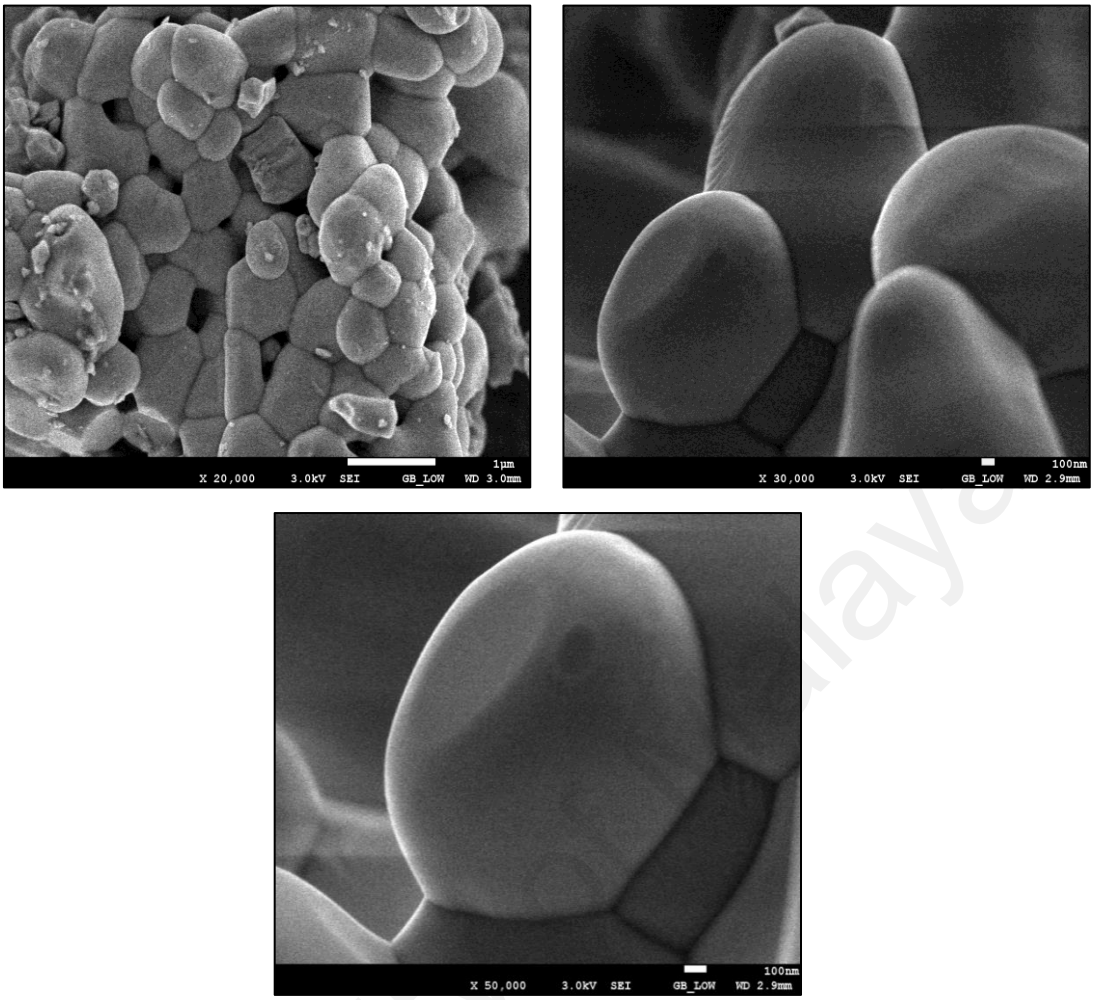

Figure 5.13: FESEM images of $Li_{0.97}Na_{0.03}MnPO_4$ sintered at 700°C (LMP3-7)

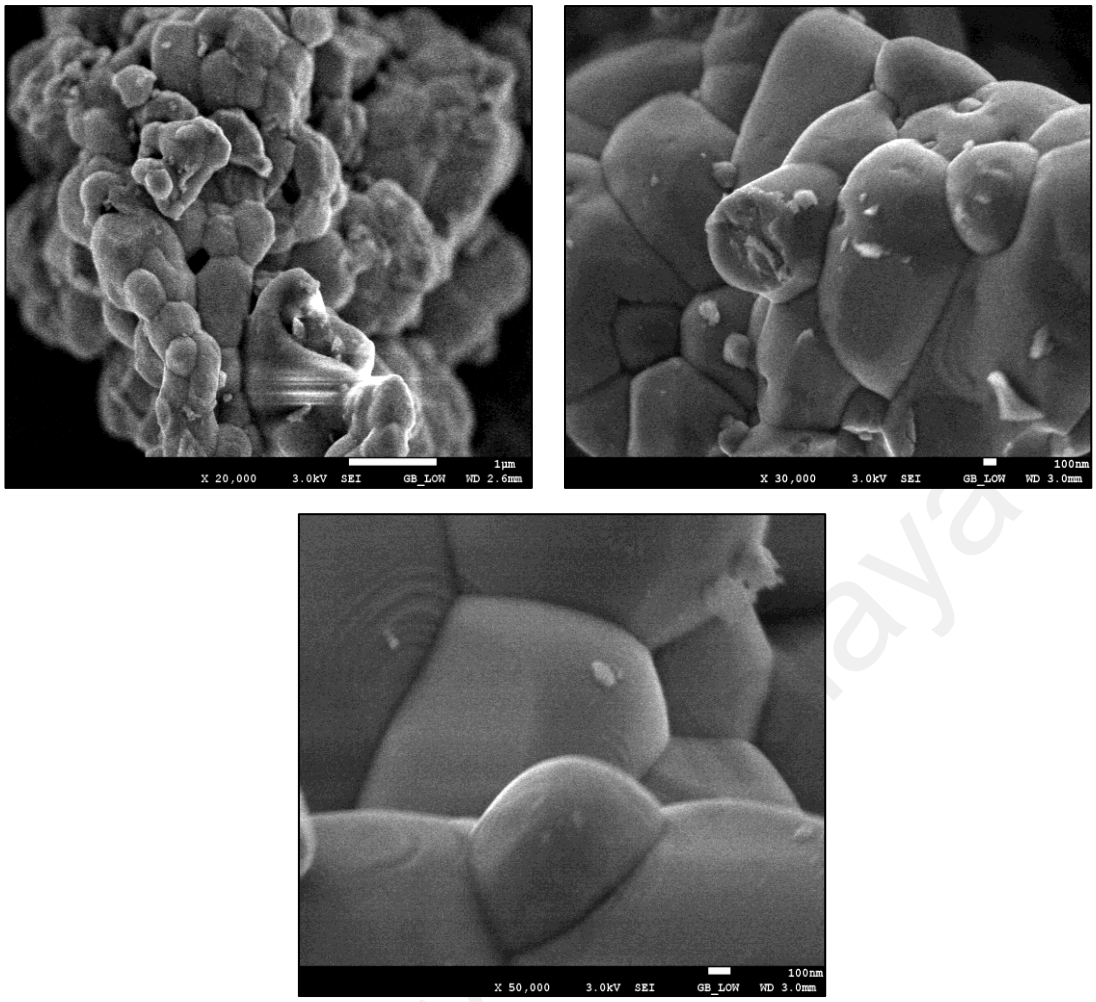

Figure 5.14: FESEM images of $Li_{0.96}Na_{0.04}MnPO_4$ sintered at 700°C (LMP4-7)

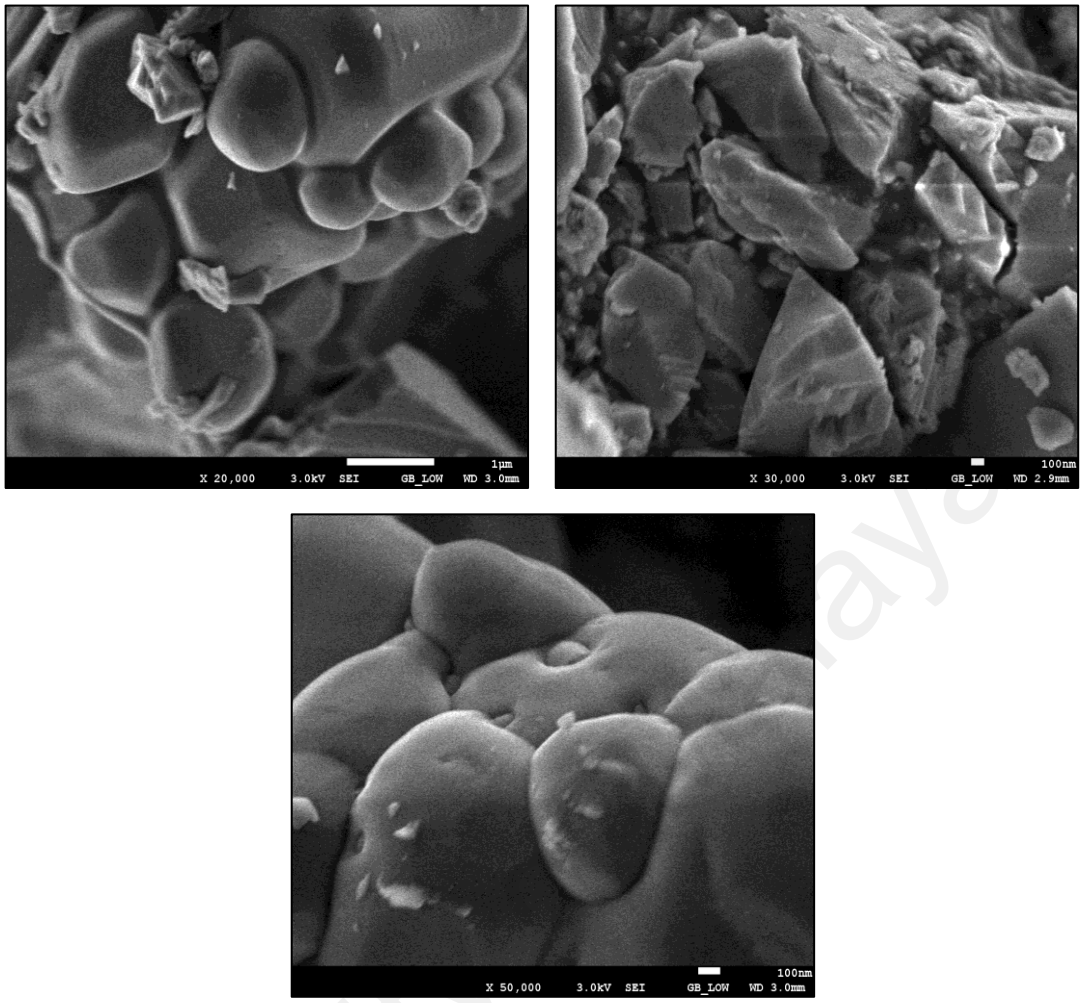

Figure 5.15: FESEM images of $Li_{0.95}Na_{0.05}MnPO_4$ sintered at 700°C (LMP5-7)

5.3.3 Transmission Electron microscopy (TEM)

TEM images of $Li_{1-x}Na_xMnPO_4$ sintered at 600 °C and 700 °C are depicted in Figure 5.16 and Figure 5.17. At both heating temperatures, crystallites size found to be decreasing with Na content. Crystallite sizes are in the range of 20 nm – 35 nm for calcination at 600 °C and 25 nm – 42 nm at 700 °C. The values are consistent with Williamson Hall results as in Table 5.2.

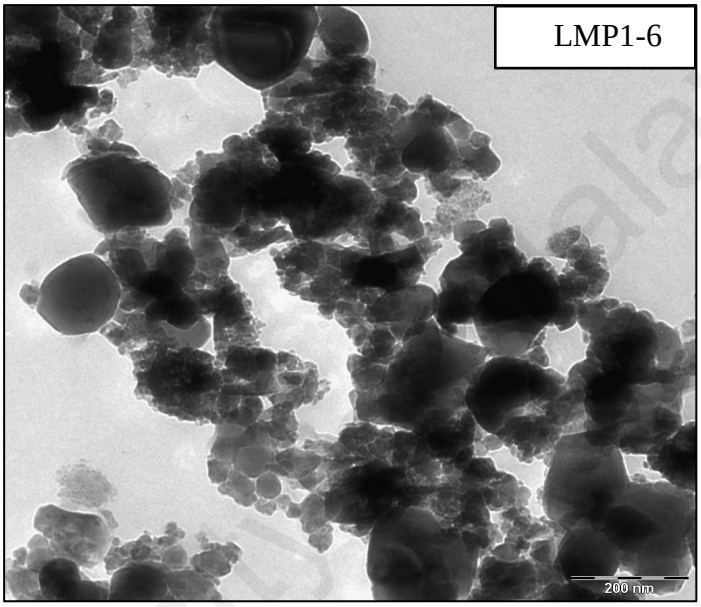

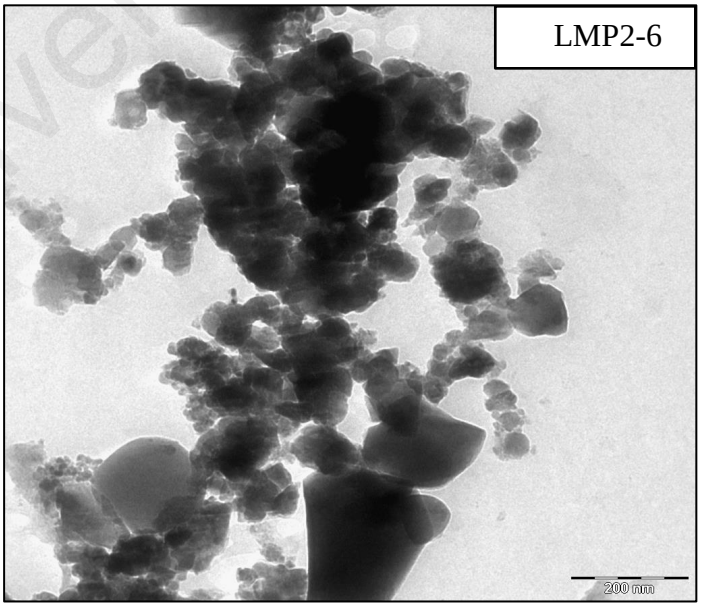

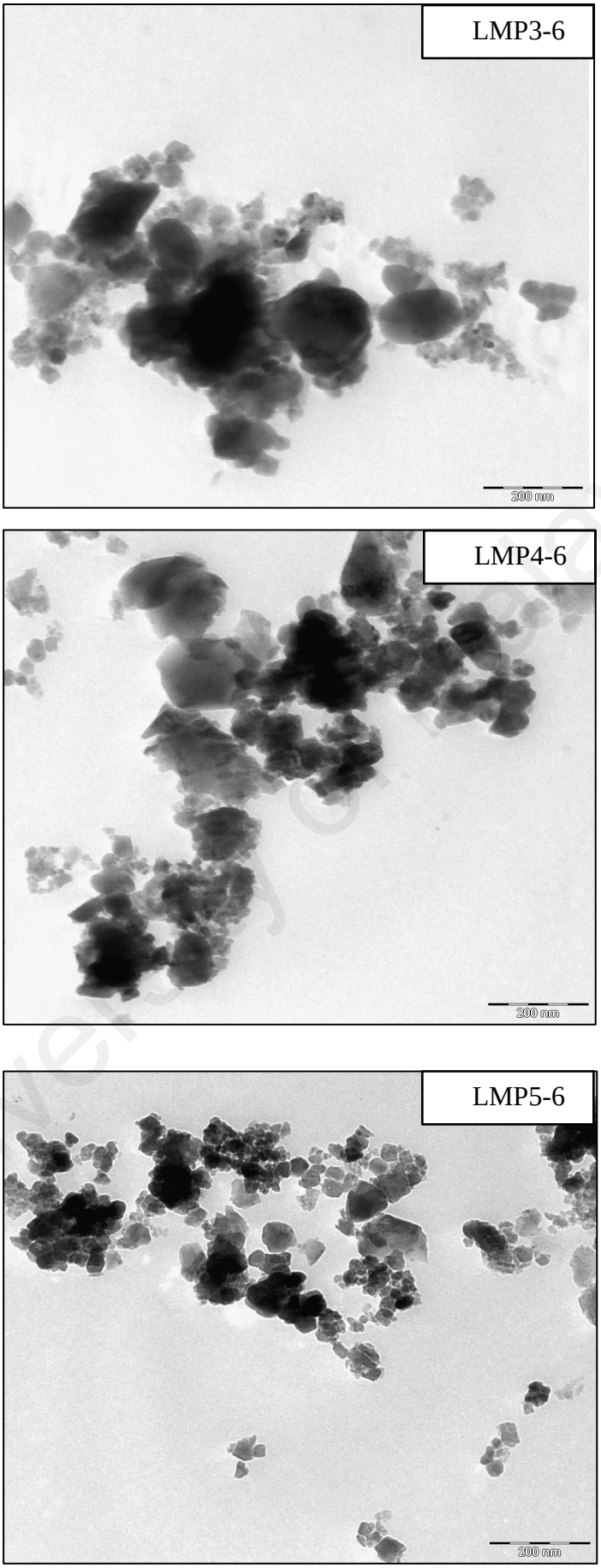

Figure 5.16: TEM of $Li_{1-x}Na_xMnPO_4$ sintered at 600°C

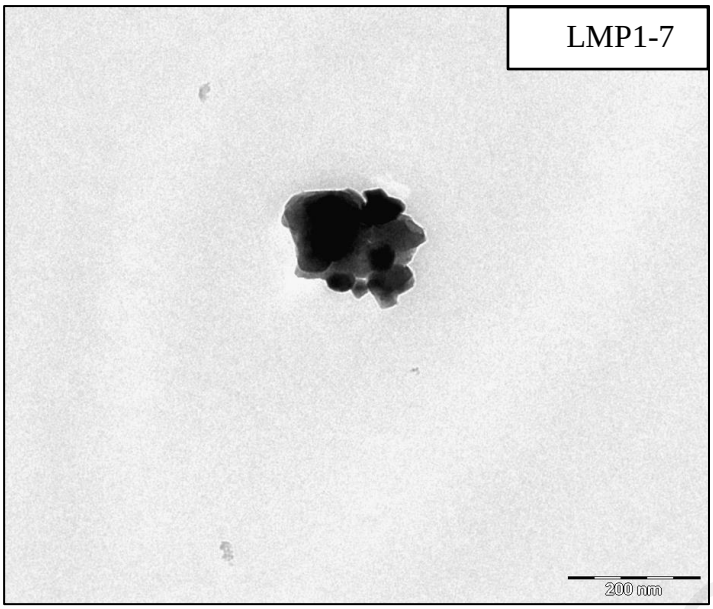

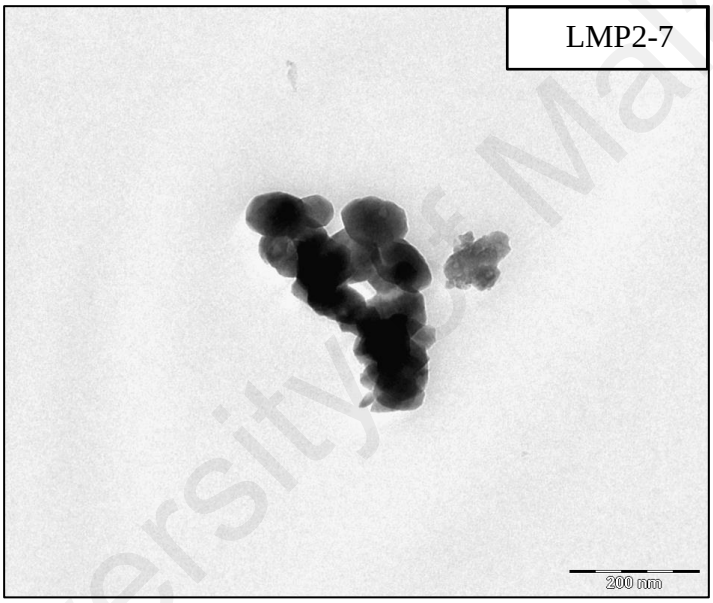

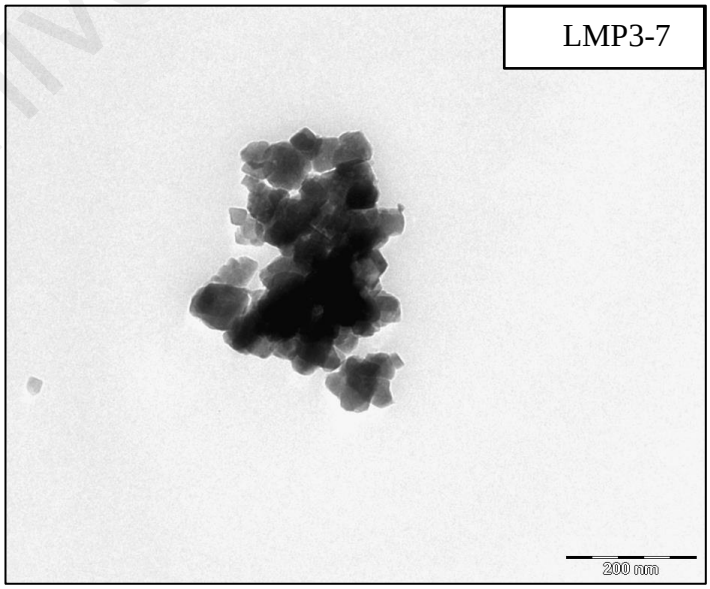

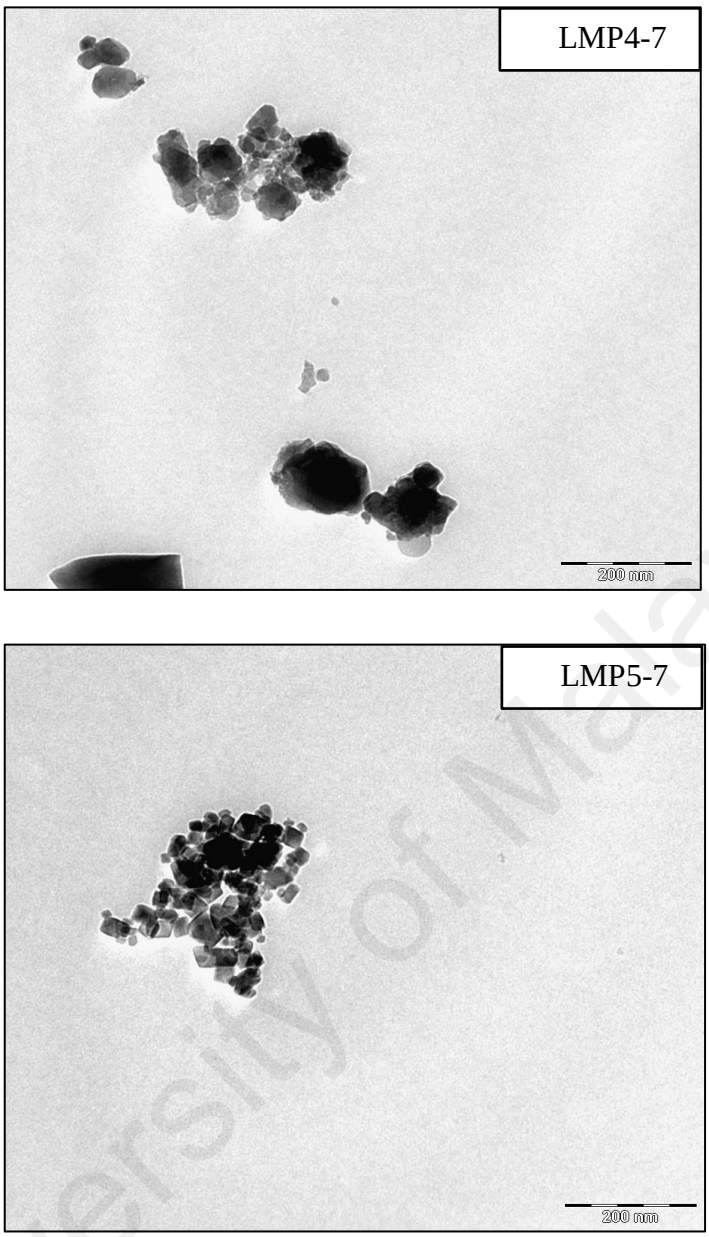

Figure 5.17: TEM of $Li_{1-x}Na_xMnPO_4$ sintered at 700 °C

5.3.4 Raman Spectroscopy

Raman spectra of $Li_{1-x}Na_xMnPO_4$ ($0.00 \leq x \leq 0.05$) at calcination temperatures of 600 °C and 700 °C are displayed in Figure 5.18 and Figure 5.19 respectively. The strongest peak at 950 cm^{-1} and peaks at 1005 cm^{-1} and 1070 cm^{-1} correspond to A_gv_1 and A_gv_3 accordingly. While peak at 438 cm^{-1} denotes A_gv_2 mode, peaks at 590 cm^{-1}, 627

cm^{-1} and 661 cm^{-1} $A_g v_4$ modes (Korona et al., 2011; Markevich et al., 2011). The peaks for all samples resemble as for $LiMnPO_4$.

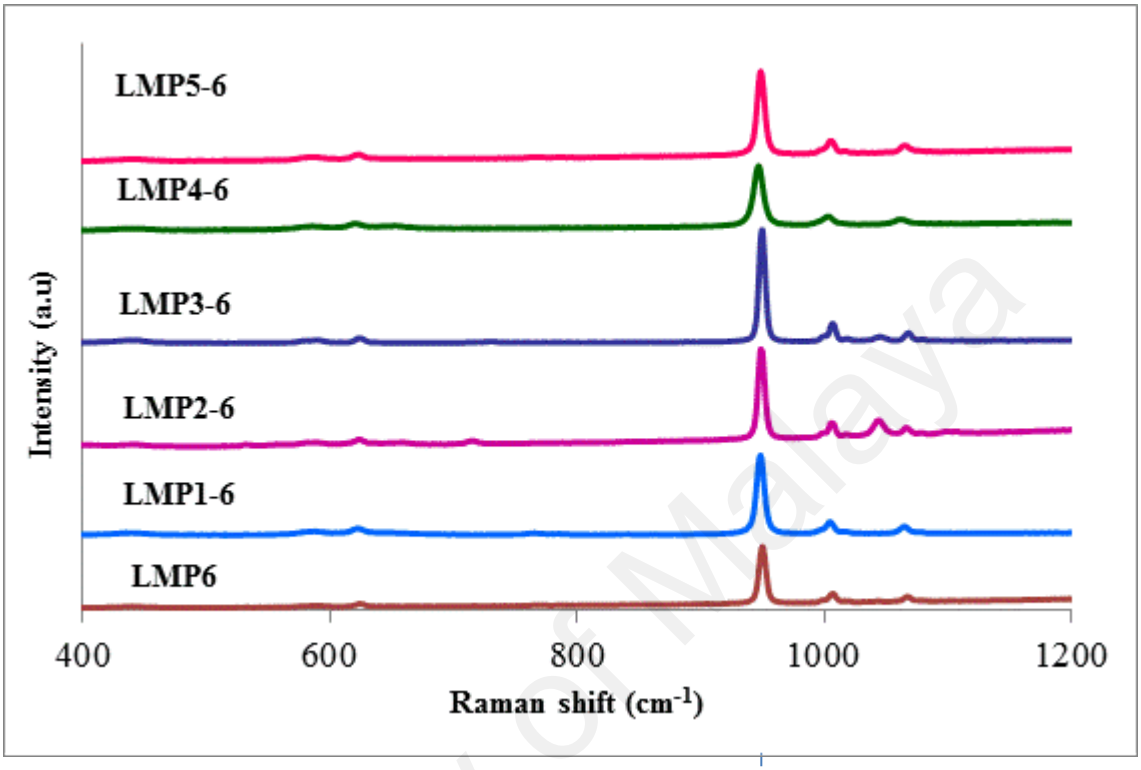

Figure 5.18: Raman spectra of $Li_{1-x}Na_xMnPO_4$ sintered at 600 °C

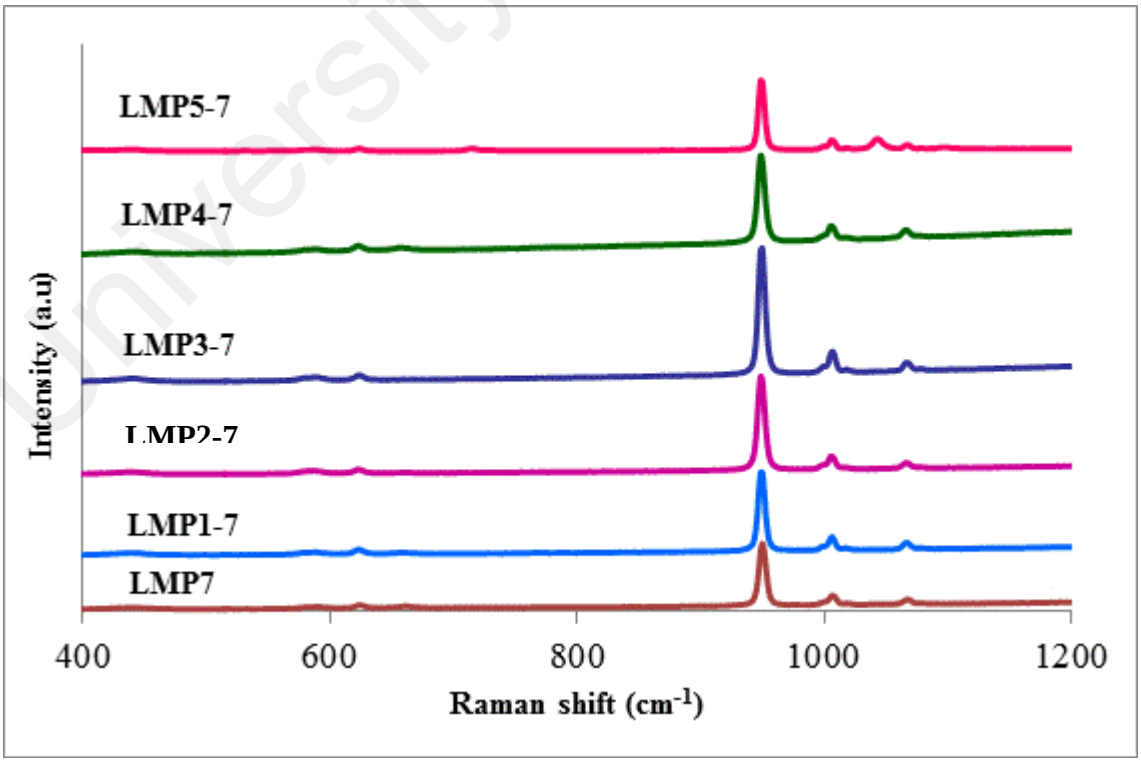

Figure 5.19: Raman spectra of $Li_{1-x}Na_xMnPO_4$ sintered at 700 °C

This indicates that small amount sodium substitution into lithium sites does not change the structure of $LiMnPO_4$. LMP3-6 and LMP3-7 were found to exhibit stronger peaks compared to other peaks due to stabilized structure (Wang et al., 2014).

5.3.5 Electrochemical analysis

Galvanostatic charge discharge experiments were carried out on $Li_{1-x}Na_xMnPO_4$ ($0.01 \leq x \leq 0.05$) cathode materials comprising coin cells over the potential range from 2.5 V – 4.5 V (vs Li^+/Li) at room temperature. Figure 5.20 illustrates the discharge capacities of $Li_{1-x}Na_xMnPO_4$ ($0.01 \leq x \leq 0.05$) at sintering temperature of 600 °C. Pristine $LiMnPO_4$ exhibits initial discharge capacity of 66.4 $mAhg^{-1}$ and increases to 69.7 $mAhg^{-1}$ with the Na^+ substitution of x = 0.01 in the $Li_{1-x}Na_xMnPO_4$. While x = 0.02 and x = 0.03 in the $Li_{1-x}Na_xMnPO_4$ structure leads to discharge capacity of 74.5 $mAhg^{-1}$ and 79.7 $mAhg^{-1}$. These results indicate the increase of capacity about 13.3 $mAhg^{-1}$ in $Li_{0.97}Na_{0.03}MnPO_4$ compared to $LiMnPO_4$. Therefore, the enhanced cycling performance is attributed to the structure stabilization with Na^+ ions, which act as pillar (Park, Shin, & Sun, 2006; Qiu et al., 2013). Apart from that, Jahn Teller distortion is related to the Mn-Mn distance within the crystalline structure. Na substitution also makes distance of Mn-Mn becomes longer because Na^+ ions are larger compared to Li^+ ions. This weakens Jahn Teller effect and cycling stability getting stronger (Sun & Xu, 2014).

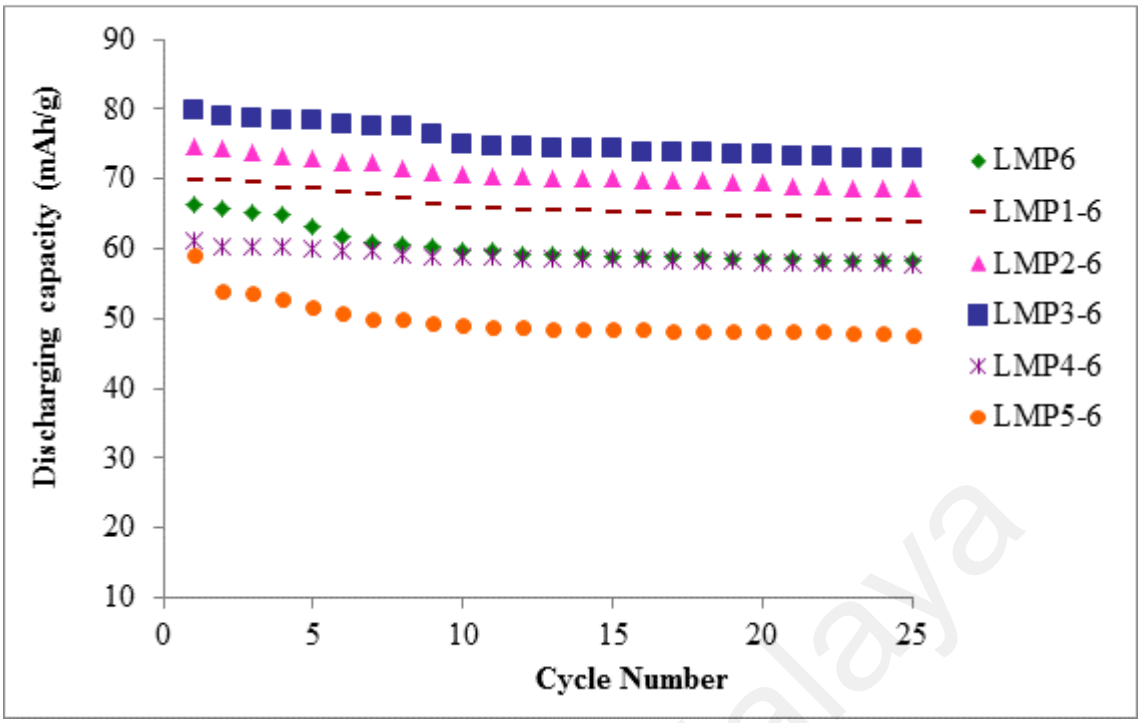

Figure 5.20: Discharge capacities of $Li_{1-x}Na_xMnPO_4$ sintered at 600 °C

However, when the substitution of Na level in $Li_{1-x}Na_xMnPO_4$ reaches x = 0.04 and 0.05, first discharge capacity is recorded at 61.2 $mAhg^{-1}$ and 59.2 $mAhg^{-1}$ which is lower than $LiMnPO_4$.

Figure 5.21 presents variation of discharge capacities versus number of cycles for samples obtained at sintering temperature of 700 °C. At the initial cycles, discharge capacities of 86.3 mAh g^{-1}, 88.9 mAh g^{-1}, 91.2 mAh g^{-1}, 92.4 mAh g^{-1}, 84.3 mAh g^{-1} and 83.3 mAh g^{-1} observed for x = 0.00, 0.01, 0.02, 0.03, 0.04 and 0.05 in $Li_{1-x}Na_xMnPO_4$ respectively. At the same time, coulombic efficiency improved from 83.3 % (pristine $LiMnPO_4$) to 87.6 % ($Li_{0.97}Na_{0.03}MnPO_4$) respectively. The discharge capacity increased while increasing the Na content (from x = 0.00 to x = 0.03), resulting the good structure stabilization (Gong et al., 2014).

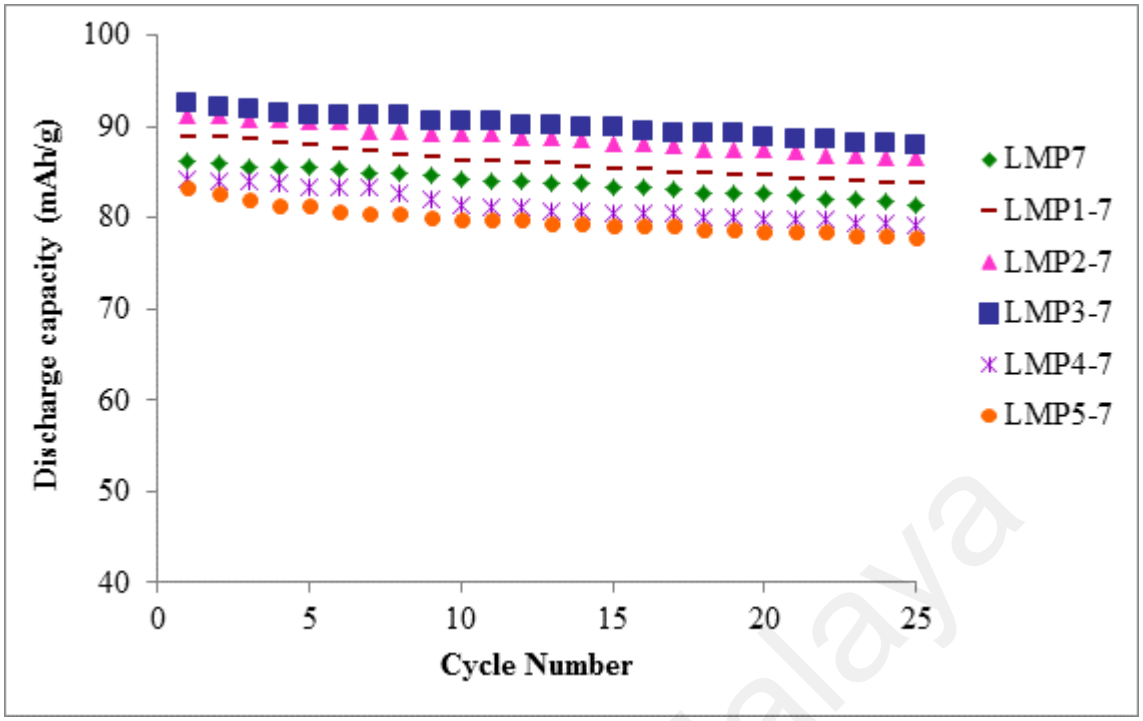

Figure 5.21: Discharge capacities of $Li_{1-x}Na_xMnPO_4$ sintered at 700 °C

This improved capacity signifies the smoother intercalation and deintercalation process within the materials (Fang et al., 2008). However, beyond the addition of Na (> 0.03) lead to deterioration the capacitive nature due to structural instability and weak electrochemical performance (Dong, Xu, Xiong, Sun, & Zhang, 2013; Kuang, Zhao, & Liang, 2011). $Li_{0.97}Na_{0.03}MnPO_4$ demonstrated the maximum cycling stability than that of other samples due to moderate doping of Na**.**

Samples obtained from both sintering temperatures present similar discharge capacities pattern for 25 cycles. While comparing both sintering temperatures, $Li_{0.97}Na_{0.03}MnPO_4$ is exhibiting the best cycling performance among the other compounds. Hence, Figure 5.22 compares the capacity retention of both $Li_{0.97}Na_{0.03}MnPO_4$ materials for 60 cycles. Initial charge capacities of $Li_{0.97}Na_{0.03}MnPO_4$ sintered at 600°C and 700°C are 100.3 $mAhg^{-1}$ and 105.4 $mAhg^{-1}$ which give irreversible capacities of 13.0 $mAhg^{-1}$ and 20.6 $mAhg^{-1}$ accordingly. $Li_{0.97}Na_{0.03}MnPO_4$

sintered at 600°C and 700°C deliver discharge capacities of 64.8 $mAhg^{-1}$ and 77.8 mAh g^{-1}at the 60th cycle which corresponds to capacity retention of 78.8 % and 89.8 %. The difference in the capacity retention maybe be arise from minor structural defect tend to form at sintering temperature of 600°C which could be solved at 700°C (Hua-jun Zhu et al., 2014a). This clearly describes that sintering temperature is one of the important factor in the synthesis process in order to form better structural properties hence leads to good electrochemical properties.

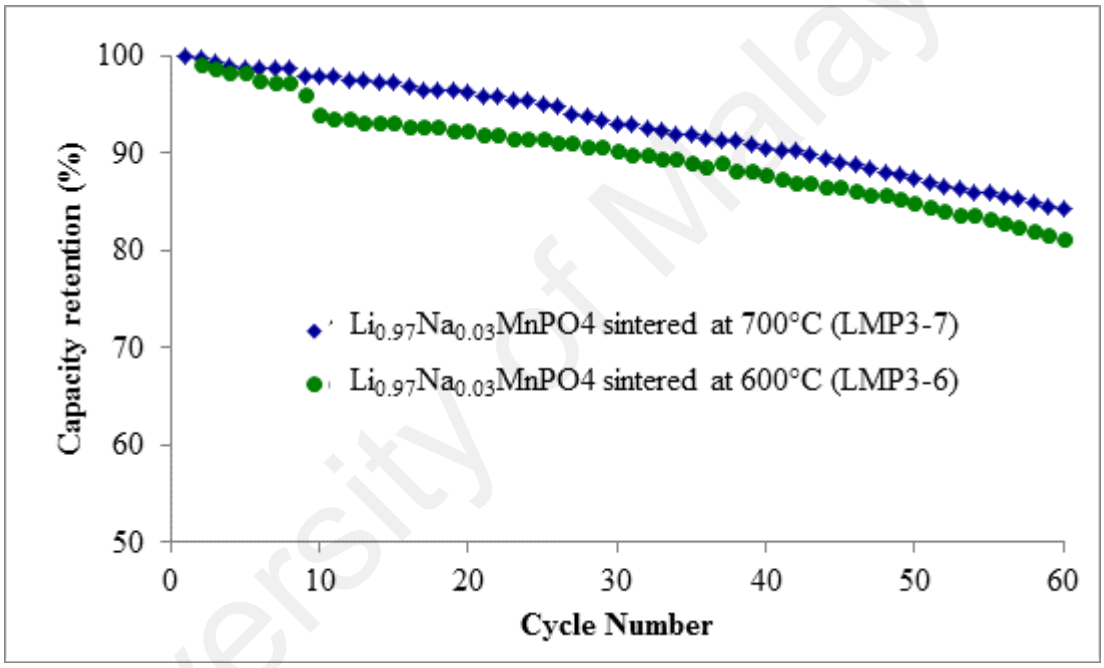

Figure 5.22: Capacity retention comparison of $Li_{0.97}Na_{0.03}MnPO4$ sintered at 600°C and 700°C

Impedance spectra of $Li_{0.97}Na_{0.03}MnPO_4$ which obtained at 600°C and 700 °C can be observed in Figure 5.23. The spectra show both samples has semicircle which demonstrates charge transfer resistance. This ascertains increased of electronic conductivity hence facilitates smooth lithium ion movement to active materials (Hu et al., 2016). The observed R_{ct} value for $Li_{0.97}Na_{0.03}MnPO_4$ (600°C) found to be 23 Ω and $Li_{0.97}Na_{0.03}MnPO_4$ (700°C) is about 19 Ω. This describes that partial Na substitution able to reduce charge transfer resistance (Zhaoyong Chen, Xie, Li, & Xu, 2014).

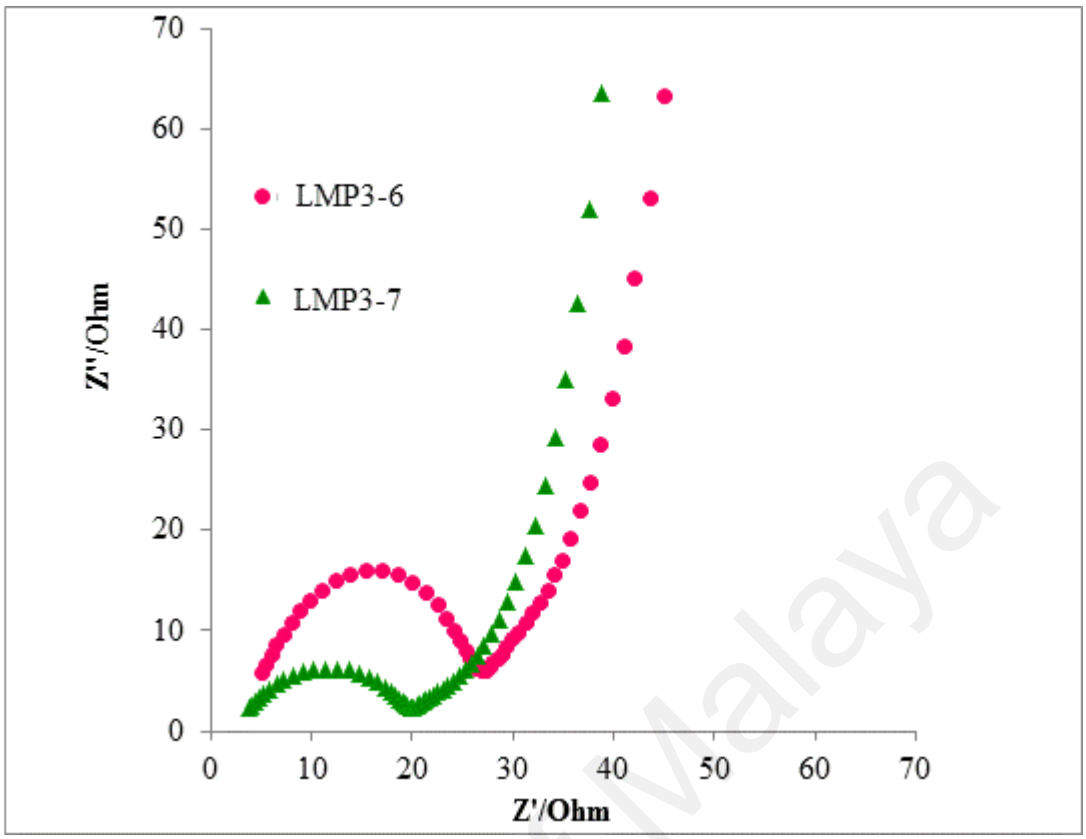

Figure 5.23: Impedance spectra of $Li_{0.97}Na_{0.03}MnPO_4$ 600°C and 700°C

5.4 Conclusion

This work demonstrated the effect of Na doping in $LiMnPO_4$. The different concentration of Na was substituted in $LiMnPO_4$ system via sol gel method. The XRD pattern confirmed that the well indexed crystalline structure. Addition of Na ions into the crystal structure expands the Li slab space. The maximum discharge capacity of 92.45 mAh g^{-1} was achieved in $Li_{0.97}Na_{0.03}MnPO_4$ than that of pristine $LiMnPO_4$ (86.26 mAh g^{-1}) with maximum cyclic stability of 84.15 % up to 60 cycles. Irreversible capacity loss was reduced by sodium addition of $Li_{0.97}Na_{0.03}MnPO_4$ than that of pristine $LiMnPO_4$. Therefore, these experimental results suggested that the superior electrochemical performance can be attained through optimizing adequate Na-doping in $LiMnPO_4$ towards lithium ion battery application.

CHAPTER 6: STRUCTURE AND ELECTROCHEMICAL PROPERTIES OF ZnO COATED $LiMnPO_4$ CATHODE MATERIALS

6.1 Introduction

This chapter will demonstrate the synthesis and characterization of ZnO coated $LiMnPO_4$ with varying amount of (1 wt.%, 2 wt.%, 3 wt.%) ZnO. The effects of different amount of zinc oxide as coating layer on structural and electrochemical properties are clearly explored.

6.2 Experimental details

6.2.1 *Materials*

Lithium acetate ($LiC_2H_3O_2$) and zinc acetate $Zn(CH_3COO)_2{\cdot}4H_2O$ were purchased from Aldrich. Manganese acetate $Mn(CH_3COO)_2{\cdot}4H_2O$ and ammonium dihydrogen phosphate $(NH_4)H_2PO_4$ were obtained from Friendmann Schmidt.

6.2.2 Synthesis of ZnO coated $LiMnPO_4$

(a) Preparation of $LiMnPO_4$

$LiMnPO_4$ was synthesized by sol gel method. Appropriate amount of 0.03 mole lithium acetate ($LiC_2H_3O_2$) and 0.03 mole manganese acetate $Mn(CH_3COO)_2{\cdot}4H_2O$ were dissolved in distilled water. Ammonium dihydrogen phosphate $(NH_4)H_2PO_4$ was added into the above solution followed by drops of nitric acid and oxalic acid. Then the solution was stirred and heated until achieve a solid product. Finally, it was sintered at 700 °C for 3 hours.

(b) Preparation of different wt.% of ZnO coated $LiMnPO_4$

ZnO precursor solution was prepared by dissolving zinc acetate in distilled water. As prepared $LiMnPO_4$ was added into the above ZnO precursor solution and continuously stirred at 70 °C. The heating was continued until the reaction completed, resulting in the form of dry powder. Finally the coated samples were calcinated at 700 °C for 3 hours. The amount of zinc oxide in the solution was fixed at mass ratios of ZnO: $LiMnPO_4$ = 1 wt. %, 2 wt. % and 3 wt. % respectively.

6.2.3 Structural and electrochemical characterizations

The structural crystallinity of pristine $LiMnPO_4$ and ZnO coated $LiMnPO_4$ were characterized by X-ray diffraction analysis (XRD) using Siemens D 5000 diffractometer. The surface morphology and surface purity were examined via field emission scanning electron microscopy (FESEM, Microscope model JSM 7600-F), transmission electron microscopy (TEM, Leo Libra 120) and energy dispersive spectroscopy (EDS) mapping (FEG Quanta 450, EDX-OXFORD).

The obtained $LiMnPO_4$ was then mixed with carbon to form $LiMnPO_4$/C prior to fabrication. The cathode was prepared using $LiMnPO_4$/C and TAB (72:28) in ethanol to form the paste. Then it was cast on the stainless steel mesh and dried at 120 °C for 12 hours. Electrochemical properties of the active materials were tested by coin cells using lithium metal as an anode. 1 M $LiPF_6$ dissolved in a mixture of ethylene carbonate (EC)/ dimethyl carbonate (DMC) (1:1 in volume) was used as an electrolyte. The galvanostatic charge/discharge performances were tested in the voltage range of 2.5 – 4.5 V on a Neware battery system. Electrochemical impedance spectroscopy (EIS) tests were recorded.

6.3 Results and discussion

6.3.1 X-Ray Diffraction (XRD)

The X-Ray diffraction (XRD) patterns in Figure 6.1 displaying structural properties of pristine and 1.0 wt.%, 2.0 wt.%, 3.0 wt.% ZnO coated $LiMnPO_4$. The results revealed that the all diffraction peaks in pristine $LiMnPO_4$ and zinc oxide coated $LiMnPO_4$ were corresponding to the olivine crystallize in the orthorhombic structure with space group of Pnmb which was well matched with JCPDS No. 74-0375 (Zhang et al., 2015; Zheng et al., 2015). No additional peaks present for ZnO phase which confirms the coating only covers the outer layer and doesn't diffuse into the $LiMnPO_4$.

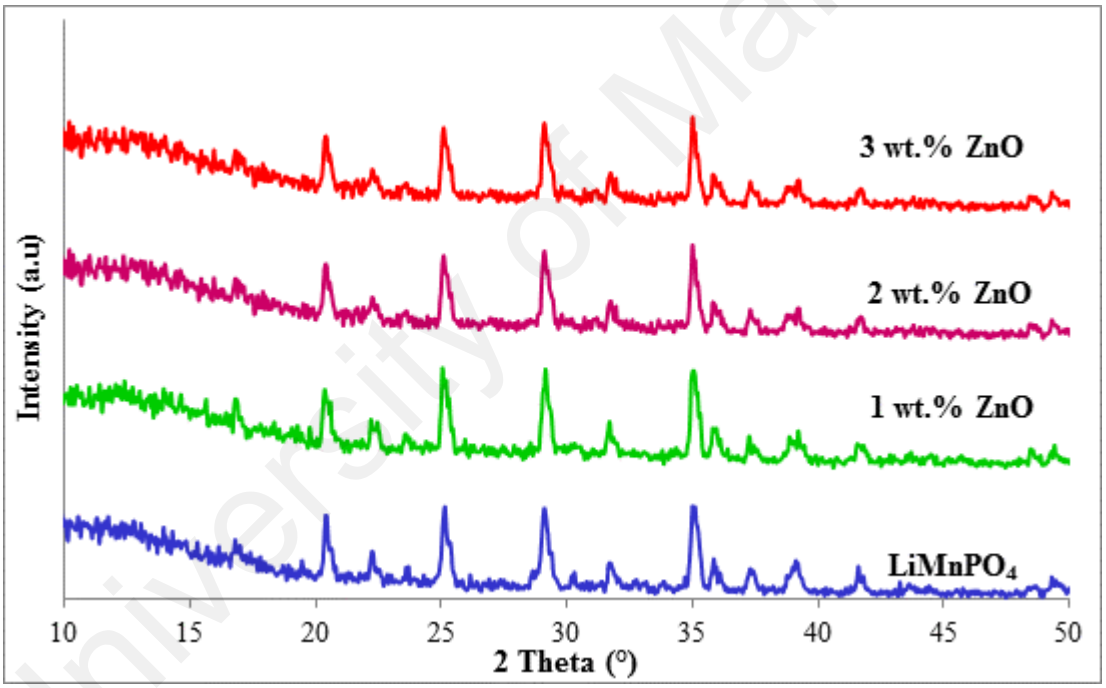

Figure 6.1: XRD of ZnO coated $LiMnPO_4$

The values of hkl, 2θ, full width half maximum and d spacing obtained from XRD results are listed in Table 6.1.

Table 6.1: 2θ, FWHM and d spacing of ZnO coated $LiMnPO_4$

1.0 wt.% ZnO coated $LiMnPO_4$

hkl	2θ (°)	FWHM (°)	d-spacing (Å)
(011)	20.405	4.34881	0.258
(111/021)	25.058	3.55083	0.226
(121/200)	29.141	3.06191	0.348
(131)	35.042	2.55866	0.324
(221)	39.209	2.29582	0.361
(222)	51.705	1.76651	0.411
(023/260)	61.134	1.51472	0.619

2.0 wt.% ZnO coated $LiMnPO_4$

hkl	2θ (°)	FWHM (°)	d-spacing (Å)
(011)	20.563	4.34958	0.277
(111/021)	25.284	3.54362	0.248
(121/200)	29.305	3.06536	0.348
(131)	35.145	2.55907	0.344
(221)	37.4	2.29609	0.262
(222)	51.833	1.76211	0.456
(023/260)	61.289	1.51125	0.668

3.0 wt.% ZnO coated $LiMnPO_4$

hkl	2θ (°)	FWHM (°)	d-spacing (Å)
(011)	20.402	4.31587	0.227
(111/021)	25.11	3.51966	0.308
(121/200)	29.108	3.04515	0.317
(131)	35.036	2.55144	0.313
(221)	39.204	2.40259	0.357
(222)	51.844	1.76246	0.377
(023/260)	61.085	1.51581	0.669

In order to calculate crystallite size and strain values of the ZnO coated samples, Williamson Hall (W-H) method has been approached. The plots from the W-H method have been analyzed as in Figure 6.2.

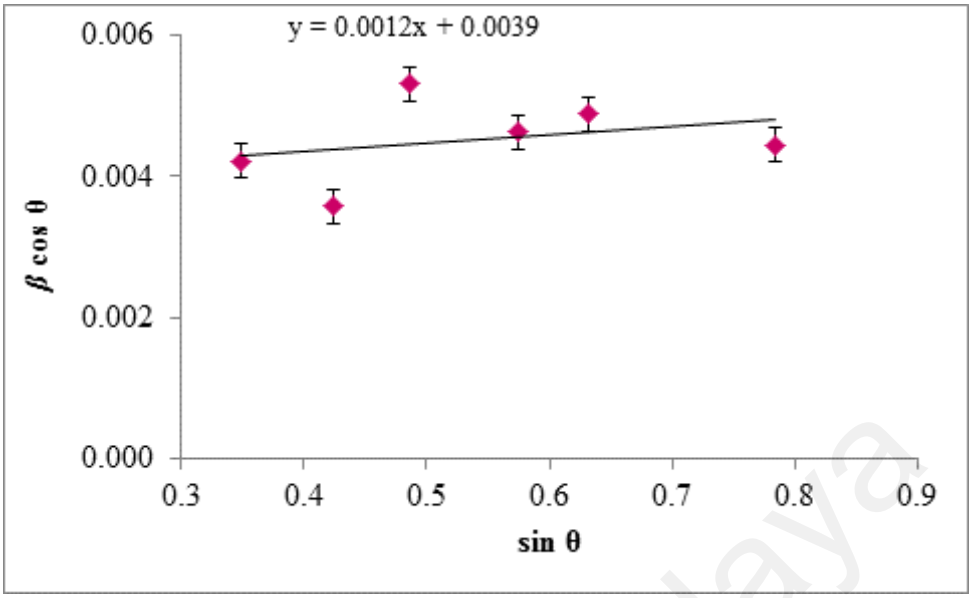

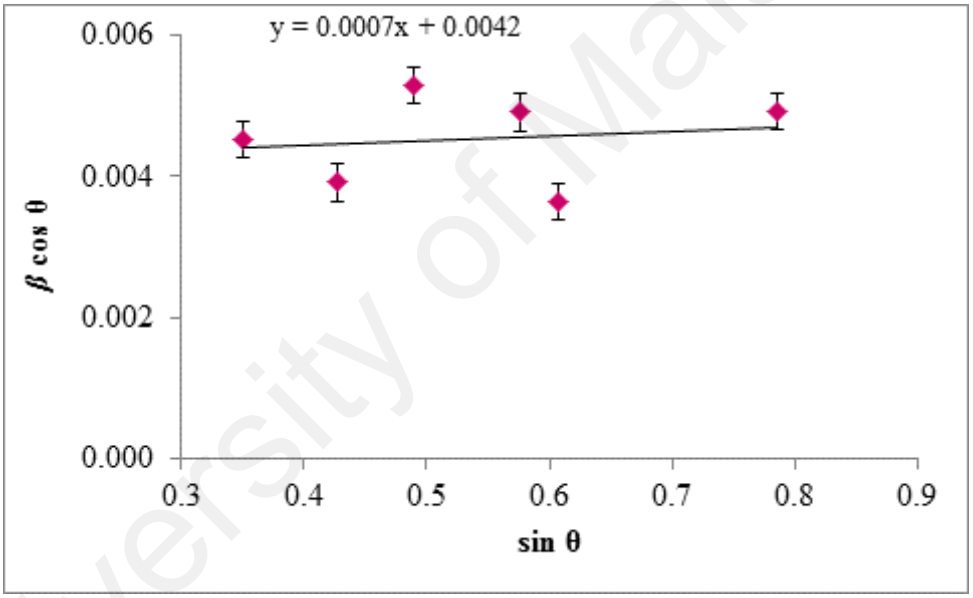

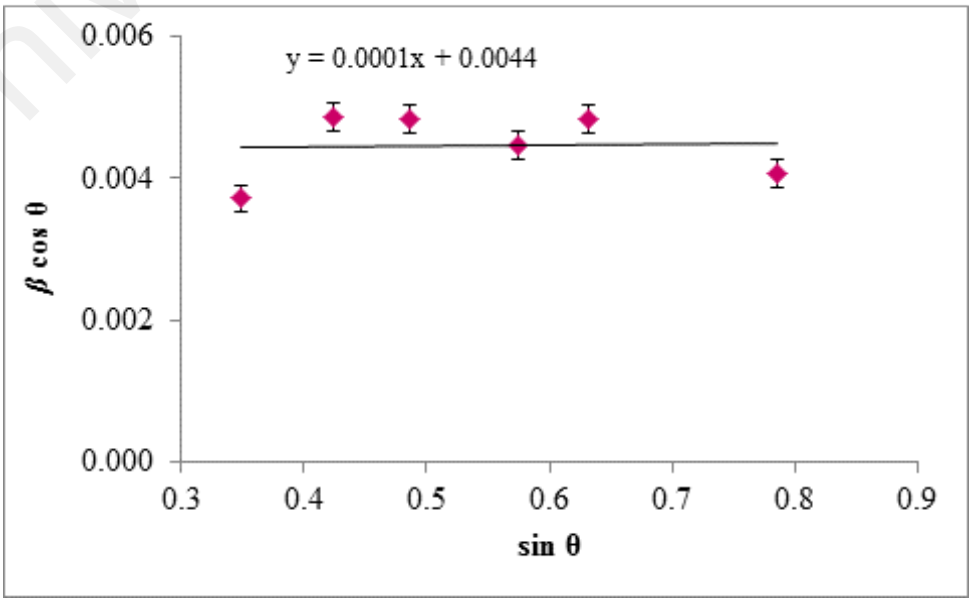

Figure 6.2: Williamson-hall plots of $LiMnPO_4$

Table 6.2 summarizes data from W-H plots. Crystallite size of the ZnO coated cathode materials ranging from 35.5 nm to 31.5 nm which corresponds to 1 wt.% to 3 wt.% coating amount. Whereas strain of the samples are 3.00×10^{-4}, 1.75×10^{-4} and 2.50×10^{-5} for 1 wt.%, 2 wt.% and 3 wt.% ZnO coated $LiMnPO_4$ respectively. ZnO coating was found to reduce crystallite size and strain of the particles compared to pristine $LiMnPO_4$ with crystallite size of 45.0 nm and strain of 7.74×10^{-4}.

Table 6.2: Mean crystallite size and strain values of ZnO coated sample

Sample	Intercept	Slope	Crystallite size (nm)	Strain
1 wt.% ZnO	0.0039	0.0012	35.5	3.00×10^{-4}
2 wt.% ZnO	0.0042	0.0007	33.0	1.75×10^{-4}
3 wt.% ZnO	0.0044	0.0001	31.5	2.50×10^{-5}

6.3.2 Field Emission Scanning Electron Microscopy (FESEM)

The surface morphologies of both pristine $LiMnPO_4$ and zinc oxide coated samples were examined using field emission scanning electron microscope (FESEM), which is presented in Figure 6.3, Figure 6.4 and Figure 6.5. Well crystallized particles are clearly observed for both uncoated and coated samples and the morphology does not face any changes after the coating process. The FESEM images exhibited that the densely packed arrangement of particles in ZnO based $LiMnPO_4$. Even though ZnO is successfully coated on $LiMnPO_4$ but the coating layer on particles is not visible in the images implying that the coating is very thin. To verify ZnO coating EDAX analysis were performed for all coated samples.

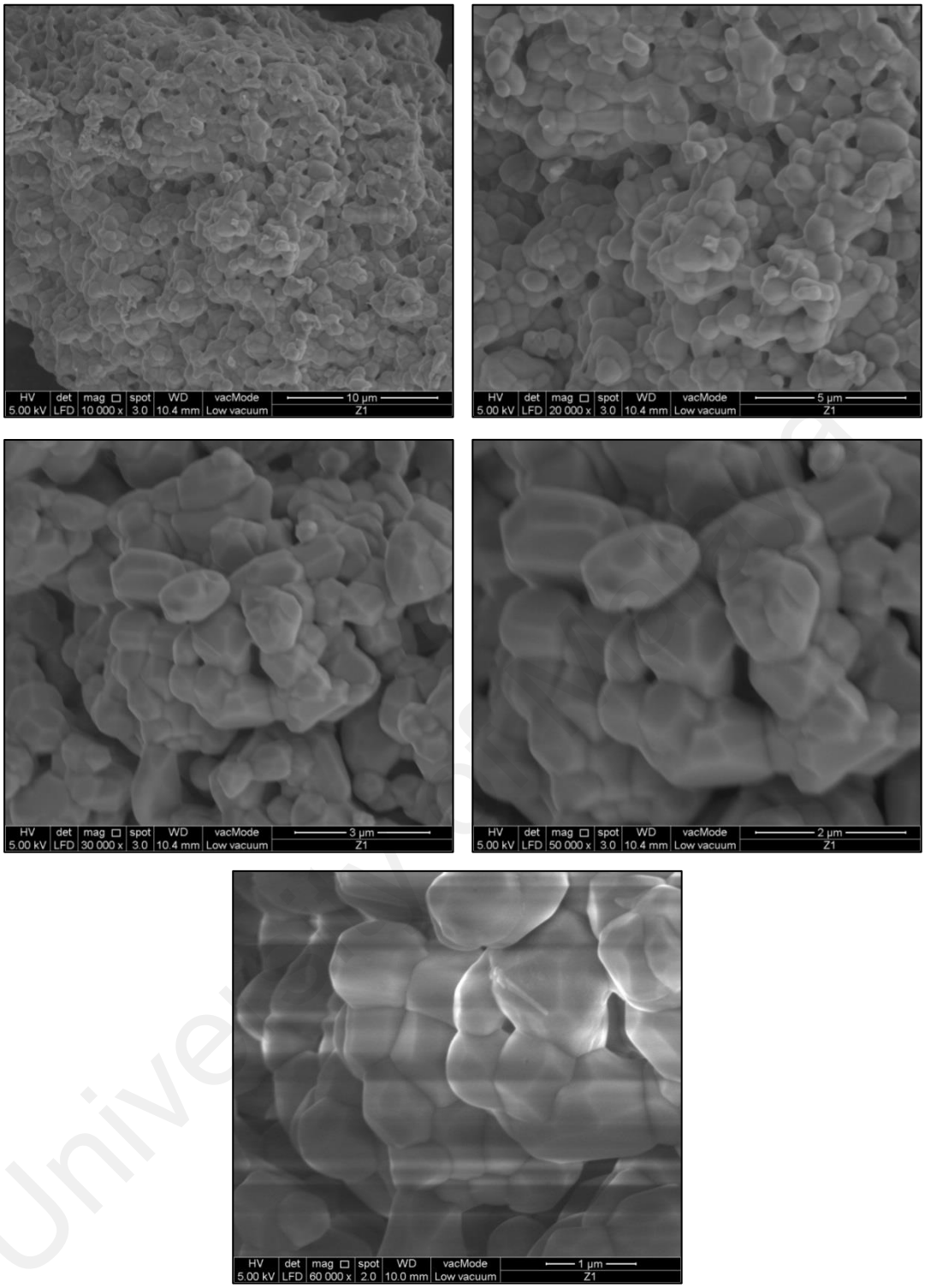

Figure 6.3: FESEM images of 1 wt.% ZnO coated $LiMnPO_4$ at different magnifications

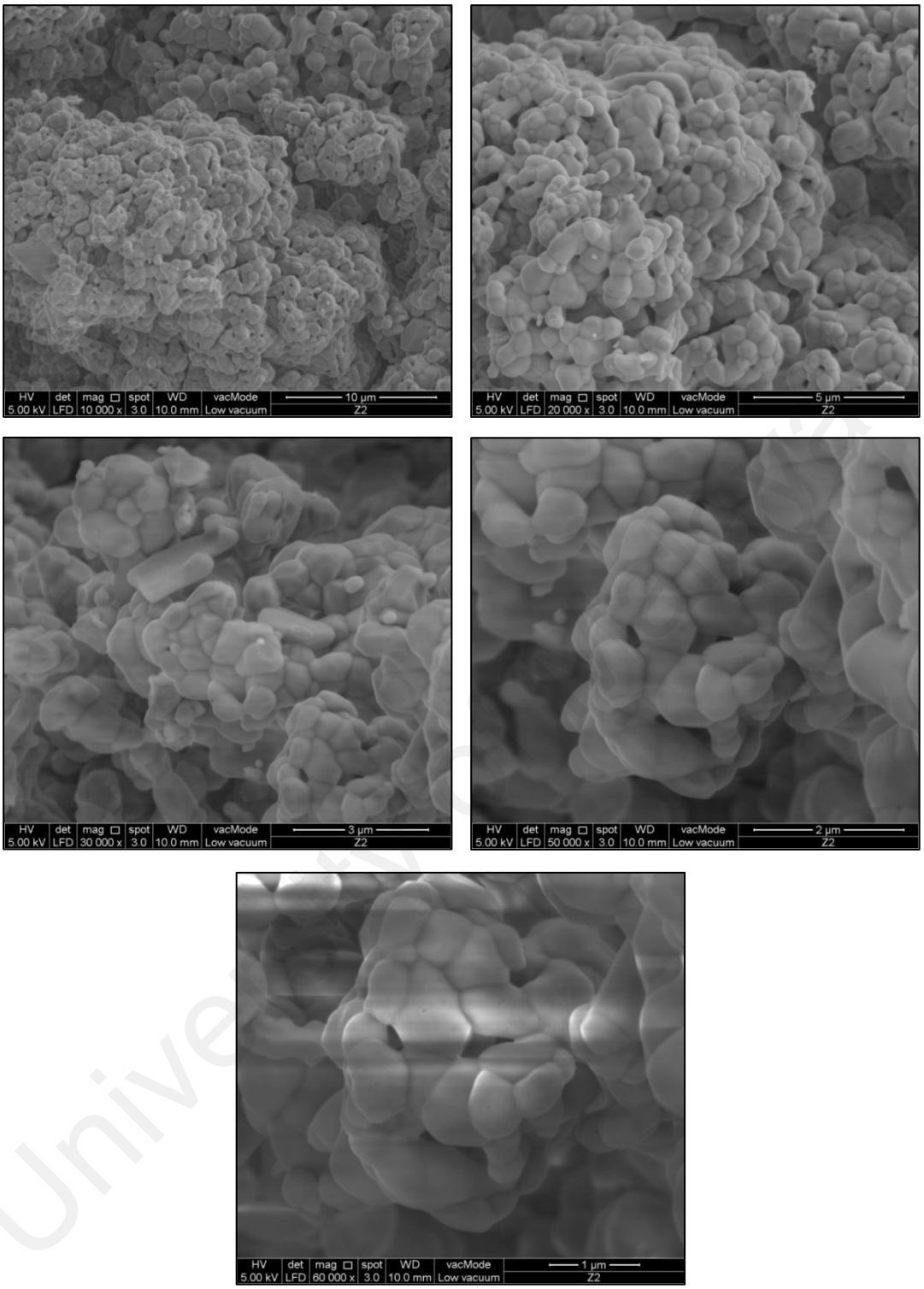

Figure 6.4: FESEM images of 2 wt.% ZnO coated $LiMnPO_4$ at different magnifications

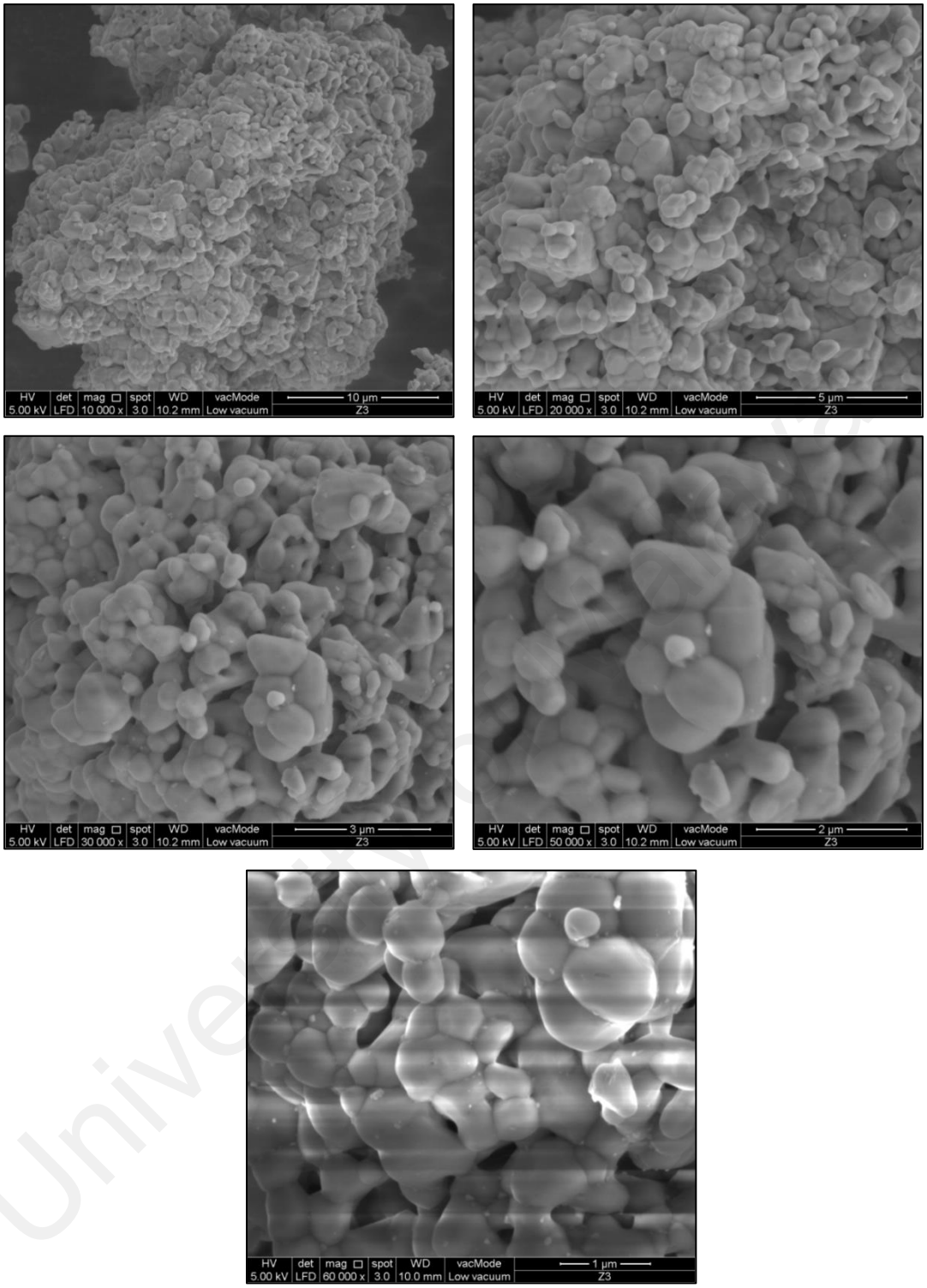

Figure 6.5: FESEM images of 3 wt.% ZnO coated $LiMnPO_4$ at different magnifications

For each coated sample, EDAX analysis was performed at 5 different spots to verify ZnO coating. Figure 6.6 displays selected spots of the 1wt. % ZnO coated $LiMnPO_4$.

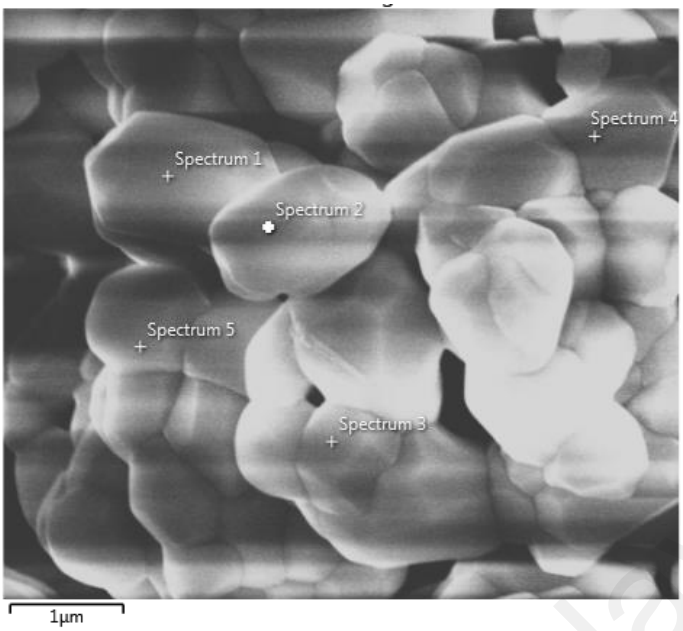

Figure 6.6: Selected spots of 1wt. % ZnO coated $LiMnPO_4$ for EDAX analysis

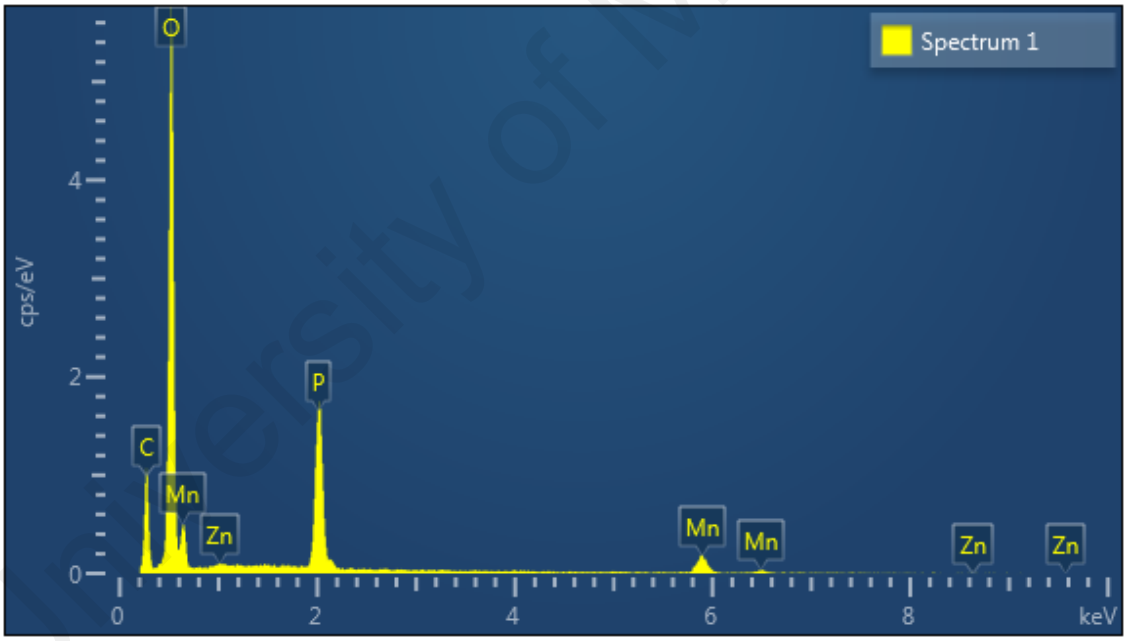

Figure 6.7: EDAX spectra of 1wt. % ZnO coated $LiMnPO_4$

As in Figure 6.7, one of the selected surface spots in 1 wt. % ZnO coated $LiMnPO_4$ sample reveal the presence of ZnO layer. Small Zn peaks in EDAX spectra clearly relates to thin layer of ZnO coating on $LiMnPO_4$.

Figure 6.8 shows surface spots of 2 wt. % ZnO coated $LiMnPO_4$ that chosen for EDAX analysis. Five different areas were selected to justify ZnO layer on $LiMnPO_4$. EDAX spectrum of one of the spots is presented as following.

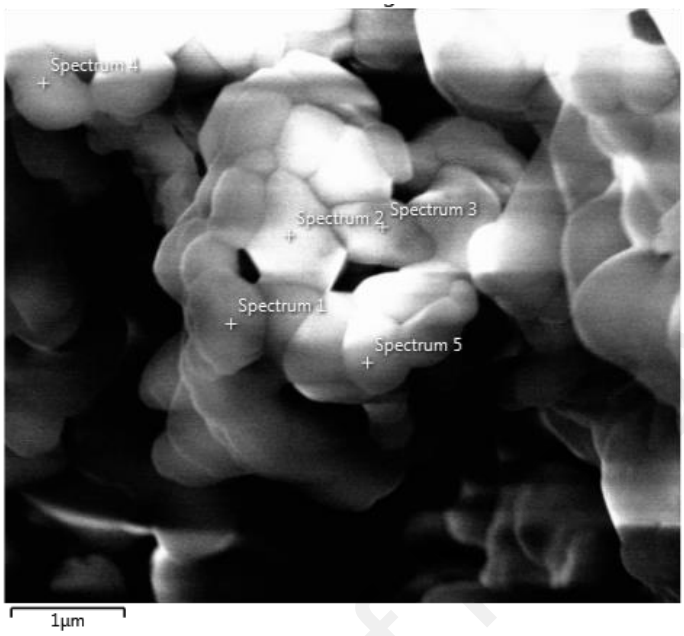

Figure 6.8: Selected spots of 2wt. % ZnO coated $LiMnPO_4$ for EDAX analysis

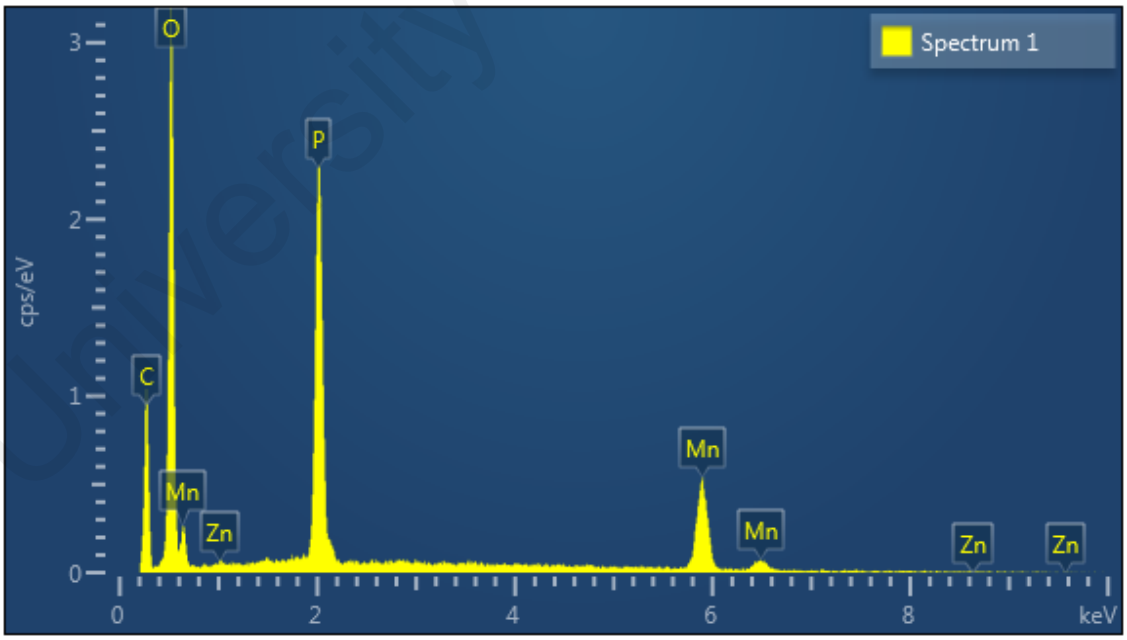

Figure 6.9: EDAX spectra for selected spots of 2wt. % ZnO coated $LiMnPO_4$

little amount of Zn. Figure 6.10 depicts the spots of 3 wt. % ZnO coated $LiMnPO_4$ that examined for EDAX analysis.

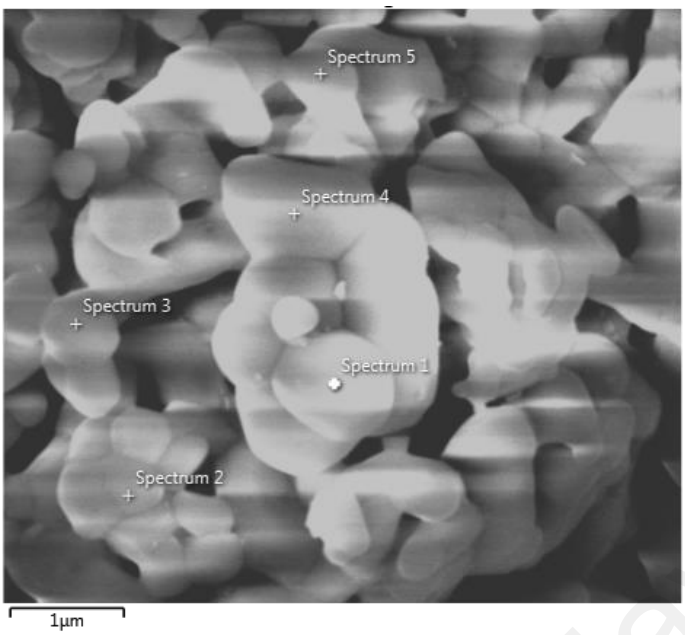

Figure 6.10: Selected spots of 3wt. % ZnO coated $LiMnPO_4$ for EDAX analysis

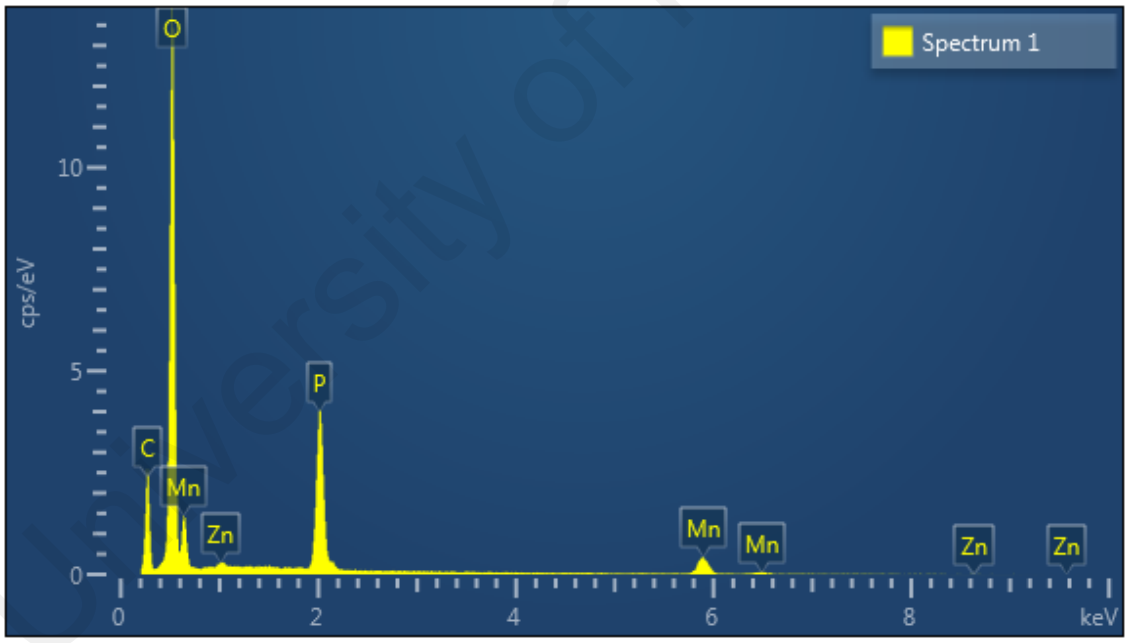

Figure 6.11: EDAX spectra for selected spots of 2wt. % ZnO coated $LiMnPO_4$

Figure 6.11 also confirms that presence of ZnO layer on $LiMnPO_4$ when the coating amount increased to 3 weight percent. From all the EDAX analysis of $LiMnPO_4$, it can be observed that peaks corresponding to Zn are very light compared to other components such as O (oxygen), Mn (manganese), P (phosporus) and C (carbon). These would be strong evidence to prove that presence of ZnO layer on $LiMnPO_4$ is very thin

when weight percentage of coating amount is at 1wt. %, 2wt. % and 3wt. % (Singhal, Tomar, Burgos, & Katiyar, 2008; Jiangtao Zhu, Tang, Tang, & Ma, 2015).

6.3.3 Transmission Electron microscopy (TEM)

Figure 6.12 portrays TEM images of $LiMnPO_4$ and 1 wt. %, 2 wt. %, 3 wt. % ZnO coated $LiMnPO_4$. The images apparently show dark particle as in (a) which denotes $LiMnPO_4$ and images (b), (c) and (d) surrounded by grey line corresponds to ZnO coating.

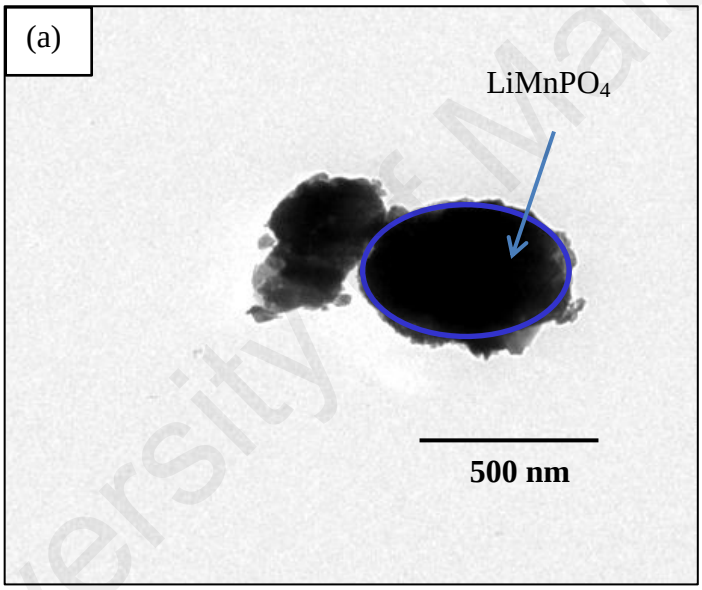

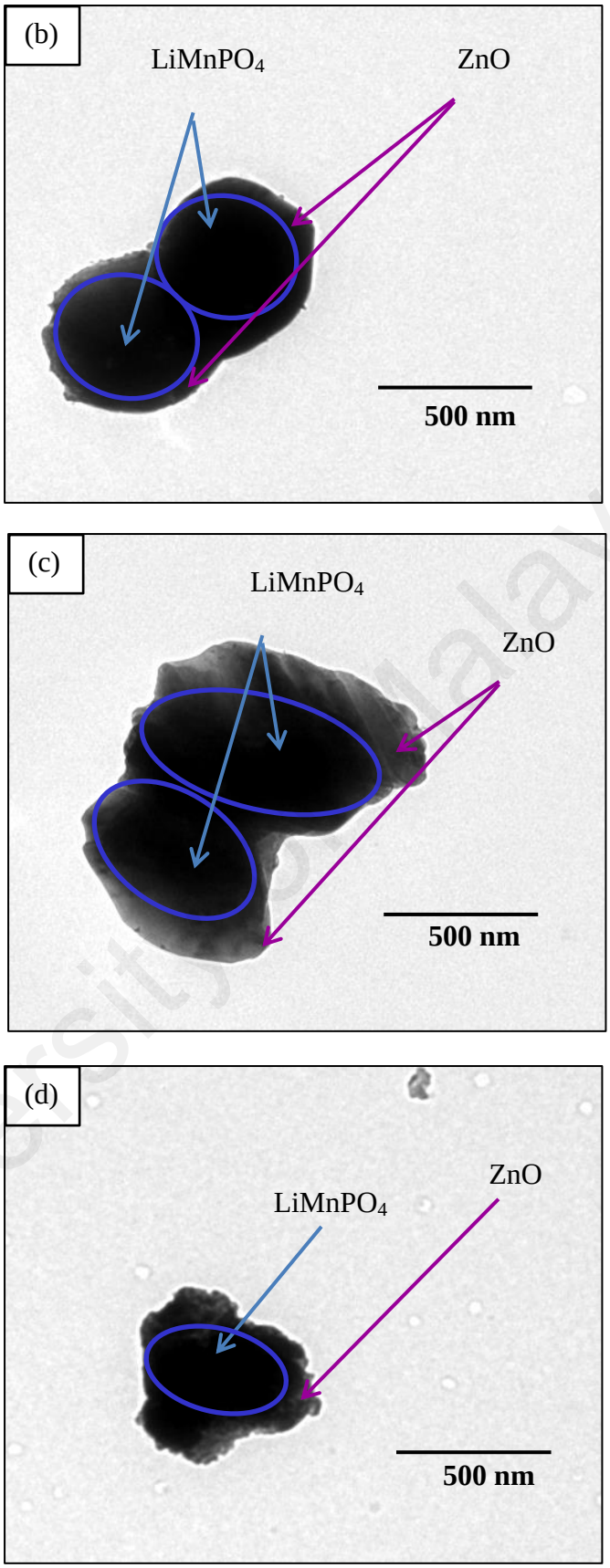

Figure 6.12: TEM images of (a) $LiMnPO_4$ (b) 1 wt. % ZnO coated $LiMnPO_4$ (c) 2 wt. % ZnO coated $LiMnPO_4$ (d) 3 wt. % ZnO coated $LiMnPO_4$

6.3.4 Raman Spectroscopy

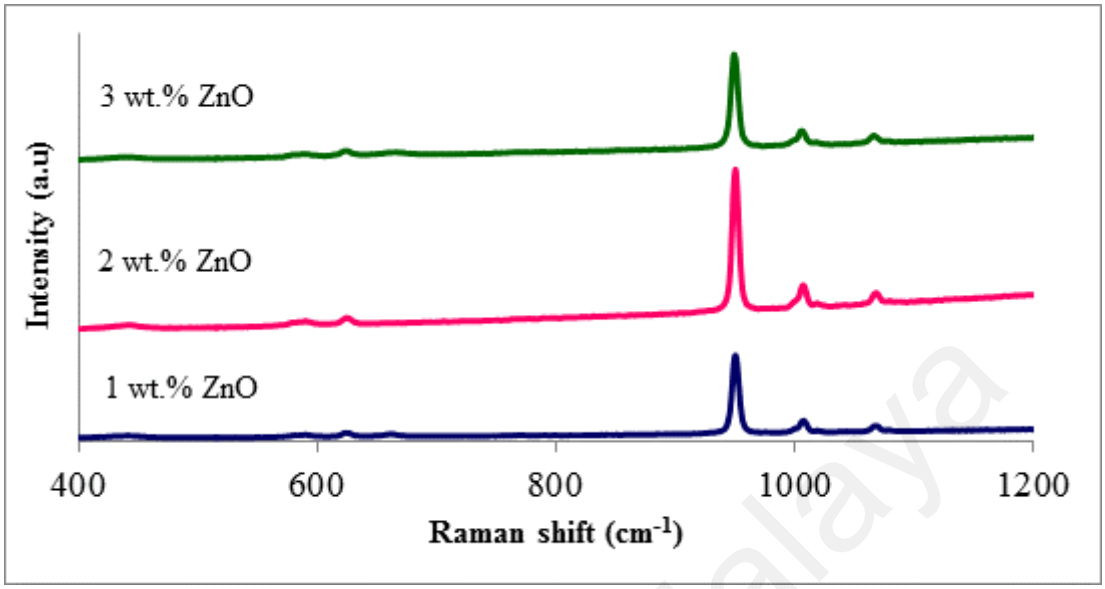

Figure 6.13: Raman spectra of ZnO coated $LiMnPO_4$

Figure 6.13 depicts Raman spectra of ZnO coated $LiMnPO_4$ with different coating amount. Raman active modes as in pristine sample have been identified in ZnO coated samples. All the spectra dominated by strong peak at 950 cm^{-1} which corresponds to Ag symmetric P-O stretching vibration of v_1. While peaks at 1005 cm^{-1} and 1070 cm^{-1} attributed to the asymmetric stretching vibration of PO_4 anion (v_3). v_4 vibrations can be noticed at 590 cm^{-1}, 627 cm^{-1} and 661 cm^{-1} while v_2 vibration can be observed at 438 cm^{-1} (Markevich et al., 2011; Michalska et al., 2015). There is no distinct structure transformation of $LiMnPO_4$ after the ZnO coating within 3 wt.% coating amount.

6.3.5 Electrochemical analysis

Figure 6.14 compares first charge and discharge curves of pristine and ZnO coated samples at cut off voltages of 2.5 V and 4.5 V. The initial charge and discharge capacities of pristine $LiMnPO_4$, 1 wt.% ZnO, 2 wt.% ZnO and 3 wt.% ZnO coated

$LiMnPO_4$ samples are 103.5 $mAhg^{-1}$, 86.2 $mAhg^{-1}$; 106.1 $mAhg^{-1}$, 96.3 $mAhg^{-1}$; 105.4 $mAhg^{-1}$, 102.2 $mAhg^{-1}$; 113.9 $mAhg^{-1}$, 90.1 $mAhg^{-1}$ respectively.

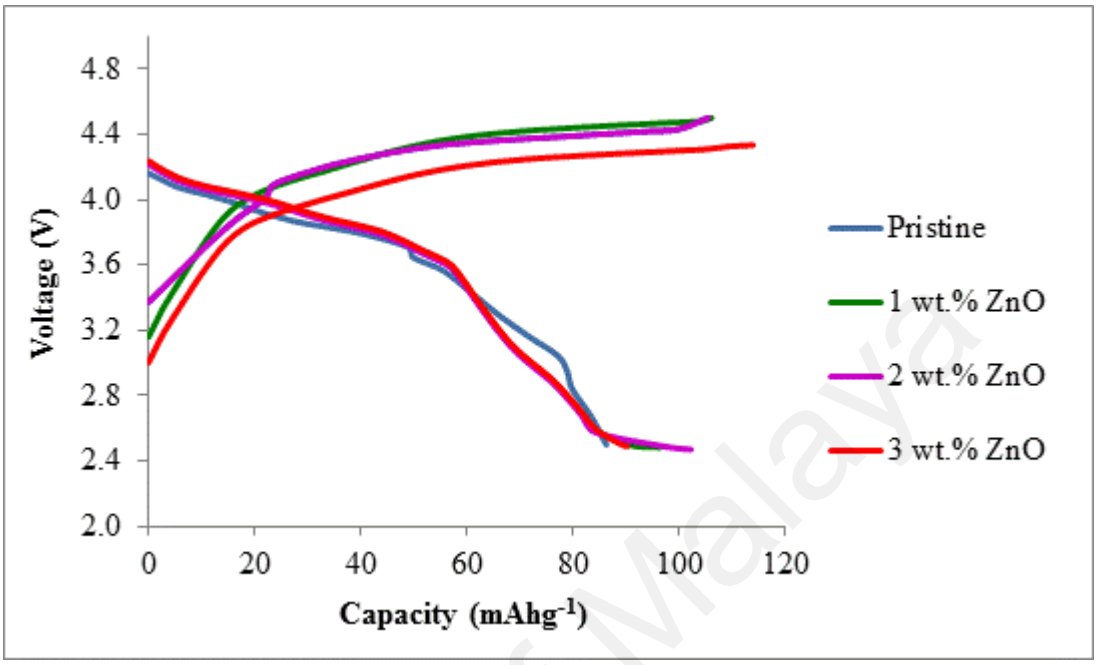

Figure 6.14: Initial charge discharge curves of ZnO coated $LiMnPO_4$

From these results, initial electrochemical activity can be deduced as in Figure 6.15. Data confirmed that the smaller irreversible capacity loss (3.2 $mAhg^{-1}$) was observed in 2 wt.% ZnO coated $LiMnPO_4$, while the largest irreversible capacity loss (23.7 $mAhg^{-1}$) appeared in 3 wt.% ZnO coated $LiMnPO_4$ respectively. The observed initial couloumbic efficiency ranges for pristine $LiMnPO_4$, 1 wt.%**,** 2 wt.% and 3 wt.% ZnO coated $LiMnPO_4$ corresponds to 83.3 %, 90.8 %, 96.9 % and 79.1 % respectively. The maximum couloumbic efficiency (96.9 %) was observed in 2 wt.% ZnO coated $LiMnPO_4$ than that of other samples. It implies that coating layer controls the structural degradation at higher voltage and maintains crystal structure with less defects (Ilango, Subburaj, Prasanna, Jo, & Lee, 2015; Shang, Lin, Lu, Huang, & Yu, 2015). This also explained the presence of ZnO coating, which leads to avoid direct reaction between active materials and electrolyte protects manganese from dissolve into the electrolyte,

resulting to prevent Mn dissolution. Hence minimizes the electrolyte oxidation (Yanping Chen, Zhang, Chen, Wang, & Lu, 2014; Lu et al., 2014).

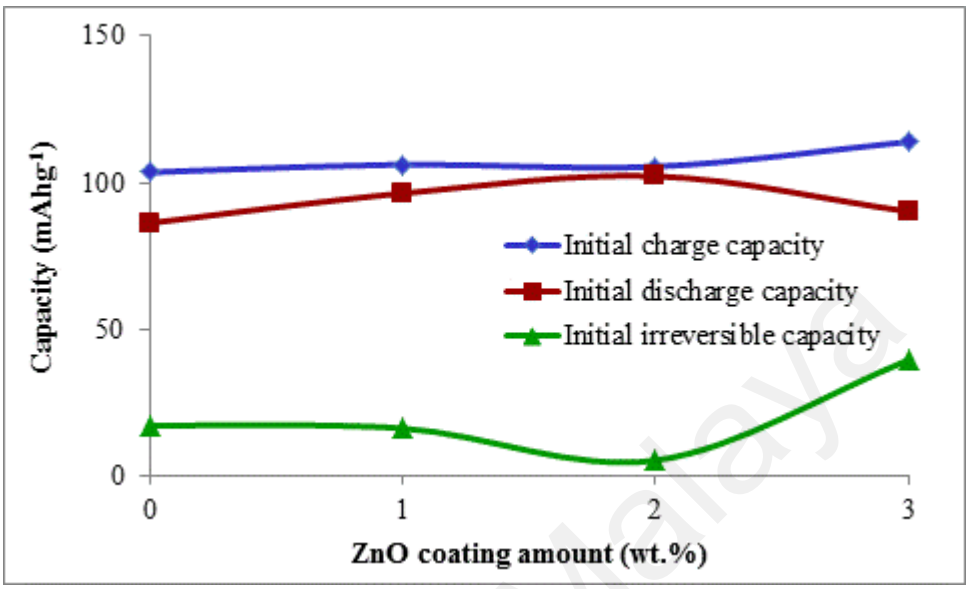

Figure 6.15: Initial electrochemical profiles of ZnO coated $LiMnPO_4$

Figure 6.16 describes the discharge capacities of pristine and zinc oxide coated samples in the voltage range of 2.5 – 4.5 V. 2 wt.% ZnO coated $LiMnPO_4$ exhibits better discharge capacity performance up to 100 cycles followed by 1 wt.% and 3 wt.% ZnO coated samples. Pristine sample exhibits initial performance was almost same as coated samples. But it is declining with increasing number of cycles due to lack of stability. 3 wt.% ZnO coated sample was less effective than other coated samples, which may be due to the excess amount of ZnO and particle aggregations, resulting in the reduction of electronic conductivity (Ting Liu, Zhao, Wang, & Nan, 2012). The concentration of coating also played an important role in order to achieve the desired electrochemical improvement (Zhiyuan Wang, Enzuo Li, Chunnian He, Chunsheng Shi, Jiajun Li, 2008).

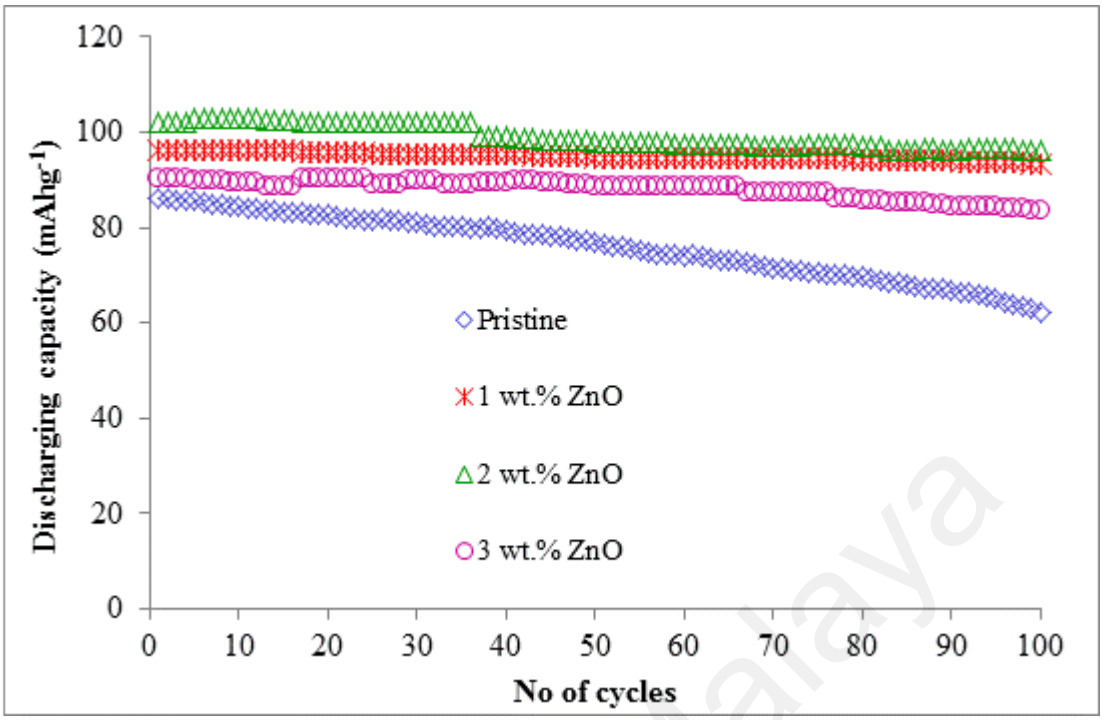

Figure 6.16: Discharge capacities of ZnO coated $LiMnPO_4$

Figure 6.17 relates the capacity retention with the coating amount. At a glance, it can be noticed that pristine sample exhibits lowest capacity retention among other samples at 50th and 100th cycles. Discharge capacity of bare $LiMnPO_4$ becomes 76.8 $mAhg^{-1}$ which only retains about 85.5 %. 1 wt.% ZnO coated $LiMnPO_4$ exhibited capacity retention of 89.8 % at 50th cycle. Moreover, discharge capacities of 2 wt.% and 3 wt.% ZnO coated samples were found to be 97.98 $mAhg^{-1}$ and 88.87 $mAhg^{-1}$ with cyclic retention of 95.8 % and 98.5 % at 50th cycle respectively. While testing the cyclic retention at 100th cycle, the discharge capacity becomes 62.1 $mAhg^{-1}$, 93.1 $mAhg^{-1}$, 96.3 $mAhg^{-1}$ and 78.8 $mAhg^{-1}$ for pristine $LiMnPO_4$, 1 wt.% ZnO**,** 2 wt.% ZnO and 3 wt.% ZnO coated $LiMnPO_4$ samples respectively. Sahan et al (Şahan, Göktepe, Patat, & Ülgen, 2010) reported that hydrogen fluoride (HF) produced during cycling test, while $LiPF_6$ used as a electrolyte, resulting to the Mn dissolution. Herein, HF is produced by reaction of traces of water molecules which commonly found in commercial electrolyte with $LiPF_6$ salt (Cho et al., 2015; Y. Cui & Xu, 2015). This leads to damage of the

active materials during electrochemical cycling process due to continuous production of HF, suggesting the loss of capacitive nature (Cui & Xu, 2015; Liu, Huang, & Yu, 2015). However, this issue can be overcome by introducing the ZnO as a protective layer for $LiMnPO_4$ to restrict unavoidable reactions with electrolyte during cycling process.

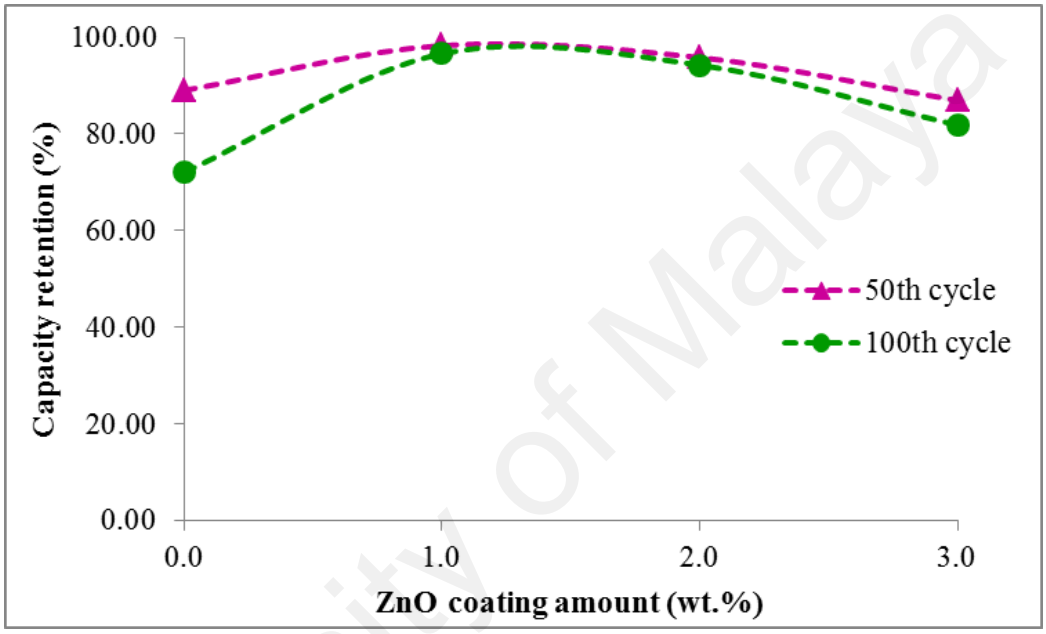

Figure 6.7: Capacity retention of pristine and coated $LiMnPO_4$

To further understand the effect of ZnO coating on $LiMnPO_4$, electrochemical impedance spectroscopy (EIS) was employed. Figure 6.18 portrays the Nyquist plots for ZnO coated $LiMnPO_4$ composed of semicircles. Charge transfer resistance (R_{ct}) value of 2 wt.% ZnO coated sample lowest value of 18 Ω and R_{ct} value reached to 28 Ω for 1 wt.% ZnO coated sample. Highest R_{ct} value of 43 Ω was recorded for 3 wt.% ZnO coated sample.

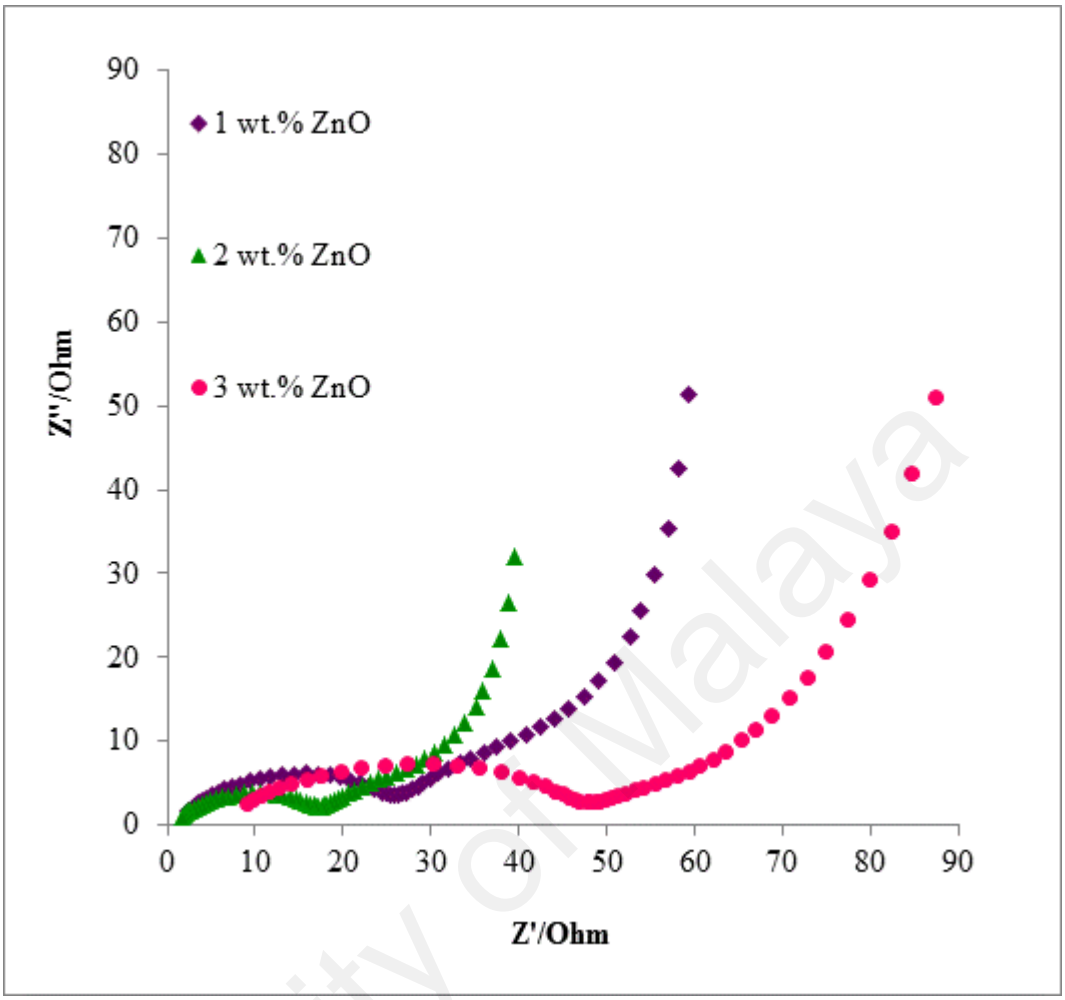

Figure 6.8: EIS spectra of ZnO coated $LiMnPO_4$

. This strongly proves that ZnO coating reduced R_{ct} of pristine sample from 57 Ω in earlier chapter which emphasizing thin ZnO layer on $LiMnPO_4$ increases electronic conductivity at surface. Hence, this encourages easy lithium ions tranfer into active materials thus improved charge discharge process (Amaresh et al., 2013; Kong et al., 2016; Jiangang Li, Wang, Zhang, & He, 2009; Zhao, Liu, Hu, Sun, & Xiao, 2015). On the other side, 3 wt.% ZnO coated sample exhibits high R_{ct} value caused by additional polarization might be accountable for its poor electrochemical activity (Amaresh et al., 2013).

6.4 Conclusion

Thin ZnO layer has been applied on the outer layer of $LiMnPO_4$. Presence of ZnO coating on $LiMnPO_4$ clearly shows the improvement towards the electrochemical performance. High initial discharge capacity recorded for ZnO coated $LiMnPO_4$ compared to pristine $LiMnPO_4$. In this work, 2 wt.% ZnO coated $LiMnPO_4$ found to be exhibits high discharge capacity with improved capacity retention than that of other samples. Therefore, these results confirmed that the ZnO coated $LiMnPO_4$ plays a significant role in lithium ion battery application.

CHAPTER 7: ELECTROCHEMICAL PERFORMANCE OF Al, Cu DOPED $LiMnPO_4$ CATHODE MATERIALS

7.1 Introduction

This chapter is focused on Al, Cu dual doping in $LiMnPO_4$ via structural and electrochemical characterizations. Al, Cu substituted $LiMnPO_4$ were prepared using two different ratios in small amount. Results from this chapter will give insightful implications for dual substituted $LiMnPO_4$ cathode materials.

7.2 Experimental details

7.2.1 Materials

Lithium acetate ($LiC_2H_3O_2$) and aluminium acetate ($C_4H_7AlO_5$) were purchased from Aldrich. Manganese acetate $Mn(CH_3COO)_2{\cdot}4H_2O$, copper acetate $Cu(CH_3COO)_2{\cdot}4H_2O$ and ammonium dihydrogen phosphate $(NH_4)H_2PO_4$ were obtained from Friendmann Schmidt.

7.2.2 Synthesis of $LiMn_{1-x}Al_{0.5x}Cu_{0.5x}PO_4$ (x = 0.1, 0.2) materials

Pristine $LiMnPO_4$ and $LiMn_{1-x}Al_{0.5x}Cu_{0.5x}PO_4$ (x = 0.1, 0.2) were obtained via sol gel method. 1.0 mole lithium acetate ($LiC_2H_3O_2$), 1.0 mole manganese acetate $Mn(CH_3COO)_2{\cdot}4H_2O$ and aimed amount of aluminium acetate and copper acetate (0.1 mole and 0.05 mole) were dissolved in distilled water. 1.0 mole Ammonium dihydrogen phosphate $(NH_4)H_2PO_4$ was added into the above mixture followed by drops of 1 M nitric acid. Then the solution was stirred and heated until attain the final product. Further, the obtained samples were heated at the temperature of 700 °C for 3 hours to get desired crystalline samples.

7.2.3 Structural and electrochemical characterizations

The crystalline structures and morphologies of the samples were characterized by X-ray diffraction (XRD, Siemens D 5000 diffractometer), scanning electron microscope (SEM, Quanta FEG 450), transmission electron microscope (TEM, Leo Libra 120) and Raman spectra (In-via Raman Microscope). The doping concentration and materials purities were analysed by Energy Dispersive Spectroscopy (EDS, FEG Quanta 450, EDX-OXFORD).

The obtained pristine $LiMnPO_4$, $LiMn_{0.9}Al_{0.05}Cu_{0.05}PO_4$ and $LiMn_{0.8}Al_{0.1}Cu_{0.1}PO_4$ were mixed with carbon to form $LiMnPO_4$/C before the fabrication initiated. The cathode was prepared by mixing of 28 mg active material and 4 mg conductive binder (Teflonized acetylene black) in ethanol medium. Then it was pressed on stainless steel mesh and dried at 120°C for 12 hours. Lithium metal, 1 M $LiPF_6$ in a mixture of ethylene carbonate (EC)/ dimethyl carbonate (DMC) (1:1 in volume) and microporous polypropylene were used as anode, electrolyte and separator respectively. The electrochemical activity was evaluated by charge discharge cycles using Neware battery system in the voltage range of 2.5 V–4.5 V. Electrochemical impedance spectra were recorded.

7.3 Results and discussion

7.3.1 X-Ray Diffraction (XRD)

XRD analysis was done to examine structural changes of the Al, Cu doped ($LiMn_{0.9}Al_{0.05}Cu_{0.05}PO_4$ and $LiMn_{0.8}Al_{0.1}Cu_{0.1}PO_4$) samples. XRD patterns in Figure 7.1 displays bare and binary doped materials of $LiMnPO_4$ are well crystallized in olivine structures, which are indexed by orthorhombic with Pnmb space group. Al, Cu doped

$LiMnPO_4$ reflect similar pattern of pristine $LiMnPO_4$ as all fundamental diffraction peaks (020), (111/021), (200/121), (131), (221), (222) and (341) demonstrate consistency with standard data (JCPDS No. 74-0375). Doped Al and Cu are not altering the crystal structure of $LiMnPO_4$. Characteristic peaks of the doped $LiMnPO_4$ show increasing intensities as compared with pristine $LiMnPO_4$, which is confirmed the improvement of structural crystallinity (Arumugam, Kalaignan, Vediappan, & Lee, 2010; Talebi-Esfandarani & Savadogo, 2014; Z. Wu & Zhou, 2012).

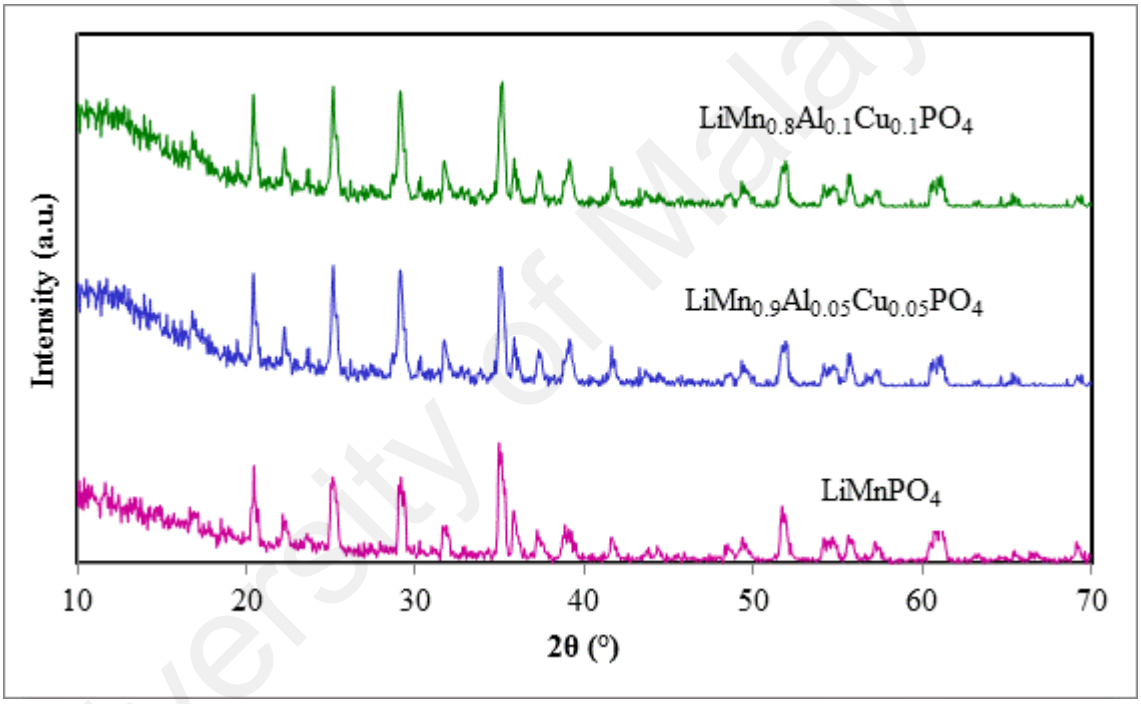

Figure 7.1: XRD of Al and Cu doped $LiMnPO_4$

Diffraction peaks found to be slightly shifted to higher 2θ as in Figure 7.2. It could explained as lattice shrinkage due to the smaller ionic radii of Al^{3+} (0.51 Å) and Cu^{2+} (0.87 Å) than Mn^{2+} (0.97 Å) (Ni & Gao, 2011; Zhaohui Tang, Li, & Wang, 2013). Calculated lattice constants based on hkl values for pristine $LiMnPO_4$, $LiMn_{0.9}Al_{0.05}Cu_{0.05}PO_4$ and $LiMn_{0.8}Al_{0.1}Cu_{0.1}PO_4$ are 6.135 Å, 6.126 Å and 6.056 Å respectively which corresponds to volume of 309.30 $Å^3$, 307.53 $Å^3$ and 304.42 $Å^3$.

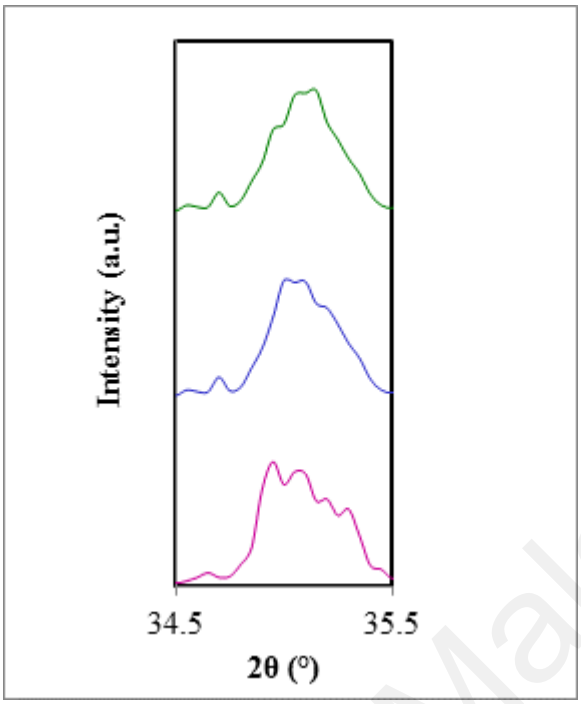

Figure 7.2: Peak shift to higher 2θ

Table 7.1 listed 2θ, FWHM and d spacing of the materials.

Table 7.1: 2θ, FWHM and d spacing of Al, Cu doped $LiMnPO_4$

$LiMn_{0.9}Al_{0.05}Cu_{0.05}PO_4$

hkl	2θ (°)	FWHM (°)	d-spacing (Å)
(020)	20.417	0.247	4.34637
(111/021)	25.209	0.349	3.52988
(200/121)	29.129	0.384	3.06314
(131)	35.138	0.309	2.55190
(222)	51.750	0.410	1.76509
(023/260)	61.145	0.449	1.51447

$LiMn_{0.8}Al_{0.1}Cu_{0.1}PO_4$

hkl	2θ (°)	FWHM (°)	d-spacing (Å)
(020)	20.548	0.377	4.31895
(111/021)	25.121	0.233	3.54210
(200/121)	29.151	0.366	3.06093
(131)	35.050	0.233	2.55808
(222)	51.793	0.517	1.76374
(023/260)	61.045	0.704	1.51671

Williamson hall plots as in Figure 7.3 have been developed to intensify effect of Al, Cu co-substitution on crystallite size and strain of the $LiMnPO_4$ cathode materials. From the plots it can be deduced (Table 7.2) that crystallite size of $LiMn_{0.8}Al_{0.1}Cu_{0.1}PO_4$ is 32.2 nm and $LiMn_{0.9}Al_{0.05}Cu_{0.05}PO_4$ is 31.5 nm. Besides that, the strain of $LiMn_{0.8}Al_{0.1}Cu_{0.1}PO_4$ found to be 3.50×10^{-4} while strain of $LiMn_{0.9}Al_{0.05}Cu_{0.05}PO_4$ is about 2.00×10^{-4}.

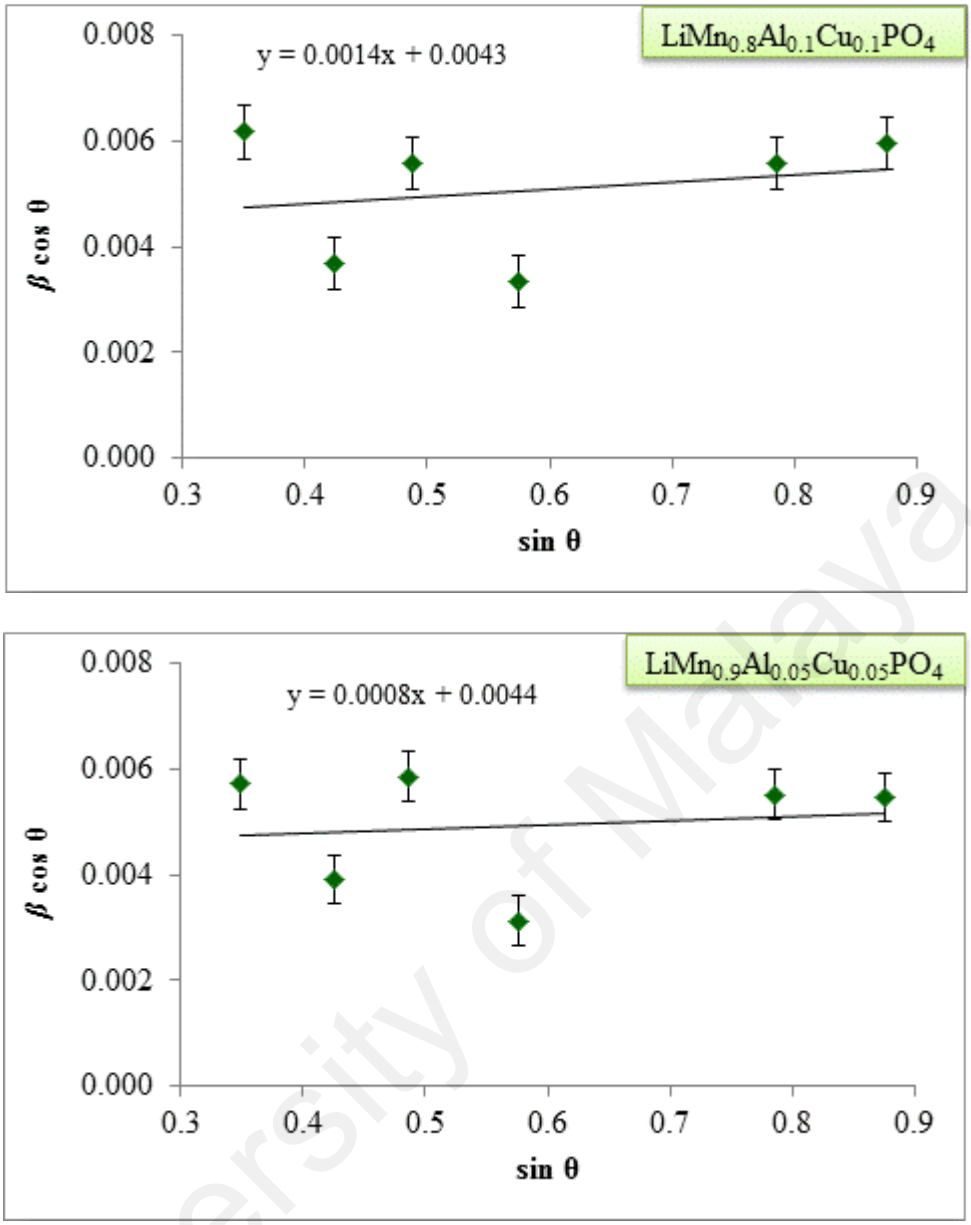

Figure 7.3: Williamson-hall plots of $LiMn_{1-x}Al_{0.5x}Cu_{0.5x}PO_4$ (x = 0.1, 0.2)

Table 7.2: Mean crystallite size and strain values of Al, Cu doped $LiMnPO_4$

Sample	Intercept	Slope	Crystallite size (nm)	Strain
$LiMn_{0.8}Al_{0.1}Cu_{0.1}PO_4$	0.0043	0.0014	32.2	3.50×10^{-4}
$LiMn_{0.9}Al_{0.05}Cu_{0.05}PO_4$	0.0044	0.0008	31.5	2.00×10^{-4}

The values of crystallite sizes and strain are lesser compared to pristine $LiMnPO_4$. This confirms that substitution of aluminium and copper successfully reduces crystallite size and strain simultaneously.

7.3.2 Field Emission Scanning Electron Microscopy (FESEM)

The morphologies of $LiMn_{0.9}Al_{0.05}Cu_{0.05}PO_4$ and $LiMn_{0.8}Al_{0.1}Cu_{0.1}PO_4$ are examined using FESEM with different magnifications are displayed in Figure 7.4 and Figure 7.5. Distinct grains can be noticed for all the samples. When Al and Cu substituents introduced into the materials, particles sizes are reduced. The particles sizes are in the range of 430 nm – 520 nm for $LiMn_{0.9}Al_{0.05}Cu_{0.05}PO_4$ and 260 nm – 350 nm for $LiMn_{0.8}Al_{0.1}Cu_{0.1}PO_4$ samples respectively. The smaller size of the binary doped $LiMnPO_4$ particles can shorten lithium migration pathways and also enhanced electrochemical activity (Cai et al., 2015; Chang, Peng, & Hung, 2015).

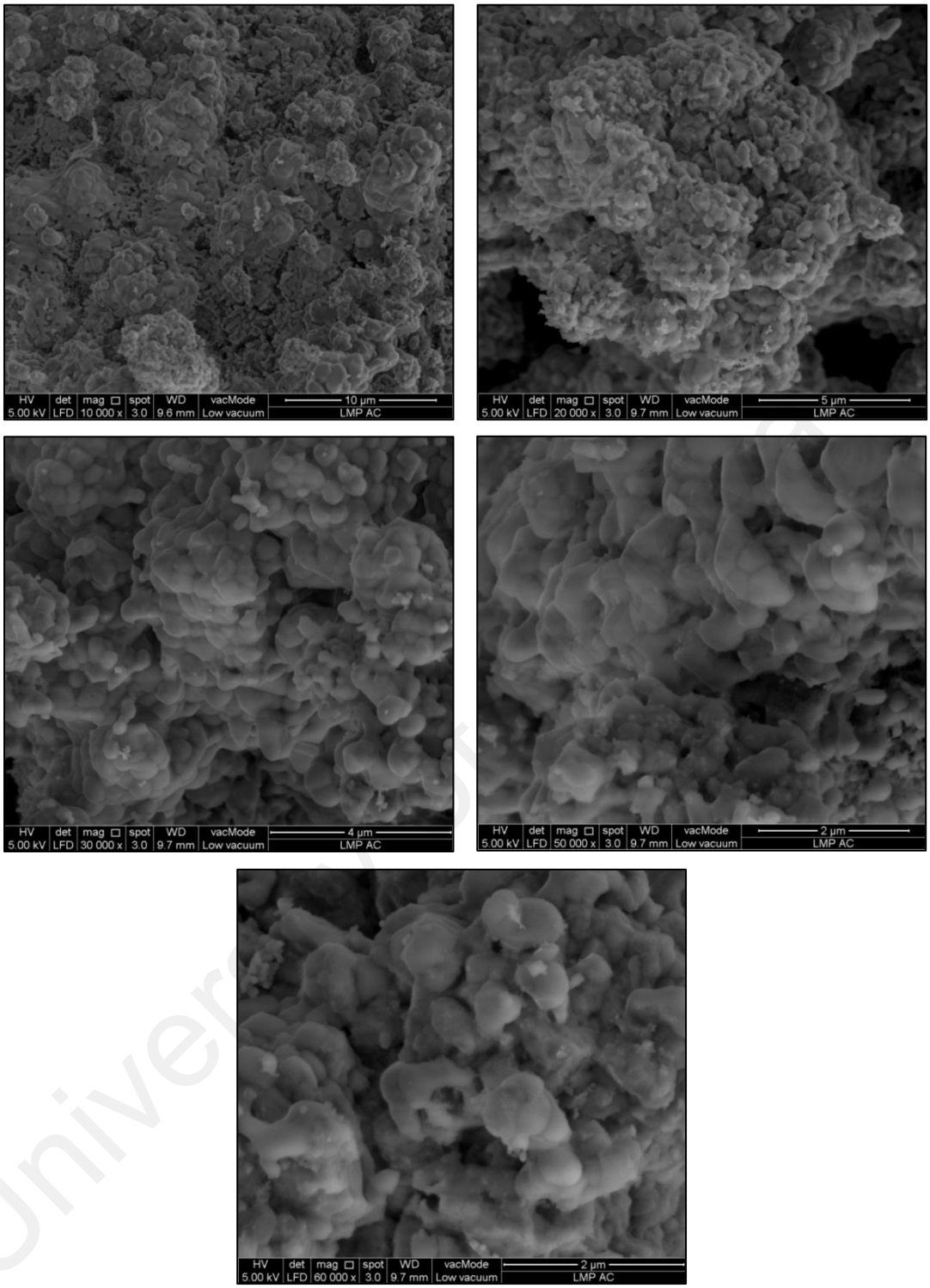

Figure 7.4: FESEM images of $LiMn_{0.9}Al_{0.05}Cu_{0.05}PO_4$ at different magnifications

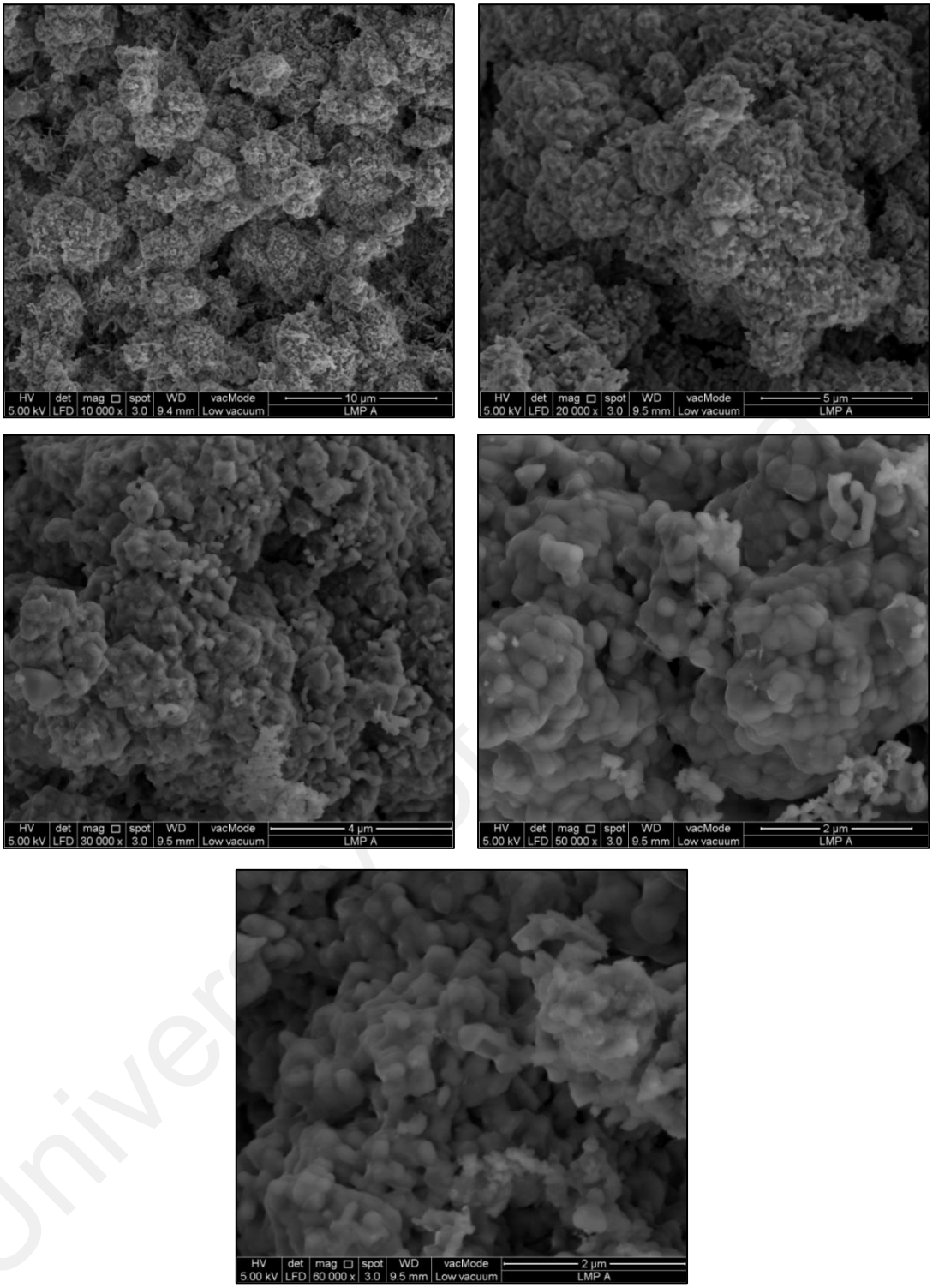

Figure 7.5: FESEM images of $LiMn_{0.8}Al_{0.1}Cu_{0.1}PO_4$ at different magnifications

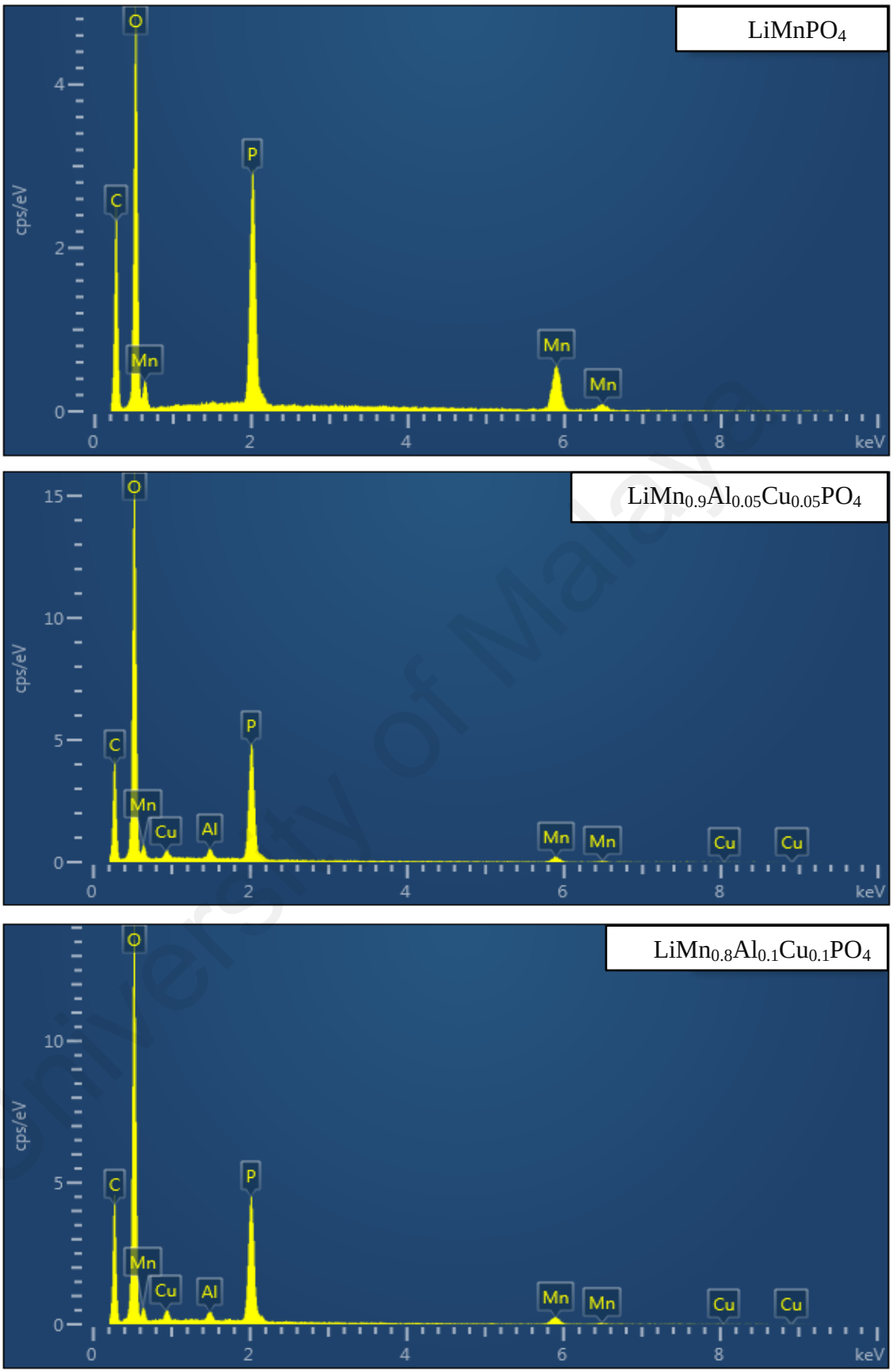

Figure 7.6: EDAX of pristine and doped $LiMnPO_4$

Energy dispersive analysis of x-rays (EDAX) was carried out to verify chemical compositions of synthesized compounds as shown in Figure 7.6. EDAX pattern of undoped sample displays the existence of manganese, phosphorus and oxygen. While $LiMn_{0.9}Al_{0.05}Cu_{0.05}PO_4$ and $LiMn_{0.8}Al_{0.1}Cu_{0.1}PO_4$ samples exhibit the presence of aluminium and copper together with manganese, phosphorus and oxygen in the structure. Carbon peaks in all samples correspond to oxalic acid in the synthesis process. Lithium cannot be identified because of its low energy level (Zhao et al., 2013).

7.3.3 Transmission Electron microscopy (TEM)

TEM images of $LiMn_{0.9}Al_{0.05}Cu_{0.05}PO_4$ and $LiMn_{0.8}Al_{0.1}Cu_{0.1}PO_4$ are shown in Figure 7.7. $LiMn_{0.9}Al_{0.05}Cu_{0.05}PO_4$ displays crystallites in the range of 30 nm – 32 nm whereas $LiMn_{0.8}Al_{0.1}Cu_{0.1}PO_4$ exhibits crystallites in the range of 32 nm – 33 nm. These values are consistent with crystallite values that obtained via Williamson-hall method in earlier section. Hence, TEM characterization suggests that the synthesized samples contain crystallites in the nanometers size which will help in shorter distance of lithium ion diffusion and increases contact area of electrode with electrolyte. As a result, it will enhance electrochemical performance of lithium ion batteries (Chen, Li, Gratzel, Kostecki, & Mao, 2012).

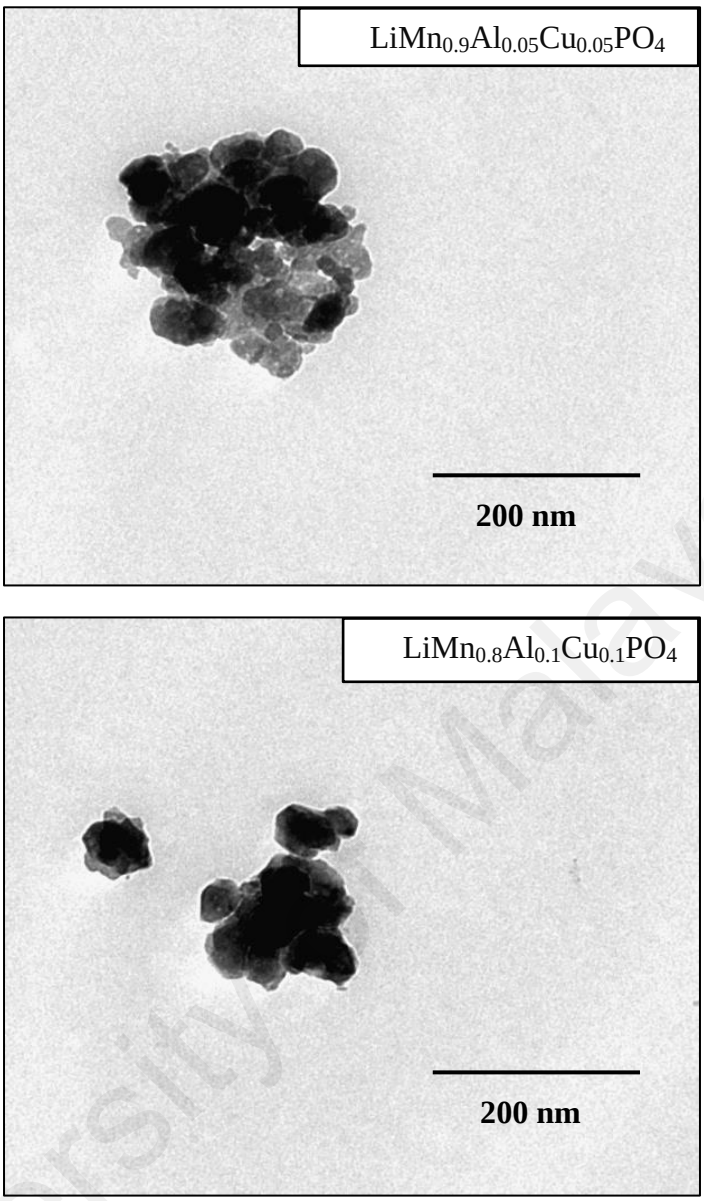

Figure 7.7: TEM images of $LiMn_{0.9}Al_{0.05}Cu_{0.05}PO_4$ and $LiMn_{0.8}Al_{0.1}Cu_{0.1}PO_4$

7.3.4 Raman Spectroscopy

Figure 7.8 displays Raman spectra of pristine and doped $LiMnPO_4$. All the samples demonstrate strong and sharp peak at 950 cm^{-1} which can be accredited to the intramolecular stretching of PO_4^{3-} (Kim et al., 2012; Korona et al., 2011). The peaks at 1005 cm^{-1} and 1070 cm^{-1} denote asymmetric stretching vibration of PO_4 tetrahedron. Furthermore, the broad peak at 438 cm^{-1} belongs to symmetric $A_g v_2$ mode. The other peaks at 590 cm^{-1}, 627 cm^{-1} and 661 cm^{-1} indicate symmetric $A_g v_4$ modes respectively (Michalska et al., 2015).

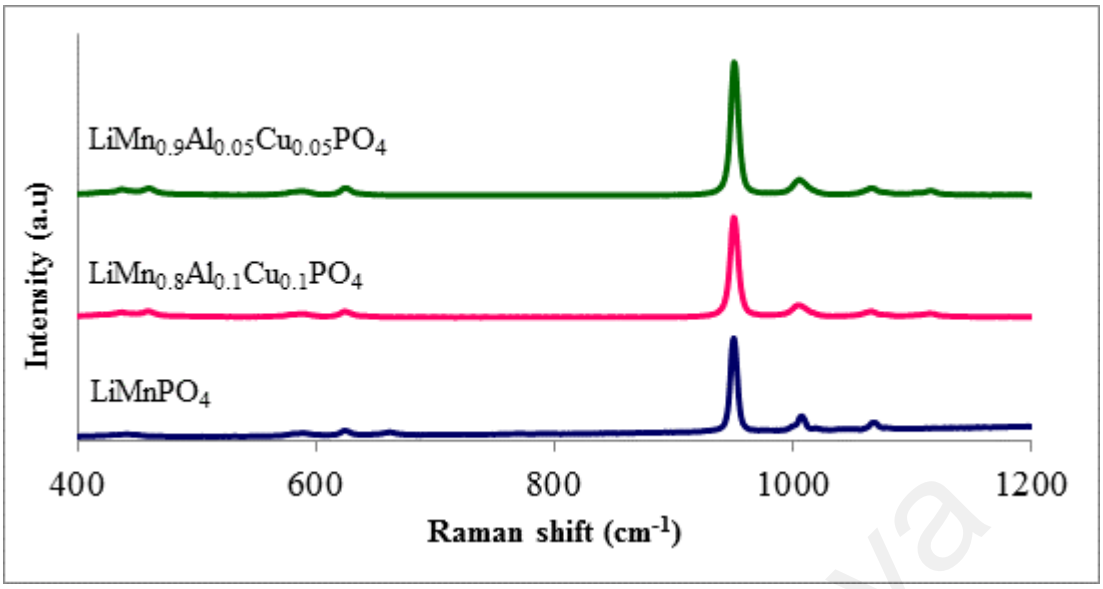

Figure 7.8: Raman spectra of pristine and doped $LiMnPO_4$

This will be evidence that the small amount of doping does not give significant effect on structure of $LiMn_{0.9}Al_{0.05}Cu_{0.05}PO_4$ and $LiMn_{0.8}Al_{0.1}Cu_{0.1}PO_4$. On contrary, the increasing peaks in Raman spectra strengthen XRD results that structural stability achieved by the doped samples.

7.3.5 Electrochemical analysis

Charge discharge profiles of pristine $LiMnPO_4$, $LiMn_{0.9}Al_{0.05}Cu_{0.05}PO_4$ and $LiMn_{0.8}Al_{0.1}Cu_{0.1}PO_4$ at a current rate of 0.05 C are presented in Figure 7.9 in between 2.5 V – 4.5 V (1C corresponds to 171 $mAhg^{-1}$). Initial charge capacity of pristine $LiMnPO_4$ found to be 151 $mAhg^{-1}$ while initial discharge capacity of 103 $mAhg^{-1}$.

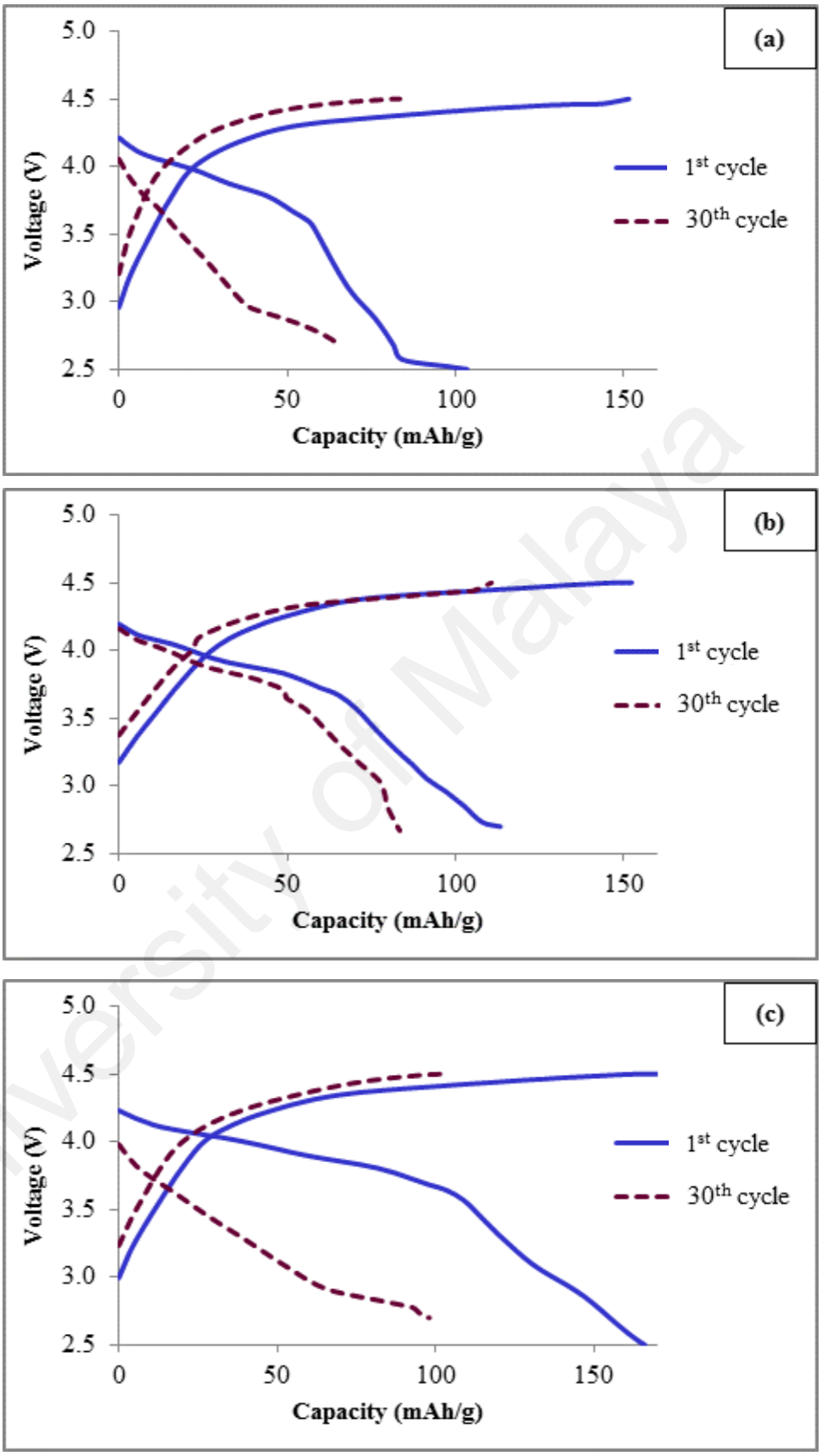

Figure 7.9: Charge discharge curves at 1st cycle and 30th cycle of (a) Pristine $LiMnPO_4$, (b) $LiMn_{0.9}Al_{0.05}Cu_{0.05}PO_4$ and (c) $LiMn_{0.8}Al_{0.1}Cu_{0.1}PO_4$

Meanwhile $LiMn_{0.9}Al_{0.05}Cu_{0.05}PO_4$ recorded initial charge capacity and discharge capacity of 152 $mAhg^{-1}$ and 113 $mAhg^{-1}$ respectively which is 74 % initial couloumbic efficiency. $LiMn_{0.8}Al_{0.1}Cu_{0.1}PO_4$ releases charge capacity of 170 $mAhg^{-1}$ and highest discharge capacity of 166 $mAhg^{-1}$. Smallest irreversible capacity loss about 4 $mAhg^{-1}$ can be observed for $LiMn_{0.8}Al_{0.1}Cu_{0.1}PO_4$. At the 30th cycle, pristine $LiMnPO_4$ and $LiMn_{0.9}Al_{0.05}Cu_{0.05}PO_4$ exhibit discharge capacity of 64 $mAhg^{-1}$ and 83 $mAhg^{-1}$ which gives capacity retention 62 % and 73 % respectively. However, $LiMn_{0.8}Al_{0.1}Cu_{0.1}PO_4$ remains its high discharge capacity of 97 $mAhg^{-1}$ even though the capacity retention only about 59 %.

Figure 7.10 demonstrates the variation of discharge capacity versus cycle number for pristine $LiMnPO_4$, $LiMn_{0.9}Al_{0.05}Cu_{0.05}PO_4$ and $LiMn_{0.8}Al_{0.1}Cu_{0.1}PO_4$. Al, Cu co-doped $LiMnPO_4$ exhibits improved discharge capacity compared to bare sample. $LiMn_{0.8}Al_{0.1}Cu_{0.1}PO_4$ presents high discharge capacity for 50 cycles among the samples. At 50th cycle, $LiMnPO_4$ delivered 42 $mAhg^{-1}$, while $LiMn_{0.9}Al_{0.05}Cu_{0.05}PO_4$ and $LiMn_{0.8}Al_{0.1}Cu_{0.1}PO_4$ display 33 $mAhg^{-1}$ and 61 $mAhg^{-1}$. The plot confirms that Al doping into the olivine structure shrinks lattice constant thus defeat Jahn-Teller distortion (Guo et al., 2014) and enhances lithium ion mobility (Zhang, Liu, Zhang, & Li, 2010). On the other hand, Cu^{2+} substitution able to stabilize the structure as a pillar (Cao, Yuan, Xie, & Zhan, 2010). Cu^{2+} doping has been explained that could bring two possible effects on conductivity. Either it creates new impurity energy level in the forbidden band which enhances electronic conductivity or it causes diffusion channel blockage which reduces ionic conductivity. Thus, the overall conductivity will be determined by the major component (Ni & Gao, 2011). In this work, Al co-doping is being compensated with Cu. Trivalent aluminum ions (Al^{3+}) and divalent copper ions

(Cu^{2+}) doping stimulate the average valence state of manganese ion to compensate charge neutrality, hence Jahn-Teller distortion depressed (Ding et al., 2015).

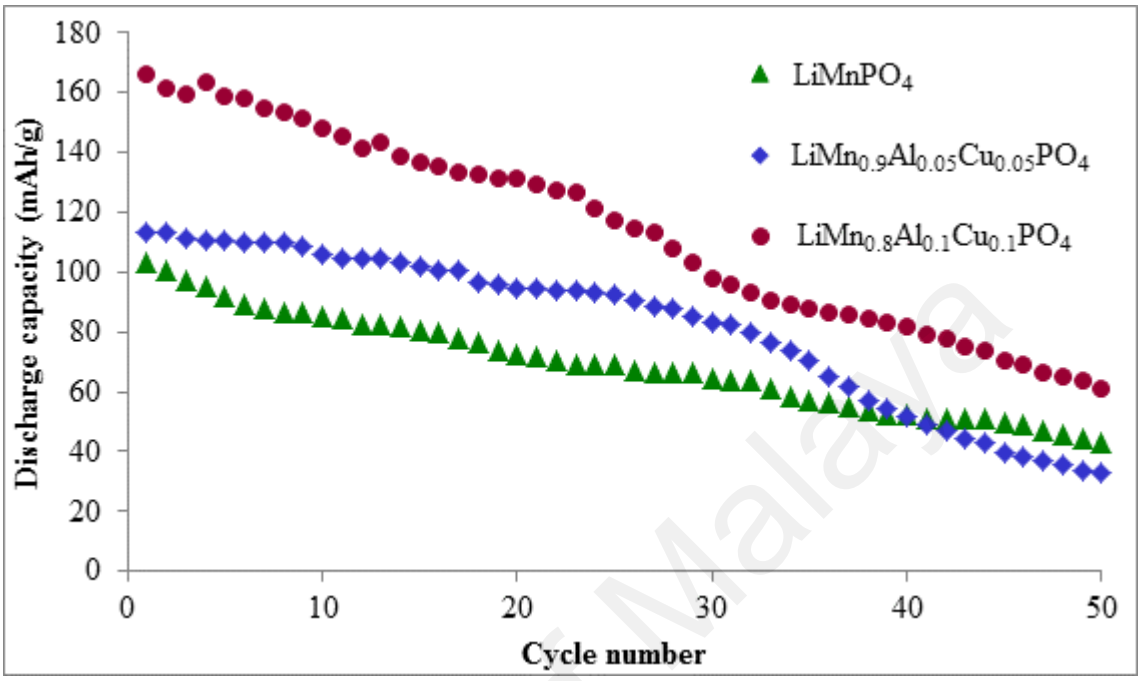

Figure 7.10: Discharge capacities of pristine and doped $LiMnPO_4$

Figure 7.11 portrays capacity retention of $LiMn_{0.8}Al_{0.1}Cu_{0.1}PO_4$ for 50 cycles. At 10th cycle, discharge capacity of $LiMn_{0.8}Al_{0.1}Cu_{0.1}PO_4$ became 148 mAhg^{-1} which gives capacity retention of 89 %. The discharge capacity declined to 132 mAhg^{-1} and 98 mAhg^{-1} respectively at 20th and 30th cycles accordingly. Thus, this accredited to capacity retention of 59 % and 49 % at 20th and 30th cycles. At 50th cycle, capacity retention seems to be at 36 % which remains discharge capacity of 61 mAhg^{-1}. Good capacity retention can be noticed for $LiMn_{0.8}Al_{0.1}Cu_{0.1}PO_4$ materials, hence making it improved version of $LiMnPO_4$.

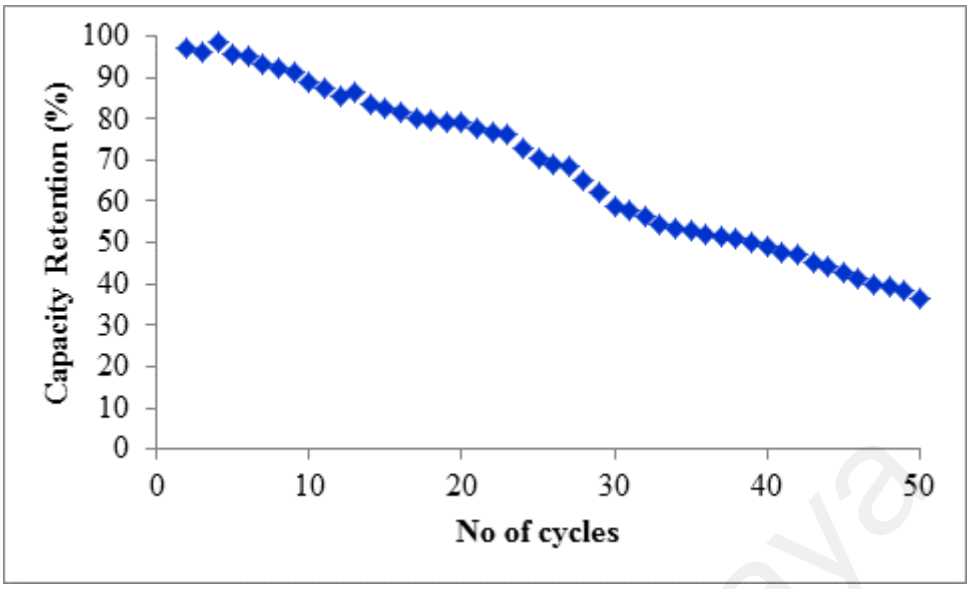

Figure 7.11: Capacity retention of $LiMn_{0.8}Al_{0.1}Cu_{0.1}PO_4$

Both Al and Cu were found to increase the electronic conductivity of the sample as illustrated in Figure 7.12. Semicircle in electrochemical impedance spectra denotes charge transfer resistance (R_{ct}) (Qian et al., 2013). From the results, it can be noticed that R_{ct} of pristine $LiMnPO_4$ is 51 Ω. $LiMn_{0.8}Al_{0.1}Cu_{0.1}PO_4$ indicates smallest R_{ct} value of 47 Ω followed by 49 Ω for $LiMn_{0.9}Al_{0.05}Cu_{0.05}PO_4$. Therefore, enhanced cycling performance of Al, Cu co-substituted $LiMnPO_4$ could be attributed to the smooth Li^+ transfer and lower transfer resistance (Hong et al., 2014; Zhao et al., 2015).

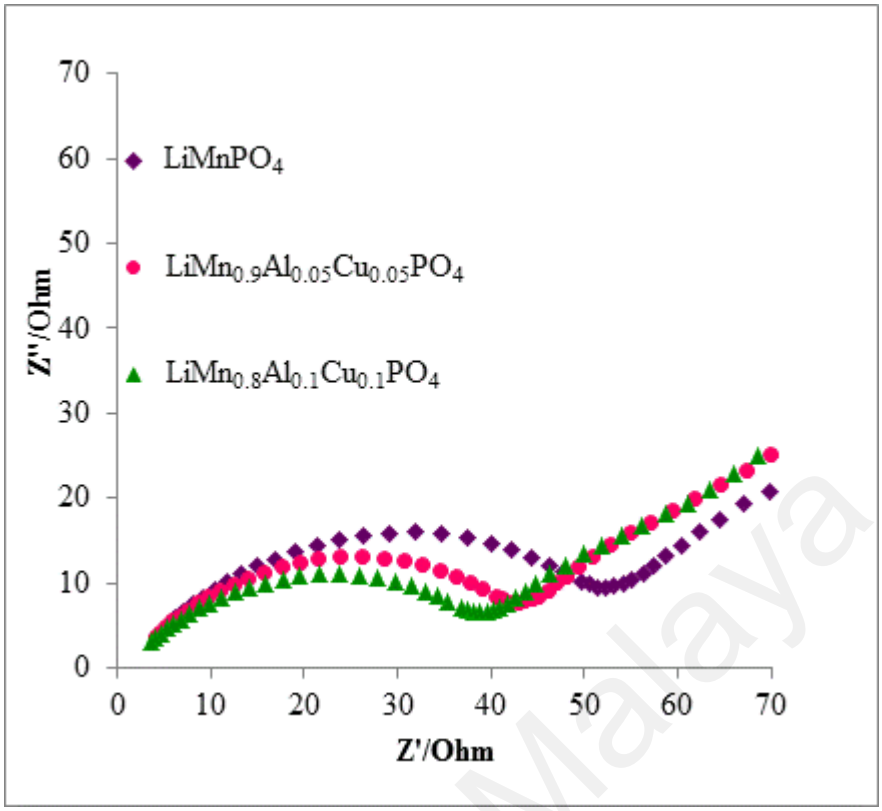

Figure 7.12: Electrochemical impedance spectra of pristine and doped $LiMnPO_4$

7.4 Conclusion

Pristine $LiMnPO_4$, $LiMn_{0.9}Al_{0.05}Cu_{0.05}PO_4$ and $LiMn_{0.8}Al_{0.1}Cu_{0.1}PO_4$ were obtained via sol gel method. Dual substitution for Mn in $LiMnPO_4$ has a noticeable influence on the electrochemical performance. XRD reveals Al and Cu doped into the structure without any amendment. $LiMn_{0.8}Al_{0.1}Cu_{0.1}PO_4$ delivered highest discharge capacity of 166 $mAhg^{-1}$ and $LiMn_{0.9}Al_{0.05}Cu_{0.05}PO_4$ exhibited initial discharge capacity of 152 $mAhg^{-1}$ at 0.05C. Reduced charge transfer resistance observed for $LiMn_{0.8}Al_{0.1}Cu_{0.1}PO_4$ and $LiMn_{0.9}Al_{0.05}Cu_{0.05}PO_4$ corresponds to 47 Ω and 49 Ω respectively compared to pristine $LiMnPO_4$ (51 Ω).

CHAPTER 8: DISCUSSION

In this work, $LiMnPO_4$ cathode materials were prepared and explored for their abilities to become successful applications in electrochemical devices. At initial stage, $LiMnPO_4$ cathode materials were synthesized via sol gel method assisted by oxalic acid and nitric acid. Sol gel method was employed considering its positive effects such as molecular level mixing, highly homogeneous particles, shorter time and lower synthesis temperature (Danks, Hall, & Schnepp, 2016). Presence of oxalic acid as chelating agent improves mixture of reactants (Dou et al., 2012; Jian et al., 2014) while nitric acid controls pH value of the product (Kandhasamy, Pandey, et al., 2012; Lingjun et al., 2015; Minakshi et al., 2012).

Different sintering temperatures were studied to intensify the effects on structural and morphological characterizations. From the observations, it can be clearly concluded that rising of sintering temperatures increases particle size of the samples (Naceur et al., 2014). It is noteworthy that agglomerated particles at high calcination temperatures are not made up of single crystal (Guo et al., 2013). But higher calcination temperature successfully unites crystallites and reducing lattice defects (Shirsath et al., 2011). Optimized sintering temperature from the above mentioned procedure was chosen to be at 700 °C considering low strain value accompanied by smaller mean crystallite size value. It also delivered highest discharge capacity compared to samples obtained from other sintering temperatures.

Next, sodium was partially substituted into lithium sites of $LiMnPO_4$ cathode materials in the range of $Li_{1-x}Na_xMnPO_4$ ($0.00 \leq x \leq 0.05$). Two different heating temperatures of 600 °C and 700 °C also varied for all as prepared composites. Na^+ ions served as pillars offer wider space for lithium ions transmission (Park et al., 2006; Qiu

et al., 2013). This provides the smoother intercalation and deintercalation process within the materials. Jahn Teller distortion related to the Mn-Mn distance suppressed by sodium substitution which makes distance of Mn-Mn becomes longer because Na^+ ions are larger compared to Li^+ ions (Sun & Xu, 2014). From the findings, $Li_{1-x}Na_xMnPO_4$ when x = 0.03 exhibited good cycling performances at both heating temperatures. Nonetheless, when the addition of sodium exceeds (> 0.03) it deteriorates the capacitive nature due to structural instability and weak electrochemical performance (Dong et al., 2013; Kuang et al., 2011). Between the two different calcination temperatures, $Li_{0.97}Na_{0.03}MnPO_4$ sintered at 700°C performed better electrochemical stability compared to 600°C. This could be attributed to minor structural defects that formed at sintering temperature of 600°C which could be resolved at 700°C. Higher sintering temperature strengthens structural stability that is essential for continuous cycling performance (Hua-jun Zhu et al., 2014a).

Furthermore, $LiMnPO_4$ cathode materials also were coated with zinc oxide (ZnO). As limited works reported on metal oxide coated $LiMnPO_4$, ZnO coating is an initial attempt towards $LiMnPO_4$ cathode material preparation. ZnO was selected as coating agent owing to its beneficial factors such as low cost, environmental friendly, thermal and structural stability (Jiangtao Zhu et al., 2015). The amount of ZnO coating that applied on $LiMnPO_4$ was varied as 1 wt. %, 2 wt. % and 3 wt. %. Coating layer on active materials prevents structural instability at higher voltage and maintains crystal structure with minor imperfections (Ilango et al., 2015; Shang et al., 2015). Another essential point is HF attack that occurs during cycling test employing $LiPF_6$ as an electrolyte, causing to the Mn dissolution (Şahan et al., 2010). Herein, the presence of ZnO coating protects manganese from dissolve into the electrolyte by shielding to elude direct contact between active materials and electrolyte and minimizes the electrolyte

oxidation (Yanping Chen et al., 2014; Lu et al., 2014). While analysing in terms of weight percentage of coating amount on $LiMnPO_4$, it can be evidently noticed that it also played an imperative role in order to achieve the desired electrochemical enhancement (Zhiyuan Wang, Enzuo Li, Chunnian He, Chunsheng Shi, Jiajun Li, 2008). 3 wt.% ZnO coated sample showed poor cycling performance than other coated samples, which possibly due to the excess amount of ZnO coating leads to reduction of electronic conductivity (Ting Liu et al., 2012). EIS testing similarly revealed that 3 wt.% ZnO coated sample has high R_{ct} value of 43 Ω caused by extra polarization might be responsible for its poor electrochemical activity (Amaresh et al., 2013). 2 wt.% ZnO coated $LiMnPO_4$ sample exhibited higher discharge capacity with enriched capacity retention than that of other prepared samples.

Apart from that, aluminium and copper were dual substituted in $LiMnPO_4$ cathode materials at different amount namely $LiMn_{0.9}Al_{0.05}Cu_{0.05}PO_4$ and $LiMn_{0.8}Al_{0.1}Cu_{0.1}PO_4$. Both Al and Cu have some impressive assets such as ample and inexpensive, hence chosen for co-substitution (Guo et al., 2014; Ma, Fan, et al., 2014). The outcomes in this work explained that Al doping into the olivine structure decreases lattice constant thus improves Jahn-Teller distortion (D. Guo et al., 2014) and enhances lithium ion movement (Zhang et al., 2010) while Cu^{2+} substitution can be able to stabilize the structure as a pillar (Cao et al., 2010). Trivalent aluminum ions (Al^{3+}) and divalent copper ions (Cu^{2+}) doping promote the average valence state of manganese ion to compensate charge neutrality, hence Jahn-Teller distortion reduced (Ding et al., 2015). R_{ct} values of the doped samples reduced compared to pristine. Thus, greater cycling performance of Al, Cu co-substituted $LiMnPO_4$ could be ascribed to the smooth Li^+ transfer and reduced transfer resistance (Hong et al., 2014; Zhao et al., 2015).

$LiMn_{0.8}Al_{0.1}Cu_{0.1}PO_4$ demonstrated high discharge capacity and enhanced cycling properties.

Structural properties are important factors that evaluating electrochemical performance of cathode materials. Hence, modifications such as partial sodium substitution in lithium sites, metal oxide coating and metal ion substitution reduce strain of the particles and form smaller crystallite sizes. All the samples exhibit XRD peaks that are assigned to the orthorhombic structure of $LiMnPO_4$ (JCPDS No. 74-0375) with space group of Pnmb (Zhang et al., 2015; Zheng et al., 2015).

On comparing the best performing sample in each modification, interesting outcomes were established. Pristine $LiMnPO_4$ cathode materials that obtained at sintering temperature of 700 °C delivered first discharge capacity of 103.4 $mAhg^{-1}$ at 0.05 C, 86.3 $mAhg^{-1}$ at 0.1 C while $LiMn_{0.8}Al_{0.1}Cu_{0.1}PO_4$ achieved discharge capacity of 166.6 $mAhg^{-1}$ at 0.05 C. 2 wt.% ZnO coated $LiMnPO_4$ demonstrated initial discharge capacity of 102.2 $mAhg^{-1}$ at 0.1 C and $Li_{0.97}Na_{0.03}MnPO_4$ exhibited discharge capacity of 92.4 $mAhg^{-1}$ at 0.1 C.

While comparing pristine $LiMnPO_4$ cathode materials that synthesized via sol gel method with other similar works that employed sol gel technique, as far there are two works reported on $LiMnPO_4$ synthesis by sol gel method. In earlier work of Sheng Kui et al (Sheng-kui et al., 2012), the obtained sample reached 122.6 $mAhg^{-1}$ at 0.05 C. At a glance, it is higher compared to current work (103.4 $mAhg^{-1}$) but it should be noted that PEG400 (polyethylene glycol) was added in their sol gel process beside citric acid. While citric acid serves as carbon source (Wi et al., 2012; Xiang et al., 2013), addition of PEG would be another carbon source (Tao & Wang, 2015). Hence, sol gel method

that utilized by Sheng Kui et al (Sheng-kui et al., 2012) have used double carbon source while current work only used oxalic acid as single carbon source.

In another work, sol gel method was accompanied by ball milling and liquid nitrogen quenching to produce $LiMnPO_4$ (Wu et al., 2013). To compare the results with this work, $LiMnPO_4$ without liquid nitrogen quenching is focused. $LiMnPO_4$ that synthesized by citric acid assisted sol gel method delivered 94.0 $mAhg^{-1}$ at 0.05 C and 81.6 $mAhg^{-1}$ at 0.1 C. Hence, it can be concluded that sol gel method in our work employing oxalic acid with nitric acid established enhanced capacity. This synthesis route was used for all other modification including substitution and coating.

At 0.05 C, $LiMn_{0.8}Al_{0.1}Cu_{0.1}PO_4$ displays superior capacity compared to undoped $LiMnPO_4$ cathode materials. It exhibited charge capacity of 170 $mAhg^{-1}$ and highest discharge capacity of 166 $mAhg^{-1}$. Discharge capacity of $LiMn_{0.8}Al_{0.1}Cu_{0.1}PO_4$ became 60.8 $mAhg^{-1}$ at 50th cycle meanwhile pristine sample showed 42.6 $mAhg^{-1}$. The capacity is improved compared to other substituted $LiMnPO_4$ cathode materials at 0.05 C whereas $LiFe_{0.25}Mn_{0.75}PO_4/C$ delivered 130 $mAhg^{-1}$ (Li Chen et al., 2012), $LiMn_{0.8}Fe_{0.2}PO_4$ exhibited 160.6 $mAhg^{-1}$ (Yang et al., 2015) and $LiMn_{0.9}Fe_{0.05}Co_{0.05}PO_4/C$ displayed 145 $mAhg^{-1}$ (Xiang et al., 2015).

$LiMn_{0.9}Al_{0.05}Cu_{0.05}PO_4$ recorded initial charge capacity and discharge capacity of 152 $mAhg^{-1}$ and 113 $mAhg^{-1}$ respectively which is 74 % initial couloumbic efficiency. Smallest irreversible capacity loss about 4 $mAhg^{-1}$ can be observed for $LiMn_{0.8}Al_{0.1}Cu_{0.1}PO_4$. At the 30th cycle, pristine $LiMnPO_4$ and $LiMn_{0.9}Al_{0.05}Cu_{0.05}PO_4$ exhibit discharge capacity of 64 $mAhg^{-1}$ and 83 $mAhg^{-1}$ which gives capacity retention

62 % and 73 % respectively. However, $LiMn_{0.8}Al_{0.1}Cu_{0.1}PO_4$ remains its high discharge capacity of 97 $mAhg^{-1}$ even though the capacity retention only about 59%.

At 0.1 C, 2 wt. % ZnO coated $LiMnPO_4$ cathode materials demonstrated good cycling performance than bare $LiMnPO_4$. Best to our knowledge, Li conductive Li_3VO_4 coating (Dong et al., 2014) and hybrid CeO_2/C coating (Chen et al., 2015b) were applied on $LiMnPO_4$. There is no work reported on unique nanostructured metal oxide coated $LiMnPO_4$. This is the initial approach to apply ZnO coating on $LiMnPO_4$ and the results would not be able to comparable to any other work. Similar reasons applicable for $Li_{0.97}Na_{0.03}MnPO_4$ because no research has been done using partial sodium substitution in lithium sites of $LiMnPO_4$. Even though, capacity that has been obtained for $Li_{0.97}Na_{0.03}MnPO_4$ quite low but this will be initial step towards sodium substitution in lithium sites and provides insight of changes that happen in structural and electrochemical properties.

Al, Cu co-doped samples seem to be promising candidates for cathode materials at low current rates while ZnO coated samples would be excellent choice for high current rates. Doping and metal oxide coating can be accompanied together in future work for better electrochemical properties.

CHAPTER 9: CONCLUSIONS AND FUTURE WORKS

9.1 Conclusions

Important conclusions drawn from this research project are summarized below.

i. $LiMnPO_4$ cathode materials from synthetic strategy of sol gel method aided by oxalic acid and nitric acid provide good structural and morphology assets. Besides that, sintering temperature was optimized efficiently to yield improved structural properties by reducing strain and crystallite size of the grains. Hence, it provides outcomes with enhanced electrochemical properties.

ii. Partially substitution of sodium into lithium sites of $LiMnPO_4$ cathode materials at optimal level remarkably improved electrochemical activity. Interestingly, Na^+ ions served as pillars to create broader space for lithium ions diffusion and effectively suppressed Jahn Teller distortion.

iii. ZnO coated $LiMnPO_4$ cathode materials displayed high discharge capacity with superior capacity retention than pristine sample. Eco-friendly ZnO coating shielded the active materials from electrolyte which lead to negative side reactions that affect cycling properties. Thus, it promotes smoother intercalation processes.

iv. Dual substitution of aluminum and copper for manganese in $LiMnPO_4$ cathode materials has a significant influence on the electrochemical performance. Structural stabilization and electronic conductivity of the co-doped samples increased compared to pristine which leads to excellent electrochemical performance.

9.2 Future works

While analyzing conclusions from this work, subsequent points are effectively recommended for future works.

i. Sol gel technique that has been used throughout this study can be developed by varying sintering time as this work fixed the time for 3 hours. In future work, sintering temperature can be act as controlled variable and sintering time can be varied. Maybe some interesting structural and electrochemical properties can be established occupying this approach too.

ii. Partial sodium substitution on lithium sites of $LiMnPO_4$ cathode materials can be accompanied by ZnO coating to further improve cycling properties. Meanwhile aluminum and copper co-doped $LiMnPO_4$ cathode materials also can be coated with ZnO to upgrade the electrochemical activity.

iii. Optimized sodium level in lithium sites of $LiMnPO_4$ that demonstrated enhanced capacity can be incorporated with optimized level of aluminum and copper co-substitution in manganese sites of $LiMnPO_4$. This will produce $Li_aNa_bMnAl_cCu_dPO_4$ composites with a, b, c, d are optimum level of substituents.

REFERENCES

Afyon, S., Kundu, D., Darbandi, A. J., & Hahn, H. (2014). A low dimensional composite of hexagonal lithium manganese borate ($LiMnBO_3$), a cathode material for Li-ion batteries. *Journal of Materials Chemistry A: Materials for energy and sustainability*, *2*, 18946–18951.

Afyon, S., Kundu, D., Krumeich, F., & Nesper, R. (2013). Nano $LiMnBO_3$, a high-capacity cathode material for Li-ion batteries. *Journal of Power Sources*, *224*, 145–151.

Afyon, S., Mensing, C., Krumeich, F., & Nesper, R. (2014). The electrochemical activity for nano-$LiCoBO_3$ as a cathode material for Li-ion batteries. *Solid State Ionics*, *256*, 103–108.

Akimoto, S., & Taniguchi, I. (2013). Nanocomposite cathode of lithium batteries with high rate performance. *Journal of Power Sources*, *242*, 627–630.

Allen, J. L., Jow, T. R., & Wolfenstine, J. (2011). Improved cycle life of Fe-substituted $LiCoPO_4$. *Journal of Power Sources*, *196*, 8656–8661.

Allen, J. L., Thompson, T., Sakamoto, J., Becker, C. R., Jow, T. R., & Wolfenstine, J. (2014). Transport properties of $LiCoPO_4$ and Fe-substituted $LiCoPO_4$. *Journal of Power Sources*, *254*, 204–208.

Alyoshin, V. A., Pleshakov, E. A., Ehrenberg, H., & Mikhailova, D. (2014). Platelike $LiMPO_4$ (M = Fe , Mn , Co , Ni) for Possible Application in Rechargeable Li Ion Batteries : Beyond Nanosize. *Journal of Physical Chemistry C*, *4*, 17426–17435.

Amaresh, S., Karthikeyan, K., Kim, K. J., Kim, M. C., Chung, K. Y., Cho, B. W., & Lee, Y. S. (2013). Facile synthesis of ZrO_2 coated Li_2CoPO_4F cathode materials for lithium secondary batteries with improved electrochemical properties. *Journal of Power Sources*, *244*, 395–402.

Aono, S., Urita, K., Yamada, H., & Moriguchi, I. (2012). Electrochemical property of $LiMnPO_4$ nanocrystallite-embedded porous carbons as a cathode material of Li-ion battery. *Solid State Ionics*, *225*, 556–559.

Aravindan, V., Karthikeyan, K., Ravi, S., Amaresh, S., Kim, W. S., & Lee, Y. S. (2010). Adipic acid assisted sol – gel synthesis of Li_2MnSiO_4 nanoparticles with improved lithium storage properties. *Journal of Materials Chemistry*, *20*, 7340–7343.

Arumugam, D., Kalaignan, G. P., Vediappan, K., & Lee, C. W. (2010). Synthesis and electrochemical characterizations of nano-scaled Zn doped $LiMn_2O_4$ cathode materials for rechargeable lithium batteries. *Electrochimica Acta*, *55*(28), 8439–8444.

Asep Bayu Dani Nandiyanto, & Okuyama, K. (2011). Progress in developing spray-drying methods for the production of controlled morphology particles : From the nanometer to submicrometer size ranges. *Advanced Powder Technology*, *22*(1), 1–19.

Baddour-hadjean, R., & Pereira-Ramos, J.-P. (2010). Raman Microspectrometry Applied to the Study of Electrode Materials for Lithium Batteries. *Chemical Reviews*, 1278–1319.

Bakenov, Z., & Taniguchi, I. (2011). Synthesis of spherical $LiMnPO_4$/C composite microparticles. *Materials Research Bulletin*, *46*, 1311–1314.

Bao, L., Xu, G., Wang, J., Zong, H., Li, L., Zhao, R., Zhou, S., Shena. G., Han, G. (2015). Hydrothermal synthesis of flower-like $LiMnPO_4$ nanostructures self-assembled with (010) nanosheets and their application in Li-ion batteries. *CrystEngComm*, *17*, 6399–6405.

Bard, A. J., Faulkner, L. R., York, N., @bullet, C., Brisbane, W., & Toronto, S. E. (1944). *Electrochemical Methods Fundamentals and Applications*. *Electrochemistry*. New York: Wiley.

Barpanda, P., Djellab, K., Recham, N., & Tarascon, J. (2011). Direct and modified ionothermal synthesis of $LiMnPO_4$ with tunable morphology for rechargeable Li-ion batteries. *Journal of Materials Chemistry*, *21*, 10143–10152.

Bhaskar, A., Mikhailova, D., Kiziltas-Yavuz, N., Nikolowski, K., Oswald, S., Bramnik, N. N., & Ehrenberg, H. (2014). 3d-Transition metal doped spinels as high-voltage cathode materials for rechargeable lithium-ion batteries. *Progress in Solid State Chemistry*, *42*(4), 128–148.

Bhuwaneswari, M. S., Dimesso, L., & Jaegermann, W. (2010). Preparation of LiCoPO4 powders and films via sol–gel. *Journal of Sol-Gel Science and Technology*, *56*, 320–326.

Brent Fultz, & Howe, J. (2015). *Transmission Electron Microscopy and Diffractometry of Materials*. New York: Springer (Vol 1).

Brutti, S., Manzi, J., Bonis, A. De, Lecce, D. Di, Vitucci, F., Paolone, A., … Panero, S. (2015). Controlled synthesis of $LiCoPO_4$ by a solvo-thermal method at 220 C. *Materials Letters*, *145*, 324–327.

Cai, Y., Huang, Y., Wang, X., Jia, D., Pang, W., Guo, Z., … Tang, X. (2015). Facile synthesis of $LiMn_2O_4$ octahedral nanoparticles as cathode materials for high capacity lithium ion batteries with long cycle life. *Journal of Power Sources*, *278*, 574–581.

Cao, X., Yuan, C., Xie, L., & Zhan, H. (2010). Low-temperature synthesis of Cu-doped $Li_{1.2}V_3O_8$ as cathode for reversible lithium storage. *Ionics*, *16*, 39–44.

Chang, Y.-C., Peng, C.-T., & Hung, I.-M. (2015). Synthesis and electrochemical properties of $LiFe_{0.95}V_xNi_{0.05-x}PO_4$/C cathode material for lithium-ion battery. *Ceramics International*, *41*(4), 5370–5379.

Chen, D., Shao, G., Li, B., Zhao, G., Li, J., Liu, J., … Zhang, H. (2014). Synthesis, crystal structure and electrochemical properties of $LiFePO_4F$ cathode material for Li-ion batteries. *Electrochimica Acta*, *147*, 663–668.

Chen, D., Wei, W., Wang, R., Lang, X., Tian, Y., & Guo, L. (2012). Facile synthesis of 3D hierarchical foldaway-lantern-like $LiMnPO_4$ by nanoplate self-assembly, and electrochemical performance for Li-ion batteries. *Dalton Transactions*, *41*, 8822–8828.

Chen, F., Tao, F., Wang, C., Zhang, W., & Chen, L. (2015). The in fl uence of improved carbon coating layer with nanometer-sized CeO_2 interconnector on the enhanced electrochemical performance of. *Journal of Power Sources*, *285*, 367–373.

Chen, H., Chen, M., Du, C., Cui, Y., & Zuo, P. (2016). Synthesis and electrochemical performance of hierarchical nanocomposite of carbon coated $LiCoPO_4$ crosslinked by graphene. *Materials Chemistry and Physics*, *171*, 6–10.

Chen, J., Zhang, H., Wang, M., Liu, J., Li, C., & Zhang, P. (2016). Improving the electrochemical performance of high voltage spinel cathode at elevated temperature by a novel electrolyte additive. *Journal of Power Sources*, *303*, 41–48.

Chen, L., Dilena, E., Paolella, A., Bertoni, G., Ansaldo, A., Colombo, M., … Manna, L. (2016). Relevance of LiPF6 as Etching Agent of $LiMnPO_4$ Colloidal Nanocrystals for High Rate Performing Li-ion Battery Cathodes. *Applied Materials Interfaces*, *8*, 4069–4075.

Chen, L., Yuan, Y., Feng, X., & Li, M. (2012). Enhanced electrochemical properties of $LiFe_{1-x}Mn_xPO_4/C$ composites synthesized from $FePO_4.2H_2O$ nanocrystallites. *Journal of Power Sources*, *i*, 344–350.

Chen, L., Zhao, Y., An, X., Liu, J., Dong, Y., Chen, Y., & Kuang, Q. (2010). Structure and electrochemical properties of $LiMnBO_3$ as a new cathode material for lithium-ion batteries. *Journal of Alloys and Compounds*, *494*(1-2), 415–419.

Chen, P., Wu, H., Huang, S., & Zhang, Y. (2016). Template synthesis and lithium storage performances of hollow spherical $LiMn_2O_4$ cathode materials. *Ceramics International*, *42*(8), 10498–10505.

Chen, R., Zhao, T., Zhang, X., & Wu, F. (2016). Advanced cathode materials for lithium-ion batteries using nanoarchitectonics. *Nanoscale Horizons*, *1*, 423 – 444.

Chen, X., Li, C., Gratzel, M., Kostecki, R., & Mao, S. S. (2012). Nanomaterials for renewable energy production and storage. *Chemical Society Reviews*, 7909–7937.

Chen, Y., Xie, K., Pan, Y., & Zheng, C. (2011). Nano-sized $LiMn_2O_4$ spinel cathode materials exhibiting high rate discharge capability for lithium-ion batteries. *Journal of Power Sources*, *196*(15), 6493–6497.

Chen, Y., Zhang, Y., Chen, B., Wang, Z., & Lu, C. (2014). An approach to application for $LiNi_{0.6}Co_{0.2}Mn_{0.2}O_2$ cathode material at high cutoff voltage by TiO_2 coating. *Journal of Power Sources*, *256*, 20–27.

Chen, Z., Cao, L., Chen, L., Zhou, H., Zheng, C., Xie, K., & Kuang, Y. (2015). Mesoporous $LiFeBO_3/C$ hollow spheres for improved stability lithium-ion battery cathodes. *Journal of Power Sources*, *298*, 355–362.

Chen, Z., Xie, T., Li, L., & Xu, M. (2014). Characterization of Na-substituted $LiNi_{1/3}Co_{1/3}Mn_{1/3}O_2$ cathode materials for lithium-ion battery. *Ionics*, *20*, 629–634.

Cheng, F., Wan, W., Tan, Z., Huang, Y., Zhou, H., Chen, J., & Zhang, X. (2011). High power performance of nano-$LiFePO_4$/C cathode material synthesized via lauric acid-assisted solid-state reaction. *Electrochimica Acta*, *56*(8), 2999–3005.

Cheol, B., Singh, L., Lee, K., Kim, M., Cho, M., Yarger, J. L., … Lee, Y. (2015). Enhanced electrochemical performance of $LiFe_{0.4}Mn_{0.6}(PO_4)_{1-x}(BO_3)_x$ as cathode material for lithium ion batteries. *Journal of Electroanalytical Chemistry*, *756*, 56–60.

Cho, W., Kim, S., Ho, J., Yim, T., Woo, S., Lee, K., … Kim, Y. (2015). Improved electrochemical and thermal properties of nickel rich $LiNi_{0.6}Co_{0.2}Mn_{0.2}O_2$ cathode materials by SiO_2 coating. *Journal of Power Sources*, *282*, 45–50.

Cho, W., Kim, S.-M., Song, J. H., Yim, T., Woo, S.-G., Lee, K.-W., … Kim, Y.-J. (2015). Improved electrochemical and thermal properties of nickel rich $LiNi_{0.6}Co_{0.2}Mn_{0.2}O_2$ cathode materials by SiO_2 coating. *Journal of Power Sources*, *282*, 45–50.

Cui, Y., & Xu, S. (2015). High tap density of $Ni_3(PO_4)_2$ coated $LiNi_{1/3}Co_{1/3}Mn_{1/3}O_2$ with enhanced cycling performance at high cut-off voltage. *Chinese Journal of Chemical Engineering*, *23*(1), 315–320.

Cui, Y.-T., Xu, N., Kou, L.-Q., Wu, M.-T., & Chen, L. (2014). Enhanced electrochemical performance of different morphological C/$LiMnPO_4$ nanoparticles from hollow-sphere Li_3PO_4 precursor via a delicate polyol-assisted hydrothermal method. *Journal of Power Sources*, *249*, 42–47.

Dai, E., Fang, H., Yang, B., Ma, W., & Dai, Y. (2015). Synthesis of vanadium doped $LiMnPO_4$ by an improved solid-state method. *Ceramics International*, *41*(6), 8171–8176.

Dai, Z., Wang, L., He, X., Ye, F., Huang, C., Li, J., … Ouyang, M. (2013). Morphology regulation of nano $LiMn_{0.9}Fe_{0.1}PO_4$ by solvothermal synthesis for lithium ion batteries. *Electrochimica Acta*, *112*, 144–148.

Danks, A. E., Hall, S. R., & Schnepp, Z. (2016). The evolution of "sol–gel" chemistry as a technique for materials synthesis. *Materials Horizontal*, *3*, 91-112.

Das, B., Pohl, A., Chakravadhanula, V. S. K., Kübel, C., & Fichtner, M. (2014). LiF/Fe/V_2O_5 nanocomposite as high capacity cathode for lithium ion batteries. *Journal of Power Sources*, *267*, 203–211.

Deng, C., Zhang, S., Fu, B. L., Yang, S. Y., & Ma, L. (2010). Characterization of Li_2MnSiO_4 and Li_2FeSiO_4 cathode materials synthesized via a citric acid assisted sol-gel method. *Materials Chemistry and Physics*, *120*, 14–17.

Deng, D., Kim, G., Lee, Y., & Cho, J. (2009). Green energy storage materials : Nanostructured TiO 2 and Sn-based anodes for lithium-ion batteries. *Energy & Environmental Science*, *2*, 818–837.

Dimesso, L., & Becker, D. (2012). Investigation of graphitic carbon foams/$LiNiPO_4$ composites. *Journal of Solid State Electrochemistry*, *16*, 3791–3798.

Dimesso, L., Spanheimer, C., & Jaegermann, W. (2013). Effect of the Mg-substitution on the graphitic carbon foams — $LiNi_{1-y}Mg_yPO_4$ composites as possible cathodes materials for 5 V applications. *Materials Research Bulletin*, *48*(2), 559–565.

Ding, X., Zhou, H., Liu, G., Yin, Z., Jiang, Y., & Wang, X. (2015). Electrochemical evaluation of $LiAl_{0.05}Ni0_{.05}Mn_{1.9}O_4$ cathode material synthesized via electrospinning method. *Journal of Alloys and Compounds*, *632*, 147–151.

Dinh, H., Mho, S., Kang, Y., & Yeo, I. (2013). Large discharge capacities at high current rates for carbon-coated $LiMnPO_4$ nanocrystalline cathodes. *Journal of Power Sources*, *244*, 189–195.

Dinh, H., Mho, S., Yeo, I., Kang, Y., & Kim, D. (2015). Superior high rate capability of size-controlled $LiMnPO_4$/C nanosheets with preferential orientation. *RSC Advances*, *5*, 100709–100714.

Diouf, B., & Pode, R. (2015). Potential of lithium-ion batteries in renewable energy. *Renewable Energy*, *76*, 375–380.

Doi, T., Yatomi, S., Kida, T., Okada, S., & Yamaki, J. (2009). Liquid-Phase Synthesis of Uniformly Nanosized $LiMnPO_4$ Particles and Their Electrochemical Properties for Lithium-Ion Batteries. *Crystal Growth & Design*, *9*, 10–12.

Dong, J., Yu, X., Sun, Y., Liu, L., Yang, X., & Huang, X. (2013). Triplite $LiFeSO_4F$ as cathode material for Li-ion batteries. *Journal of Power Sources*, *244*, 716–720.

Dong, X., Xu, Y., Xiong, L., Sun, X., & Zhang, Z. (2013). Sodium substitution for partial lithium to significantly enhance the cycling stability of Li_2MnO_3 cathode material. *Journal of Power Sources*, *243*, 78–87.

Dong, Y., Wang, L., Zhang, S., Zhao, Y., Zhou, J., Xie, H., & Goodenough, J. B. (2012). Two-phase interface in $LiMnPO_4$ nanoplates. *J. Power Sources*, *215*, 116–121.

Dong, Y., Zhao, Y., Duan, H., & Liang, Z. (2014). Enhanced electrochemical performance of $LiMnPO_4$ by Li + -conductive Li_3VO_4 surface coating. *Electrochimica Acta*, *132*, 244–250.

Dou, J., Kang, X., Wumaier, T., Hua, N., Han, Y., & Xu, G. (2012). Oxalic acid-assisted preparation of $LiFePO_4$/C cathode material for lithium-ion batteries. *Journal of Solid State Electrochemistry*, *16*(5), 1925–1931.

Dou, S. (2013). Review and prospect of layered lithium nickel manganese oxide as cathode materials for Li-ion batteries. *Journal of Solid State Electrochemistry*, *17*(4), 911–926.

Dou, S. (2015). Review and prospects of Mn-based spinel compounds as cathode materials for lithium-ion batteries. *Ionics*, *21*(11), 3001–3030.

Etacheri, V., Marom, R., Elazari, R., Salitra, G., & Aurbach, D. (2011). Challenges in the development of advanced Li-ion batteries : a review. *Energy & Environmental Science*, *4*, 3243–3262.

Fallis, A. . (2013). *Raman spectroscopy for nanomaterials characterization*. New York: Springer.

Fan, J., Yu, Y., Wang, Y., Wu, Q., Zheng, M., & Dong, Q. (2016). Nonaqueous synthesis of nano-sized $LiMnPO_4$@C as a cathode material for high performance lithium ion batteries. *Electrochimica Acta*, *194*, 52–58.

Fang, H., Pan, Z., Li, L., Yang, Y., Yan, G., Li, G., & Wei, S. (2008). The possibility of manganese disorder in $LiMnPO_4$ and its effect on the electrochemical activity. *Electrochemistry Communications*, *10*, 1071–1073.

Fang, H., Yi, H., Hu, C., Yang, B., Yao, Y., & Ma, W. (2012). Effect of Zn doping on the performance of $LiMnPO_4$ cathode for lithium ion batteries. *Electrochimica Acta*, *71*, 266–269.

Fang, L., Zhang, H., Zhang, Y., Liu, L., & Wang, Y. (2016). Design and synthesis of two-dimensional porous Fe-doped $LiCoPO_4$ nano-plates as improved cathode for lithium ion batteries. *Journal of Power Sources*, *312*, 101–108.

Fell, C. R., Chi, M., Meng, Y. S., & Jones, J. L. (2012). In situ X-ray diffraction study of the lithium excess layered oxide compound $Li[Li_{0.2}Ni_{0.2}Mn_{0.6}]O_2$ during electrochemical cycling. *Solid State Ionics*, *207*, 44–49.

Feng, Y., Zhang, H., Fang, L., Ouyang, Y., & Wang, Y. (2015). Designed synthesis of a unique single-crystal Fe- doped $LiNiPO_4$ nanomesh as an enhanced cathode for lithium ion batteries. *Journal of Materials Chemistry A: Materials for energy and sustainability*, *3*, 15969–15976.

Fu, L. J., Liu, H., Li, C., Wu, Y. P., Rahm, E., Holze, R., & Wu, H. Q. (2005). Electrode materials for lithium secondary batteries prepared by sol – gel methods. *Progress in Polymer Science*, *50*, 881–928.

Fu, X., Chang, Z., Chang, K., Li, B., Tang, H., Shangguan, E., … Wang, H. (2015). Glucose assisted synthesis of hollow spindle $LiMnPO_4$/C nanocomposites for high performance Li-ion batteries. *Electrochimica Acta*, *178*, 420–428.

Gaberscek, M., Dominko, R., & Jamnik, J. (2007). The meaning of impedance measurements of $LiFePO_4$ cathodes: A linearity study. *Journal of Power Sources*, *174*(2), 944–948.

Gan, Y., Chen, C., Liu, J., Bian, P., Hao, H., & Yu, A. (2015). Enhancing the performance of $LiMnPO_4$/C composites through Cr doping. *Journal of Alloys and Compounds*, *620*, 350–357.

Gao, H., Wang, L., Zhang, Y., Zhang, A., & Song, Y. (2014). Tartaric acid assisted synthesis of Li_2FeSiO_4/C : Effect of carbon content on the electrochemical performance of Li_2FeSiO_4/C for lithium ion batteries. *Powder Technology*, *253*, 638–643.

Gao, Z., Pan, X., Li, H., Xie, S., Yi, R., & Jin, W. (2013). Hydrothermal synthesis and electrochemical properties of dispersed $LiMnPO_4$ wedges. *CrystEngComm*, *15*, 7808–7814.

Gao, Z., Sun, K., Cong, L., Zhang, Y., Wang, R., Xie, H., … Su, Z. (2016). High performance 5 V $LiNi_{0.5}Mn_{1.5}O_4$ spinel cathode materials synthesized by an improved solid-state method. *Journal of Alloys and Compounds*, *654*, 257–263.

Gasteiger, H., Krischer, K., & Scrosati, B. (2013). Electrochemical cells: basics. In *Lithium Batteries: Advanced Technologies and Applications* (pp 1-19). New York: Wiley.

Girish, H., & Shao, G. (2015). Advances in high-capacity Li_2MSiO_4(M = Mn, Fe, Co, Ni, .) cathode materials for lithium-ion batteries. *RSC Advances*, *5*(1), 98666–98686.

Gong, C., Lv, W., Qu, L., Bankole, O. E., Li, G., Zhang, R., … Lei, L. (2014). Syntheses and electrochemical properties of layered $Li_{0.95}Na_{0.05}Ni_{1/3}Co_{1/3}Mn_{1/3}O_2$ and LiNi1/3Co1/3Mn1/3O2. *Journal of Power Sources*, *247*, 151–155.

Gong, Z., & Yang, Y. (2011). Recent advances in the research of polyanion-type cathode materials for Li ion batteries. *Energy & Environmental Science*, *4*, 3223–3242.

Gu, Y., Wang, H., Zhu, Y., Wang, L., Qian, Y., & Chu, Y. (2015). Hydrothermal synthesis of 3D-hierarchical hemoglobin-like $LiMnPO_4$ microspheres as cathode materials for lithium ion batteries. *Solid State Ionics*, *274*, 106–110.

Gummow, R. J., Han, G., Sharma, N., & He, Y. (2014). Li_2MnSiO_4 cathodes modified by phosphorous substitution and the structural consequences. *Solid State Ionics*, *259*, 29–39.

Guo, D., Li, B., Chang, Z., Tang, H., Xu, X., & Chang, K. (2014). Facile synthesis of $LiAl_{0.1}Mn_{1.9}O_4$ as cathode material for lithium ion batteries : towards rate and cycling capabilities at an elevated temperature. *Electrochimica Acta*, *134*, 338–346.

Guo, H., Wu, C., Xie, J., Zhang, S., Cao, G., & Zhao, X. (2014). Controllable synthesis of high-performance $LiMnPO_4$ nanocrystals by a facile one-spot solvothermal process. *Journal of Materials Chemistry A*, *2*(27), 10581.

Guo, X., Yan, H., Zhao, S., Li, Z., Li, Y., & Liang, X. (2013). Effect of calcining temperature on particle size of hydroxyapatite synthesized by solid-state reaction at room temperature. *Advanced Powder Technology*, *24*(6), 1034–1038.

Gutierrez, A., Ruimin Qiao, Wang, L., Wanli, Y., Feng, W., & Manthiram Arumugam. (2014). High-Capacity, Aliovalently Doped Olivine $LiMn_{1-3x/2}V_{x\square x2}PO_4$ Cathodes without Carbon Coating. *Chemistry of materials*, *26*, 3018–3026.

Han, B., Meng, X., Ma, L., & Nan, J. (2016). Nitrogen-doped carbon decorated $LiFePO_4$ composite synthesized via a microwave heating route using polydopamine as carbon – nitrogen precursor. *Ceramics International*, *42*(2),

2789–2797.

Han, D., Ryu, W., Kim, W., Lim, S., Kim, Y., Eom, J., & Kwon, H. (2013). Tailoring Crystal Structure and Morphology of $LiFePO_4$/C Cathode Materials Synthesized by Heterogeneous Growth on Nanostructured $LiFePO_4$ Seed Crystals. *Applied Materials Interfaces*, *5*, 1342–1347.

Han, H., Qiu, F., Liu, Z., & Han, X. (2015). ZrO_2-coated $Li_3V_2(PO_4)_3$/C nanocomposite : A high-voltage cathode for rechargeable lithium-ion batteries with remarkable cycling performance. *Ceramics International*, *41*(7), 8779–8784.

Hanafusa, R., Kotani, K., Ishidzu, K., Oka, Y., & Nakamura, T. (2016). Electrochemical study of $LiMn_{1.5}Ni_{0.5}O_4$ spinel oxides prepared by two-step process. *Solid State Ionics*, *288*, 180–183.

Hee, W., Yuan, D., Qian, J., Ai, X., Yang, A., & Cao, Y. (2013). Enhanced high-rate capability and cycling stability of Na-stabilized layered $Li_{1.2}[Co_{0.13}Ni_{0.13}Mn_{0.54}]O_2$ cathode material. *J. Mater. Chem. A*, *1*, 11397–11403.

Hildebrandt, S., Eva, A., Komissinskiy, P., Fasel, C., Fritsch, I., & Alff, L. (2012). Sol – gel synthesis of sodium and lithium based materials. *Journal of Sol Gel Science and Technology*, *63*, 307–314.

Hong, Y., Tang, Z., Hong, Z., & Zhang, Z. (2014). $LiMn_{1-x}Fe_xPO_4$ (x = 0, 0.1, 0.2) nanorods synthesized by a facile solvothermal approach as high performance cathode materials for lithium-ion batteries. *Journal of Power Sources*, *248*, 655–659.

Hong, Y., Tang, Z., & Zhang, Z. (2015). Enhanced electrochemical properties of $LiMnPO_4$/C composites by tailoring polydopamine-derived carbon coating. *Electrochimica Acta*, *176*, 369–377.

Hu, C. L., Yi, H. H., Wang, F. X., Xiao, S. Y., Wu, Y. P., Wang, D., & He, D. L. (2014). Boron doping at P-site to improve electrochemical performance of $LiMnPO_4$ as cathode for lithium ion battery. *Journal of Power Sources*, *255*, 355–359.

Hu, C., Yi, H., Fang, H., Yang, B., Yao, Y., Ma, W., & Dai, Y. (2010). Improving the electrochemical activity of $LiMnPO_4$ via Mn-site co-substitution with Fe and Mg. *Electrochemistry Communications*, *12*(12), 1784–1787.

Hu, G., Zhang, M., Liang, L., Peng, Z., Du, K., & Cao, Y. (2016). Mg–Al–B co-substitution $LiNi_{0.5}Co_{0.2}Mn_{0.3}O_2$ cathode materials with improved cycling performance for lithium-ion battery under high cutoff voltage. *Electrochimica Acta*, *190*, 264–275.

Hu, L., Qiu, B., Xia, Y., Qin, Z., Qin, L., Zhou, X., & Liu, Z. (2014). Solvothermal synthesis of Fe-doping $LiMnPO_4$ nanomaterials for Li-ion batteries. *Journal of Power Sources*, *248*, 246–252.

Hu, M., Pang, X., & Zhou, Z. (2013). Recent progress in high-voltage lithium ion batteries. *Journal of Power Sources*, *237*, 229–242.

Hu, Y., Wang, G., Liu, C., Chou, S., Zhu, M., & Jin, H. (2016). $LiFePO_4$/C nanocomposite synthesized by a novel carbothermal reduction method and its electrochemical performance. *Ceramics International*, *42*(9), 11422–11428.

Huang, Q., Wu, Z., Su, J., Long, Y., Lv, X., & Wen, Y. (2016). Synthesis and electrochemical performance of Ti – Fe co-doped $LiMnPO_4$/C as cathode material for lithium-ion batteries. *Ceramics International*, *42*(9), 11348–11354.

Huang, Y., Chernova, N. A., Yin, Q., Wang, Q., Quackenbush, N. F., Leskes, M., … Whittingham, M. S. (2016). What Happens to $LiMnPO_4$ upon Chemical Delithiation? *Inorganic Chemistry*, *55*, 4335–4343.

Hudaya, C., Hun, J., Kee, J., & Choi, W. (2014). SnO_2-coated $LiCoO_2$ cathode material for high-voltage applications in lithium-ion batteries. *Solid State Ionics*, *256*, 89–92.

K. J. K., Assat, G., & Manthiram, A. (2015). Microwave-Assisted Solvothermal Synthesis of Three Polymorphs of $LiCoPO_4$ and Their Electrochemical Properties. *Chemistry of materials*, *27*, 5543–5549.

Ilango, P. R., Subburaj, T., Prasanna, K., Jo, Y. N., & Lee, C. W. (2015). Physical and electrochemical performance of $LiNi_{1/3}Co_{1/3}Mn_{1/3}O_2$ cathodes coated by Sb_2O_3 using a sol–gel process. *Materials Chemistry and Physics*, *158*, 45–51.

Iturrondobeitia, A., Goni, A., Muro, I. G. De, Lezama, L., Kim, C., Doe, M., & Cabana, J. (2015). High-Voltage Cathode Materials for Lithium-Ion Batteries: Freeze-Dried $LiMn_{0.8}Fe_{0.1}M_{0.1}PO_4$/C (M = Fe, Co, Ni, Cu) Nanocomposites. *Inorganic Chemistry*, *54*, 2671–2678.

Jian, X. M., Wenren, H. Q., Huang, S., Shi, S. J., Wang, X. L., Gu, C. D., & Tu, J. P. (2014). Oxalic acid-assisted combustion synthesized $LiVO_3$ cathode material for lithium ion batteries. *Journal of Power Sources*, *246*, 417–422.

Jiang, Y., Yang, Z., Mei, F., Zhou, Y., Xu, J., & Huang, Y. (2016). Self-template synthesis of $Li_{1.13}Ni_{0.30}Mn_{0.57}O_2$ anothorn spheres and nanorods as high-performance cathode materials for lithium-ion batteries. *Journal of Alloys and Compounds*, *658*, 867–874.

Jie-qun, L. I. U., Sheng-kui, Z., Ling, W. U., Kang, W. A. N., & Fan, L. Ü. (2012). Electrochemical performance of $LiVPO_4F$/C synthesized by different methods. *Transactions of Nonferrous Metals Society of China*, *22*, 157–161.

Jin, Y., Lu, M., Wang, T., Yang, C., & Duh, J. (2014). Synthesis of high-voltage spinel cathode material with tunable particle size and improved temperature durability for lithium ion battery. *Journal of Power Sources*, *262*, 483–487.

Jo, M., Yoo, H., Jung, Y. S., & Cho, J. (2012). Carbon-coated nanoclustered $LiMn_{0.71}Fe_{0.29}PO_4$ cathode for lithium-ion batteries. *Journal of Power Sources*, *216*, 162–168.

Ju, S. H., & Kim, D.-W. (2013). Effect of Calcination Temperature on the Structure and Electrochemical Performance of $LiMn_{1.5}Ni_{0.5}O_4$ Cathode Materials. *Bulletin of the*

Korean Chemical Society, *34*(1), 59–62.

Jugovic, D., & Uskokovi, D. (2009). A review of recent developments in the synthesis procedures of lithium iron phosphate powders. *Journal of Power Sources*, *190*, 538–544.

Kandhasamy, S., Pandey, A., & Minakshi, M. (2012). Polyvinylpyrrolidone assisted sol–gel route $LiCo_{1/3}Mn_{1/3}Ni_{1/3}PO_4$ composite cathode for aqueous rechargeable battery. *Electrochimica Acta*, *60*, 170–176.

Kandhasamy, S., Singh, P., Thurgate, S., Ionescu, M., Appadoo, D., & Minakshi, M. (2012). Olivine-type cathode for rechargeable batteries : Role of chelating agents. *Electrochimica Acta*, *82*, 302–308.

Kang, J., Song, J., Kim, S., Gim, J., Jo, J., Mathew, V., … Kim, J. (2013). A high voltage $LiMnPO_4$–$LiMn_2O_4$ nanocomposite cathode synthesized by a one-pot pyro synthesis for Li-ion batteries. *RSC advances*, *3*, 25640–25643.

Karthickprabhu, S., Hirankumar, G., Maheswaran, A., Bella, R. S. D., & Sanjeeviraja, C. (2014). Structural and electrical studies on Zn^{2+} doped $LiCoPO_4$. *Journal of Electrostatics*, *72*, 181–186.

Kayyar, A., Huang, J., Samiee, M., & Luo, J. (2012). Construction and Testing of Coin Cells of Lithium Ion Batteries. *Journal of Visualized Experiments*, (66), 1–5.

Kim, G. T., Jeong, S. S., Joost, M., Rocca, E., Winter, M., Passerini, S., & Balducci, (2011). Use of natural binders and ionic liquid electrolytes for greener and safer lithium-ion batteries. *Journal of Power Sources*, *196*(4), 2187–2194.

Kim, J. C., Seo, D., & Ceder, G. (2015). Theoretical capacity achieved in a $LiMn_{0.5}Fe_{0.4}Mg_{0.1}BO_3$ cathode by using topological disorder. *Energy & Environmental Science*, *8*, 1790–1798.

Kim, J., Vijaya, R., Zhu, L., & Kim, Y. (2015). Improving electrochemical properties of porous iron substituted lithium manganese phosphate in additive addition electrolyte. *Journal of Power Sources*, *275*, 106–110.

Kim, K., Cho, Y., Kam, D., Kim, H., & Lee, J. (2010). Effects of organic acids as reducing agents in the synthesis of $LiFePO_4$. *Journal of Alloys and Compounds*, *504*(1), 166–170.

Kim, T., Park, H., Lee, M., Lee, S., & Song, H. (2012). Restricted growth of $LiMnPO_4$ nanoparticles evolved from a precursor seed. *Journal of Power Sources*, *210*, 1–6.

Kim, W., Ryu, W., Han, D., Lim, S., Eom, J., & Kwon, H. (2014). Fabrication of Graphene Embedded $LiFePO_4$ Using a Catalyst Assisted Self Assembly Method as a Cathode Material for High Power Lithium-Ion Batteries. *Applied Materials Interfaces*, *6*, 4731–4736.

Kisu, K., Iwama, E., Onishi, W., & Nakashima, S. (2014). Ultrafast nano-spherical single-crystalline $LiMn_{0.792}Fe_{0.198}Mg_{0.010}PO_4$ solid-solution confined among unbundled interstices of SGCNTs. *Journal of Materials Chemistry A: Materials*

for energy and sustainability, *2*, 20789–20798.

Koleva, V., Zhecheva, E., & Stoyanova, R. (2011). Facile synthesis of $LiMnPO_4$ olivines with a plate-like morphology from a dittmarite-type $KMnPO_4 \cdot H_2O$ precursor. *Dalton Transition*, *40*(100), 7385–7394.

Kong, J. Z., Wang, S. S., Tai, G. A., Zhu, L., Wang, L. G., Zhai, H. F., … Li, H. (2016). Enhanced electrochemical performance of $LiNi_{0.5}Co_{0.2}Mn_{0.3}O_2$ cathode material by ultrathin ZrO_2 coating. *Journal of Alloys and Compounds*, *657*, 593–600.

Korona, K. P., Papierska, J., Kamińska, M., Witowski, A., Michalska, M., & Lipińska, L. (2011). Raman measurements of temperature dependencies of phonons in $LiMnPO_4$. *Materials Chemistry and Physics*, *127*, 391–396.

Kou, L., Chen, F., Tao, F., Dong, Y., & Chen, L. (2015). High rate capability and cycle performance of Ce-doped $LiMnPO_4$/C via an efficient solvothermal synthesis in water/diethylene glycol system. *Electrochimica Acta*, *173*, 721–727.

Kuang, Q., Zhao, Y., & Liang, Z. (2011). Synthesis and electrochemical properties of Na-doped $Li_3V_2(PO_4)_3$ cathode materials for Li-ion batteries. *Journal of Power Sources*, *196*(23), 10169–10175.

Kucinskis, G., Bajars, G., & Kleperis, J. (2013). Graphene in lithium ion battery cathode materials: A review. *Journal of Power Sources*, *240*, 66–79.

Kumar, P. R., Venkateswarlu, M., & Satyanarayana, N. (2012). Three-dimensional lithium manganese phosphate microflowers for lithium-ion battery applications. *Journal of Applied Electrochemistry*, *42*, 163–167.

Kwon, N. H., & Fromm, K. M. (2012). Enhanced electrochemical performance of <30nm thin $LiMnPO_4$ nanorods with a reduced amount of carbon as a cathode for lithium ion batteries. *Electrochimica Acta*, *69*, 38–44.

Kwon, S. N., Song, J., & Mumm, D. R. (2011). Effects of cathode fabrication conditions and cycling on the electrochemical performance of $LiNiO_2$ synthesized by combustion and calcination. *Ceramics International*, *37*(5), 1543–1548.

Lee, E.-S., Huq, A., & Manthiram, A. (2013). Understanding the effect of synthesis temperature on the structural and electrochemical characteristics of layered-spinel composite cathodes for lithium-ion batteries. *Journal of Power Sources*, *240*, 193–203.

Lee, J., Park, M., Anass, B., Park, J., Paik, M., & Doo, S. (2010). Electrochemical lithiation and delithiation of $LiMnPO_4$: Effect of cation substitution. *Electrochimica Acta*, *55*(13), 4162–4169.

Lee, K., Kang, L., Uhm, S., Sik, J., Kim, D., & Seon, H. (2013). Synthesis and characterization of $LiMnBO_3$ cathode material for lithium ion batteries. *Current Applied Physics*, *13*(7), 1440–1443.

Lee, S., & Soo, S. (2013). Journal of Solid State Chemistry Lithium transition metal fl uorophosphates (Li_2CoPO_4F and Li_2NiPO_4F) as cathode materials for lithium ion

battery from atomistic simulation. *Journal of Solid State Chemistry*, *204*, 329–334.

Lee, Y. C., Han, D. W., Park, M., Jo, M. R., Kang, S. H., Lee, J. K., & Kang, Y. (2014). Tailored Surface Structure of $LiFePO_4C$ Nano fibers by Phosphidation and Their Electrochemical Superiority for Lithium Rechargeable Batteries. *Applied Materials Interfaces*, *6*, 9435–9441.

Lee, Y., & Lee, H. (2014). Improved lithium storage capacities of $LiMnBO_3$/C via simple high-energy milling. *Materials Letters*, *132*, 401–404.

Lemine, O. M. (2009). Microstructural characterisation of α- Fe_2O_3 nanoparticles using, XRD line profiles analysis, FE-SEM and FT-IR. *Superlattices and Microstructures*, *45*(6), 576–582.

Li, C., Hua, N., & Wang, C. (2011). Chelation-assisted method for the preparation of cathode. *Journal of Solid State Electrochemistry*, *15*, 1971–1976.

Li, H., Luo, Y., Xie, J., Zhang, Q., & Yan, L. (2015). Effect of lithium and fluorine doping on the electrochemical and thermal stability of $LiNi_{0.5}Mn_{1.5}O_4$ spinel cathode material. *Journal of Alloys and Compounds*, *639*, 346–351.

Li, H., Wang, Y., Yang, X., Liu, L., Chen, L., & Wei, J. (2014). Improved electrochemical performance of 5 V $LiCoPO_4$ cathode materials via yttrium doping. *Solid State Ionics*, *255*, 84–88.

Li, J., Bao, A., & Mo, G. (2014). Effect of multi-walled carbon nanotubes on the electrochemical performance of $LiVPO_4F$ cathode material for rechargeable lithium-ion batteries. *Solid State Ionics*, *264*, 45–48.

Li, J., & Hitch, M. (2016). Characterization of the microstructure of mechanically-activated olivine using X-ray diffraction pattern analysis. *Minerals Engineering*, *86*, 24–33.

Li, J., Wang, L., Zhang, Q., & He, X. (2009). Electrochemical performance of SrF2-coated $LiNi_{1/3}Co_{1/3}Mn_{1/3}O_2$ cathode materials for Li-ion batteries. *Journal of Power Sources*, *190*(1), 149–153.

Li, L., Liu, J., Chen, L., Xu, H., Yang, J., & Qian, Y. (2013). Effect of different carbon sources on the electrochemical properties of rod-like $LiMnPO_4$–C nanocomposites. *RSC Advances*, *4*, 6847–6852.

Li, S., Xu, L., Li, G., Wang, M., & Zhai, Y. (2013). In-situ controllable synthesis and performance investigation of carbon-coated monoclinic and hexagonal $LiMnBO_3$ composites as cathode materials in lithium-ion batteries. *Journal of Power Sources*, *236*, 54–60.

Li, W., Zhang, H., Mu, Y., Liu, L., & Wang, Y. (2015). Unique synthesis of novel octahedral micro/nano-hierarchical $LiFePO_4$ cages as an enhanced cathode material for lithium-ion batteries. *Journal of Materials Chemistry A: Materials for energy and sustainability*, *3*, 15661–15667.

Li, X., Liu, S., Jin, H., Meng, Y., & Liu, Y. (2014). Ionothermal synthesis and

electrochemical analysis of Fe doped $LiMnPO_4$/C composites as cathode materials for lithium-ion batteries. *Journal of Alloys and Compounds*, *614*, 7–12.

Liao, L., Wang, H., Guo, H., Zhu, P., Xie, J., Jin, C., … Zhao, X. (2015). Facile solvothermal synthesis of ultrathin $LiFe_xMn_{1-x}PO_4$ nanoplates as advanced cathodes with long cycle life and superior rate capability. *Journal of Materials Chemistry A: Materials for energy and sustainability*, *3*, 19368–19375.

Li-e Li, Jing Liu, Liang Chen, Huayun Xu, Jian Yang and Yitai Qian. (2013). Effect of different carbon sources on the electrochemical properties of rod-like $LiMnPO_4$–C nanocomposites. *RSC advances*, *4*, 6847–6852.

Lin, M., Chen, Y., Chen, B., Wu, X., Kam, K., Lu, W., … Yuan, J. (2014). Morphology-Controlled Synthesis of Self-Assembled $LiFePO_4$/C/RGO for High-Performance Li-Ion Batteries. *Applied Materials Interfaces*, *6*, 17556–17563.

Lingjun, L., Ming, X., Zhaoyong, C., Xiang, Z., Qiaobao, Z., Huali, Z., Kaili, Z. (2015). High-performance lithium-rich layered oxide materials: Effects of chelating agents on microstructure and electrochemical properties. *Electrochimica Acta*, *174*, 446–455.

Liu, C., Neale, Z. G., & Cao, G. (2016). Understanding electrochemical potentials of cathode materials in rechargeable batteries. *Biochemical Pharmacology*, *19*(2), 109–123.

Liu, J., Liao, W., & Yu, A. (2014). Electrochemical performance and stability of $LiMn_{0.6}Fe_{0.4}PO_4$/C composite. *Journal of Alloys and Compounds*, *587*, 133–137.

Liu, J., Liu, X., Huang, T., & Yu, A. (2013). Synthesis of nano-sized $LiMnPO_4$ and in situ carbon coating using a solvothermal method. *Journal of Power Sources*, *229*, 203–209.

Liu, L., Qiu, Y., Mai, Y., Wu, Q., & Zhang, H. (2015). Influences of neodymium doping on magnetic and electrochemical properties of $Li_3V_2(PO_4)_3$/C synthesized via a sol-gel method. *Journal of Power Sources*, *295*, 246–253.

Liu, M., Huang, H., Lin, C., Chen, J., & Liao, S. (2014). Mg gradient-doped $LiNi_{0.5}Mn_{1.5}O_4$ as the cathode material for Li-ion batteries. *Electrochimica Acta*, *120*, 133–139.

Liu, T., Wu, B., & Wu, X. (2014). Realizing Fe substitution through diffusion in preparing $LiMn_{1-x}Fe_xPO_4$-C cathode materials from MnPO4·H2O. *Solid State Ionics*, *254*, 72–77.

Liu, T., Zhao, S., Wang, K., & Nan, C. (2012). CuO-coated $Li[Ni_{0.5}Co_{0.2}Mn_{0.3}]O_2$ cathode material with improved cycling performance at high rates. *Electrochimica Acta*, *85*, 605–611.

Liu, X., Huang, T., & Yu, A. (2015). Surface phase transformation and CaF_2 coating for enhanced electrochemical performance of Li-rich Mn-based cathodes. *Electrochimica Acta*, *163*, 82–92.

Liu, X.-M., Gao, W.-L., & Ji, B.-M. (2011). Synthesis of $LiNi_{1/3}Co_{1/3}Mn_{1/3}O_2$ nanoparticles by modified Pechini method and their enhanced rate capability. *Journal of Sol-Gel Science and Technology*, *61*(1), 56–61.

Liu, Y., Wang, S., Tao, D., Dai, Y., & Yu, J. (2015). Electrochemical characterization for lithium vanadium phosphate with different calcination temperatures prepared by the sol–gel method. *Materials Characterization*, *107*, 189–196.

Longo, R. C., Xiong, K., Kc, S., & Cho, K. (2014). Crystal structure and multicomponent effects in Tetrahedral Silicate Cathode Materials for Rechargeable Li-ion Batteries. *Electrochimica Acta*, *121*, 434–442.

Lu, C., Wu, H., Chen, B., Liu, H., & Zhang, Y. (2015a). cathode material by uniform surface nanocoating with samarium fluoride through depositional-hydrothermal route. *Journal Of Alloys And Compounds*, *634*, 75–82.

Lu, C., Wu, H., Chen, B., Liu, H., & Zhang, Y. (2015b). Improving the electrochemical properties of $Li_{1.2}Mn_{0.52}Co_{0.08}Ni_{0.2}O_2$ cathode material by uniform surface nanocoating with samarium fluoride through depositional-hydrothermal route. *Journal of Alloys and Compounds*, *634*, 75–82.

Lu, C., Wu, H., Zhang, Y., Liu, H., Chen, B., Wu, N., & Wang, S. (2014). Cerium fluoride coated layered oxide $Li_{1.2}Mn_{0.54}Ni_{0.13}Co_{0.13}O_2$ as cathode materials with improved electrochemical performance for lithium ion batteries. *Journal of Power Sources*, *267*, 682–691.

Lu, X., Shang, Y., Zhang, S., & Deng, C. (2015). Enhanced Lithium Ion Transport by Superionic Pathways Formed on the Surface of Two-dimensional Structured $Li_{0.85}Na_{0.15}V_3O_8$ for High-Performance Lithium Ion Batteries. *Electrochimica Acta*, *155*, 148–156.

Lu, Z., Chen, H., Robert, R., Zhu, B. Y. X., Deng, J., Wu, L., Grey, C. P. (2011). Citric Acid- and Ammonium-Mediated Morphological Transformations of Olivine $LiFePO_4$ Particles. *Chemistry of materials*, *23*, 2848–2859.

Luo, W. (2015). Effect of morphology on the physical and electrochemical properties of the high-voltage spinel cathode $LiMn_{1.5}Ni_{0.5}O_4$. *Journal of Alloys and Compounds*, *636*, 24–28.

Lv, X., Xu, Z., Li, J., Chen, J., & Liu, Q. (2016). Insights into stability , electronic properties , defect properties and Li ions migration of Na, Mg and Al-doped $LiVPO_4F$ for cathode materials of lithium ion batteries : A first-principles investigation. *Journal of Solid State Chemistry*, *239*, 228–236.

Ma, H., Shieh, K., & Qiao, T. X. (2006). Study of Transmission Electron Microscopy (TEM) and Scanning Electron Microscopy (SEM). *Nature and Science*, *4*(3), 14–22.

Ma, R., Shao, L., Wu, K., Lao, M., Shui, M., Chen, C., Wang, D., Long, N., Yuanlong, R., Shu, J. (2013). Electrochemical behaviors of hexagonal $LiMnBO_3$ as lithium storage host material for lithium-ion batteries. *Ceramics International*, *39*(8), 9309–9317.

Ma, R., Shao, L., Wu, K., Shui, M., Wang, D., Long, N., Yuanlong, R., Shu, J. (2014). Effects of oxidation on structure and performance of $LiVPO_4F$ as cathode material for lithium-ion batteries. *Journal of Power Sources*, *248*, 874–885.

Ma, T., Muslim, A., & Su, Z. (2015). Microwave synthesis and electrochemical properties of lithium manganese borate as cathode for lithium ion batteries. *Journal of Power Sources*, *282*, 95–99.

Ma, Z., Fan, Y., Shao, G., Wang, L., Song, J., Wang, G., & Liu, T. (2014). Cupric ion substituted $LiFePO_4$/C composites with enhanced electrochemical performance for Li-ion batteries. *Electrochimica Acta*, *139*, 256–263.

Ma, Z., Shao, G., Fan, Y., Wang, G., Song, J., & Liu, T. (2014). Tunable Morphology Synthesis of $LiFePO_4$ Nanoparticles as Cathode Materials for Lithium Ion Batteries. *Applied Materials Interfaces*, *6*, 9236–9244.

Markevich, E., Sharabi, R., Haik, O., Borgel, V., Salitra, G., Aurbach, D., … Stinner, C. (2011). Raman spectroscopy of carbon-coated $LiCoPO_4$ and $LiFePO_4$ olivines. *Journal of Power Sources*, *196*, 6433–6439.

Mathew, V., Gim, J., Kim, E., Alfaruqi, M. H., Song, J., & Ahn, D. (2014). A rapid polyol combustion strategy towards scalable synthesis of nanostructured $LiFePO_4$/C cathodes for Li-ion batteries. *Journal of Solid State Electrochemistry*, *18*, 1557–1567.

Michalska, M., Lipińska, L., Sikora, a., Ziółkowska, D., Korona, K. P., & Andrzejczuk, M. (2015). Structural and morphological studies of manganese-based cathode materials for lithium ion batteries. *Journal of Alloys and Compounds*, *632*, 256–262.

Minakshi, M., & Kandhasamy, S. (2012). Utilizing active multiple dopants (Co and Ni) in olivine $LiMnPO_4$. *Current Opinion in Solid State & Materials Science*, *16*(4), 163–167.

Minakshi, M., Kandhasamy, S., & Meyrick, D. (2012). Synthetic strategies for better battery performance through advances in materials and chemistry : Olivine $LiMn_{1/3}Co_{1/3}Ni_{1/3}PO_4$. *Journal of Alloys and Compounds*, *544*, 62–66.

Minakshi, M., & Meyrick, D. (2013). Reversible sodiation in maricite $NaMn_{1/3}Co_{1/3}Ni_{1/3}PO_4$ for renewable energy storage. *Journal of Alloys and Compounds*, *555*, 10–15.

Mn, L., Deng, J., Xu, Y., Xiong, L., Li, L., Sun, X., & Zhang, Y. (2016). Improving the fast discharge performance of high-voltage $LiNi_{0.5}Mn_{1.5}O_4$ spinel by Cu^{2+},Al^{3+},Ti^{4+} tri-doping. *Journal of Alloys and Compounds*, *677*, 18–26.

Moon, S., Muralidharan, P., & Kim, D. K. (2012). Carbon coating by high-energy milling and electrochemical properties of $LiMnPO_4$ obtained in polyol process. *Ceramics International*, *38*, S471–S475.

Moriya, M., Miyahara, M., Hokazono, M., & Sasaki, H. (2014). High-energy X-ray powder diffraction and atomic-pair distribution- function studies of charged /

discharged structures in carbon- hybridized Li_2MnSiO_4 nanoparticles as a cathode material for lithium- ion batteries. *Journal of Power Sources*, *263*, 7–12.

Muhammad, S., Lee, S., Kim, H., Yoon, J., Jang, D., Yoon, J., Park, J., Yoon, W. (2015). Deciphering the thermal behavior of lithium rich cathode material by in situ X-ray diffraction technique. *Journal of Power Sources*, *285*, 156–160.

Muruganantham, R., Sivakumar, M., & Subadevi, R. (2015a). A facile synthesis and characterization of $LiFePO_4$/C using simple binary reactants with oxalic acid by polyol technique and other high temperature methods. *Journal of Materials Science: Materials in Electronics*, *26*, 2095–2106.

Muruganantham, R., Sivakumar, M., & Subadevi, R. (2015b). Enhanced rate performance of multiwalled carbon nanotube encrusted olivine type composite cathode material using polyol technique. *Journal of Power Sources*, *300*, 496–506.

Muruganantham, R., Sivakumar, M., & Subadevi, R. (2016). Synthesis and electrochemical characterization of olivine-type lithium iron phosphate cathode materials via different techniques. *Ionics*, *22*(9), 1557-1565.

Muruganantham, R., Sivakumar, M., Subadevi, R., & Wu, N. (2015). A facile synthesis and characterization of $LiFePO_4$/C using simple binary reactants with oxalic acid by polyol technique and other high temperature methods. *Journal of Materials Science: Materials in Electronics*, *26*(4), 2095–2106.

Naceur, H., Megriche, A., & El Maaoui, M. (2014). Effect of sintering temperature on microstructure and electrical properties of $Sr_{1-x}(Na_{0.5}Bi_{0.5})_xBi_2Nb_2O_9$ solid solutions. *Journal of Advanced Ceramics*, *3*(1), 17–30.

Nam, T., Doan, L., Bakenov, Z., & Taniguchi, I. (2010). Preparation of carbon coated $LiMnPO_4$ powders by a combination of spray pyrolysis with dry ball-milling followed by heat treatment. *Advanced Powder Technology*, *21*(2), 187–196.

Nam, T., Doan, L., & Taniguchi, I. (2011). Cathode performance of $LiMnPO_4$/C nanocomposites prepared by a combination of spray pyrolysis and wet ball-milling followed by heat treatment. *Journal of Power Sources*, *196*(3), 1399–1408.

Nannan, Z., Yongsheng, L. I., Xiaoke, Z. H. I., & Li, W. (2016). Effect of Ce3+ doping on the properties of $LiFePO_4$ cathode material. *Journal of Rare Earths*, *34*(2), 174–180.

Ni, J., & Gao, L. (2011). Effect of copper doping on $LiMnPO_4$ prepared via hydrothermal route. *Journal of Power Sources*, *196*(15), 6498–6501.

Ni, J., & Li, L. (2015). 3D porous hierarchical Li_2FeSiO_4/C for rechargeable lithium batteries. *Journal of Materials Chemistry A: Materials for energy and sustainability*, *3*(22), 11782–11786.

Nie, P., Shen, L., Zhang, F., Chen, L., Deng, H., & Zhang, X. (2012). Flower-like $LiMnPO_4$ hierarchical microstructures assembled from single- crystalline nanosheets for lithium-ion batteries. *CrystEngComm*, *14*(13), 4284–4288.

Oghbaei, M., Baniasadi, F., & Asgari, S. (2016). Lithium iron silicate sol gel synthesis and electrochemical investigation. *Journal of Alloys and Compounds*, *672*, 93–97.

Oh, R.-G., Hong, J.-E., Jung, H.-W., & Ryu, K.-S. (2015). Electrochemical properties of $Li_{3-x}Na_xV_{2-x}Ti_x(PO_4)_3$/C cathode materials in lithium ion batteries. *Journal of Power Sources*, *295*, 1–8.

Örnek, A., Can, M., & Ye, A. (2016). Improving the cycle stability of $LiCoPO_4$ nanocomposites as 4.8 V cathode: Stepwise or synchronous surface coating and Mn substitution. *Materials Characterization*, *116*, 76–83.

Örnek, A., & Kazancioglu, M. Z. (2016). A novel and effective strategy for producing core-shell $LiNiPO_4$/C cathode material for excellent electrochemical stability using a long-time and low-level microwave approach. *Scripta Materilia*, *122*, 45–49.

Ottmann, a., Jähne, C., Meyer, H.-P., & Klingeler, R. (2015). Structural, magnetic, and electrochemical properties of $LiMn_{1-x}Ni_xPO_4$. *Materials Research Bulletin*, *63*, 6–12.

Ottmann, A., Jähne, C., Meyer, H.-P., & Klingeler, R. (2015). Structural, magnetic, and electrochemical properties of $LiMn_{1-x}Ni_xPO_4$. *Materials Research Bulletin*, *63*, 6–12.

Padhi, A. K., Nanjundaswamy, K. S., & Goodenough, J. B. (1997). Phospho-olivines as Positive-Electrode Materials for Rechargeable Lithium Batteries. *Journal of Electrochemical Society*, *144*(4) , 1188–1194.

Pan, A., Zhang, J. G., Cao, G., Liang, S., Wang, C., Nie, Z., … Liu, J. (2011). Nanosheet-structured LiV_3O_8 with high capacity and excellent stability forhigh energy lithium batteries. *Journal of Materials Chemistry*, *21*, 10077–10084.

Pan, X. L., Xu, C. Y., Hong, D., Fang, H. T., & Zhen, L. (2013). Hydrothermal synthesis of well-dispersed $LiMnPO_4$ plates for lithium ion batteries cathode. *Electrochimica Acta*, *87*, 303–308.

Pan, X., Xu, C., & Zhen, L. (2012). Synthesis of $LiMnPO_4$ microspheres assembled by plates, wedges and prismswith different crystallographic orientations and their electrochemical performance. *CrystEngComm*, *14*(100), 6412–6418.

Park, S.-H., Shin, S.-S., & Sun, Y.-K. (2006). The effects of Na doping on performance of layered $Li_{1.1-x}Na_x[Ni_{0.2}Co_{0.3}Mn_{0.4}]O_2$ materials for lithium secondary batteries. *Materials Chemistry and Physics*, *95*(2-3), 218–221.

Pieczonka, N. P. W., Liu, Z., & Kim, J. (2013). Comparative study of $LiMnPO_4$/C cathodes synthesized by polyol and solid-state reaction methods for Li-ion batteries. *Journal of Power Sources*, *230*, 122–129.

Pitchai, R., Thavasi, V., Mhaisalkar, S. G., & Ramakrishna, S. (2011). Nanostructured cathode materials: a key for better performance in Li-ion batteries. *Journal of Materials Chemistry*, *21*(30), 11040.

Potapenko, A. V, & Kirillov, S. A. (2014). Lithium manganese spinel materials for

high-rate electrochemical applications. *Journal of Energy Chemistry*, *23*(5), 543–558.

Prabu, M., Reddy, M. V, Selvasekarapandian, S., Rao, G. V. S., & Chowdari, B. V. R. (2012). Synthesis, impedance and electrochemical studies of lithium iron fluorophosphate, $LiFePO_4F$ cathode. *Electrochimica Acta*, *85*, 572–578.

Prabu, M., Selvasekarapandian, S., Kulkarni, a. R., Karthikeyan, S., Hirankumar, G., & Sanjeeviraja, C. (2011). Ionic transport properties of $LiCoPO_4$ cathode material. *Solid State Sciences*, *13*(9), 1714–1718.

Prabu, M., Selvasekarapandian, S., Kulkarni, A. R., Karthikeyan, S., & Sanjeeviraja, C. (2012). Influence of europium doping on conductivity of $LiNiPO_4$. *Transactions of Nonferrous Metals Society of China*, *22*, 342–347.

Qian, Y., Deng, Y., Shi, Z., Zhou, Y., Zhuang, Q., & Chen, G. (2013). Sub-micrometer-sized $LiMn_{1.5}Ni_{0.5}O_4$ spheres as high rate cathode materials for long-life lithium ion batteries. *Electrochemistry Communications*, *27*(3), 92–95.

Qin, Z., Zhou, X., Xia, Y., Tang, C., & Liu, Z. (2012). Morphology controlled synthesis and modification of high-performance $LiMnPO_4$ cathode materials for Li-ion batteries. *Journal of Materials Chemistry*, *22*, 21144–21153.

Qing, R., Yang, M., Shirley, Y., & Sigmund, W. (2013). Synthesis of $LiNi_xFe_{1-x}PO_4$ solid solution as cathode materials for lithium ion batteries. *Electrochimica Acta*, *108*, 827–832.

Qiu, B., Wang, J., Xia, Y., Liu, Y., Qin, L., Yao, X., & Liu, Z. (2013). Effects of Na+ contents on electrochemical properties of $Li_{1.2}Ni_{0.13}Co_{0.13}Mn_{0.54}O_2$ cathode materials. *Journal of Power Sources*, *240*, 530–535.

Qu, L., Fang, S., Yang, L., & Hirano, S. (2012). Li_2FeSiO_4/C cathode material synthesized by template-assisted sol gel process with Fe_2O_3 microsphere. *Journal of Power Sources*, *217*, 243–247.

Qu, L., Fang, S., Yang, L., & Hirano, S. (2014). Synthesis and characterization of high capacity Li_2MnSiO_4/C cathode material for lithium-ion battery. *Journal of Power Sources*, *252*, 169–175.

Qu, L., Fang, S., Zhang, Z., Yang, L., & Hirano, S. (2013). Li_2FeSiO_4/C with good performance as cathode material for Li-ion battery. *Materials Letters*, *108*, 1–4.

Qu, L., Liu, Y., Fang, S., Yang, L., & Hirano, S. (2015). Li2FeSiO4 coated by sorbitanlaurat-derived carbon as cathode of high-performance lithium-ion battery. *Electrochimica Acta*, *163*, 123–131.

Raja, M. W., Mahanty, S., & Basu, R. N. (2009). Influence of S and Ni co-doping on structure , band gap and electrochemical properties of lithium manganese oxide synthesized by soft chemical method. *Journal of Power Sources*, *192*, 618–626.

Rajammal, K., Sivakumar, D., Duraisamy, N., Ramesh, K., & Ramesh, S. (2016). Effect of sintering temperature on structural properties of $LiMnPO_4$ cathode materials

obtained by sol – gel method. *Journal of Sol-Gel Science and Technology*. *80*, 514 – 522.

Ramar, V., Saravanan, K., Gajjela, S. R., Hariharan, S., & Balaya, P. (2013). The effect of synthesis parameters on the lithium storage performance of $LiMnPO_4$/C. *Electrochimica Acta*, *105*, 496–505.

Ran, L., Liu, X., Tang, Q., Zhu, K., Tian, J., Du, J., & Shan, Z. (2013). Grinding aid assisted preparation of high performance carbon $LiMnPO_4$. *Electrochimica Acta*, *114*, 14–20.

Reddy, A. J., Kokila, M. K., Nagabhushana, H., Chakradhar, R. P. S., Shivakumara, C., Rao, J. L., & Nagabhushana, B. M. (2011). Structural, optical and EPR studies on ZnO:Cu nanopowders prepared via low temperature solution combustion synthesis. *Journal of Alloys and Compounds*, *509*(17), 5349–5355.

Reichenbächer, M., & Popp, J. (2012). Vibrational spectroscopy. In *Challenges in Molecular Structure Determination* (pp 63-143). New York: Springer.

Richards, R. G., Owen, G. R., & Gwynn, I. (1999). Low Voltage Backscattered Electron Imaging (<5 kV) Using Field Emission Scanning Electron Microscopy. *Scanning Microscopy*, *13*(1), 55–60.

Rommel, S. M., Rothballer, J., Schall, N., Brünig, C., & Weihrich, R. (2014). Characterization of the carbon-coated $LiNi_{1-y}Co_yPO_4$ solid solution synthesized by a non-aqueous sol-gel route. *Ionics*, *21*(2), 325–333.

Rong, Y., Jing, L., & Leilei, L. (2015). Synthesis and Electrochemical Performance of Li_2MnSiO_4/C as Cathode Materials with High Capacity for Lithium ion Batteries. *Rare Metal Materials and Engineering*, *44*(11), 2707–2710.

Rosaiah, P., & Hussain, O. M. (2014). Microscopic and spectroscopic properties of hydrothermally synthesized nano-crystalline $LiFePO_4$ cathode material. *Journal of Alloys and Compounds*, *614*, 13–19.

Roux, B. Le, Bourbon, C., Colin, J. F., & Pralong, V. (2015). Synthesis and electrochemical properties of $Li(Fe_{0.5}Co_{0.5})BO_3$. *RSC advances*, *5*, 72801–72804.

Rui, X., Yan, Q., Skyllas-kazacos, M., & Mariana, T. (2014). $Li_3V_2(PO_4)_3$ cathode materials for lithium-ion batteries : A review. *Journal of Power Sources*, *258*, 19–38.

Şahan, H., Göktepe, H., Patat, Ş., & Ülgen, A. (2010). Effect of the Cr2O3 coating on electrochemical properties of spinel $LiMn_2O_4$ as a cathode material for lithium battery applications. *Solid State Ionics*, *181*(31-32), 1437–1444.

Satyavani, T. V. S. L., Kumar, A. S., & Subba Rao, P. S. V. (2015). Methods of synthesis and performance improvement of lithium iron phospate for high rate Li-ion batteries: A review. *Engineering Science and Technology, an International Journal*, *19*, 178-188.

Schmidt, J. P., Chrobak, T., Ender, M., Illig, J., Klotz, D., & Ivers-Tiff??e, E. (2011). Studies on $LiFePO_4$ as cathode material using impedance spectroscopy. *Journal of Power Sources*, *196*(12), 5349–5355.

Scrosati, B., & Garche, J. (2010). Lithium batteries: Status, prospects and future. *Journal of Power Sources*, *195*(9), 2419–2430.

Scrosati, B., Hassoun, J., & Sun, Y.-K. (2011). Lithium-ion batteries. A look into the future. *Energy & Environmental Science*, *4*(9), 3287–3295.

Seo, I., Senthilkumar, B., Kim, K., Kim, J., Kim, Y., & Ahn, J. (2016). Atomic structural and electrochemical impact of Fe substitution on nano porous $LiMnPO_4$. *Journal of Power Sources*, *320*, 59–67.

Shang, Y., Lin, X., Lu, X., Huang, T., & Yu, A. (2015). Nano-TiO_2 (B) coated $LiMn_2O_4$ as cathode materials for lithium-ion batteries at elevated temperatures. *Electrochimica Acta*, *156*, 121–126.

Sheng-kui, Z., You, W., Jie-qun, L. I. U., & Jian, W. (2012). Synthesis of $LiMnPO_4$/C composite material for lithium ion batteries by sol gel method. *Transactions of Nonferrous Metals Society of China*, *22*(10), 2535–2540.

Shi, S. J., Tu, J. P., Mai, Y. J., Zhang, Y. Q., Tang, Y. Y., & Wang, X. L. (2012). Structure and electrochemical performance of CaF_2 coated $LiMn_{1/3}Ni1_{/3}Co_{1/3}O_2$ cathode material for Li-ion batteries. *Electrochimica Acta*, *83*, 105–112.

Shirsath, S. E., Kadam, R. H., Gaikwad, A. S., Ghasemi, A., & Morisako, A. (2011). Effect of sintering temperature and the particle size on the structural and magnetic properties of nanocrystalline $Li_{0.5}Fe_{2.5}O_4$. *Journal of Magnetism and Magnetic Materials*, *323*(23), 3104–3108.

Siegel, Richard W; Hu, Evelyn; Cox, D. M. E. A. (1999). *Nanotechnology for Lithium-Ion Batteries*. New York: Springer.

Singhal, R., Tomar, M. S., Burgos, J. G., & Katiyar, R. S. (2008). Electrochemical performance of ZnO-coated $LiMn_{1.5}Ni_{1.5}O_4$ cathode material. *J. Power Sources*, *183*, 334–338.

Singhal, S., Namgyal, T., Jauhar, S., Lakshmi, N., & Bansal, S. (2013). $LiFe_5O_8$ prepared by sol–gel synthesis : microstructural and morphological effects by organic and inorganic templates. *Journal of Sol Gel Science and Technology*, *66*, 155–162.

Song, Y., Kim, C., Kim, K., Hong, S. Y., & Choi, N. (2016). Exploiting chemically and electrochemically reactive phosphite derivatives for high-voltage spinel $LiNi_{0.5}Mn_{1.5}O_4$ cathodes. *Journal of Power Sources*, *302*, 22–30.

Soo, D., Na, Y., Chan, Y., & Bin, S. (2014). Recent progress in electrode materials produced by spray pyrolysis for next-generation lithium ion batteries. *Advanced Powder Technology*, *25*(1), 18–31.

Sronsri, C., Noisong, P., & Danvirutai, C. (2016). Synthesis, characterization and

vibrational spectroscopic study of Co, Mg co-doped $LiMnPO_4$. *Spectrochimica Acta Part A: Molecular and Biomolecular Spectroscopy*, *153*, 436–444.

Su, J., Liu, Z., Long, Y., Yao, H., & Lv, X. (2015). Enhanced electrochemical performance of $LiMnPO_4$/C prepared by microwave-assisted solvothermal method. *Electrochimica Acta*, *173*, 559–565.

Su, K., Liu, F., & Chen, J. (2013). Preparation of high performance carbon-coated $LiMnPO_4$ nanocomposite by an acetate-assisted antisolvent precipitation method. *Journal of Power Sources*, *232*, 234–239.

Sun, F., & Xu, Y. (2014). Effect of Na-substitution on the electrode properties of $LiMn_2O_4$. *Journal of Alloys and Compounds*, *584*, 538–541.

Sun, X., Xu, Y., Chen, G., Ding, P., & Zheng, X. (2014). Titanium doped $LiVPO_4F$ cathode for lithium ion batteries. *Solid State Ionics*, *268*, 236–241.

Syamimi, N. F., Amin Matori, K., Lim, W. F., Abdul Aziz, S., & Mohd Zaid, M. H. (2014). Effect of sintering temperature on structural and morphological properties of europium (III) oxide doped willemite. *Journal of Spectroscopy*, *2014*, 1–9.

Talebi-Esfandarani, M., & Savadogo, O. (2014). Enhancement of electrochemical properties of platinum doped $LiFePO_4$/C cathode material synthesized using hydrothermal method. *Solid State Ionics*, *261*, 81–86.

Tang, A., He, D., He, Z., Xu, G., & Song, H. (2015). Electrochemical performance of $LiMnBO_3$/C composite synthesized by a combination of impregnation and precipitation followed by annealing. *Journal of Power Sources*, *275*, 888–892.

Tang, H., Chang, Z., Zhao, H., Yuan, X., Wang, H., & Gao, S. (2013). Journal of Alloys an d Compounds Effects of precursor treatment on the structure and electrochemical properties of spinel $LiMn_2O_4$ cathode. *Journal of Alloys and Compounds*, *566*, 16–21.

Tang, Z. (2015). High-performance $LiMnPO_4$ nanorods synthesized via a facile EG-assisted solvothermal approach. *Journal of Materials Chemistry A: Materials for energy and sustainability*, *3*(19), 10267–10274.

Tang, Z., Li, X., & Wang, Z. (2013). Effects of Al doping for $Li[Li_{0.09}Mn_{0.65*0.91}Ni_{0.35*0.91}]O_2$ cathode material. *Ionics*, *19*, 1495–1501.

Tao, D., & Wang, S. (2015). Synthesis and performance of carbon-coated $Li_3V_2(PO_4)_3$ cathode materials via an oxalic acid-based sol – gel route using PEG. *Journal of Sol Gel Science Technology*, *2*, 121–131.

Tao, L., Rousse, G., Chotard, J. N., Dupont, L., Dominko, R., Levasseur, S., & Masquelier, C. (2014). Preparation, structure and electrochemistry of $LiFeBO_3$: a cathode material for Li-ion batteries. *Journal of Materials Chemistry A*, *2*, 2060–2070.

Teng, F., Hu, Z., Ma, X., Zhang, L., Ding, C., Yu, Y., & Chen, C. (2013). Electrochimica Acta Hydrothermal synthesis of plate-like carbon-coated

$Li_3V_2(PO_4)_3$ and its low temperature performance for high power lithium ion batteries. *Electrochimica Acta*, *91*, 43–49.

Thayumanasundaram, S., & Rangasamy, V. S. (2014). Synthesis and electrochemical behavior of Li_2CoSiO_4 cathode with pyrrolidinium-based ionic liquid electrolyte for lithium ion batteries. *Ionics*, *2*, 935–941.

The Nam Long Doan, & Taniguchi, I. (2011). Preparation of $LiCoPO_4$/C nanocomposite cathode of lithium batteries with high rate performance. *Journal of Power Sources*, *196*(13), 5679–5684.

Thirunakaran, R., Ravikumar, R., Gopukumar, S., & Sivashanmugam, A. (2016). Electrochemical evaluation of dual-doped $LiMn_2O_4$ spinels synthesized via co-precipitation method as cathode material for lithium rechargeable batteries. *Journal of Alloys and Compounds*, *556*(2013), 266–273.

Thirunakaran, R., Ravikumar, R., Vanitha, S., Gopukumar, S., & Sivashanmugam, A. (2011). Glutamic acid-assisted sol-gel synthesis of multi-doped spinel lithium manganate as cathode materials for lithium rechargeable batteries. *Electrochimica Acta*, *58*(1), 348–358.

Thirunakaran, R., Sivashanmugam, A., Gopukumar, S., Dunnill, C. W., & Gregory, D. H. (2008). Studies on chromium/aluminium-doped manganese spinel as cathode materials for lithium-ion batteries-A novel chelated sol-gel synthesis. *Journal of Materials Processing Technology*, *208*(1-3), 520–531.

Toprakci, O., Toprakci, H. A. K., Ji, L., Xu, G., Lin, Z., & Zhang, X. (2012). Carbon Nanotube-Loaded Electrospun $LiFePO_4$/Carbon Composite Nanofibers As Stable and Binder-Free Cathodes for Rechargeable Lithium-Ion Batteries. *Applied Materials Interfaces*, *4*, 1273–1280.

Tsuyumoto, I., & Kihara, A. (2013). Synthesis, Characterization and Charge-Discharge Properties of Layer-Structure Lithium Zinc Borate, $LiZnBO_3$. *Materials Sciences And Applications*, *4*(4), 246–249.

Vishwanathan Ramar and Palani Balaya. (2013). Enhancing the electrochemical kinetics of high voltage olivine $LiMnPO_4$ by isovalent co-doping. *Phys.Chem. Chem. Phys*, *15*, 17240–17249.

Voepel, P., Suchomski, C., Hofmann, A., Gross, S., Dolcet, P., & Smarsly, B. M. (2016). In-depth mesocrystal formation analysis of microwave-assisted synthesis of $LiMnPO_4$ nanostructures in organic solution. *CrystEngComm*, *18*, 316–327.

Wang, D., Buqa, H., Crouzet, M., Deghenghi, G., Drezen, T., Exnar, I., Kwon, N., H.Miners, J., Laetitia, P., Gratzel, M. (2009). High-performance, nano-structured $LiMnPO_4$ synthesized via a polyol method. *Journal of Power Sources*, *189*, 624–628.

Wang, D., Cao, L., Huang, J., & Wu, J. (2013). Effects of different chelating agents on the composition, morphology and electrochemical properties of LiV_3O_8 crystallites synthesized via sol-gel method. *Ceramics International*, *39*(4), 3759–3764.

Wang, H., Lai, F., Li, Y., Zhang, X., & Huang, Y. (2015). Excellent stability of spinel $LiMn_2O_4$ -based cathode materials for lithium-ion batteries. *Electrochimica Acta*, *177*, 290–297.

Wang, J., Lin, W., Wu, B., & Zhao, J. (2014). Syntheses and electrochemical properties of the Na-doped $LiNi_{0.5}Mn_{1.5}O_4$ cathode materials for lithium-ion batteries. *Electrochimica Acta*, *145*, 245–253.

Wang, K., Wang, Y., Wang, C., & Xia, Y. (2014). Graphene oxide assisted solvothermal synthesis of $LiMnPO_4$ nanoplates cathode materials for lithium ion batteries. *Electrochimica Acta*, *146*, 8–14.

Wang, L., He, X., Sun, W., Wang, J., Li, Y., & Fan, S. (2012). Crystal Orientation Tuning of $LiFePO_4$ Nanoplates for High Rate Lithium Battery Cathode Materials. *Nano Letters*, *12*, 5632 – 5636.

Wang, L., Liu, H., Tang, Z., Ma, L., & Zhang, X. (2012). $Li_3V_2(PO_4)_3$/C cathode material prepared via a sol – gel method based on composite chelating reagents. *Journal of Power Sources*, *204*, 197–199.

Wang, L., Zhou, X., & Guo, Y. (2010). Synthesis and performance of carbon-coated $Li_3V_2(PO_4)_3$ cathode materials by a low temperature solid-state reaction. *Journal of Power Sources*, *195*, 2844–2850.

Wang, M., Yang, M., Ma, L., & Shen, X. (2015). Synthesis and improved electrochemical properties of Na-substituted Li_2MnSiO_4 nanoparticles as cathode materials for Li-ion batteries. *Chemical Physics Letters*, *619*, 39–43.

Wang, S., Li, P., Shao, L., Wu, K., Lin, X., Shui, M., … Shu, J. (2015). Preparation of spinel $LiNi_{0.5}Mn_{1.5}O_4$ and Cr-doped $LiNi_{0.5}Mn_{1.5}O_4$ cathode materials by tartaric acid assisted sol – gel method. *Ceramics International*, *41*(1), 1347–1353.

Wang, Y., Shao, X., Xu, H., Xie, M., Deng, S., Wang, H., & Liu, J. (2013). Facile synthesis of porous $LiMn_2O_4$ spheres as cathode materials for high-power lithium ion batteries. *Journal of Power Sources*, *226*, 140–148.

Wang, Y., Zhao, H., Ji, Y., Wang, L., & Wei, Z. (2014). Long-life and high-rate $LiVPO_4F$/C nanocrystals modi fi ed with graphene as cathode material for lithium-ion batteries. *Solid State Ionics*, *268*, 169–173.

Wang, Y., Zhao, S., Zhai, P., Li, F., & Nan, C. (2014). Solvothermal synthesis and electrochemical performance of Li_2MnSiO_4/C cathode materials for lithium ion batteries. *Journal of Alloys and Compounds*, *614*, 271–276.

Wang, Y., Zhu, B., Wang, Y., & Wang, F. (2016). Solvothermal synthesis of $LiFePO_4$ nanorods as high-performance cathode materials for lithium ion batteries. *Ceramics International*, *42*(8), 10297–10303.

Wang, Z.-K., Shu, J., Zhu, Q.-C., Cao, B.-Y., Chen, H., Wu, X.-Y., Bartlett, B-M., Wang, K-X., Chen, J.-S. (2016). Graphene-nanosheet-wrapped LiV3O8 nanocomposites as high performance cathode materials for rechargeable lithium-ion batteries. *Journal of Power Sources*, *307*, 426–434.

Wei He, Yuan, D., Qian, J., Ai, X., Yang, H., & Cao, Y. (2013). Enhanced high-rate capability and cycling stability of Na-stabilized layered $Li_{1.2}[Co_{0.13}Ni_{0.13}Mn_{0.54}]O_2$ cathode material. *Materials Chemistry A*, *1*, 11397–11403.

Wei, C., He, W., Zhang, X., Shen, J., & Ma, J. (2016). Recent progress in hybrid cathode materials for lithium ion batteries. *New Journal of Chemistry*, *40*, 2984–2999.

Wei, C., He, W., Zhang, X.-D., Xu, F., Liu, Q.-Z., Sun, C., & Song, X. (2015). Effects of morphology on the electrochemical performances of $Li_3V_2(PO_4)_3$ cathode material for lithium ion batteries. *RSC Advances*, *5*, 54225-54245.

Whittingham, M. S. (2004). Lithium Batteries and Cathode Materials. *Chemical Reviews*, *104*(607), 4271–4302.

Wi, S., Nam, S., Oh, Y., Kim, J., Choi, H., & Park, Y. K. B. (2012). Facile synthesis of porous-carbon/$LiFePO_4$ nanocomposites. *Journal of Nanoparticle Research*, *14*, 1327–1336.

Williams, D., & Carter, C. (2009). Scattering and diffraction. In *Transmission Electron Microscopy A Textbook for Materials Science* (pp 23–39). New York: Springer.

Wu, L., Zhong, S., Lv, F., & Liu, J. (2013). Improving the electrochemical performance of $LiMnPO_4$/C by liquid nitrogen quenching. *Materials Letters*, *110*, 38–41.

Wu, Z., & Zhou, Y. (2012). Effect of Ce-doping on the structure and electrochemical performance of lithium trivanadate prepared by a citrate sol – gel method. *Journal of Power Sources*, *199*, 300–307.

Xia, H., Luo, Z., & Xie, J. (2012). Nanostructured $LiMn_2O_4$ and their composites as high-performance cathodes for lithium-ion batteries. *Progress in Natural Science: Materials International*, *22*(6), 572–584.

Xia, Q., Liu, T., Xu, J., Cheng, X., & Wu, X. (2015). High performance porous $LiMnPO_4$ nanoflakes: synthesis from a novel nanosheet precursor. *Journal of Materials Chemistry A*, *3*, 6301–6305.

Xia, X., Zhang, Y., Chao, D., Guan, C., Zhang, Y., & Li, L. (2014). Solution synthesis of metal oxides for electrochemical energy storage applications. *Nanoscale*, *6*, 5008–5048.

Xia, Y., Shi, S., Li, C., Liang, C., Gan, Y., Huang, H., … Zhang, W. (2015). Electrochemical properties of Sn-doped $Li_3V_2(PO_4)_3$ cathode material synthesized via a citric acid assisted sol–gel method. *Journal of Alloys and Compounds*, *652*, 298–306.

Xiang, M., Ye, L., Peng, C., Zhong, L., Bai, H., Su, C., & Guo, J. (2014). Study on the electrochemical performance of high-cycle $LiMg_{0.08}Mn_{1.92}O_4$ cathode material prepared by a solid-state combustion synthesis. *Ceramics International*, *40*(7), 10839–10845.

Xiang, W., Tang, Y., Wang, Y., Zhong, B., Fang, W., Liu, H., & Guo, X. (2013).

Influence of pH value and chelating reagent on performance of $Li_3V_2(PO_4)_3$/C cathode material. *Transactions of Nonferrous Metals Society of China*, *23*(5), 1395–1402.

Xiang, W., Zhong, Y., Tang, Y., Shen, H., Wang, E., Liu, H., Zhong, B., Guo, X. (2015). Improving the electrochemical kinetics of lithium manganese phosphate via co-substitution with iron and cobalt. *Journal of Alloys and Compounds*, *635*, 180–187.

Xiao, J., Chernova, N. A., Upreti, S., Chen, X., & Li, Z. (2011). Electrochemical performances of $LiMnPO_4$ synthesized from non-stoichiometric Li/Mn ratio. *Physical Chemistry Chemical Physics*, *13*, 18099–18106.

Xiao, L., Guo, Y., Qu, D., Deng, B., Liu, H., & Tang, D. (2013). Influence of particle sizes and morphologies on the electrochemical performances of spinel $LiMn_2O_4$ cathode materials. *Journal of Power Sources*, *225*, 286–292.

Xiao, P. F., Lai, M. O., & Lu, L. (2013). Transport and electrochemical properties of high potential tavorite $LiVPO_4F$. *Solid State Ionics*, *242*, 10–19.

Xu, D., Wang, P., & Shen, B. (2016). Synthesis and characterization of sulfur-doped carbon decorated $LiFePO_4$ nanocomposite as high performance cathode material for lithium-ion batteries. *Ceramics International*, *42*(4), 5331–5338.

Xu, H., Zong, J., Ding, F., Lu, Z. wei, Li, W., & Liu, X. (2016). Effects of Fe^{2+} ion doping on $LiMnPO_4$ nanomaterial for lithium ion batteries. *RSC Advances*, *6*, 27164–27169.

Xu, M., Chen, Z., Li, L., Zhu, H., Zhao, Q., Xu, L., & Peng, N. (2015). Highly crystalline alumina surface coating from hydrolysis of aluminum isopropoxide on lithium-rich layered oxide. *Journal of Power Sources*, *281*, 444–454.

Xu, X., Lee, S., Jeong, S., Kim, Y., & Cho, J. (2013). Recent progress on nanostructured 4 v cathode materials for Li-ion batteries for mobile electronics. *Materials Today*, *16*(12), 487–495.

Xu, Y., Shen, W., Wang, C., Zhang, A., Xu, Q., Liu, H., … Xia, Y. (2015). Hydrothermal synthesis and electrochemical performance of nanoparticle Li_2FeSiO_4/C cathode materials for lithium ion batteries. *Electrochimica Acta*, *167*, 340–347.

Xue Zhou, Ye Xie, Yuanfu Deng, X. Q. and G. C. (2015). The enhanced rate performance of $LiFe_{0.5}Mn_{0.5}PO_4$/C cathode material via synergistic strategies of surfactant-assisted solid state method and carbon coating†. *Journal of Materials Chemistry A*, *3*, 996–1004.

Yamane, H., Kawano, T., Fukuda, K., Suehiro, T., & Sato, T. (2012). Preparation, crystal structure and photoluminescence of lithium magnesium manganese borate solid solutions , $LiMg_{1-x}Mn_xBO_3$. *Journal of Alloys and Compounds*, *512*(1), 223–229.

Yang, B., & Yang, L. (2015). Silver-coated $LiVPO_4F$ composite with improved

electrochemical performance as cathode material for lithium-ion batteries. *Journal of Physical and Chemistry of Solids*, *87*, 228–232.

Yang, J., Kang, X., He, D., Peng, T., Hu, L., & Mu, S. (2013). Hierarchical shuttle-like Li_2FeSiO_4 as a highly efficient cathode material for lithium-ion batteries. *Journal of Power Sources*, *242*, 171–178.

Yang, J., Kang, X., Hu, L., Gong, X., He, D., Peng, T., & Mu, S. (2013). Synthesis and electrochemical performance of Li_2FeSiO_4/C/carbon nanosphere composite cathode materials for lithium ion batteries. *Journal of Alloys and Compounds*, *572*, 158–162.

Yang, R., Kang, E., Jiang, B., & Ahn, J. (2012). Effect of complexing agents on the electrochemical performance of $LiFePO_4$/C prepared by sol-gel method. *Nanoscale Research Letters*, *7*(1), 40–46.

Yang, R., Wang, L., Deng, K., Lv, M., & Xu, Y. (2016). A facile synthesis of $Li_2Fe_{1/3}Mn_{1/3}Ni_{1/3}SiO_4$/C composites as cathode materials for lithium-ion batteries. *Journal of Alloys and Compounds*, *676*, 260–264.

Yang, S.-L., Ma, R.-G., Hu, M.-J., Xi, L.-J., Lu, Z.-G., & C.Y. Chung. (2012). Solvothermal synthesis of nano-$LiMnPO_4$ from Li_3PO_4 rod-like precursor: reaction mechanism and electrochemical properties. *Journal of Materials Chemistry*, *22*, 25402–25408.

Yang, W., Bi, Y., Qin, Y., Liu, Y., & Zhang, X. (2015). $LiMn_{0.8}Fe_{0.2}PO_4$/C cathode material synthesized via co-precipitation method with superior high-rate and low-temperature performances for lithium-ion batteries. *Journal of Power Sources*, *275*, 785–791.

Yang, X., Mi, Y., Zhang, W., Wu, B., & Zhou, H. (2015). Enhanced electrochemical performance of $LiFe_{0.6}Mn_{0.4}PO_4$/C cathode material prepared by ferrocene-assisted calcination process. *Journal of Power Sources*, *275*, 823–830.

Yao, J., Shen, C., Zhang, P., Gregory, D. H., & Wang, L. (2012). Enhanced cycle ability of spinel $LiMn_2O_4$ by controlling the phase purity and structural strain. *Journal of Physics and Chemistry of Solids*, *73*(11), 1390–1395.

Yi, J., Hou, M., Bao, H., Wang, C., Wang, J., & Xia, Y. (2014). In-situ generation of Li_2FeSiO_4/C nanocomposite as cathode material for lithium ion battery. *Electrochimica Acta*, *133*, 564–569.

Yi, T., Shu, J., Zhu, Y., & Zhu, R. (2009). Advanced electrochemical performance of $LiMn_{1.4}Cr_{0.2}Ni_{0.4}O_4$ as 5V cathode material by citric-acid-assisted method. *Journal of Physics and Chemistry of Solids*, *70*, 153–158.

Yoshida, J., Stark, M., Holzbock, J., Hüsing, N., Nakanishi, S., Iba, H., … Naito, M. (2013). Analysis of the size effect of $LiMnPO_4$ particles on the battery properties by using STEM-EELS. *Journal of Power Sources*, *226*, 122–126.

Yoshio, M., Brodd, R. J., & Kozawa, A. (2015). *Lithium Ion Batteries*. New York: Springer.

Yu, Z., & Jiang, L. (2016). Design and facile synthesis of nitrogen-doped carbon decorated $LiVPO_4F$ nanocrystals as superior cathode for lithium-ion batteries. *Solid State Ionics*, *291*, 20–25.

Yuan, H., Wang, X., Wu, Q., Shu, H., & Yang, X. (2016). Effects of Ni and Mn doping on physicochemical and electrochemical performances of $LiFePO_4$/C. *Journal of Alloys and Compounds*, *675*, 187–194.

Zaghib, K., Guerfi, A., Hovington, P., Vijh, A., Trudeau, M., Mauger, A., Goodenough J., Julien, C. M. (2013). Review and analysis of nanostructured olivine-based lithium recheargeable batteries: Status and trends. *Journal of Power Sources*, *232*, 357–369.

Zeng, Y., Wu, X., Mei, P., Cong, L., Yao, C., Wang, R., Xie, H., Sun, L. (2014). Effect of cationic and anionic substitutions on the electrochemical properties of $LiNi_{0.5}Mn_{1.5}O_4$ spinel cathode materials. *Electrochimica Acta*, *138*, 493–500.

Zhai, P., Zhao, S., Cheng, H., Zhao, J., & Nan, C. (2015). Synthesis and structural stability of $Li_{2.1}Mn_{0.9}[PO_4]_{0.1}[SiO_4]_{0.9}$/C mixed polyanion cathode material for Li-ion battery. *Electrochimica Acta*, *153*, 217–224.

Zhang, B., Liu, J., Zhang, Q., & Li, Y. (2010). Electrochemical performance of Al-substituted $Li_3V_2(PO_4)_3$ cathode materials synthesized by sol-gel method. *Transactions of Nonferrous Metals Society of China*, *20*(4), 619–623.

Zhang, B., Ming, L., Zheng, J., Zhang, J., Shen, C., Han, Y., Qin, S. (2014). Synthesis and characterization of multi-layer core e shell structural $LiFeBO_3$/C as a novel Li-battery cathode material. *Journal of Power Sources*, *261*, 249–254.

Zhang, J., Luo, S., Chang, L., Bao, S., & Liu, J. (2016). In-situ growth of $LiMnPO_4$ on porous $LiAlO_2$ nanoplates substrates from AAO synthesized by hydrothermal reaction with improved electrochemical performance. *Electrochimica Acta*, *193*, 16–23.

Zhang, L., Duan, S., Peng, G., Liang, G., Zou, F., & Huang, Y. (2013). Novel synthesis of low carbon-coated $Li_3V_2(PO_4)_3$ cathode material for lithium-ion batteries. *Journal of Alloys and Compounds*, *570*, 61–64.

Zhang, L. L., Duan, S., Yang, X. L., Liang, G., Huang, Y. H., Cao, X. Z., … Lewis, C. (2015). Insight into cobalt-doping in Li_2FeSiO_4 cathode material for lithium-ion battery. *Journal of Power Sources*, *274*, 194–202.

Zhang, L., Qu, Q., Zhang, L., Li, J., & Zheng, H. (2014). Confined synthesis of hierarchical structured $LiMnPO_4$/C granules by a facile surfactant-assisted solid-state method for high-performance lithium-ion batteries. *Journal of Materials Chemistry A*, *2*, 711–719.

Zhang, W., Shan, Z., Zhu, K., Liu, S., Liu, X., & Tian, J. (2015). $LiMnPO_4$ nanoplates grown via a facile surfactant-mediated solvothermal reaction for high-performance Li-ion batteries. *Electrochimica Acta*, *153*, 385–392.

Zhang, X., Liu, S., & Huang, K. (2012). Synthesis and characterization of macroporous

$Li_3V_2(PO_4)_3$/C composites as cathode materials for Li-ion batteries. *Journal of Solid State Electrochemistry*, *2*, 937–944.

Zhang, Y., Wu, X., Lin, Y., Wang, D., Zhang, C., & He, D. (2013). Synthesis of $LiNi1_{/3}Co_{1/3}Mn_{1/3}O_2$ cathode material by a modified sol–gel method for lithium-ion battery. *Journal of Sol-Gel Science and Technology*, *68*(2), 169–174.

Zhang, Z., Liu, X., Wang, L., Wu, Y., Zhao, H., & Chen, B. (2015). Fabrication and characterization of carbon-coated Li_2FeSiO_4 nanoparticles reinforced by carbon nanotubes as high performance cathode materials for lithium-ion batteries. *Electrochimica Acta*, *168*, 8–15.

Zhao, C., Hu, Z., Zhou, Y., Fang, S., & Cai, S. (2015). Synthesis of $0.3Li_2MnO_3 \cdot {}_{0.7}LiNi_{1/3}Co_{1/3}Mn_{1/3}O_2$ cathode materials using 3-D urchin-like MnO_2 as precursor for high performance lithium ion battery. *Journal of Nanoparticle Research*, *17*(2), 89–97.

Zhao, E., Liu, X., Hu, Z., Sun, L., & Xiao, X. (2015). Facile synthesis and enhanced electrochemical performances of Li_2TiO_3-coated lithium-rich layered $Li1_{.13}Ni_{0.30}Mn_{0.57}O_2$ cathode materials for lithium-ion batteries. *Journal of Power Sources*, *294*, 141–149.

Zhao, F., Tang, Y., Wang, J., Tian, J., Ge, H., & Wang, B. (2015). Vapor-assisted synthesis of Al_2O_3 -coated $LiCoO_2$ for high-voltage lithium ion batteries. *Electrochimica Acta*, *174*, 384–390.

Zhao, H., Liu, X., Cheng, C., Li, Q., Zhang, Z., Wu, Y., Xiong, W. (2015). Synthesis and electrochemical characterizations of spinel $LiMn_{1.94}MO_4$ (M = $Mn_{0.06}$,$Mg_{0.06}$,$Si_{0.06}$, ($Mg_{0.03}Si_{0.03}$)) compounds as cathode materials for lithium-ion batteries. *Journal of Power Sources*, *282*, 118–128.

Zhao, M., Fu, Y., Xu, N., Li, G., Wu, M., & Gao, X. (2014). High performance $LiMnPO_4$/C prepared by a crystallite size control method. *Journal of Materials Chemistry A*, *2*(36), 15070–15077.

Zhao, T., Chen, S., Li, L., Zhang, X., Chen, R., Belharouak, I., … Amine, K. (2013). Synthesis , characterization , and electrochemistry of cathode material Li $[Li_{0.2}Co_{0.13}Ni_{0.13}Mn_{0.54}]O_2$ using organic chelating agents for lithium-ion batteries. *Journal of Power Sources*, *228*, 206–213.

Zhao, X., Baek, D., Manuel, J., Heo, M., Yang, R., Keun, J., … Ahn, J. (2012). Electrochemical properties of magnesium doped $LiFePO_4$ cathode material prepared by sol – gel method. *Materials Research Bulletin*, *47*(10), 2819–2822.

Zheng, J. M., Wu, X. B., & Yang, Y. (2011). A comparison of preparation method on the electrochemical performance of cathode material $Li[Li_{0.2}Mn_{0.54}Ni0_{.13}Co_{0.13}]O_2$ for lithium ion battery. *Electrochimica Acta*, *56*, 3071–3078.

Zheng, J., Ni, L., Lu, Y., Qin, C., Liu, P., Wu, T., Tang, Y., Chen, Y. (2015). High-performance, nanostructure $LiMnPO_4$/C composites synthesized via one-step solid state reaction. *Journal of Power Sources*, *282*, 444–451.

Zhiyuan Wang, Enzuo Li, Chunnian He, Chunsheng Shi, Jiajun Li, N. Z. (2008). Effect of amorphous $FePO_4$ coating on structure and electrochemical performance of $Li_{1.2}Ni_{0.13}Co_{0.13}Mn_{0.54}O_2$ as cathode material for Li-ion batteries. *Journal of Power Sources*, *183*, 741–748.

Zhou, F., Zhu, P., Fu, X., Chen, R., Sun, R., & Wong, C. (2014). Comparative study of $LiMnPO_4$ cathode materials synthesized by solvothermal methods using different manganese salts. *CrystEngComm*, *16*(5), 766–774.

Zhu, H., He, H., Xin, X., Ma, X., Zan, L., & Zhang, Y. (2015). Facile synthesis of Li_2MnSiO_4/C/graphene composite with superior high-rate performances as cathode materials for Li-ion batteries. *Electrochimica Acta*, *155*, 116–124.

Zhu, H., Zhai, W., Yang, M., Liu, X., & Chen, Y. (2014). Synthesis and characterization of $LiMnPO_4$/C nano- composites from manganese(II) phosphate trihydrate precipitated from a micro-channel reactor approach. *RSC Advances*, *4*, 25625–25632.

Zhu, H.-J., Liu, X.-M., Yang, H., & Shen, X.-D. (2014). Effect of the stirring rate on physical and electrochemical properties of $LiMnPO_4$ nanoplates prepared in a polyol process. *Ceramics International*, *40*(5), 6699–6704.

Zhu, J., Fiore, J., Li, D., Kinsinger, N. M., Wang, Q., Dimasi, E., Guo, J., Kisailus, D. (2013). Solvothermal Synthesis, Development, and Performance of $LiFePO_4$ Nanostructures. *Crystal Growth & Design*, *13*, 4659–4666.

Zhu, J., Tang, H., Tang, Z., & Ma, C. (2015). Improved electrochemical performance of zinc oxide coated lithium manganese silicate electrode for lithium-ion batteries. *Journal Of Alloys And Compounds*, *633*, 194–200.

Zhu, Y., Zhang, R. U. I., Deng, L. I., Yi, T., & Ye, M. (2015). Lithium-Ion Insertion Kinetics of Na-Doped $LiFePO_4$ as Cathode Materials for Lithium-Ion Batteries. *Metallurgical and Materials Transactions E*, *2*, 33–38.

Ziółkowska, D., Korona, K. P., Kamińska, M., Grzanka, E., & Andrzejczuk, M. (2011). Raman Spectroscopy of $LiFePO_4$ and $Li_3V_2(PO_4)_3$ Prepared as Cathode Materials. *Acta Physica Polonica A*, *120*(5), 973–975.

Zou, B., Yu, R., Deng, M., Zhou, Y., Liao, J., & Chen, C. (2016). Solvothermal synthesized $LiMn_{1-x}Fe_xPO_4$@C nanopowders with excellent high rate and low temperature performances for lithium-ion batteries. *RSC Advances*, *6*, 52271–52278.

LIST OF PUBLICATIONS AND PAPERS PRESENTED

List of publications

K. Rajammal, D. Sivakumar, Navaneethan Duraisamy, K. Ramesh, S. Ramesh, (2016). Structural and electrochemical characterizations of $LiMn_{1-x}Al_{0.5x}Cu_{0.5x}PO_4$ (x=0.0, 0.1, 0.2) cathode materials for lithium ion batteries, Materials Letters 173, 131–135.

K. Rajammal, D. Sivakumar, Navaneethan Duraisamy, K. Ramesh, S. Ramesh, (2016). Enhanced electrochemical properties of ZnO-coated $LiMnPO_4$ cathode materials for lithium ion batteries. Ionics 173, 1551–1556.

K. Rajammal, D. Sivakumar, Navaneethan Duraisamy, K. Ramesh, S. Ramesh, (2016). Effect of sintering temperature on structural properties of $LiMnPO_4$ cathode materials obtained by sol gel method, Journal of Sol Gel Science and Technologhy 80, 514 - 522.

K. Rajammal, D. Sivakumar, Navaneethan Duraisamy, K. Ramesh, S. Ramesh, (2016) Na doped $LiMnPO_4$ as an electrode material for enhanced lithium ion batteries, Bulletin of Materials Science, *Accepted Manuscript*

List of presentations

K. Rajammal, D. Sivakumar, K. Ramesh, S. Ramesh.; Oral presentation; Synthesis and characterization of high voltage olivine $LiNiPO_4$ by oxalic acid assisted sol - gel method, International Conference on Materials for Advanced Technologies (ICMAT 2015), Suntec Convention Centre, Singapore, 28th June -2nd July 2015.

K. Rajammal, D. Sivakumar, K. Ramesh, S. Ramesh.; Poster presentation; Synthesis and structural properties of nitric acid assisted $LiMnPO_4$, 6th International Conference on Postgraduate Education (ICPE 2014), Dewan Utama UTeM, Malaysia, 17th-18th December 2014.

APPENDIX

Materials Letters 173 (2016) 131–135

Contents lists available at ScienceDirect

Materials Letters

journal homepage: www.elsevier.com/locate/matlet

Structural and electrochemical characterizations of $LiMn_{1-x}Al_{0.5x}Cu_{0.5x}PO_4$ (x=0.0, 0.1, 0.2) cathode materials for lithium ion batteries

K. Rajammal [a], D. Sivakumar [b], Navaneethan Duraisamy [a,*], K. Ramesh [a], S. Ramesh [a,*]

[a] Center for Ionics University of Malaya, Department of Physics, University of Malaya, Kuala Lumpur 50603, Malaysia
[b] Faculty of Mechanical Engineering, University Technical Malaysia Melaka (UTeM), 76100 Durian Tunggal, Malacca, Malaysia

ARTICLE INFO

Article history:
Received 23 December 2015
Received in revised form
23 February 2016
Accepted 9 March 2016
Available online 10 March 2016

Keywords:
Cathode materials
Sol–gel preparation
X-ray technique
$LiMnPO_4$
Electrochemical performance

ABSTRACT

Orthorhombic $LiMnPO_4$ and its derivatives $LiMn_{1-x}Al_{0.5x}Cu_{0.5x}PO_4$ (x=0.1, 0.2) were prepared by sol gel method. The doping of Al and Cu for Mn in $LiMnPO_4$ exhibited lattice shrinkage and improvement of electronic conductivity. $LiMn_{0.8}Al_{0.1}Cu_{0.1}PO_4$ exhibited the high discharge capacity of 166 mAh g^{-1} than that of other samples such as $LiMn_{0.9}Al_{0.05}Cu_{0.05}PO_4$ (~113 mAh g^{-1}) and Pristine $LiMnPO_4$ (~103 mAh g^{-1}). These results demonstrated that Al and Cu dual doping found to be one of the alternative route to enhance the electrochemical activity of nanostructured $LiMnPO_4$.

1. Introduction

Nanostructured $LiMnPO_4$ are being measured as highly potential cathode materials due to their favorable advantages of high operating voltage (4.1 V vs Li^+/Li) with high energy density [1], ample [2], excellent cycling stability [3] and its compatibility with the commercial electrolytes [4]. However, $LiMnPO_4$ have some drawbacks that restraining $LiMnPO_4$ as an electrode material such as Jahn Teller distortion of Mn^{3+} ion and structural instability during cycling process and also low electronic conductivity cause poor electrochemical performance [1]. Herein, Jahn Teller distortion leads to exist of two phases of $LiMnPO_4$ and $MnPO_4$ throughout intercalation and deintercalation process. These structural differences deteriorate movement of electrons and lithium ions, which is affecting electrochemical properties [5].

In general, there are numerous approaches involving for improving physico-chemical properties of $LiMnPO_4$ [6,7] such that carbon coating [8,9], metal oxide coating [10,11] and particle size reduction [12,13], etc. Nevertheless, metal doping also explored to improve the performance of $LiMnPO_4$. Table S1 summarizes some of the doped $LiMnPO_4$ works reported in literatures. Consequently, in this work we examined the effects of Al and Cu dual metals substitution at Mn site in $LiMnPO_4$. Both Al and Cu have some attractive assets such as abundant and inexpensive [14,15]. Additionally, Al is light weighted among the transition metal elements [14]. Recent works utilizing Al or Cu as doping elements established good outcomes. Liu et al. concluded that Al doped $LiNi_{0.5}Mn_{1.5}O_4$ showed 70% capacity retention after 200 cycles [16]. In another study, $LiFe_{0.985}Cu_{0.015}PO_4$/C exhibited high discharge capacity of 152.4 mAh g^{-1}, 144.4 mAh g^{-1}, 126.7 mAh g^{-1} and 110.5 mAh g^{-1} at current rate of 1C, 2C, 5C and 10C respectively. Cu-doped $Li_{1.2}V_3O_8$ revealed high capacity retention during continuous cycling as compared to pristine. It proved that the initial discharge capacity of 275.9 mAh g^{-1} and retains its capacity about 264 mAh g^{-1} for 30 cycles. Current study is focused on Al, Cu dual doping in $LiMnPO_4$ via structural and electrochemical characterizations.

2. Experimental

Pristine $LiMnPO_4$ and $LiMn_{1-x}Al_{0.5x}Cu_{0.5x}PO_4$ (x=0.1, 0.2) were obtained via sol gel method. 1.0 mol lithium acetate ($LiC_2H_3O_2$), 1.0 mol manganese acetate $Mn(CH_3COO)_2 \cdot 4H_2O$ and aimed amount of aluminium acetate and copper acetate (0.1 mol and 0.05 mol) were dissolved in distilled water. 1.0 mol Ammonium dihydrogen phosphate $(NH_4)H_2PO_4$ was added into the above mixture followed by drops of 1 M nitric acid. Then the solution was stirred and heated until attain the final product. Further, the obtained samples were heated at the temperature of 700 °C for 3 h

* Corresponding authors.
E-mail addresses: naveennanoenergy@gmail.com (N. Duraisamy), rameshtsubra@gmail.com (S. Ramesh).

http://dx.doi.org/10.1016/j.matlet.2016.03.046
0167-577X/

J Sol-Gel Sci Technol (2016) 80:514–522
DOI 10.1007/s10971-016-4111-3

ORIGINAL PAPER: SOL-GEL AND HYBRID MATERIALS FOR ENERGY, ENVIRONMENT AND BUILDING APPLICATIONS

Effect of sintering temperature on structural properties of $LiMnPO_4$ cathode materials obtained by sol–gel method

K. Rajammal[1] · D. Sivakumar[2] · Navaneethan Duraisamy[1] · K. Ramesh[1] · S. Ramesh[1]

Received: 7 April 2016 / Accepted: 6 June 2016 / Published online: 16 June 2016

Abstract Nanostructured $LiMnPO_4$ cathode materials were successfully achieved by sol–gel route with the aid of oxalic acid and nitric acid. The effects of sintering temperatures on structural properties especially strain and crystallite size were analysed. The structural crystallinity and average particle sizes (42–77 nm) of $LiMnPO_4$ are significantly varied with respect to calcination temperatures. $LiMnPO_4$ obtained at 700 °C exhibits superior electrochemical performance among the samples. It delivered initial discharge capacity of 103.4 mAh g^{-1} at 0.05 C. These results revealed that the sol–gel technique could be favourable method to produce nanosized $LiMnPO_4$ as a cathode material for lithium ion batteries via optimizing calcination temperatures.

Graphical Abstract

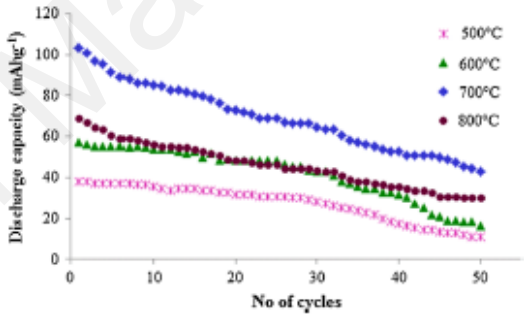

Keywords $LiMnPO_4$ · Sol–gel method · Cathode materials · Electrochemical performance · Lithium ion batteries

1 Introduction

Olivine structured lithium manganese phosphate ($LiMnPO_4$) as a cathode material for lithium ion batteries is having high capacity (170 mAh g^{-1}) and high redox potential (4.1 V vs Li^+), respectively [1]. Moreover, $LiMnPO_4$ has 20 % greater energy density compared to $LiFePO_4$ [2], working ability at high temperatures [3], low cost and ecofriendly making $LiMnPO_4$ successful cathode candidates for lithium ion batteries [1]. In contrary, its negative aspects involving low electronic conductivity and weak lithium diffusion lead to limit its application [4–6]. Strategies have been focused to overcome the above mentioned drawbacks. In this aspect, synthesis method is one of the key technique that plays

✉ S. Ramesh
rameshtsubra@gmail.com

[1] Department of Physics, Center for Ionics University of Malaya, University of Malaya, 50603 Kuala Lumpur, Malaysia

[2] Faculty of Mechanical Engineering, University Technical Malaysia Melaka (UTeM), 76100 Durian Tunggal, Malacca, Malaysia

Ionics (2016) 22:1551–1556
DOI 10.1007/s11581-016-1685-2

ORIGINAL PAPER

Enhanced electrochemical properties of ZnO-coated $LiMnPO_4$ cathode materials for lithium ion batteries

K. Rajammal[1] · D. Sivakumar[2] · Navaneethan Duraisamy[1] · K. Ramesh[1] · S. Ramesh[1]

Received: 31 December 2015 / Revised: 25 February 2016 / Accepted: 6 March 2016 / Published online: 24 March 2016

Abstract We demonstrated the effect of ZnO (different wt%)-coated $LiMnPO_4$-based cathode materials for electrochemical lithium ion batteries. ZnO-coated $LiMnPO_4$ cathode materials were prepared by the sol-gel method. X-ray diffraction (XRD) analysis indicates that there is no change in structure caused by ZnO coating, and field emission scanning electron microscopy (FESEM) images depict the closely packed particles. Galvanostatic charge-discharge tests show the ZnO-coated $LiMnPO_4$ sample has an enhanced electrochemical performance as compared to pristine $LiMnPO_4$. The 2 wt% of ZnO-based $LiMnPO_4$ exhibited maximum discharge capacity of 102.2 mAh g^{-1} than pristine $LiMnPO_4$ (86.2 mAh g^{-1}) and 1 wt% of ZnO-based $LiMnPO_4$ (96.3 mAh g^{-1}). The maximum cyclic stability of 96.3 % was observed in 2 wt% of ZnO-based $LiMnPO_4$ up to 100 cycles. This work exhibited a promising way to develop a surface-modified $LiMnPO_4$ using ZnO for enhanced electrochemical performance in device application.

Keywords Cathode materials · Surface modification · ZnO coating · $LiMnPO_4$ · Electrochemical study

✉ S. Ramesh
rameshtsubra@gmail.com

[1] Department of Physics, Center for Ionics University of Malaya, University of Malaya, 50603 Kuala Lumpur, Malaysia

[2] Faculty of Mechanical Engineering, University Technical Malaysia Melaka (UTeM), 76100 Durian Tunggal, Malacca, Malaysia

Introduction

Long life-span, high-power density, and high-energy density are the attractive factors to promote lithium ion batteries as the most suitable candidate for electric vehicles and energy storages [1, 2]. Nowadays, most of the researchers are mainly focusing on the development of new cathode materials, which play a significant role in lithium ion batteries [3]. Since 1997, olivines started to get attention as high possible candidates as cathodes materials, even though $LiMnPO_4$ is having a higher voltage (4.1 V vs Li) than that of $LiFePO_4$ (voltage 3.4 V vs Li) but lower conductivity (10^{-10} S cm^{-1}) as compared to $LiFePO_4$ (1.8×10^{-9} S cm^{-1}) which lead to hinder the high capacitance of $LiMnPO_4$ in energy storage applications [3, 4]. While considering these limitations, increasing efforts have been continuously found on the enhancement of electrochemical performance in $LiMnPO_4$.

Doping with metal elements plays an important role to enhance the ionic conductivity of $LiMnPO_4$ such as Fe [5, 6], Cr [7], Zn [8], Ni [9], V [10], etc. Moreover, some researchers focused on dual substitution [11–13]. Besides that, $LiMn_2O_4$ was incorporated with $LiMnPO_4$ by one-step polyol-assisted pyro-synthesis [14]. Herein, thermal stability of this composite was improved due to the incorporation of electrically active $LiMn_2O_4$ with non-electrically active $LiMnPO_4$ and the discharge capacity was found to be ~142 $mAhg^{-1}$.

Surface modification is one of the effective methods to overcome cycling instability at higher voltages [5, 6]. Coating reduces the side reactions of cathode and electrolyte which causes negative effects to the electrochemical performance [15–18]. Carbon coating leads to enhance the electronic conductivity of $LiMnPO_4$ [19–21]. Zhu et al. stated that the in situ carbon (4.54 wt%)-coated $LiMnPO_4$ exhibits improved

Ref.: Ms. No. BOMS-D-15-00998R1
Na doped LiMnPO4 as an electrode material for enhanced lithium ion batteries
Bulletin of Materials Science

Dear Dr Duraisamy,

I am pleased to tell you that your work has now been accepted for publication in Bulletin of Materials Science.

Thank you for submitting your work to this journal.

With kind regards

A K Shukla
Editor
Bulletin of Materials Science

Na doped $LiMnPO_4$ as an electrode material for enhanced lithium ion batteries

K. Rajammal[a], D. Sivakumar[b], Navaneethan Duraisamy[a], K. Ramesh[a], S. Ramesh[a]

[a] Center for Ionics University of Malaya, Department of Physics, University of Malaya, Kuala Lumpur 50603, Malaysia

[b] Faculty of Mechanical Engineering, University Technical Malaysia Melaka (UTeM), 76100 Durian Tunggal, Malacca, Malaysia

Corresponding author

[*] E-mail: rameshtsubra@gmail.com, Tel: +603-7967 4391, Fax: +603-7967 4146

Abstract

We report the influence of sodium (Na) incorporated lithium manganese phosphate as an active material on its performance of electrochemical study for energy storage application. The $Li_{1-x}Na_xMnPO_4$ with different mole ratios ($x = 0.00 \leq x \leq 0.05$) are synthesized via simple sol-gel method. The discharge capacity of $Li_{1-x}Na_xMnPO_4$ is varied with respect to mole ratios of sodium incorporation. The maximum discharge capacity of 154.1 $mAhg^{-1}$ is observed in $Li_{0.97}Na_{0.03}MnPO_4$, which is higher than pristine $LiMnPO_4$ and other Na incorporated $LiMnPO_4$. The maximum cyclic stability is found to be 84.15 % up to 60 cycles. Therefore, these result demonstrated that the $Na_{0.03}$ incorporated $LiMnPO_4$ play a significant role in future energy storage application.

Keywords: $LiMnPO_4$, sodium doping, cathode materials, electrochemical study, lithium ion batteries